Escola Tècnica Superior d'Enginyeries
Industrial i Aeronàutica de Terrassa
UNIVERSITAT POLITÈCNICA DE CATALUNYA

Study on conduction mechanisms of medium voltage cable XLPE insulation in the melting range of temperatures

This Thesis is submitted in partial fulfillment of the requirements for the degree of Doctor of Philosophy in Physics by

Jordi Òrrit Prat

Main supervisor: Joan Belana Punseti

DILAB - Laboratori de Física dels Materials Dielèctrics
Departament de Física i Enginyeria Nuclear
Universitat Politècnica de Catalunya

December 2011

Acknowledgements

I would like to thank my Ph.D. supervisor, Dr. Juan Belana, for his insight, guidance and support. Without his involvement in all the stages of the research this thesis would not have been possible.

I am extremely grateful to Dr. Miguel Mudarra for his support and advice, Dr. Jordi Sellarès for his teamwork and contributions, Dr. José Antonio Diego for his assistance and remarks, and Dr. Juan Carlos Cañadas for his help and patience. The work and technical expertise of Jaume Sala have been invaluable. I sincerely thank Teresa Lacorte of Department of Materials Science and Metallurgy, for her essential collaboration in FTIR studies. I am also indebted to Dr. Juan de Dios Martínez and Elisenda Casals, of General Cable S.A., for their assistance and cooperation, to Dr. Fabian Frutos and Dr. Miguel Acedo of Universidad de Sevilla, who performed ARC measurements, and to Andrés Aragoneses, Dr. Idalberto Tamayo and Alexander Lebrato for their support and encouragement.

This thesis has been possible thanks to financial support from the Spanish Ministry of Science and Technology (PETRI 2007-0060), the company General Cable S.A. and the Agència de Gestió d'Ajuts Univeristaris i de Recerca de la Generalitat de Catalunya (2009SGR1168 and 2005SGR00457).

Finalment, voldria expressar el meu més sincer agraïment a la meva família i amics per la paciència i comprensió que han tingut i el suport que m'han ofert durant tot el temps que ha durat aquest treball, especialment als meus pares, Josep i Núria, i a la Roser.

Table of contents

1. INTRODUCTION TO POLYMERS AND DESCRIPTION OF POLYETHYLENE PROPERTIES

Prior to study the characteristics of *XLPE power cables* electrical properties and conduction mechanisms thoroughly, it can be convenient to place a brief description of polymers and, particularly, of polyethylene.

Polymers can be found naturally in living things like paper, starch, leather, silk, cotton, rubber, wool or wood. There are also synthetic polymers like synthetic rubber, plastics or fiberglass. Natural polymers have been present in human activity for centuries and synthetic ones are increasing their presence more and more. For this reason, a big amount of scientists are focusing their research on physical properties of polymer materials.

In the case of polyethylene this research has been frequently centered on properties related to its service as electrical insulation. Dielectric spectroscopy and electrical characterization can be useful to determine such properties and to relate them to other chemical and physical features. The purpose of this chapter is to summarize the basic chemical and physical knowledge of polymers that can provide the context where this work is placed.

1.1 Chemical structure of polymers

A *polymer* (from the Greek word *polymeros* –πολυμέρος– that means "composed of many parts") is a substance composed of molecules characterized by the multiple repetition of one or more species of atoms or groups of atoms, linked to each other in amounts sufficiently great to provide a set of properties that do not vary markedly with the addition or removal of one or few of the repeating units. These large molecules are named *macromolecules*. The term "macromolecule" is used as a synonym for polymer, but there is also another usage of the term that doesn't incorporate the repetition of parts [1]. In the simplest case, these repeating groups form a linear chain. These are named linear macromolecules (linear polymers) and the chain can have different shapes. In the case of the branched polymers the macromolecules are composed of a main chain with one or more substituent side chains. Star polymers, comb polymers and brush polymers are special cases of this polymer type. There are also cross-linked polymers with a branch point from which at least four chains emanate. A polymer molecule with a high degree of cross-linking is referred to as a *polymer network*. The unit forming the repetitive pattern is called *constitutional repeating unit* (CRU) [2] or *structural repeating unit* (SRU) [3], whereas the source molecule from which the polymer is obtained is a *mer* or *monomer* (this term sometimes is used to designate de repeating unit too). Traditionally, the name of one polymer was composed by the name of the monomer with the prefix "poly", like polyethylene, polypropylene, etc. However, currently it is preferred a structure-based nomenclature consisting in names of the sort poly(CRU) [4].

A polymer derived from one species of (real, implicit or hypothetical[a]) monomer is a *homopolymer*. On the other hand, polymers derived from more than one species of

[a] 'Many polymers are made by the mutual reaction of complementary monomers. These monomers can readily be visualized as reacting to give an 'implicit monomer', the homopolymerization of which would give the actual product, which can be regarded as a homopolymer. Common examples are poly(ethylene

monomer are *copolymers* (or *heteropolymers*). Regarding the *polymer backbone* structure, there are *homochain* or *heterochain* polymers depending on if the main chain is constructed from atoms of a single element or of two or more elements. For instance, polyethylene is a C-chain homopolymer: 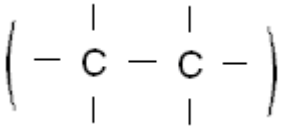

Furthermore, the asymmetric homochain polymers can be classified according to their *tacticity* (or *stereoregularity*), that is, the regularity of *substituent* (an atom or group of atoms substituted in place of a hydrogen atom on the main chain of a hydrocarbon) positions if the molecule could be laid out flat. Thus, *isotactic* polymers have all the substituents on the same side; in *syndiotactic* polymers the substituents alternate consecutively and *atactic* polymers have them randomly alternated.

1.2 Chemical reactions in polymers

By the chemical point of view, there are three possible types of reactions [5]:

a) Reactions that respect the macromolecular skeleton: reactions of substitution and cyclization.

b) Reactions that fragment the molecular chain, like degradation reactions.

c) Reactions that increase the molecular net by creating transverse bonds; those are cross-linking and branching reactions.

In the context of this work, it is interesting to see the b) and c) cases:

1.2.1 Chemical degradation reactions

Degradation reactions are those that, by means of the action of different agents, can cause a molecular weight decrease and an alteration of the physical properties of polymers. Maintaining these degrading phenomena during enough time leads to a macromolecular skeleton total destruction. As a consequence, to study these reactions is very important from the industrial point of view.

Although chemical properties of macromolecular compounds are strongly dependent on those of their monomers, degradation mechanisms of polymers are not always similar to those of monomeric units. These differences (in the decomposition temperature or in the by-products) could be explained by two reasons:

- Macromolecules frequently present labile structural anomalies (ether bonds, peroxide, head-to-head bonds, etc) from which reactions initiate.

---

terephthalate) and poly(hexamethylene adipamide)'; 'Some polymers are obtained by the chemical modification of other polymers such that the structure of the macromolecules that constitute the resulting polymer can be thought of as having been formed by the homopolimerization of a hypothetical monomer. These polymers can be regarded as homopolymers. Example: poly(vinyl alcohol)' [6].

- A lot of simple reactions become multiple reactions, due the environment created by the molecular structure in which the reaction evolves.

Otherwise, there are two possible groups of degradation mechanisms:

- Degradations by random reactions, in which the macromolecular skeleton split at random, that lead to fragments with a molecular weight considerable higher than of monomers.

- Multiple depolymerization reactions, corresponding to a release of successive monomeric units, starting from a chain end.

There are also different degrading agents that can affect polymers in different ways:

1) Heat is a powerful degrading agent. Below 200ºC most polymers suffer changes in their properties, essentially due to breaks of bonds C-C or C-H. To obtain more thermal resistant compounds it is necessary to use mineral skeletons with silicon, boron, fluorine or phosphorus. In the case of depolymerization, it is possible to improve the polymer thermostability by modifying the chemical nature of chain end from which reaction initiates, or adding an undepolymerizable *comonomer* to the main chain. Furthermore, thermal degradation takes part in the polymerization mechanism, carried out under the heat action, limiting the macromolecular chain growth.

2) Many polymers (polypeptides, cellulose) can be affected by hydrolysis reactions. In these, water can react not only with substituents but also with the main chain.

3) Ozone is an active degrading agent, even in the small concentrations that it can be found in the atmosphere. Thus, ozone causes breaks on strained rubber perpendicular to the straining direction. This degradation is due to an ozone fixation in macromolecular skeleton‘s double bonds, provoking in this way the breaks. This phenomenon is accompanied of a considerable decrease of mechanic and elastic properties of the polymer.

4) In many cases peroxides are responsible of macromolecular compounds *aging* (mechanical resistance loss, dielectrical properties loss, insolubility). Their presence in polymers can be due to polymerization or cross-linking by-products or, alternatively, due to oxygen and light combined action over impurities or polymeric chains.

5) Light and, principally, UV radiation degrade the polymers either directly when they have chromophore groups in their structure or in their extremities, due to an initiator, or by absorbent impurities that generate radicals which can initiate breaks in chains.

6) Finally, there are those degradations suffered by macromolecular compounds submitted to mechanical actions like crushing, straining and extrusion. Those degradations can decrease their molecular weight. The mechanism of this type of

degradation could consist in double bond brakes. In other cases, it could be caused by peroxides originated due the presence of oxygen.

1.2.2 Cross-linking reactions

Cross-linking reactions seek to create transverse bonds between lineal macromolecules to obtain a three-dimensional macromolecular net. There are different ways to achieve this goal:

1) Adding to the monomer, during polymerization, a certain quantity of compound with two polymerization functions. For example, introducing divinylbenzene into a vinylic polymerization produces a cross-linked compound.

2) Using a chemical agent (called *catalyst* or *initiator*) capable of react with the macromolecular chain groups. Usually, it is necessary to heat the polymer to initiate the cross-linking reaction. This process is generally known as *curing* and, after it, the shape of the polymer is irreversibly set. For this reason these polymers are known as *thermosets*. On the other hand, polymers that are not cross-linked, and can be remoulded to other shapes, are known as *thermoplastics*.

3) By submitting the polymer to ionizing radiations to form free radicals in the chains that can recombine to obtain transverse bonds.

In the second case, a typical curing process is that of the *vulcanization*. This method is applied to natural rubber or similar plastic materials and involves high temperature and the addition of curing agents like sulfur or peroxide. This kind of reaction is widely used to give some polymers useful properties as elasticity or strength. For instance, the insulation of power cables operating from 11 kV up to 500 kV is made from *cross-linked polyethylene*, and this is generally obtained from peroxide cross-linkeable low density polyethylene by means of vulcanization [7]. In this process, the material is heated at high temperatures where the peroxide (usually a 1–2%) decomposes and radicals are generated. These radicals take away hydrogen atoms from the polymer backbone creating *macroradicals*. And when two macroradicals combine a cross-link is formed.

As a result of these reactions, above the *melting point* (for *semi-crystalline polymers*) or above the *glass transition temperature* (in case of *amorphous polymers*) a cross-linked polymer becomes rubber-like rather than liquid. For this reason, polymers for which this happens at room temperature are known as *rubbers*.

1.3 Physical structure [8]

At the most elemental level, the polymeric physical structure is defined by the *molecular conformation*. Since the intermolecular forces in polymers are of the secondary, van der Waals' type, there is an optimum intermolecular spacing at which their potential energy is a minimum. Thus the total internal free energy of a system of molecules is lower when the molecules adopt a regular structure rather than a random arrangement. For this reason the *crystallization* is spontaneous in most solids. However, only few polymers have a completely regular crystal structure. In fact, most *crystalline*

polymers are always semi-crystalline, which results in a density smaller than the calculated on the basis of the physical dimensions and molecular mass of their crystallographic unit cell. In such semi-crystalline polymers the long molecules can traverse several discrete crystallites. In polyethylene, the most stable conformation of the polymer chain is a simple planar zig-zag (*trans conformation*), since the separation of adjacent hydrogen atoms is greater than their van der Waals' diameter (0.239 nm) and this conformation minimizes the Gibbs free energy. For other homopolymer chains that have larger side group molecules this is not possible since it would leave no sufficient spacing for the side group atoms to fit. These molecules adopt a minimal energy configuration resulting in a helical chain structure. More complicated structures, including most heterochain molecules, tend to have less apparent regularity to their molecular conformation.

In amorphous polymers the molecules are randomly oriented and coiled up. Some polymers are generally considered as amorphous but can in fact display crystallinity if their chains are partially aligned by strains introduced during manufacture as it happens with poly(vinyl chloride). By using a freely-jointed chain model (in which the joints are the covalent bonds) it can be seen for a random or *Gaussian* chain that the mean distance between the chain ends is $l \cdot n^{1/2}$, where l is the length of each rigid segment between joints and n is the number of randomly oriented segments.

Below their glass transition temperature, T_g, amorphous polymers become a *glass*. In this state the polymer can be thought of as cross-bonded by van der Waals' attractions between molecules and there are no segmental motions of the backbone but just intra-segmental movements. Above the glass transition temperature, thermal fluctuations are too great for these bonds to be effective and the un-cross-linked amorphous polymers are viscous liquids. For cross-linked amorphous materials and those with very long and entangled chains, chains become constrained by their neighbors and true liquid behavior cannot be established above the T_g, where they behave as rubbers.

In amorphous polymers and in the amorphous regions of semi-crystalline polymers the easiness of polymer chains segmental motions decreases catastrophically (*i.e.* with an increasing rate of decrease) as the temperature drops towards the glass transition temperature. This behavior causes a slowing down in the return to equilibrium of induced mechanical strains and dielectric polarization following removal of the applied stress. This phenomenon can be traced through the mechanical and dielectric responses of the polymer chains (the so-called *α relaxation* associated with main-chain motions) at a constant temperature close to the T_g. As the temperature of the measurements is reduced the observed relaxation time increases and eventually becomes sufficiently long for a non-equilibrium state to exist for an observable period. Thus, when the system is cooled at a constant rate a change in the magnitudes of several physical properties is observed at the glass transition temperature for which the non-equilibrium state becomes metastable. If the temperature is further lowered in this region, the macroscopic viscosity and the relaxation rate asymptotically approach infinity at a temperature T'_g, which defines the *rigid* state. Between T_g and T'_g the metastable non-equilibrium state will exist long enough to be observable, but will allow a slow structural relaxation via segmental motion which thereby increases in density. This time dependent change as the system moves towards thermal equilibrium is what is known as *physical aging* (not to be confused with the more general concept of "aging" that appears in section 1.5). Below T'_g the material is essentially rigid except for intra-

segmental motions (which give rise to the so-called *β relaxation*, observable by dielectric or mechanic measurements) and aging is expected to be practically non-existent. On the other hand, it has been suggested that semi-crystalline polymers will also present this form of aging at temperatures above their bulk T_g because the amorphous regions adjacent to the crystallites will have higher glass transition temperatures than that of the rest.

Polymers that usually are found in a semi-crystalline state at room temperature can be obtained in an amorphous form by quick quenching from the melted state. Then, the polymer is a *super-cooled liquid* that becomes a glass when it is cooled down below the T_g, as it happens with the always amorphous polymers. But if a semi-crystalline polymer is cooled from its liquid state through the *melting temperature* (T_m) at a lower rate, then crystallization will take place in the material. During this process, the polymer specific volume (which is the reciprocal of the density) drops abruptly reflecting the closer and regular packing of molecules into crystalline structures. Both amorphous and semi-crystalline polymers are mechanically rubbery at temperatures between the melting and glass transition temperatures. In the rigid glassy state below the glass transition temperature the specific volume of both amorphous and semi-crystalline polymers continues to decrease with temperature, but a slower rate.

1.4 General description of polyethylene

The polyethylene (*PE*) is a simple non-polar polymer obtained from polymerization of ethylene and formed by chains of methylene units (-CH_2-)

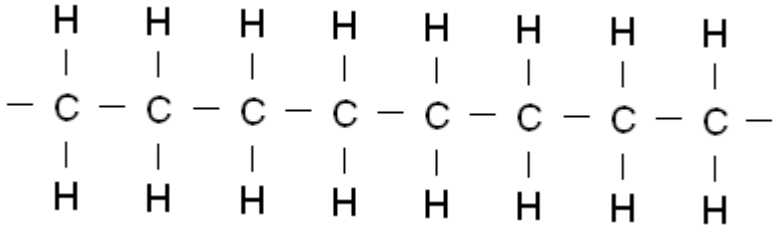

In IUPAC nomenclature the preferred source-based name for polyethylene is polyethene while the correct structure-based one is poly(methylene)[b].

The molecule known as ethylene (ethene in IUPAC nomenclature[c]), C_2H_4, is found in a gaseous state under normal temperature and pressure conditions. It consists of two CH_2 groups connected by a double bond, CH_2=CH_2:

[b] 'The Commission recognized that a number of common polymers have semisystematic or trivial source-based names that are well established by usage; it is not intended that they be immediately supplanted by the structure-based names. Nevertheless, it is hoped that for scientific communication the use of semisystematic or trivial source-based names for polymers will be kept to a minimum' [9].

[c] 'The name "ethylene" should be used for a divalent group, "-CH_2CH_2-" only. For the monomer, "CH_2=CH_2" the correct name is "ethene"' [10].

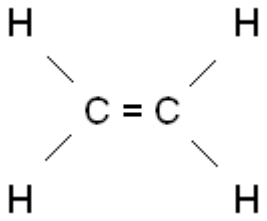

X-ray diffraction measurements have proven a linear structure of polyethylene and that the distance between molecules of polymer chain is 2.53Å [11]. Nevertheless, chains can contain ramifications as it happens in commercial polyethylenes. This chain branching can difficult the formation of crystalline structures.

The polyethylene is a solid, off-white translucent and insipid material. It is a thermoplastic semi-crystalline polymer whose density and crystalline degree depend on the type. Its melting range of temperatures goes from 50ºC to 105–130ºC. In the melted state, polyethylene becomes transparent. Its glass transition temperature (T_g) is located below the room temperature [12].

The polyethylene is sensitive to oxidation, especially at high temperatures, which lead to a worsening of its electrical properties (oxidation enhances homocharge and the conduction current in polyethylene [13] and reduces DC *breakdown strength* [14]). This makes necessary the use of antioxidants in electrical applications like in power cables insulation.

The polyethylene has interesting physical properties like electrical insulating power, resistance to low temperatures and a low water absorption degree. It also has chemical inertness and it is not attacked by acids, bases, salts or other chemical reagents [15] (PE can work with sulphuric acid or nitric acid at 98% and 50%, respectively). At room temperature, most polyethylene types are not soluble in any solvent. At 60ºC they are soluble in aliphatic, aromatic or chlorinated hydrocarbons (except in the case of XLPE). Some polar liquids like alcohols, aldehydes, esters, ketones and phenols can be absorbed by polyethylene making it fragile.

Due to its electrical, mechanical and chemical properties, polyethylene has several applications: pipe, coatings, film, electrical insulation, cable and wire jacketing, packaging, fittings, tubing…

By modifying the polymerization conditions, branching can be produced or inhibited to a large extent in PE. Since branching reduces the potential for regular molecular packing and so lowers the density, it produces the *Low Density Polyethylene* (*LDPE*). On the other hand, there is a non-branched PE, the *High Density Polyethylene* (*HDPE*). Although LDPE has worse mechanical properties than HDPE, it has excellent electrically insulating ones. Cross-linked polyethylene (abbreviated XLPE or PEX) is obtained from LDPE by means of vulcanization. Another commercial type of polyethylene is the *Linear Low Density Polyethylene* (*LLDPE*), a copolymer of ethylene with a comonomer such as butane hexane or octane. Unlike LDPE, it contains no long–chain branches, only short ones. Some of the physical parameters of the main commercial PE grades are summarized in Table 1.1, and their chains configurations are

schematically represented in Figure 1.1. In the case of XLPE, there are properties like the crystallinity and the melting temperature that do not have a fixed value but they depend on the cross-linking process features.

Property	Units	HDPE	LLDPE	LDPE	XLPE
Breakdown Strength, E_B	kV/mm	100	75	75	50
Dielectric Constant, ε_r		2.3	2.3	2.2	2.4
Volume Resistivity, ρ	Ω·cm	5×10^{17}	5×10^{17}	5×10^{17}	10^{16}
Dielectric Loss, *tan* δ (1MHz)		10^{-3}	10^{-3}	$2x10^{-4}$	10^{-3}
Crystallinity	%	80–95	70–80	55–65	—
Density	g/cm^3	0.95	0.93	0.92	0.92
Melting Point	ºC	130	120	110	—
Tensile Strength	MPa	25	15	13	31

Table 1.1. Polyethylene parameters [16].

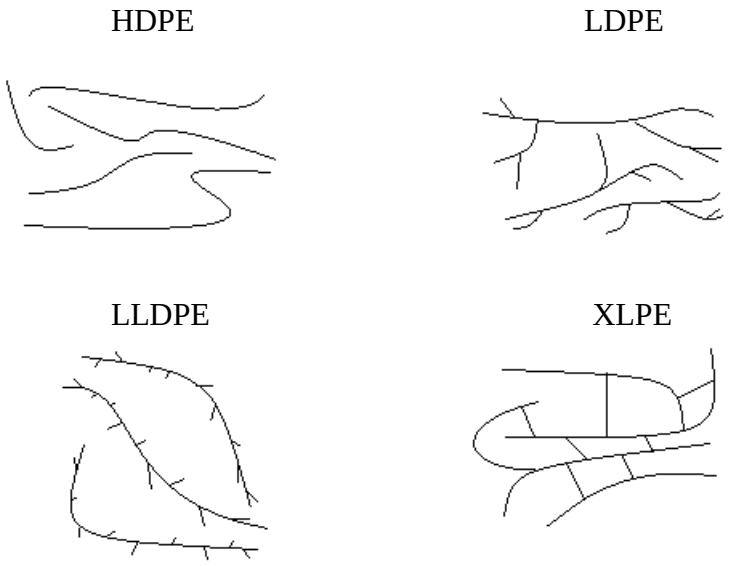

Figure 1.1. Chains configuration diagram for the main commercial polyethylene grades.

Besides the four mentioned categories, there are also other commercial PE grades like *High Density Cross-linked Polyethylene* (*HDXLPE*), *Ultra High Molecular Weight Polyethylene* (*UHMWPE*), *High Molecular Weight Polyethylene* (*HMWPE*), *Medium Molecular Weight Polyethylene (MMWPE), Medium Density Polyethylene* (*MDPE*),

Linear Medium Density Polyethylene (*LMDPE*), *Low Molecular Weight Polyethylene* (*LMWPE*), *Ultra Low Molecular Weight Polyethylene* (*ULMWPE* or *PE-WAX*) or *Very Low Density Polyethylene* (*VLDPE*).

1.5 Morphology, aging, degradation and breakdown of polyethylene

At room temperature polyethylene is found in the semi-crystalline state. The crystalline fraction is formed when the material is cooled down from the melt. This phase is organized in *lamellae* normal to the chain axis, whose structure is related to the characteristics of the thermal treatment and the conditions of crystallization. In lamellae, the PE chains are aligned in planar zig-zag arrays with a *trans* conformation. Usually they are found radially ordered by forming *spherulites* around a nucleating site in an amorphous background, as it is shown in Figure 1.2. The diameter of a typical spherulite is of ~40μm, the lamellae are ~100nm wide and their cross-sections around ~20nm in the PE chain direction (*c axis*) [17]. Annealing at high temperatures increases the thickness of the lamellae as at higher temperatures longer chains crystallize. On the other hand, higher molecular weight results in larger spherulites. Therefore, molar fraction of the crystalline phase depends on the type of polyethylene (for instance, see the Table 1.1).

Polyethylene used in power cables insulation is cross-linked by chemical initiators like peroxides, which link polymeric chains between them and create a net. By cross-linking, polyethylene electrical, chemical and mechanical features are improved and when the material is heated above its melting temperature it remains compact. This results quite useful since polyethylene crystalline fraction melts at relatively low temperatures.

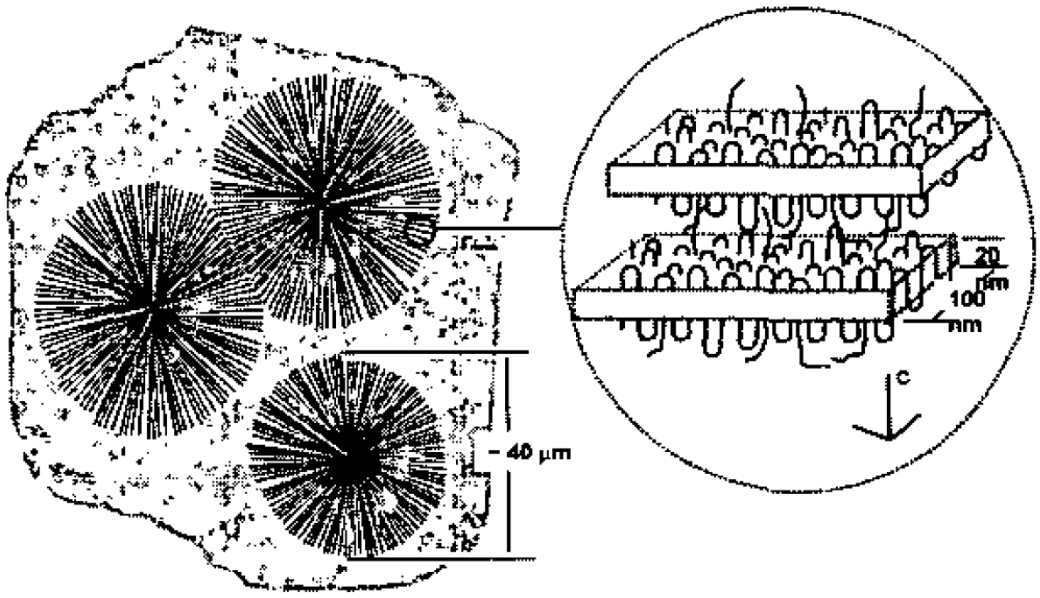

Figure 1.2. Morphology of semi-crystalline PE showing spherulitic arrays of lamellar crystallites in an amorphous background [17].

However, cross-linking polyethylene produces smaller spherulites and thinner lamellae. The addition of antioxidant will counteract the development of spherulites and only stacks of lamellae are formed, as may happen in XLPE power cable insulation [18].

Furthermore, Muccigrosso and Phillips [19], who have worked with 138 kV cable insulation supplied by Phelps-Dodge Wire and Cable Co., state that, though the basic morphological unit remains the lamellae, they may be arranged in other than radial arrays. In this sense, at interfaces the lamellar growth must be columnar or transcrystalline. Besides, fabrication techniques like extrusion can originate a row-nucleated morphology like it happens in polymer films that have been extended by 100% before crystallization. In this case, lamellae grow from fibrils outwards normal to the direction of applied stress during crystallization. At pre-strain levels lower than 100%, sheaf-like spherulites oriented in the deformation direction appear.

In the referred work [19], the crystalline morphology of XLPE cable insulation and its relation to the cavity distribution have been determined. And the conclusions have been summarized as follows:

1. The crystalline morphology is predominantly spherulitic.

2. The larger cavities (5 to 10μm) are found at the junctions of three or more spherulites. These have been related by some authors to the presence of water in the cable.

3. The spherulitic boundaries contain micro-cavities and micro-channels which may be related to initiator by-products.

4. The spherulite boundaries oriented in the radial direction of the cable are likely to contain more defective structures.

5. Columnar growth is present in the outer skin (0.5mm thick). Circumferential cracks result at the interface of columnar and spherulitic growth.

6. The inner surface is 3mm thick and contains a row-nucleated morphology indicative of extensional flow in the melt. Circumferential cracks appear throughout this region, generally between morphological units.

The existing relationship between the crystalline morphology and cavities or voids is crucial as they can contribute to the electrical treeing through the insulator. A network of cavities throughout insulator represents a pathway for treeing that would consist in electrical discharges between consecutive cavities. Therefore, the morphology of XLPE is one of the main fields of work in the analysis of the electrical breakdown in power cable insulation.

Related with this subject are the so called **"**water trees**".** Water trees are dendritic patterns which can grow in polyethylene insulation in the presence of AC electric field and water [20]. Moureau et al. indicate that in the growth region, water trees consist of "tracks" of oxidised polymer which connect micro voids in the structure of the polyethylene [21]. In general, water trees are not the direct cause of failure of XLPE cable. However, electrical trees can initiate from water trees under surge conditions.

Recently, a typology for aging, degradation and breakdown processes has been suggested [22]. Breakdown is an event that is sudden and catastrophic, so the insulation cannot withstand the service voltage afterwards. Whereas breakdown occurs in less than

a second, degradation takes place over a period of time ranging from hours to years. Degradation is a process that increases the probability of breakdown and decreases the breakdown strength. Both breakdown and degradation are irreversible and directly observable (by the peep-hole through insulation in the case of breakdown whereas in the case of degradation microscopic or chemical techniques may be necessary). When degradation is diagnosed the prognosis is poor and the system is prone to breakdown. The processes involved in degradation, like the mentioned water treeing, take place on a micrometric or greater scale. In the case of water trees, they reduce the breakdown strength and lead to changes in the dielectric and viscoelastic responses. Typically, after a period of months to years, water treeing gives rise to electrical treeing. This degradation process, after a period of hours to weeks, leads to breakdown. This can be a discharge arc through the electrical tree or/and thermal breakdown if the tree is enough conductive. When degradation is quite advanced *partial discharges* (*PDs*) tend to appear. For this reason, PDs phenomena can be used as a degradation marker and a diagnostic tool [23]. Since some features of degradation and breakdown processes present a stochastic behavior, the relation between breakdown events and the breakdown voltage or the time to breakdown is also stochastic and fit the Weibull statistics [24].

The least well-known and clear process is the aging. It involves phenomena at molecular scale like nano-voids, bond scissions, traps formation, oxidation, etc. Although they may not reduce the breakdown voltage they can lead to degradation. Despite being difficult to observe, aging occurs throughout the insulation and along the entire service life. In the past two decades, different life models have been proposed by (i) Dissado, Montanari and Mazzanti (DMM) [25], (ii) the Bangor group including Lewis, Llewellyn, Griffiths, Sayers and Betteridge [26], and (iii) Crine and Parpal [27]. According to these theories, the aging rate is supposed to increase in regions of high space charge concentration (model (i)), high electro-mechanical stress (ii), or in regions of free volume that allow high local currents (iii). Model (ii) considers the breaking of chemical bonds as a starting point for the aging. In model (i), space charge accumulates at centers giving rise to enhanced electric fields and, electro-mechanically, to the formation of centers of aging (e.g. local chain scission). In model (iii), electrically induced mechanical deformation of intermolecular (van der Waals) bonds is the first step. Therefore, whilst model (i) considers that space charge is the cause of aging, model (iii) assumes that it is the effect. However, all three models agree on the idea that a section of the polyethylene can transfer between two alternative local states by overcoming an energy barrier. They consider that moieties (small regions) of the polymer may exist in either of the two states. In an unaged polymer, most of the moieties are in state 1 whereas, as aging progresses, more and more moieties switch to state 2. Moieties can surmount the energy barrier between the states by means of thermal activation. In model (ii), these states would comprise unbroken and broken bonds whereas the other two models are more general and may include molecular chain reconfigurations for example. The presence of a local electric field changes the relative proportions of the polymer in each of the alternative states at equilibrium and, according to the model (i), causes irreversible changes when a threshold field is exceed. It also accelerates the rate of approach to the equilibrium distribution from any arbitrary starting distribution. It is assumed that changes from state 1 to state 2 will eventually strain, and possibly lead to, nanometer and sub-micron sized voids when a sufficient concentration of moieties have switched to state 2. Therefore, regions of reduced density or free volume throughout the insulation will be formed. Areas that are

mechanically weakened in this way will increase in size leading to super-micron sized voids and the more rapid degradation associated with hot electrons injection, partial discharging and electrical treeing. On the other hand, since these processes are temperature dependent, aging results should therefore show a dependence on temperature. Thus, models (i) and (iii) arrive at different expressions relating the time to breakdown with field and temperature. However, to elucidate which theory is the most suitable more experimental data is necessary.

Recently, Crine [28] has presented a modification in model (iii) that includes the role of the electro-mechanical energy of the strained molecules at high fields. He concludes that C-C bonds breaking under moderate fields might explain aging processes and many electrical properties of polymers (including some results that had been fitted to *Sckottky*, *Poole-Frenkel* and *Space Charge Limited Currents* models[d]). Thus, once the bonds have been mechanically broken and radicals are formed, all the classical effects might occur and induce the breakdown. However, at high fields strain energy should be taken into account.

Currently it is accepted that the electrical failure of polymeric cable insulation is normally caused by the growth of damage starting from weak points like contaminants, protrusions and voids (*CPVs*) [29]. So, by manufacturing more perfect and cleaner XLPE, the features of the cable insulation have been improved. Thereby, the understanding of the aging mechanisms involved in the production of "macrodefects" (>10μm) from "microdefects" (<10nm) may be quite useful in order to make progresses in manufacturing processes. Related with this, the *European ARTEMIS* [30] program goals are the understanding of the electrical degradation and aging processes, the development of diagnostic methodologies for evaluating the state of aging and the reliability of in-service power cables, and the improvement of design and manufacturing techniques. ARTEMIS partners include manufacturers, material suppliers, electricity distributors, and a number of universities throughout Europe. Results show that combined thermal and electrical aging reduces the total void concentration and increases the total void internal surface area [31]. Other likely candidates for "aging markers" [29] are changes in voltage thresholds for space charge accumulation, increase of conductivity and electroluminescence, changes in apparent carrier mobility, changes in interphase fraction using FTIR, Raman and long period spacing by SAXS, relative band strengths in the fluorescence spectra, quantitative chemical characteristics extracted form FTIR spectra, and changes in the *Arrhenius plot* of the conductivity measured using low frequency and low field dielectric spectroscopy.

Finally, Boukezzi et al. [32] have studied the effect of aging just thermal on the XLPE. They have detected some chemical changes like oxidation (carbonyl groups such as aldehyde or ketone increase with aging). Furthermore, although this aging process does not modify the crystalline structure, it has a great effect on the crystallinity degree. Thus, crystalline fraction increases at the beginning of ageing and then it decreases. Reduction in crystallinity degree is more pronounced with higher ageing temperature. On the other hand, other authors have studied the effect of the cross-linking by-products and the results show that they influence the conductivity, space charge formation and charge traps generation in XLPE insulation [33–35].

[d] These models are discussed in chapter 2.

References

[1] Elk, S. B. *Journal of Molecular Structure (Theochem)*. **589–90** (2002), 27.

[2] International Union of Pure and Applied Chemistry. "Compendium of Macromolecular Nomenclature". Blackwell Scientific Publications, Oxford, UK (1991).

[3] Patterson, J. A.; Schultz, J. L. and Wilks, E. S. *J. Chem. Inf. Comput. Sci*. **35** (1995), 8.

[4] Kahovec, J.; Fox, R. B. and Hatada, K. *Pure Appl. Chem.* **74** (2002), 1921.

[5] Champetier, G. and Monnerie, L. "Introducción a la Química Macromolecular". ESPASA-CALPE, S.A., Madrid, Spain (1973), pp. 93–108.

[6] Extracted from "Glossary of basic terms in polymer science (IUPAC Recommendations 1996)". Jenkins, A. D.; Kratochvfl, P.; Stepto, R. F. T.; Suter U. W. *Pure Appl. Chem.* **68** (1996), 2287.

[7] Smedberg, A. and Gustafsson, B. *Proceedings of the 6th International Conference on Properties and Applications of Dielectric Materials*, **1** (2000), 243.

[8] Dissado L. A. and Fothergill J. C. "Electrical Degradation and Breakdown in Polymers". Peter Peregrinus Ltd. on behalf of the Institution of Electrical Engineers, London, UK (1992), chapters 1 and 3.

[9] Extracted from Kahovec et al. (2002).

[10] Extracted from "A Guide to IUPAC Nomenclature of Organic Compounds" IUPAC, *Blackwell Scientific Publications*, Oxford, UK (1993).

[11] Bayer, E. M. "Química de las materias plásticas" Editorial Científico-Médica, Barcelona (1965), p. 174.

[12] McCrum, N. G.; Read, B. E. and Williams, G. "Anelastic and Dielectric Effects in Polymeric Solids". Dover Publications, Inc., New York, USA (1991).

[13] Ieda, M.; Mizutani, T.; Suzuoki, Y. and Yokota Y. *IEEE. Trans. Electr. Insul*, **25** (1990), 509.

[14] Banmongkol, C.; Mori, T.; Mizutani, T.; Ishioka, M.; Ishino, I. IEEE Annual Report – *Conference on Electrical Insulation and Dielectric Phenomena*. (1997) 33.

[15] Bayer (1965) [11], p. 177.

[16] Wang, X.; Yoshimiura, N. *Proc. 1998 International Symposium on Electrical Insulating Materials*. Japan (1998), 109.

[17] Lewis, T. J.; IEEE Trans. Dielectr. Electr. Insul. **9** (2002), 717.

[18] Nilsson, H.; Dammert, R. C.; Campus, A.; Sneck A. and Jakasuo-Jansson, H. *IEEE 6th International Conference on Conduction and Breakdown in Solid Dielechics*. Vasteras, Sweden (1998), 365.

[19] Muccigrosso J. and Phillips P.J. *IEEE Trans. Electr. Insul.* **13** (1978), 172.

[20] Boggs, S.; Densley, J. and Kuang, J. *IEEE Trans. on Power Delivery*. **13** (1998), 310.

[21] Moreau, E.; Mayoux, C.; Laurent, C. and Boudet A. IEEE Trans. on Electr. Insul. **28** (1993), 54.

[22] Fothergill, J. C. *Proceedings of the 9th International Conference on Solid Dielectrics*, Winchester, UK (2007), 1.

[23] Gargari, S. M.; Wouters, P. A. A. F.; van der Wielen, P. C. J. M. and Steennis, E. F. *Proceedings of the 10th International Conference on Solid Dielectrics*. Potsdam, Germany (2010), 434.

[24] Dissado and Fothergill (1992) [8], chapter 14.

[25] Dissado, L.A.; Mazzanti, G. and Montanari G.C. *IEEE Trans.* Dielectr. Electr. Insul. **4** (1997), 496.

[26] Lewis, T. J.; Llewellyn, J. P.; van der Sluijs, M. J.; Freestone, J. and Hampton, R. N. *7th Conference on Dielectric Materials Measurements and Applications*. UK (1996), 220.

[27] Crine, J. P. *IEEE Trans. Dielectr. Electr. Insul.* **4** (1997), 487.

[28] Crine, J. P. *Proceedings of the 10th International Conference on Solid Dielectrics*. Potsdam, Germany (2010), 545.

[29] Fothergill, J. C.; Montanari, G. C.; Stevens, G. C.; Laurent, C.; Teyssedre, G.; Dissado, L. A.; Nilsson, U. H. and Platbrood, G. *IEEE Trans. Dielectr. Electr. Insul.* **10** (2003), 514. .

[30] "Ageing and Reliability TEsting and Monitoring of power cables: diagnosis for Insulation Systems" 5th Framework Program for Research and Technological Development of the European Union, project number BRPR-CT98-0724, 1998-2002.

[31] Markey L. and Stevens G. C. *J. Phys. D: Appl. Phys.* 36 (2003), 2569.

[32] Boukezzi, L.; Boubakeur, A.; Laurent, C. and Lallouani, M. *Iran Polym. J.* **17** (2008), 611.

[33] Hirail, N.; Minami, R.; Shibata, K.; Ohki, Y.; Okashita, M. and Maeno T. Annual Report – *Conference on Electrical Insulation and Dielectric Phenomena*. (2001), 478.

[34] Suh, K. S.; Hwang, S. J.; Noh, J. S. and Takada, T. *IEEE Trans.* Dielectr. Electr. Insul. 1 (1994), 1077.

[35] Hussin, N. and Chen, G. *Journal of Physics: Conference Series*. (2009), 183.

2. CHARGE TRANSPORT AND TRANSIENT CURRENTS IN INSULATING MATERIALS

2.1 Introduction

Together with dielectric properties, any study on the insulating features of a material has to consider also the charge transport properties. In this chapter we summarize the principles of the charge transport processes in totally or partially amorphous insulating materials. The influence of the nature of electrodes, the band structure, the nature of the charge carriers and the role of the bulk and the union at sample interfaces are discussed here. In addition, transient currents, attributed to both dipolar or charge transport processes, are analyzed and the most widely accepted models are commented. Finally, in the last section some computer simulation models for charge transport are discussed.

2.2 Conduction in insulating materials

When a stationary field is applied to any dielectric material, it takes place a transient regime that is governed by dielectric as well as charge transport processes. The electric current density as a function of the time *t* and the position inside the material *x*, is given by

$$J(x,t) = \rho(x,t)\,\mu(T)F + \sigma(T)F - \delta\frac{\partial\rho}{\partial x} + \frac{\partial D}{\partial t}, \tag{2.1}$$

where $\rho(x,t)$ is the *excess charge density*, $\mu(T)$ is the *drift mobility*, $\sigma(T)$ is the *ohmic conductivity*, δ is the *diffusion coefficient*, F is the *electric field*, $D=\varepsilon_0 F+P$ is the *electric displacement*, ε_0 the *vacuum permittivity* and P the *polarization density*. In a neutral medium it holds that $\frac{\partial\rho}{\partial x}=0$.

After a sufficiently long time, a new situation is reached in which the electric response consists in a stationary conduction current, that is, electric current is governed only by charge transport processes (for steady state it holds that $\frac{\partial D}{\partial t}=0$).

All the materials are conductive to a greater or lesser degree, and all of them suffer some kind of dielectric breakdown when the applied field is high enough. For low applied fields the conduction process is *ohmic* in most materials (the current density J is linear with the field F). If the applied field intensity increases, then conductivity becomes field-dependent and it looses the linearity typical of Ohm's law. Conductivity in dielectric materials can be electronic, ionic or both at once. The separation between the two contributions in experiments is difficult, especially for high electric fields.

When electrical measurements are performed on insulating materials it is necessary to establish electrical contacts on the samples, which are usually metallic. The effect of this union on the conductivity is significant, becoming decisive in the case of thin sheets. Therefore, in the next subsections the main features of the different types of contacts are reviewed.

2.2.1 Metallic electrodes

Although polymeric insulating materials are found in glassy or polycrystalline forms, the existence of a band structure is widely accepted. The *band* or *energy gap* (the minimum energy required to excite the electrons from the valence to the conduction band by direct or indirect transition) is wide, which implies that there are few intrinsic charge carriers free at room temperature. The presence of impurities (ions coming from the reagents used in the material preparation) or defects (chain ends, intergranular interfaces…) in such materials can introduce a significant amount of charge carriers in *donor* or *acceptor* levels in the band gap [1,2].

When metal and insulator are brought in contact, their *Fermi levels* are equalized resulting in a transfer of electrons in one or the other direction, depending on the values of their *work functions*, W_m and W_d for metal and dielectric, respectively (work function is the minimum energy needed to remove an electron from a solid material to a point immediately outside the solid surface, that is, the energy needed to move an electron from the Fermi level into vacuum). Thus, a charge distribution is formed close to the interphase, which gives rise to a potential barrier that controls the electron flow through the union, as it can be seen in Figure 2.1. The barrier height W that hinders the metal electrons movement towards the insulator is given by

$$W = W_m - \chi \tag{2.2}$$

where χ is the *affinity* of the insulator, the energy difference between the bottom edge of the conduction band and the vacuum level. Otherwise the contact potential or potential barrier seen by the electrons moving towards the metal electrode is

$$eV_c = W_m - W_d \tag{2.3}$$

where e is the electron charge. When an external field is applied all the voltage falls across the insulator. Thus, whereas V_c can be modified, W is supposed to be independent of the voltage.

In Figure 2.1, the three types of metal-insulator contacts are depicted. These contact types are classified according to their behavior in relation to the conduction processes [3]. In this chapter we suppose that in the dielectric there is a certain concentration of donor levels (it behaves analogously to an *n-type* semiconductor). In the case that the levels were acceptors the treatment is analogous [4].

2.2.1.1 Injecting electrodes (ohmic contact)

The *ohmic* or *injecting contact* takes place when the work function of the metal is lower than the dielectric. When Fermi levels are equalized, a transfer of electrons to the insulator conduction band occurs and a negative space charge region is formed in the insulator. The effect of the local electric fields in this region bends the bottom edge of the insulator conduction band upward as depth increases, until the equilibrium is reached in the dielectric bulk. This region with negative space charge is termed *accumulation region* and has a width labelled λ (Figure 2.1 (a)). Equilibrium is reached

when the energy difference between the Fermi level and the conduction band bottom edge is $W_d - \chi$.

If the contact is poled so electrons move from the insulator to the electrode, these do not found a potential barrier on its way. On the other hand, if the poling field is opposite, the accumulation region behaves as an effective cathode and it provides a sufficient amount of electrons for the conduction. Thus, electrical current is determined by the bulk characteristics of the insulator, since the contact is able to provide or extract charge carriers from the dielectric at the rate imposed by the conduction processes.

Ohmic contacts are specified mathematically by $F_{electrode}=0$, where $F_{electrode}$ is the field at the ohmic electrode, regardless of the carrier emission current [5].

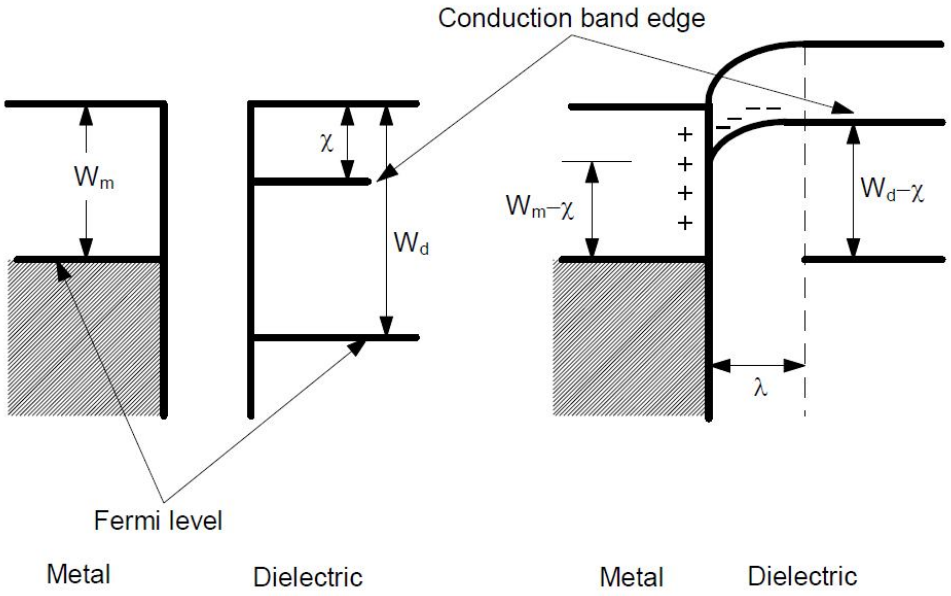

(a)

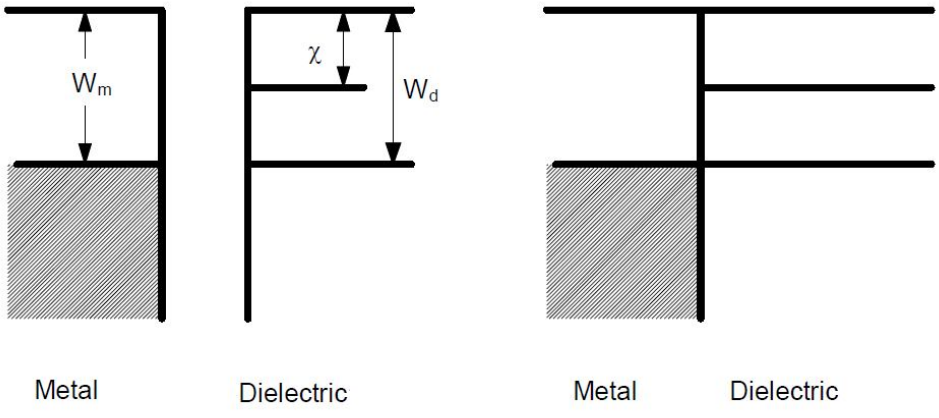

(b)

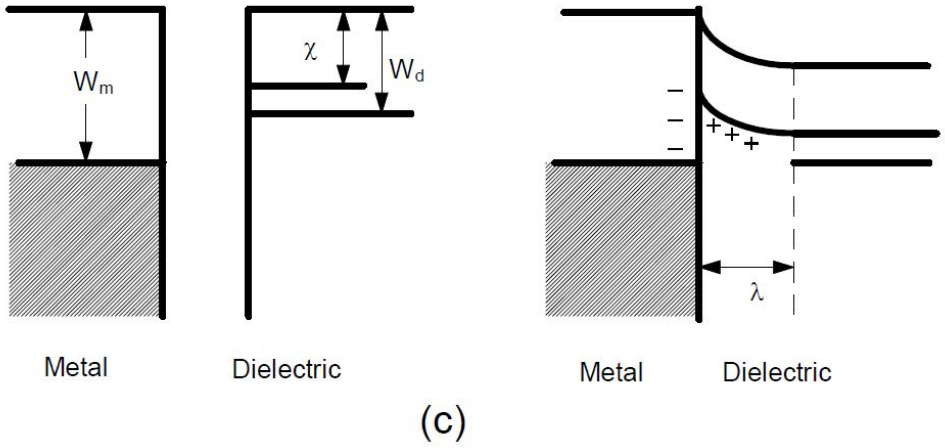

Figure 2.1. Energy diagram of the three metal-insulator unions before (left) and after (right) the contact: (a) Injecting contact. (b) Neutral contact. (c) Blocking contact.

2.2.1.2 Blocking electrodes (Schottky contact)

Figure 2.1 (b) shows the metal-insulator contact if the metal work function is higher than the insulator. When the union is established, some electrons move from the dielectric to the metal until equilibrium is reached. This results in a region of the insulator with an excess of non-balanced positive charge, formed by ionized donor levels. This λ wide zone is called *depletion region*. Like in the ohmic union, the presence of space charge leads to a curvature of the conduction band bottom edge, although in this case the band bends downward with depth.

In this case, the behavior of the union is determined by the density of donor states in the depletion region. If the amount of donor states is low, the curvature of the conduction band bottom edge will be negligible, resulting in a neutral contact-like behavior. If the density is high, it behaves analogously to a semiconductor. Then, the union becomes a *Schottky* or *rectifier contact*. When the insulator is negatively biased with respect to the metal due to an external applied voltage *V*, electron movement to the metal is favored by the decrease of the potential barrier, $e(V_c - V)$. But if the insulator is positively biased, the barrier height in the direction to the metal increases while *W* remains constant. Therefore, the movement of electrons through the insulator-metal union is comparatively favored if the insulator is negatively biased.

Blocking contacts are specified mathematically by $J_{electrode}=0$, where $J_{electrode}$ is the electron/hole emission at the blocking cathode/anode, regardless of the field at the electrode [5].

2.2.1.3 Neutral contact

Figure 2.1 (c) shows a diagram of the *neutral contact*. In this kind of contact the work functions of the metal and the dielectric are equal, and so their conduction and valence bands are not altered by the union. When the applied fields are low, the cathode can provide electrons to the insulator conduction band to balance the carriers that flow towards the anode due to the conduction process. In this case the behavior of the contact is ohmic. By increasing the electric field intensity, the current supplied by the electrode

reaches a limit value and the conduction looses its ohmic behavior. The limit is determined by the saturation value of the thermionic emission through the barrier amid the materials. This limit is given by the *Richardson equation* (see section 2.3.1, equation (2.6)).

2.2.2 Intrinsic and extrinsic conduction

In first approach, insulators can be described as semiconductors which band gap is of at least 5eV. Some crystalline (like sodium chloride, lithium fluoride) or amorphous (like PMMA) insulators are transparent and colorless. This is due to the fact that even the most energetic photons of the visible spectrum (around 3.18eV) can not be absorbed by electron transitions. Others, like polyethylene or Teflon, seem to be opaque. However, this is due to morphologic irregularities, which give rise to refractive index fluctuations, than a true absorption by electron excitation [6].

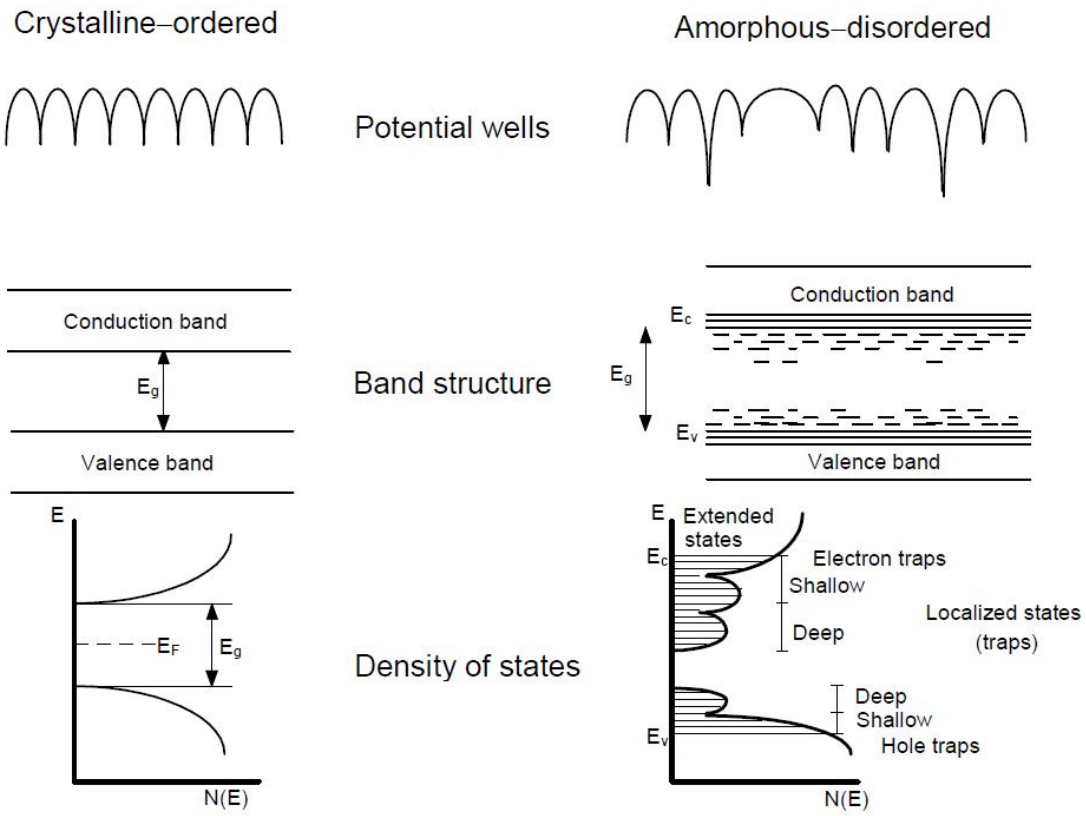

Figure 2.2. The potential well distribution, the band structure and the *density of states N(E)* are shown for amorphous and crystalline insulators.

Generally, organic polymers are amorphous or, at best, partially crystalline materials. Therefore, although there can be crystalline domains in polymers, they should be considered as materials with short-range order but long-range disorder. The order is decisive for the formation of energy band structure. The short-range order allows the existence of non-localized levels, and so, the presence of conduction and valence bands separated by a band gap. This is corroborated by the previously commented transparency in the visible region of many polymers. The high disorder degree in the spatial arrangement as well as the composition of these materials results in the presence of localized states in the band gap. The arrangement of potential wells, the band

structure and the *density of sates, N(E)*, can be observed in the Figure 2.2. Between the valence and conduction bands there is a distribution of localized states that make the band limits appear blurred, and it is difficult to establish the energy at which carriers are non-localized [7].

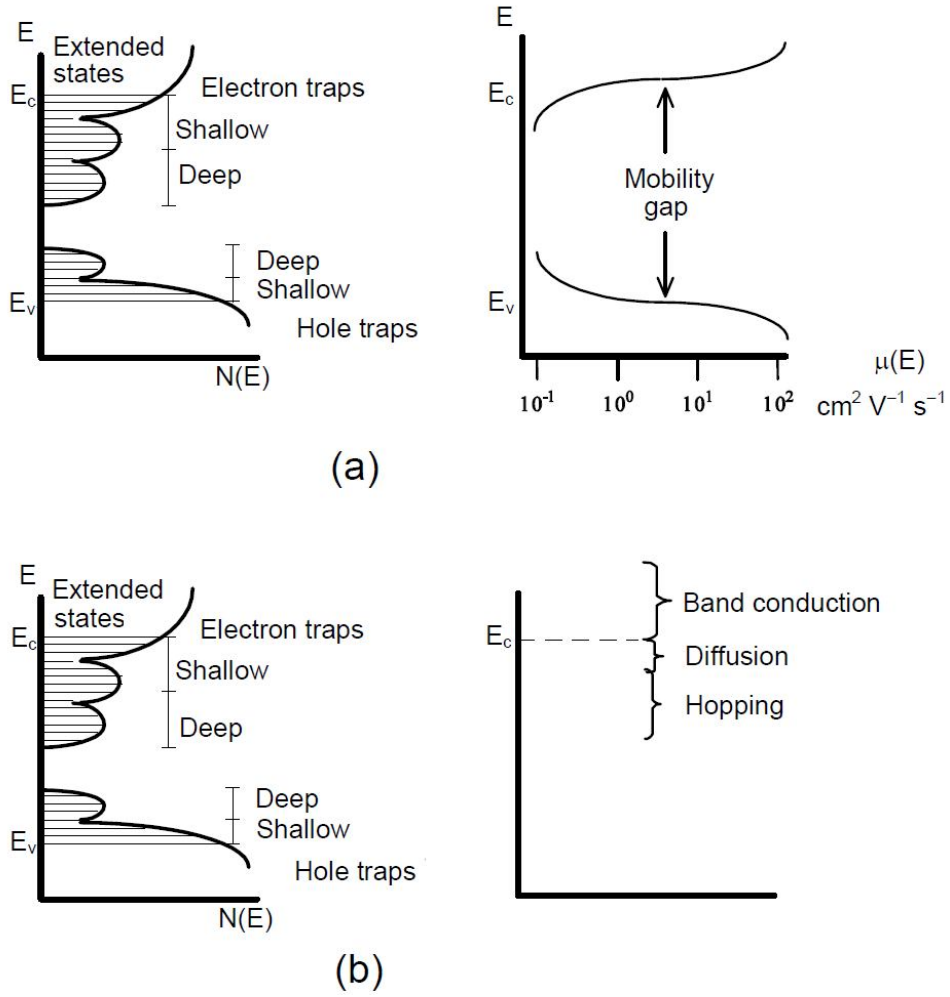

Figure 2.3. (a) Mobility gap. (b) Possible electron transport processes.

Mott proposed a definition of the energy bands in amorphous materials based in the carrier mobility, μ, as Figure 2.3 shows [8]. The critic energy E_c (or E_v in the case of holes) at which the electron mobility decreases 3 orders of magnitude, separates the non-localized states from the localized ones and determines the *mobility gap* limit [7]. Thus, there are several possible charge transport processes (Figure 2.3):

1. *Charge transport by carrier excitation into non-localized (extended) states.* The charge carriers have enough energy to shift to the non-localized states band, that is, above E_c (or below E_v if we consider the existence of acceptor levels and conduction by holes), where they move under the action of the applied electric field. In this case, the charge carriers are subjected to the same collision processes that in crystals and, if the solid has not a strict periodicity, to trapping and diffusion. The order of magnitude of the resulting mobility is about few cm^2/Vs.

2. *Charge transport by hopping between localized states*. Below E_c there is a localized states distribution originated by the lack of long-range order. Since there can be a great amount of these states, many of the charge carriers will be found in them at any time. These carriers only take part in the conduction process if they receive enough energy to move to non-localized states or to "jump" to a next localized state. Such energy can be obtained by optical excitation or thermal activation. In this transport process by hops between states, the maximum values that carrier mobility can reach are about 10^{-1}–10^{-2}cm^2/Vs.

3. *Charge transport by diffusion*. If charge carriers trapped in states near the conduction band (or the valence band in the case of holes) are diffused through the neighboring atoms, they can move by means of Brownian-like motion. Then, the mobility can be calculated by an approach consisting in considering a hopping process between states with similar energies ($\Delta E \approx 0$) and high overlapping degree (tunnel factor≈1). The mobilities obtained by this method have intermediate values with respect to the non-localized states conduction and the conduction by hopping between localized states.

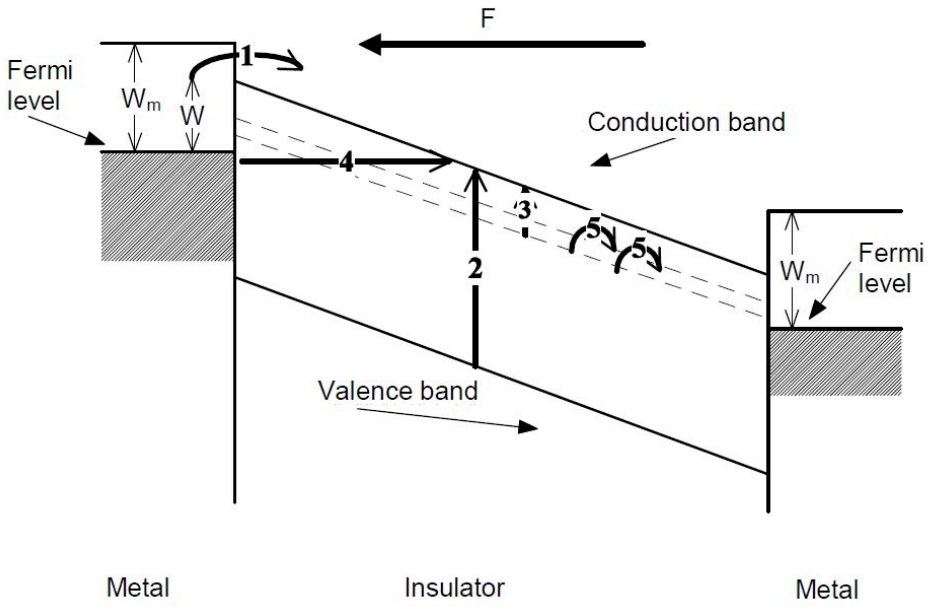

Figure 2.4. Electron conduction processes through a dielectric in a metal-insulator-metal configuration (1) Schottky emission; (2) Electron excitation from the valence band to the conduction band; (3) Thermal excitation of trapped electrons; (4) Quantum tunnelling from the electrodes; (5) Conduction processes by hopping between localized states.

There is a great dispersion in the electric conductivity values obtained by different authors for the same material. This is a clue that there are extrinsic factors affecting the charge transport process in the material. On the one hand, there is the commented effect of the electrodes nature, which in some cases can inject an amount of carriers much higher than those intrinsic ones present in the material in an equilibrium state. On the other hand, some impurities and defects can be present in dielectric materials as a result of the preparation process. Such impurities and defects can give rise to donor or acceptor levels. Besides, ionized impurities can move through the material in a process similar to ionic conduction. As it was previously argued, an essential point of the conduction in amorphous or semi-crystalline materials is the presence of "traps" or

localized states. Trap concentration depends on the preparation process of the material and can reach values as high as 10^{18}cm^{-3} [9].

In Figure 2.4, the most common electron transport processes in a metal-insulator-metal system are depicted. These can be classified in processes limited by the metal-insulator union and processes limited by the bulk, depending on which factor governs the current [10].

2.3 Electrode–limited conduction processes

2.3.1 Schottky effect

From a physical point of view the potential barrier in the metal-insulator union can not be considered completely abrupt (Figure 2.5). When an electron escapes from the metallic electrode a force between them appears. It can be calculated by the *image potential energy* method. If we suppose that the electron has penetrated a distance *x* into the dielectric, its image charge will be at a distance *2x* from it. In the case of a neutral contact, the potential barrier will not be that shown in Figure 2.1 (b), but

$$W_S = W + W_i = W - \frac{e^2}{16\pi\varepsilon x} \tag{2.4}$$

where W_i is the potential energy associated to the electron-electrode interaction, and ε the permittivity of the material. The barrier shape is represented by the dashed line in Figure 2.5.

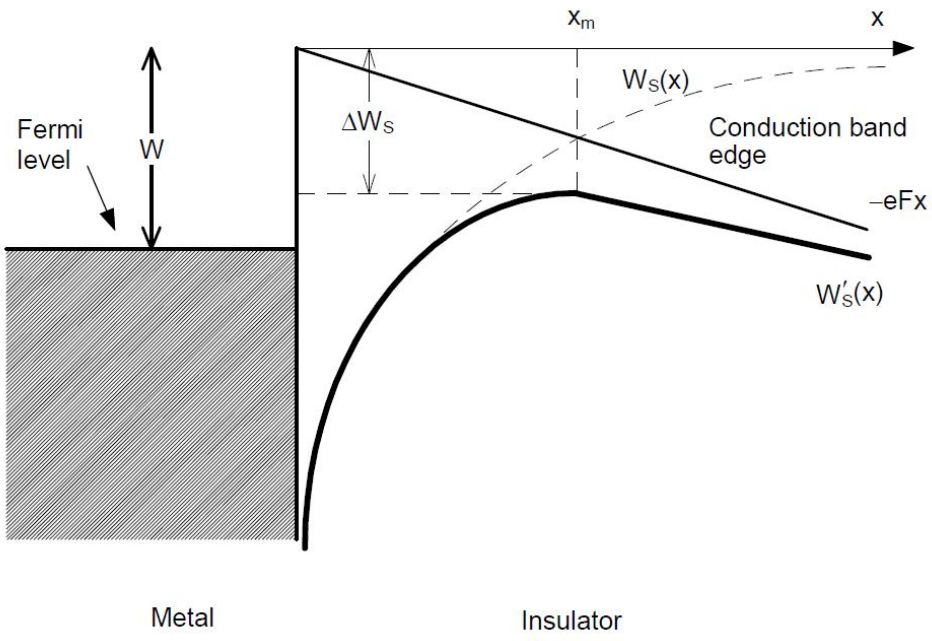

Figure 2.5. Energy diagram of the metal-insulator contact in a process of electron emission from the metal to the insulator conduction band, according to the Schottky model.

If an electric field is applied so the contact acts as a cathode, a new term, $-eFx$, should be added to the potential energy. This implies that the insulator conduction band bottom

edge becomes inclined. Therefore, the potential energy needed by the electron to escape from the metallic electrode is

$$W_S' = W - \frac{e^2}{16\pi\varepsilon x} - eFx \tag{2.5}$$

which is depicted by the bold line in Figure 2.5. This involves an effective decrease of the potential barrier given by ΔW_S. Thus, the maximum current density that this union can provide, given by the Richardson equation [11]

$$J = AT^2 \exp\left(-\frac{W}{kT}\right) \tag{2.6}$$

has to be modified to take into account this effect. This results in the *Richardson-Schottky equation*

$$J = AT^2 \exp\left(-\frac{W - \Delta W_S}{kT}\right) = AT^2 \exp\left(-\frac{W}{kT}\right) \exp\left(\frac{\beta_S F^{\frac{1}{2}}}{kT}\right) \tag{2.7}$$

where $A = 4emk^2/h^3 \approx 120 A/cm^2K^2$, $\beta_S = \sqrt{\frac{e^3}{4\pi\varepsilon}}$ and k and h are the Boltzmann and Planck constants, respectively, and m is the electron mass. This equation is generally valid for moderate electric fields and temperatures. In a situation with high fields and high temperatures, tunneling emission processes become important.

2.3.2 Field emission from electrode (Tunneling)

From previous sections it can be inferred that the higher is the applied field in the metal-insulator interphase, the thinner is the potential barrier. In Figure 2.6 it can be observed that the barrier thickness at the Fermi level is *W/eF*, where *W* is measured in eV. For sufficiently high field values, electrons can directly move by tunneling from the metal to the insulator conduction band through the barrier.

The current density originated by this process is given by the *Fowler-Nordheim equation* [12]:

$$J_T = \frac{e^2F^2}{8\pi hW} \exp\left(-\frac{8\pi\sqrt{2me}W^{\frac{3}{2}}}{3hF}\right). \tag{2.8}$$

The Fowler-Nordheim equation corresponds to the limit situation in which the temperature is zero (in Kelvin units). At higher temperatures quantum tunneling has to compete with thermally activated processes. So it will be better observed at low temperatures. In the case of very thin dielectrics, the electron wave function can have a still significant value in the opposite metal-insulator interphase, so the electron can go across the dielectric from one electrode to the other by tunneling [13].

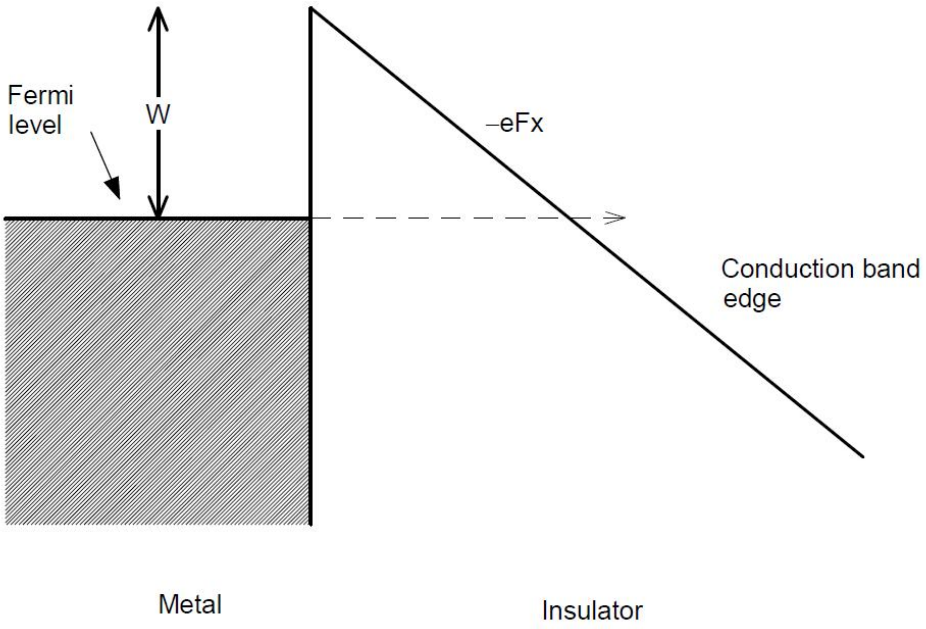

Figure 2.6. Tunneling mechanism through a metal-insulator neutral contact.

2.4 Bulk–limited conduction processes

2.4.1 Ohmic conduction

This process takes place in neutral materials in a stationary state, in which the mobile carrier density n is uniform. In this situation:

$$J = \sigma F = ne\mu F \tag{2.9}$$

where the material conductivity σ is independent of the applied field F.

The previous situation is common in metals and neutrality is kept in many homogeneous semiconductors, but it is not expected in good insulators. They present deviations from the ohmic characteristics due to bulk inhomogeneities and the electrodes behavior. However, most polymers show ohmic behavior for applied fields up to 10^4V/m [14].

2.4.2 Poole-Frenkel effect

Figure 2.7 shows the decrease in the potential barrier W of a neutral trapping center, due to the application of an external electric field. The barrier drops by ΔW_{PF} due to a mechanism that is conceptually very similar to the Schottky effect [15]. In the case of the Schottky emission, the image charge and the charge carrier distances to the electrode are equal, so the distance of the carrier to the image is twice the distance to the electrode. However, in the case of the Poole-Frenkel effect, the trapping center does not change its position. This difference is the cause that the Poole-Frenkel barrier drop is twice the Schottky barrier decrease.

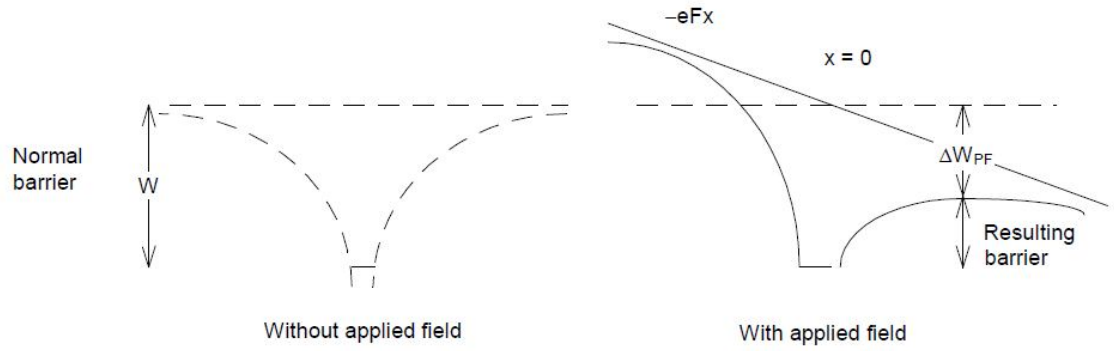

Figure 2.7. Scheme of the potential barrier drop due to Poole-Frenkel effect.

The resulting current density is given by

$$J = J_0 \exp\left(\frac{\beta_{PF} F^{\frac{1}{2}}}{kT}\right) \tag{2.10}$$

where $J_0 \propto F \exp\left(-\frac{W_d}{kT}\right)$ [16] is the current density at low fields resulting from the carrier thermal excitation and $\beta_{PF} = \sqrt{\frac{e^3}{\pi\varepsilon}}$.

2.4.3 Ionic conduction

Ionic conduction in a dielectric is the process in which electric current is carried by the motion of negative (anion) and/or positive (cation) ions. This could arise in a dielectric in two different manners: in an ionic crystal which basic constituents are ions, and physical imperfections (vacancies or interstitial ions) alone can be responsible for mechanisms of current flow, while in a non-ionic substance chemical imperfections are required to supply the mobile species [17]. In the following, for simplicity we will consider the ion vacancies as the solely charge carriers (a vacancy electrically behaves as the vacant ion but with the opposite charge).

If there are several species of mobile vacancies in the material then the conductivity is [18]

$$\sigma = \sum_i n_i q_i \mu_i \ , \tag{2.11}$$

where n_i, q_i and μ_i are the ion vacancy number density, the ion vacancy charge and the ion vacancy mobility, respectively, of any species. In figure 2.8, the motion of a cation vacancy (which has a $-q$ charge) is considered. This vacancy moves across the material by means of "hops" over a potential barrier *W*, from one position to the next. Hereafter we suppose the simplest case that all the equilibrium positions are equivalent and all the barriers are equal.

If N is the number density of ionizable molecules, W_d is the bond–dissociation energy, q is the ion charge, d is the distance between nearest neighbor positions and ν_0 is the ion frequency of attempts to escape from the trap, the conductivity of ion vacancies moving under low electric fields ($eFd<<kT$) is

$$\sigma = n_a q\mu_a + n_c q\mu_c = \frac{Nd^2q^2}{kT}\exp\left(-\frac{W_d}{kT}\right)\left[\nu_{0a}\exp\left(-\frac{W_a}{kT}\right)+\nu_{0c}\exp\left(-\frac{W_c}{kT}\right)\right] \tag{2.12}$$

where the a and c subscripts refer to the magnitudes associated to the anion and cation vacancies, respectively. Here we have assumed that vacancies are produced in pairs, as generally occurs, and that the number of cations is equal to the number of anions.

If the mobility of one species (for instance, cation vacancies) is much higher than the other, a thermally activated conductivity can be obtained:

$$\sigma = \frac{Nd^2q^2\nu_{0c}}{kT}\exp\left(-\frac{W'}{kT}\right) \tag{2.13}$$

where $W' = W_c + W_d/2$ is the total activation energy of ionic conductivity.

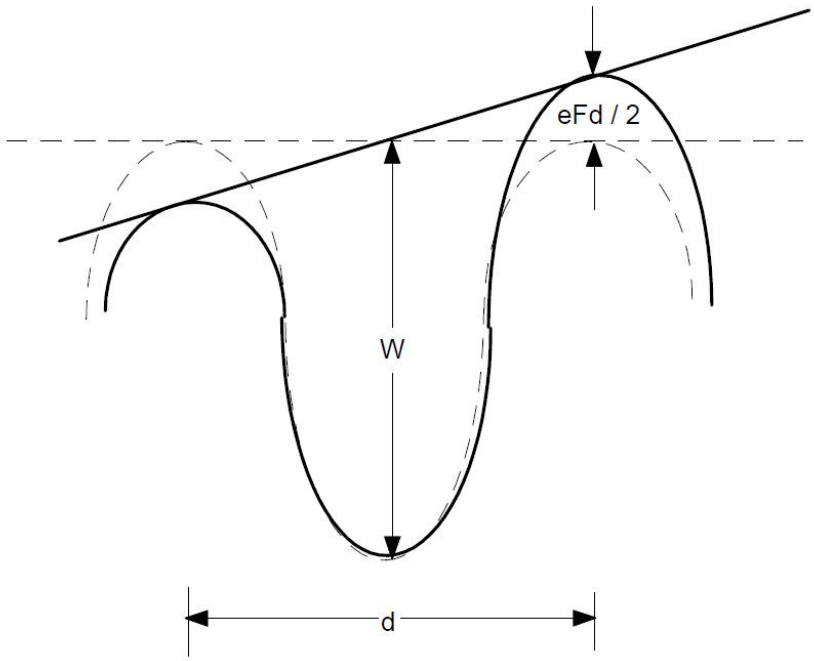

Figure 2.8. Energy diagram for the cationic vacancy motion under an applied electric field.

In the case of high applied fields, the current density will depend on the hyperbolic sine of the field since the mobility is given by the following expression [19]

$$\mu_{c/a} = \frac{2d\nu_{0c/a}}{F}\exp\left(\frac{W_{c/a}}{kT}\right)\sinh\left(\frac{eFd}{2kT}\right). \tag{2.14}$$

2.4.4 Conduction by hopping between localized states

If the density of localized states near the Fermi level is high, carrier transport by hopping between localized states can occur. Since this mechanism can be masked by the conduction in extended states, it can be observed more clearly in materials with a wide band gap [20]. The conductivity in the case of hopping between localized states is given by the *Mott's law*:

$$\sigma = \sigma_0 \exp\left[-\left(\frac{T_0}{T}\right)^{\frac{1}{4}}\right] \tag{2.15}$$

where T_0 is constant at sufficiently low temperatures and the pre-exponential factor σ_0 is not easy to evaluate theoretically [21]. However, this expression has been very successful in experimental verifications carried out with amorphous materials, especially at low temperatures [22].

2.5 Combined electrode and bulk effects on conduction processes

2.5.1 Space charge limited currents (SCLC)

Suppose a dielectric without donor or acceptor centers and sufficiently thick to not experience tunneling processes. If the injection of excess charge is possible and the carrier mobility is low, the material may not be able to transport all the injected charge. Then, a space charge distribution is formed and, so, neither the carrier density nor the electric field will be constant across the material thickness. The corresponding electrical behavior can be described by a model based on the following hypotheses:

1. One of the electrodes is ohmic and the potential barrier in the interphase is very low.

2. The current is independent of the position in the sample.

Under these hypotheses the resulting equation for the current density in a flat L thick sample of a dielectric, under an applied voltage V, is [23]

$$J = \frac{9}{8}\varepsilon\mu\frac{V^2}{L^3}, \tag{2.16}$$

which is known as *Mott-Gurney equation* or *Child's law for solids*. If both electrodes are injecting, then the carrier mobility μ has to be replaced by an effective mobility μ_{eff} [24]. This equation predicts a current dependency with squared voltage. However the values resulting from the equation are higher than the measured in experiments. Rose suggested that if the dielectric contains trapping centers, the equation should be modified by a factor $\alpha=\rho_f/\rho_t$, which represents the quotient of the free and the trapped charge density [25]. Thus, the Child's law for solids with traps is given by

$$J = \frac{9}{8}\varepsilon\mu\alpha\frac{V^2}{L^3}\ . \tag{2.17}$$

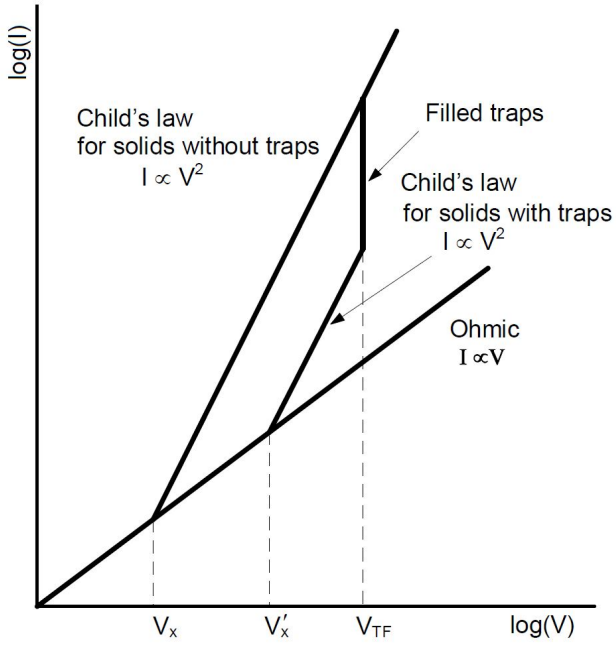

Figure 2.9. Scheme of *I-V* profiles for space charge limited currents.

In the Figure 2.9 the *I-V* profiles resulting from the space charge limited currents are represented. At low voltages the current is ohmic. By increasing the voltage, the system reaches a limit at $V=V_x$, at which the material can not transport all the injected carriers and the current becomes controlled by the space charge. In the case of solids without traps this limit value is given by

$$V_X = \frac{8neL^2}{9\varepsilon} \ . \tag{2.18}$$

The presence of traps in the solid shifts the limit voltage to a higher value, V_x', enlarging the ohmic region. If the applied voltage continues to increase, at V_{TF} all the traps have been filled and the current reaches the level corresponding to the Child's law for solids without traps. This phenomenon is similar to the dielectric breakdown, although in this case the process is reversible.

If instead of plane parallel geometry a cylindrical configuration is assumed (like it occurs in XLPE cable samples), the SCL current is [26]

$$I = 2\pi\varepsilon\mu L\left(\frac{V}{r_a}\right)^2 \tag{2.19}$$

for $r_a >> r_c$, where r_a and r_c are the outer and the inner cylinder radii and the ohmic contact boundary condition is applied in r_c ($F(r_c)=0$). L is the cylinder length. The *reverse current*, that is, the SCL current that flows when the contact at r_a, assumed ohmic, is biased for injection, is given by

$$I_r = I\left[\ln\left(\frac{r_a}{r_c}\right)\right]^{-2}. \tag{2.20}$$

The general SCLC theory assumes that traps are located in a discrete energy level. However, the traps can be distributed in energy. An interesting case is the exponential distribution, in which the trap concentration per unit energy decreases exponentially with energy from the band edge. The distribution function can be conveniently written as

$$f_T(E) = \left(\frac{N_T}{kT_T}\right)\exp\left(\frac{E - E_c}{kT_T}\right), \tag{2.21}$$

where $f_T(E)$ is the concentration of traps per unit energy, $E<E_c$ is the considered energy, N_T is the total concentration of traps and T_T is a temperature parameter characterizing the trap distribution. This configuration results in a current dependence on V^n, where n can be higher than 2. The mathematical expression is [27]

$$J = N_c \mu e^{(1-l)}\left[\frac{\varepsilon l}{N_T(l+1)}\right]^l \left(\frac{2l+1}{l+1}\right)^{l+1}\frac{V^{l+1}}{L^{2l+1}} \tag{2.22}$$

where $l = \frac{T_T}{T} = n-1$ and N_c is the effective density of states in the conduction band. In the case of cylindrical configuration the obtained currents are [26]

$$I = 2\pi L N_c \mu e^{(1-l)}\left[\frac{2\varepsilon l}{N_T(l+1)}\right]^l \left(\frac{2l}{l+1}\right)^{l+1}\frac{V^{l+1}}{r_a^{2l}}, \tag{2.23}$$

$$I_r = I\left[\frac{2l}{l+1}\ln\left(\frac{r_a}{r_c}\right)\right]^{-(l+1)}. \tag{2.24}$$

2.5.2 Steady-state, space charge limited hopping conduction of injected carriers, with Poole–field lowering of deep traps (Nath-Kaura-Perlman model)

In 1989, Nath and Perlman developed a charge transport model for the LLDPE. It was based in a space charge limited (SCL) hopping conduction of injected carriers, modulated by trap depth Poole–field lowering [28]. Often, the classical charge transport models had had little success in describing the electrical behavior of polymers. The goal was to develop a new theory that took into account the morphological characteristics of semi-crystalline polymers and that was consistent with polymer theories. They assumed band conduction or band tail conduction in the crystalline regions (band tail states are those for electron energies ranging between midgap –localized– to valence band or conduction band –extended– [29]). Hopping conduction was assumed in the amorphous region. Deep traps were assumed to lie at crystalline-amorphous boundaries. These traps are responsible for the Poole field lowering and contribute to the steady-state conduction, when the temperature is sufficiently high, by means of thermal excitation of

charge trapped during the initial transient state. Used LLDPE samples were doped with different concentrations of oxidized LDPE powder. The carbonyl groups present in the dopant were considered as the hopping sites lying in the amorphous region. In this first work, Nath and Perlman considered a field dependent mobility (see equation (2.14)). Such type of mobility also depends on the distance between hopping traps. Therefore, two of the model parameters were the distance between deep traps and the distance between hopping traps. At fields higher than 4×105V/cm (for temperatures between 50 and 85ºC), the experimental currents are electrode rather than space charge limited and lie below the predicted curves.

In a second paper published in 1990, Nath and Perlman, along with Kaura, improved the previous model and compared its results for LLDPE with other charge transport models, obtaining better agreement with experimental results in the case of the new theory [30]. Band conduction was assumed in the crystalline regions, while band tail conduction with small hopping activation energy was considered in band tail states of the amorphous region. In this case, the hopping mobility in band tail states depended on neither the field nor the distance between hopping sites. Unlike the previous work, here the LLDPE samples were not doped with oxidized LDPE, and hopping occurred through tail states in amorphous region without considering the carbonyl groups (although the presence of a dopant increases the density of hopping sites).

The Nath-Kaura-Perlman equations can be found as follows. Suppose a material that is electrically inhomogeneous. In such case, the free charge density and electric field are functions of position in the steady state. The current density with zero displacement and diffusion components is given by

$$J = \mu\rho_f(x)F(x) \tag{2.25}$$

where μ is a field independent drift mobility, ρ_f is the free charge density and F is the electrical field. *Poisson's equation* is

$$\frac{dF(x)}{dx} = \frac{\rho_{tot}}{\varepsilon} \tag{2.26}$$

where $\rho_{tot}=\rho_t+\rho_f$ is the total charge density and ρ_t is the trapped charge density. The detrapping parameter is given by

$$\theta_0 = \left(\frac{N_C}{N_T}\right)\exp\left(-\frac{W_t}{kT}\right) \tag{2.27}$$

where N_C is the effective density of states, N_T the total density of traps and W_t the trap depth below the conduction band edge. With Poole–field lowering of the trap depth:

$$\theta = \left(\frac{N_C}{N_T}\right)\exp\left[-\left(\frac{W_t}{kT}-\frac{e\lambda' F(x)}{2kT}\right)\right] = \frac{\rho_f}{\rho_{tot}}, \tag{2.28}$$

where λ' is the deep trap site separation and e is the electron charge. This expression is valid provided that the trap density exceeds $10^{18}/cm^3$. Combining equations (2.26) and (2.28), one obtains

$$\frac{dF(x)}{dx} = \frac{\rho_f(x)}{\theta\varepsilon}. \tag{2.29}$$

By putting equations (2.27), (2.28) and (2.29) into equation (2.25), then we have

$$J = \mu\theta_0\varepsilon F(x)\exp\left[\frac{e\lambda' F(x)}{2kT}\right]\frac{dF(x)}{dx}. \tag{2.30}$$

By doing

$$p = \frac{e\lambda'}{2kT}\ ;\ y = pF(x) \tag{2.31}$$

equation (30) then becomes

$$J = \left(\frac{\mu\theta_0\varepsilon}{p^2}\right) y\left[\exp(y)\right]\frac{dy}{dx}. \tag{2.32}$$

Integrating equation (2.32) over the sample thickness d, and using the SCL condition $F(0)$=0, it results in

$$J = \left(\frac{\mu\theta_0\varepsilon}{p^2 d}\right)\left[(y_d - 1)\exp(y_d) + 1\right] \tag{2.33}$$

where $y_d = pF_d$, and F_d is the field at the rear electrode in the steady state.

The thermally activated hopping mobility in band tail states is

$$\mu = \mu_0 \exp\left(-\frac{W_\mu}{kT}\right) \tag{2.34}$$

where μ_0 is a constant and W_μ is the hopping energy for the transport states, assumed to be small compared to W_t. From equations (2.27), (2.31), (2.33) and (2.34) one obtains

$$\frac{I}{T^2} = B\exp\left(\frac{W}{kT}\right)\left[(y_d - 1)\exp(y_d) + 1\right] \tag{2.35}$$

where I is the current, $B = 4A\mu_0\varepsilon N_C k^2 / e^2\lambda'^2 N_T d$, A the cross-sectional area and $W = W_\mu + W_t$ is the total activation energy. A semilog plot of I/T^2 vs. $1/T$ for constant y_d, *i.e.* for constant F_d (which is related to the applied field $F_A = V/d$) gives W.

It is possible to determine the current-field characteristics, if a relation between the applied field F_A and F_d is found. The applied voltage across the sample is given by

$$V = \int_0^d F(x)dx . \tag{2.36}$$

From equations (2.31) and (2.32),

$$dx = \left(\frac{\mu\theta_0\varepsilon}{p^2 J} \right) y\left[\exp(y)\right]dy \tag{2.37}$$

and $F(x)=y/p$. Therefore equation (2.36) becomes

$$V = \left(\frac{\mu\theta_0\varepsilon}{p^3 J} \right) \int_0^{y_d} y^2 \exp(y)dy \tag{2.38}$$

and, finally,

$$V = \left(\frac{\mu\theta_0\varepsilon}{p^3 J} \right) \left[\left(y_d^2 - 2y_d + 2 \right) \exp(y_d) - 2 \right]. \tag{2.39}$$

Substituting by J from equation (2.33), we have

$$\frac{pV}{d} = \frac{\left[\left(y_d^2 - 2y_d + 2 \right) \exp(y_d) - 2 \right]}{\left[\left(y_d - 1 \right) \exp(y_d) + 1 \right]} \tag{2.40}$$

which gives the relation between the applied field $F_A=V/d$ and the field F_d at the rear electrode ($y_d=pF_d$) in the steady state. The current-field characteristics can be obtained numerically from equation (2.33) and (2.40) by selecting values of y_d, solving for J from equation (2.33), and V/d from equation (2.40).

Boudou et al. used this model to analyze the influence of cross-linking by-products and antioxidants on the LDPE morphology and trap distribution [31–33]. Good agreement between experiment and the theory for fields higher than 8×10^6V/m was found [33].

2.6 Transient (absorption/resorption) currents

After an application of a step voltage to a polymer dielectric, the current observed in an external circuit decays in most cases with time until a steady current is reached. This steady state current may be many orders of magnitude less than the initial value of the absorption current. The discharge (resorption) current flowing through the sample when the field is removed and with electrodes shorted through an electrometer, is usually a mirror image of the charging current except that a steady state current does not occur for the discharging case.

As commented in section 2.2, the transient currents in dielectric materials can be originated totally or partially by dielectric processes. The simplest model for the dynamic behavior of orientational polarization (permanent dipoles) is the Debye theory [34]. According to this model, when an electric field is applied the polarization behavior is given by

$$\frac{dP}{dt} = \frac{P_{eq} - P}{\tau} \tag{2.41}$$

where τ is the relaxation time and P_{eq} is the polarization at the equilibrium state. This equation results in

$$P(t) = P_{eq}\left[1 - \exp\left(-\frac{t}{\tau}\right)\right]. \tag{2.42}$$

The displacement current will be

$$J_D = \frac{dP}{dt} = P_{eq}\frac{\exp\left(-\frac{t}{\tau}\right)}{\tau}. \tag{2.43}$$

In the case of depolarization the first-order differential equation (2.41) becomes

$$\frac{dP}{dt} = -\frac{P}{\tau}. \tag{2.44}$$

For large poling times, $t_p \to \infty$, it can be assumed that $P(\infty)=P_{eq}=P_0$. Then the depolarization equation is

$$P(t) = P_0 \exp\left(-\frac{t}{\tau}\right). \tag{2.45}$$

where the time origin is now set at the moment in which the field is removed. In this case, the current density has an opposite direction to the polarization derivative:

$$J_D = -\frac{dP}{dt} = P_0\frac{\exp\left(-\frac{t}{\tau}\right)}{\tau}. \tag{2.46}$$

Apart form displacement current, we have to take into account that there can be more contributions to the transient current and, in the case of the charging process, the steady state contribution has to be considered also. Anyway, experimental results generally differ from Debye model predictions [34]. However, many solid dielectrics fit well a power law like

$$I = A(T)t^{-n} \tag{2.47}$$

for times t much longer than the RC relaxation time of the capacitive circuit, where n is usually close to 1, $A(T)$ is a temperature dependent factor and I the transient current. This dielectric response is known as the *Curie-von Shweidler law* [35]. Das-Gupta lists the different dielectric and electrical processes that can originate the decreasing transient current [36]:

1) Fast and slow dipole orientation.
2) Electrode polarization.
3) Charge injection leading to trapped space charge effects.
4) Tunneling of charge from electrodes to empty traps.
5) Hopping of charge carriers from one localized state to another.

A summary of the characteristic features of each of the mechanisms is shown in Table 2.1. Thus, some of the possible mechanisms can be discarded in some cases by varying parameters such as electric field, temperature, electrode material and sample thickness.

Process	Field dependence of isochronal current	Thickness dependence of isochronal current at constant field	Electrode material dependence	Temperature dependence	Time dependence $I \propto t^{-n}$	Relation between charging and discharge transients
Electrode polarization	$\propto F^p$ where $p=1$	not specified	strongly dependent through blocking parameter	thermally activated	initially $n=0.5$ followed by $n>1$	mirror images
Dipole orientation, uniformly distributed in bulk	$\propto F^p$ where $p=1$	independent	independent	thermally activated	$0 \leq n \leq 2$	mirror images
Charge injection forming trapped space charge	related to mechanism controlling charge injection	independent	related to mechanism controlling charge injection	related to mechanism controlling charge injection	$0 \leq n \leq 1$	dissimilar
Tunneling	$\propto F^p$ where $p=1$	L^{-1}	strongly dependent	independent	$0 \leq n \leq 2$	mirror images
Hopping	$\propto F^p$ where $p=1$	independent	independent	thermally activated	$0 \leq n \leq 2$	mirror images

Table 2.1. Summary of the characteristics of the mechanisms responsible for transient currents. L is the thickness and F is the electric field strength [36].

When the polarization process has not been completed during the charging period, then the magnitude of the depolarization current is not the same as that of the polarization current [37]. The resulting power law depolarization current is then given by

$$I(t) = A(T)t^{-n}\left[1-\left(\frac{t_p}{t}+1\right)^{-n}\right] \tag{2.48}$$

where t_p is the poling time. This expression gives for $t<<t_p$, $I(t)\propto t^{-n}$, and for $t>>t_p$, $I(t)\propto t^{-n-1}$.

According to the apparent universality of the power law in empirical data, Jonscher proposed a *universal relaxation law* for the materials that show a loss peak in the *frequency domain* [38]:

$$I(t) \propto \frac{1}{\left(\omega_p t\right)^n + \left(\omega_p t\right)^{1+m}} \tag{2.49}$$

where ω_p is the *loss peak frequency*, and n, m fall into the range (0, 1). This equation is consistent with the empirical observation that for short times,

$$t << \omega_p^{-1} \Rightarrow I(t) \propto t^{-n} \tag{2.50}$$

while for long times,

$$t >> \omega_p^{-1} \Rightarrow I(t) \propto t^{-m-1}. \tag{2.51}$$

This Jonscher equation is suitable for dielectric dipolar systems and, also, for deep trapping in space charge regions of p-n junctions. The parameters n and m can be related with *small flip transitions* and *fluctuations* or *flip-flop transitions*, respectively, within the frame of the *many-body* model developed by Dissado and Hill [39,40]. However, for charge carrier dominated dielectric systems with no loss peak, the current is characterized by two power laws with exponents $-n_1$ and $-n_2$, close to 1 and 0, respectively, where n_1, $n_2 \in (0, 1)$ [41].

Along with the power law, the *Kohlrausch-Williams-Watts* (*KWW*) *stretched exponential* function has also been successful in fitting some of the experimental data [42]:

$$\varphi_{KWW}(t) = \exp\left[-\left(\frac{t}{\tau}\right)^{\beta}\right] \qquad 0<\beta<1. \tag{2.52}$$

The current follows the derivative of the decay function

$$I(t) \propto \frac{\beta t^{\beta-1}}{\tau^{\beta}} \exp\left[-\left(\frac{t}{\tau}\right)^{\beta}\right]. \tag{2.53}$$

In 1991, Weron proposed to approach the analysis on the relaxation phenomena from the mathematical theory of stochastic processes [41]. For this stochastic analysis it was adopted the concept of clusters developed by Dissado and Hill [43]. A cluster is defined

as a group of relaxing entities having common motions resulting from mutual interactions. Individual clusters are separated by energy barriers preventing their merging together. In this model, the relaxing entities can be either dipoles or charge carriers. A transition between localized orientations or positions is followed by a gradual adjustment of the surrounding dipoles or charges (*screened hopping*). The obtained time domain response is in agreement with equations (2.50) and (2.51) for short and long times, respectively, being $n=1-D$ and $m=D/(k-1)$. Here, D is a fractal dimension that falls into (0,1) and k is a parameter that determines how fast the structural reorganization of clusters spread out. For $k=1$ there is no clusters effect and the response function is the KWW (equation (2.53)) by doing $D=\beta$.

Finally, a unified model of absorption current and conduction current in polymers was developed by Lowell [44], in which the behavior of charges trapped on a flexible polymer network are responsible for both contributions.

2.7 Charge transport simulation in polyethylene

Until the first half of the last decade, only a few computer simulation models were developed to describe the experimental results for the charge transport phenomena [45–47]. In 2004, Le Roy et al. developed a bipolar model for the LDPE, based on Alison and Hill's work [45], with the aim to reproduce at the same time space charge profiles, *electroluminescence* (*EL*) and current. This model was successfully applied to experimental data obtained for several *direct current* (*DC*) voltage application protocols (step field increase and polarization/depolarization schemes) in two subsequent works [48,49]. The numerical methods used in the charge transport simulations were described by Le Roy et al. in 2006 [50].

In this model, two kinds of carriers are considered, being either trapped or mobile. A mobile electron in the conduction band (hole in the valence band) is associated with a constant effective mobility. This mobility accounts for the possible trapping and detrapping in shallow traps, in which the time of residence is short. Deep trapping is described through a single trapping level for each kind of carrier. Charge carriers have a certain probability to escape from deep traps by overcoming a potential barrier that is included in the detrapping coefficients. The recombination of carriers is also considered. A small quantity of mobile negative and positive charges is supposed to be initially distributed uniformly within the dielectric while keeping it electrically neutral. Dipolar polarization and diffusion are neglected. Also, internal generation of carriers is not considered. Fundamental equations are the *transport equation* (2.25) and the *Poisson's equation* (2.26), in which the field and charge densities are now position and time dependent, and the *continuity equation* (the time-derivative of the charge carrier density plus the divergence of current density equal a carrier source, which, in this case, depends on the trapping, detrapping and recombination probabilities, along with the carrier and trap densities). These equations have a specific form for the interfaces and are complemented by boundary conditions. Charge generation is supposed to result from injection at the electrodes according to the Schottky law (2.7), being for electrons and holes.

The same authors along with other researchers [51] developed a second model that assumes the existence of an exponential distribution of trap depth for electrons and holes, with an upper limit in trap depth. In this second model the fundamental equations

are the same as for the first. Also, charges are supplied through Schottky injection at both electrodes. However, in this case, charges move within the insulation through a hopping mechanism described by equation (2.14), which is charge density and field dependent. On the other hand, in this model no recombination is considered.

The results of simulations of the two models were compared with experimental data, for the external current and the space-time evolution of the electrical space charge distribution, in a paper published in 2006 [52]. For both models, although a fit to the experimental data could be obtained in the charging period, discharging was in general too slow. As a consequence, it was argued that attempting to explain space charge accumulation and transient currents by a single process could be misleading. Thus, some possible ways to make the models more realistic were pointed out: unraveling the nature of charging and discharging currents, considering dipolar contributions (neglected in the models since the polyethylene is normally a weakly polar material) or taking into account low mobility ionic species.

In recent years, this kind of computer simulation models also has been applied to TSDC with promising results [53,54].

References

[1] Vanderschueren, J. and Gasiot, J. in “Thermally Stimulated Relaxation in Solids”. Edited by Braünlich, P. Springer-Verlag Berlin Heidelberg, Germany (1979), pp. 135–223.

[2] Van Turnhout, J. in “Electrets”. Edited by Sessler, G. M. Springer-Verlag Berlin Heidelberg, Germany (1980), pp. 81–216.

[3] Van Turnhout (1980) [2], p. 94.

[4] Albella, J. M. and Martínez, J. M. “Física de Dieléctricos” Marcombo, Barcelona (1984), section 8.1.

[5] O’Dwyer, J. J. “The theory of electrical conduction and breakdown in solid dielectrics. Monographs on the Physics and Chemistry of Materials”. Oxford University Press, London, UK (1973), pp. 157–159.

[6] Coelho, R. and Aladenize, B. “Les diélectriques, propietés dieléctriques des matériaux isolants. Traité des Nouvelles Technologies” Hermes, Paris, France (1993), p. 18.

[7] Van Turnhout (1980) [2], pp. 90–95.

[8] Mott, N. F. and Davis, E. A., “Electronic processes in non-crystalline rnaterials”. Clarendon Press, Oxford, UK (1971).

[9] Ku, C. C. and Liepins, R. “Electrical properties of polymers: Chemical principles “. Hanser Publishers, Munich, Germany (1987), p. 229.

[10] Albella and Martínez (1984) [4], chapter 8.

[11] Ku and Liepins (1987) [9], p. 220.

[12] Coelho and Aladenize (1993) [6], p. 63.

[13] O’Dwyer (1973) [5], p. 94.

[14] Ku and Liepins (1987) [9], p. 216.

[15] Coelho and Aladenize (1993) [6], p. 21.

[16] Albella and Martínez (1984) [4], p. 166.

[17] O’Dwyer (1973) [5], p. 18.

[18] O’Dwyer (1973) [5], p. 2.

[19] O’Dwyer (1973) [5], p. 110.

[20] Coelho and Aladenize (1993) [6], p. 24.

[21] Mott and Davies (1971) [8], p. 221.

[22] Coelho and Aladenize (1993) [6], p. 25.

[23] Coelho and Aladenize (1993) [6], pp. 37–44.

[24] O'Dwyer (1973) [5], pp. 159–167.

[25] Mudarra, M. "Estudio de la Carga de Espacio en Polímeros Amorfos por Espectroscopia Dieléctrica". Ph.D. Thesis. Universitat Politècnica de Cataluña (2000), p. 53.

[26] Lampert, M. A. and Mark, P. "Current Injection in Solids". Academic Press, New York, USA (1970), chapter 8, pp. 157–184.

[27] Lampert and Mark (1970) [26], pp. 72–77.

[28] Nath, R. and Perlman, M. M. *J. Appl. Phys.* **65** (1989), 4854.

[29] Dong, J. and Drabold, D. A. *Phys. Rev. B.* **54** (1996), 10284.

[30] Nath, R.; Kaura, T. and Perlman, M. M. *IEEE Trans. Electr. Insul.* ***25*** (1990), 419.

[31] Boudou, L.; Guastavino, J.; Zouzou, N.; Martinez-Vega, J.; *Proceedings of the IEEE 7th International Conference on Solid Dielectrics*. Eindhoven, the Netherlands (2001), 245.

[32] Boudou, L.; Guastavino, J.; Zouzou, N. and Martinez-Vega, J. *Polymer International*. **50** (2001), 1046.

[33] Boudou, L. and Guastavino, J. *J. Phys. D: Appl. Phys.* **35** (2002), 1555.

[34] Albella and Martínez (1984) [4], pp. 101–111.

[35] Jonscher, A. K. "Dielectric Relaxation in Solids" Chelsea Dielectric Press, London, UK (1983), pp. 1–12.

[36] Das-Gupta, D. K. *IEEE Trans. Dielectr. Electr. Insul.* **4** (1997), 149.

[37] Adamec, V. and Calderwood, J. H. *J. Phys. D: Appl. Phys.* **11** (1978), 781.

[38] Jonscher (1983) [33], pp. 254–293.

[39] Dissado, L. A. and Hill, R. M. *Nature*. **279** (1979), 685.

[40] Dissado, L. A. and Hill, R. M. *Phil. Mag.* **B41** (1980), 625.

[41] Jonscher, A. K. “Universal Relaxation Law”. Chelsea Dielectric Press, London, UK (1996), pp. 1–44.

[42] Weron, K. *J. Phys.: Condens. Matter*. **3** (1991), 221 .

[43] Jonscher (1996) [39], pp. 350–360.

[44] Lowell, J. *J. Phys. D: Appl. Phys.* **23** (1990), 205.

[45] Alison J. M. and Hill R. M. *J. Phys. D: Appl. Phys.* **27** (1994), 1291.

[46] Fukuma, M.; Nagao, M. and Kosaki, M. *Proceedings of the International Conference on Properties and Applications of Dielectric Materials.* Brisbane, Australia (1994), 24.

[47] Kaneko, K.; Mizutani, T. and Suzuoki, Y. *IEEE Trans. Dielectr. Electr. Insul*. **6** (1999), 152.

[48] Le Roy, S.; Teyssedre, G. and Laurent, C. *IEEE Trans. Dielectr. Electr. Insul*. **12** (2005), 644.

[49] Le Roy, S.; Teyssedre, G.; Montanari, G. C.; Palmieri, F. and Laurent, C. *J. Phys. D: Appl. Phys.* **39** (2006), 1427.

[50] Le Roy, S. Teyssedre, G. and Laurent, C. *IEEE Trans. Dielectr. Electr. Insul*. **13** (2006), 239.

[51] Boufayed, F.; Le Roy, S.; Teyssedre, G.; Laurent, C.; Segur, P.; Cooper, E.; Dissado, L. A. and Montanari, G. C. *Proceedings of the 8th International Conference on Solid Dielectrics*. Toulouse, France (2004), 562.

[52] Boufayed, F.; Teyssèdre, G.; Laurent, C.; Le Roy, S.; Dissado, L. A. Ségur, P. and Montanari, G. C. *J. Appl. Phys.* **100** (2006), 104105.

[53] Le Roy, S.; Baudoin, F.; Boudou, L.; Laurent, C. and Teyssèdre, G. *Proceedings of the 10th International Conference on Solid Dielectrics*. Potsdam, Germany (2010), 703.

[54] Le Roy, S.; Baudoin, F.; Boudou, L.; Laurent, C. and Teyssèdre, G. *Proceedings of the IEEE Conference on Electrical Insulation and Dielectric Phenomena (CEIDP)*. Virginia Beach, USA (2009), 154.

3. MOTIVATION AND OBJECTIVES OF THE THESIS

3.1 State of the art

Since power cables with extruded XLPE insulation were introduced in 1960s [1], a lot of research has been focused on electrical, mechanical, thermal and chemical properties of polyethylene [2]. The electrical conduction mechanisms for several ranges of temperatures and fields, and the effect of manufacturing processes and additives on them, have been analyzed both theoretically and experimentally by many authors [3–12]. From the current versus voltage (*I-V*) characteristics some authors found that, while at low electric fields there is an ohmic behavior, at higher fields conduction can be explained by the space charge limited currents (SCLC) model [3–6]. Others observed that the current is limited by the electrode at high electric fields, following the Richardson-Schottky law [7]. However, due to polyethylene particularities, the classical models for crystalline and amorphous solids have not been completely successful to fit and explain the experimental data [8]. This fact led to the development of a specific model by Nath, Kaura and Perlman [9], which also was successfully applied by other authors [10–12]. On the other hand, while conductivity and dielectric loss studies on thin film polyethylene samples are abundant, the studies carried out on entire XLPE power cable samples are scarcer. However, it is not possible to study the conduction mechanisms of power cables with measurements on thin film samples because the morphological characteristics are different, the carbon black filled polymer semiconducting screens of cables may contribute to their dielectric response, and the concentration distribution of insulation defects is not the same in both cases [13].

Polyethylene conduction mechanisms are usually associated to the presence of space charge in its bulk. It is accepted that space charge present in insulating materials increases the local field and affects the conduction processes [14–16] and the dielectric strength [17,18] for high electric fields. Also, as it was commented in chapter 1, space charge can have an influence on polyethylene insulation aging and degradation [19,20], limiting its industrial features. As a consequence, it is interesting to determine the causes and evolution of the processes of formation and relaxation of this type of charge. Thus, the study of space charge in MV XLPE cables may provide clues about the most suitable composition (cross-linking agents, antioxidants…) or manufacturing processes (vulcanization time, extrusion parameters…) in order to enhance their operational lifetime [21]. Currently, research on new materials for power cable insulations, with improved features with respect to space charge accumulation, is being developed.

Several space charge measuring techniques have been developed in recent decades (*Thermal Pulse* (*TP*), *Thermal Step* (*TSM*), *Pressure Wave Propagation* (*PWP*), *Laser Induced Pressure Pulse* (*LIPP*), *Pulsed Electroacoustic* (*PEA*) and other) [22–26]. Among them, the most widely used one is the PEA. The possibility of “see” net amounts of space charge has involved some modifications of classical schemes about dielectric phenomena. Thus, the observation of periodical charge packets crossing PE samples from one electrode to the other at high fields [27], has resulted in a noticeable amount of research aimed at understanding this phenomenon [28].

Space charge relaxations have been studied by techniques like *time* or *frequency domain dielectric spectroscopy* or *Thermally Stimulated Depolarization Currents* (TSDC).

TSDC are especially useful for the space charge relaxation analysis due to its high resolution and low equivalent frequency [29].

Apart from space charge relaxations, TSDC also can detect dipolar relaxations in polar polymers. Although polyethylene is a non-polar polymer, it usually presents a small amount of dielectric loss **[**30]. The major part of this loss is attributed to the relaxation of small concentration of residual carbonyl groups attached to the main chain. In addition, the polymer sometimes is oxidized to increase its dielectrical response. The polar groups can act as a trace for the molecular or structural changes that happen in the material. On the other hand, additives and impurities present in the material can also have a polar behavior and thus provide a TSDC response.

Berticat et al. [31] obtained the TSDC spectra of LDPE and HDPE, and compared them with the relaxation map provided by classical dielectric spectroscopy. In the case of LDPE, several complex relaxation modes appeared: γ_3 (between 100 and 127K), γ_2 (137–160K), γ_1 (174–226K), β (238–265K), α (277–331K). The α-relaxation was associated with the crystalline fraction –although in amorphous polymers the α label is usually used to designate the relaxation associated with glass transition, in crystalline polymers it is often related to the crystalline regions [32]–; the β-relaxation involves motions that imply branch points or cross-links as tie points for the chains in the amorphous region; γ_1 is also located in the amorphous region and has been attributed to the glass transition; γ_2 has been associated with local mode relaxation; γ_3 involves the crystalline regions. In the case of the HDPE, the only γ-relaxation obtained is the γ_3. Dreyfus et al. [33] found that in polyethylene doped with ionic additives the α-relaxation appeared at higher temperatures (70ºC and above) and with a higher activation energy. Ronarc'h and Haridoss [34] found the LDPE β and γ peaks at 240K and 130K, respectively. All of the commented peaks (α, β and γ) are related to structural and molecular relaxations also detectable by *dynamical mechanical spectroscopy*. Such relaxations can imply dipolar relaxations or the destruction of traps and the subsequent release of charge carriers, which lead to currents detectable by TSDC. However, the α peak has also been associated with space charges that escape from structural defects via thermal excitation [35,36].

In the literature on the polyethylene space charge study by TSDC, a recurrent characteristic of the TSDC spectrum is the appearance of *homopolar* peaks related with space charge at temperatures ranging from 50º to 110ºC [33, 37–41]. It is worth to note that this is precisely the range in which the XLPE melts, according to our DSC measurements, and that the cable service temperature is about 90ºC.

In 1975, Hashimoto et al. [38] obtained the threshold conditions for the appearance of a homopolar peak at 70ºC, in function of the poling electric field (F_p) and the polarization temperature (T_p). This peak was associated with the relaxation of electrons that had been injected from the electrodes and were trapped inside crystals. Also, a *heteropolar* peak appeared at 50ºC and was attributed to the charge carriers released from traps located in the boundaries between crystalline and amorphous regions.

A little later, in 1978, Dreyfus et al. [33] performed TSDC studies on space charge in high voltage XLPE cables. They employed the *mobility model* (see section 4.3.6) to explain the behavior of the stimulated current. Homopolar peaks at 80, 90 and 98ºC were associated with electrons (injected from the cathode) accumulated near the anode,

positive ions accumulated near the cathode, and negative ions accumulated near the anode, respectively, during polarization. A heteropolar peak between 100ºC and 105ºC was attributed to heterocharges slightly separated acting like dipoles. On the other hand, they also worked with samples doped with antioxidants and found that these were responsible for the appearance of another heteropolar peak at 84ºC, originated by injected homocharge trapped in the defects introduced by such antioxidants (here the terms "homocharge" and "heterocharge" refer to the charge located near an electrode with the same/different polarity, respectively; the terms "heteropolar" and "homopolar" peak in this thesis has to do with the direction of the depolarization current in relation to the polarization).

In 1990, Ieda et al. [39] performed TPC and TSDC studies on the oxidation effect, charge injection and electric conduction in PE. They considered that oxidation increases the conduction current. The addition of oxidation products to the polyethylene surface rises hole and electron injection. Also, electron injection, which is the origin of most of the increase in current, predominates over hole injection. Finally, they associate homo space charge with the injection of electrons that relax at 40ºC, resulting in a homopolar TSDC peak.

Das-Gupta and Scarpa [40] obtained a homopolar peak between 70ºC and 80ºC in XLPE samples electrically aged by the action of alternating fields in water at lab temperature. The intensity of the peak first rose with aging and then decreased and tended to disappear. A heteropolar peak between 50ºC and 60ºC was also observed in low annealed samples.

In 2000, Matallana et al [41] analyzed the behavior of space charge in polyethylene-based new materials for high voltage cables, and found a TSDC homopolar peak placed at about 70ºC for LDPE. They used the *Creswell-Perlman model* (see section 4.3.4) to determine the activation energies of the peaks.

In other polymeric materials, Borisova et al. [42] considered that inhomogeneity in conductivity between the regions near the surfaces and the bulk of thin polymeric layers, determines the conformity to natural laws of homocharge accumulation and polarization phenomena in these polymeric layers. Thus, the homopolar current is explained through the *Maxwell-Wagner model* (see section 4.3.3).

The present Ph.D. thesis has been developed in the framework of the research on XLPE power cables carried out by the DILAB group [43], and its collaboration with the BICC General Cable started in 1998. As result of this research, in 2002 Dr. I. Tamayo presented his Ph.D. thesis [37], which constituted an exhaustive and systematic TSDC study on the XLPE insulation in the melting range of temperatures, complemented by other techniques like FTIR, SEM and X-ray diffraction. The TSDC spectra of the analyzed cable samples and its evolution with the thermal and electrical aging were provided for many TSDC parameter combinations and variations. Two articles presenting some of the main conclusions were published in 2003 [44] and 2004 [45].

For the experimental part of his thesis, Tamayo used samples belonging to six different types of power cables provided by General Cable. The cables were single conducting and, in the service regime, they operated within a voltage range from 12 kV to 20 kV and at a temperature around 90ºC. Any of the six cable types presented at least two of

the manufacturing parameters different from the rest. To simplify the nomenclature they were designated by letters A to F. Taking into account the differences among cable types, three groups were formed whose members differ only in the final temperature reached during the manufacturing process and the cooling rate (the three groups are: A and B, C and D, and E and F). Significant differences were not observed among the thermograms obtained by differential scanning calorimetry (DSC), which mean that the crystallinity was almost the same for the six XLPE samples.

In chapter 5 of the Tamayo's Ph.D. thesis, an as-received sample of any cable type was analyzed by TSDC. Conventional electrets were formed from the samples by poling at a temperature close to the operational one. Thereby, the discharge could be recorded along the melting range of temperatures. The measurements were performed on complete cable samples, including the semiconducting screens (SC) in contact with the inner and external surfaces of XLPE insulation.

From the TSDC analysis, it was observed that the initial spectra of the two cable samples of each group were similar. However, the sample that had reached a higher temperature during the manufacture, and that had been cooled at a higher rate, tended to have a lower response than the other cable type of the group. On the other hand, significant differences were found between samples of the different groups. These results confirmed that TSDC were sensitive enough to detect differences that can be attributed to the composition and to the manufacturing process. On the other hand, the spectra of some cable samples presented a homopolar peak when they were annealed at high temperatures. With more annealing, the homopolar relaxation disappeared. Special attention was put on this phenomenon due to its possible relation to space charge and, also, due to its transient behavior associated with the annealing. Cable D was the most prone one to present the homopolar peak (it was the one that needed the least annealing time to experience the polarity reversal, and under some conditions it was the only one to do so). Also, it was the cable with the lowest TSDC response, so the research was focused initially on this type of power cable (the area enclosed by the TSDC curve can be considered a measure of the electric charge accumulated during the polarization; the lower is the charge accumulated in service conditions, the better is the sample behavior with respect to the breakdown phenomena [46]).

A problem that the TSDC study of XLPE insulation presents is the fact that to can analyze the spectrum and characteristics of any material, they must be repetitive if the measurements are reproduced for the same experimental conditions. However, from the results obtained from consecutive TSDC measurements carried out on a cable sample, it was concluded that they were not repetitive since the material changed when it was electrically and thermally treated during the TSDC process. The only way to achieve the repeatability and reproducibility was by using a new as-received sample, identical to the original, in any new measurement. Therefore, it was not possible to define a stable TSDC spectrum for the XLPE cable samples. Besides, it was determined that the higher is the annealing temperature, the faster is the evolution of the spectra. So, to obtain an appropriate description of the material behavior it was necessary to carry out a systematic study on the influence of the factors responsible for the observed evolution.

In TSDC spectra of cable D insulation obtained by Tamayo, three main peaks (Figure 3.1) appeared recurrently for several conditions of polarization: the heteropolar peak at 105ºC, which temperature matches the fusion temperature obtained by DSC (and, so, it

is sometimes called the “fusion peak”); the homopolar peak between 95 and 100ºC (referred as “99ºC” or “97ºC” peak); and the structured heteropolar peak located at 80ºC. By annealing the samples at high temperatures (or simply by performing consecutive TSDC discharges in which high temperatures were reached), it was observed an evolution process in which the homopolar peak was formed around 97ºC and, subsequently, it increased its intensity in each new discharge. With further annealing, it decreased and, finally, it disappeared and the full spectrum recovered the heteropolar condition [37]. A third heteropolar peak was found at about 95ºC, which disappeared with the annealing (it is worth to note that it appeared at almost the same temperature as the homopolar peak).

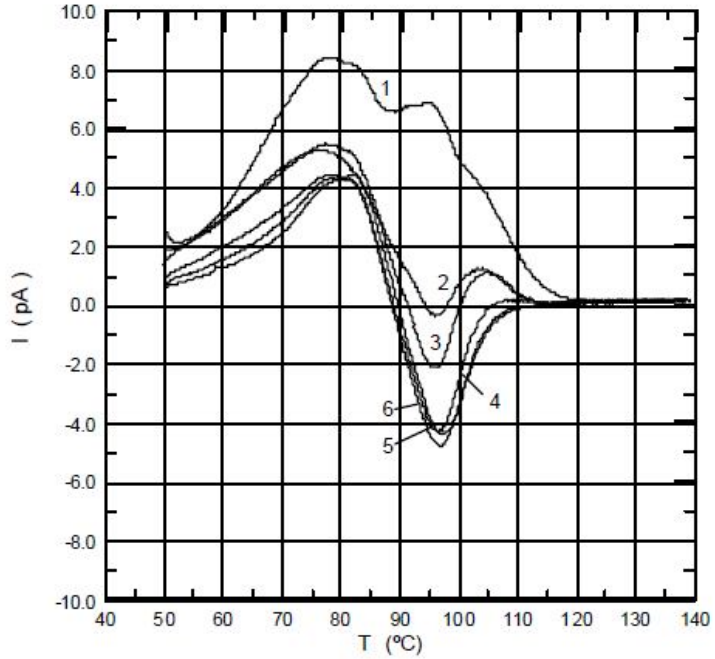

Figure 3.1. Consecutive discharges of a D sample. TSDC (conventional) conditions: V_p=8kV; T_p=80ºC; t_p=60min; t_s=5min; T_s=50ºC; T_f=140ºC; v_h=2.5ºC/min; v_c=1ºC/min [37].

In chapter 6, Tamayo studied the effect of the annealing temperature and time on the TSDC spectra evolution of the six types of power cable. The annealing temperatures chosen for the study were: 40ºC, 65ºC, 90ºC, 130ºC and 140ºC. The samples were poled for one hour at the same temperature that they had been annealed. At 40ºC the only samples that showed homopolar peaks were the E and F. However, at higher temperatures these are the only two that never showed a homopolar peak during the evolution with thermal aging.

In TSDC discharges obtained from samples annealed at 130ºC and at 140ºC, it was observed that, after the homopolar transient was exhausted, the heteropolar response tended to increase in intensity as annealing time increased. A possible explanation could arise from the fact that the XLPE ages or degrades at high temperatures, and this can generate charge carriers that would rise the heteropolar TSDC response. Nevertheless, FTIR results indicated that, for the annealing times used, only the samples annealed at 200ºC presented a significant increase of the oxidation and, so, the increase of the heteropolar current in the samples annealed at 130ºC and 140ºC should not be attributed to such phenomenon. However, due to the difference in the sensibility of the TSDC and FTIR techniques, there was the possibility that the last do not distinguish very small

amounts of aging that the former does. Otherwise, the increase of the area below the TSDC curves for the samples annealed at 130ºC, and at 140ºC, could also be originated by the free charge increase due to ionization and dissociation of components like antioxidants and cross-linking by-products [47–50].

On the other hand, one of the main results obtained from TSDC measurements were the differences between cables E and F –for which the annealing at higher temperatures did not result in a current reversal– and the rest of the samples. By means of a set of experiments, which involved TSDC measurements performed on several combinations of XLPE insulations and semiconducting screens belonging to different cables, Tamayo identified the outer semiconducting screen of cable D as the responsible for the polarity reversal (all the samples incorporated the same outer SC screen as cable D except cables E and F). The obtained results were explained by assuming that there is some diffusion from the semiconductor D at high temperatures, and that this diffusion is the final cause of the inversion.

The hypothesis of the diffusion from the SC screens was checked by a FTIR study on the semiconductor-XLPE interface for cables D and F, as representatives of the group of cables in which the reversal took place and the one in which it did not, respectively.

The spectrum corresponding to a 300mm layer cut from the outer surface of an as-received cable D showed new absorption bands at 1557, 1638, 1744 and 3300cm^{-1} that do not belong to the polyethylene (see Figure 3.2; the cable D spectrum is superimposed to the PE, XLPE and XLPE with antioxidants spectra). These results suggested that these new bands corresponded to chemical species diffused from the semiconducting screens to the XLPE, during the manufacturing processes at temperatures above 200ºC.

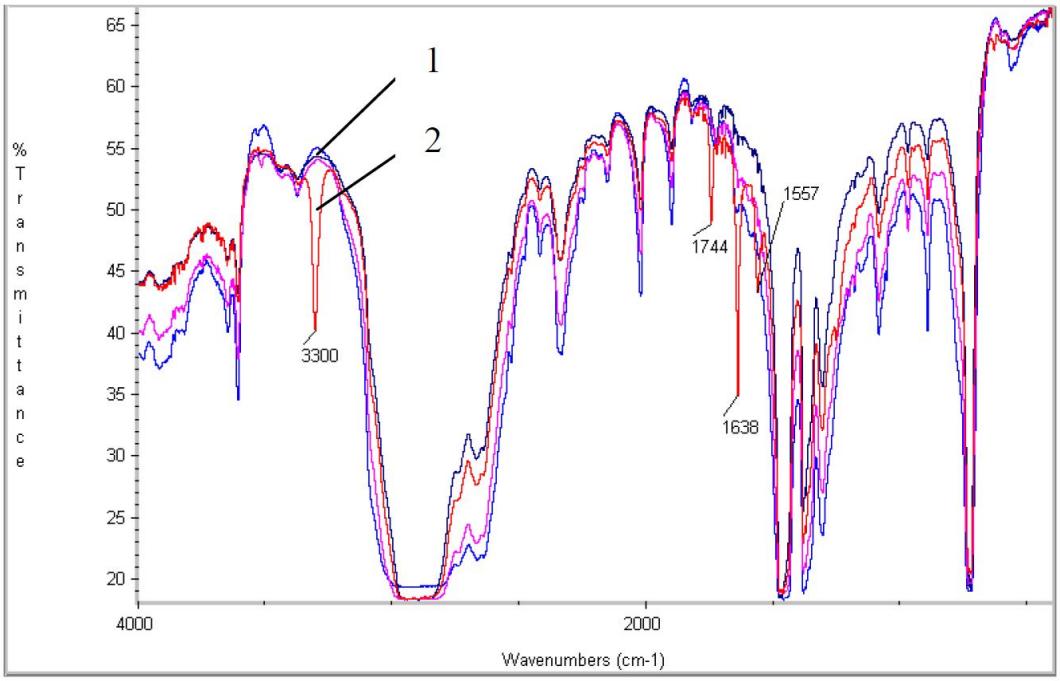

Figure 3.2. FTIR spectra of the samples: 1: PE, (XLPE) and XLPE with antioxidant; 2: Cable D XLPE insulation [37].

The FTIR results obtained from XLPE insulation layers at different depths showed that the transmittance of the mentioned bands increased with the depth. This implied that in the deeper layers the amount of the chemical components that originated them is lower. The total studied thickness was 1.2mm; at such depth these bands almost disappeared.

With respect to the annealing, a similar study was performed with samples D and F annealed at 140ºC for three hours and three days. The obtained spectra showed an evolution of the bands in function of the annealing time. It was observed that, in the case of cable D, the penetration of the diffused components to deeper layers dominated over the diffusion of new components from the SC shield. On the other hand, in the case of the cable F only the band at 1744cm^{-1} appeared. The rest of the bands of the cable D not shared with the pure XLPE were not found in this cable. In this case, the annealing could lead to some diffusion from the semiconducting screen while the already diffused components during the manufacturing process penetrated into deeper layers. Both processes occurred at the same level.

Finally, FTIR spectra were obtained from a sample F that had been in contact with the outer SC screen of the cable D, during an annealing of 25 hours at 110ºC. This sample F showed the transient homopolar peak like the cable D –although in this case it was briefer– due to the effect of the contact with the semiconducting screen at high temperatures. In this case, all the absorption bands found in the cable D insulation, 3300, 1744, 1638 and 1557cm^{-1}, were detected in the spectrum. This experience proved that the same components diffused to the cable D insulation during the manufacturing process, also were diffused to the F sample by annealing at 110ºC.

In addition to the Tamayo's measurements, the "Laboratorio Físico Central de Investigaciones" in Manlleu, belonging to General Cable, performed a study on the diffusion from the semiconducting screens, and the influence of the temperature and the time of contact between the semiconductor and the insulation. The previous results were verified and it was determined the diffusion takes place above a threshold temperature between 80ºC and 114ºC and it is higher as the temperature and the contact time increase.

FTIR measurements on SC layers of cables D and F resulted in a spectrum very similar to that of the ethylene-vinyl acetate, EVA. This agrees the fact that usually the outer semiconducting layers contain EVA as the major component. Nevertheless, in semiconductor D the absorption lines at 3300, 1744, 1638 and 1557cm^{-1}, associated to the components diffused into the insulation, clearly appeared. These peaks also appeared in the spectrum obtained from semiconductor F. However, apart from the absorption band at 1744cm^{-1}, in this case the peaks were far less significant than in the semiconductor D. In EVA spectrum only the absorption band at 1744cm^{-1} was found. The bands at 3300, 1638 and 1557cm^{-1} were due to other components that were present in the studied semiconductors together with the EVA.

Some transference of chemical components from the SC layers to the XLPE insulation was also detected by Scanning Electron Microscopy (SEM) and Energy Dispersive X-Ray Spectrometry (EDS) measurements. Besides, the microphotographs of the annealed samples suggested that the diffused components placed in the regions near the surface, penetrated into the insulation bulk with the annealing at 140ºC.

In his Ph.D. thesis, Tamayo performed other complementary measurements to understand the effect of annealing on XLPE insulation. Thus, insulation resistivity was measured for several temperatures, and it was observed that at low temperatures (40ºC and 60ºC) resistivity increases with the annealing time while at high temperatures (80ºC and 95ºC) it decreases. For fixed annealing conditions, resistivity decreases as temperature rises. On the other hand, the X-ray diffraction spectra proved that there is a decrease in the XLPE lattice constant with the annealing at 140ºC in flat samples. With respect to the crystallinity, by using DSC it was observed that the crystallinity degree almost does not change with the annealing at 140ºC for the studied annealing times (up to 72 hours).

Qualitative model to explain the behavior of XLPE cables

According to the model proposed in the Tamayo's Ph.D. thesis, the diffused impurities would interact with the crystals generating defects, probably in the surface of the crystals. These defects would behave as trapping centers for the charge carriers injected during the polarization, which would discharge homopolarly during the subsequent heating ramp. Cable D reached temperatures around 280ºC in the manufacturing processes. This allowed the diffused components to reach depths of the order of 1mm. In the layers close to the semiconductor the components concentration was very high, and it decreased with the depth.

FTIR and SEM/EDS results showed that, in the case of the cable D, the annealing at 140ºC makes the diffused components penetrate to deeper positions in the insulation, while the concentration of such elements decreases in the outer regions. This new diffusion generates more and more defects as it affects new crystals. By this way, the amount of trapping centers grows with the annealing until it reaches its limit value. This limit is determined by the amount of crystals in the region affected by the diffusion and by the amount of diffusion for an annealing time and at a certain temperature.

The increase of the amount of traps and its saturation with the annealing results in an analogous evolution of the trapped charge. The amount of the trapped charges increases until it saturates; this allows to explain that the homopolar peak intensity grows until it reaches a limit. Thus, the homopolar peak appearance and its maximum intensity are governed by the relation between the amount of diffused impurities and the number of crystals and their size.

On the other hand, a heteropolar process was also considered. Such phenomenon would also depend on the annealing time and temperature. The heteropolar current origin was explained as follows: the XLPE insulation contains impurities coming from cross-linking by-products, antioxidants, semiconductor components, and other contaminants associated to the polyethylene base production and the cable manufacturing process. Some of these impurities can be ionized and/or dissociated giving rise to free charge in the material bulk [51–54]. Under an applied field, this charge tends to accumulate heteropolarly close to the electrodes. Such components could be found either in the amorphous regions or inside the crystals, and, even, in the interfaces.

In the TSDC discharge, the XLPE melting process starts at about 50ºC giving rise to the relaxation of the free charge found in the amorphous phase. According to the model, this free charge release contributes to the heteropolar peaks at 57ºC, 73ºC and 87ºC.

When the melting ends, the charges that are placed inside the crystals relax and give rise to the heteroplar peak at 105ºC. Tamayo considered that the fact that the homopolar peak has its maximum at 99ºC, very close to the crystals fusion (105ºC), allowed to assume that the charge that responses homopolarly during the melting is located at the crystals surface.

Assuming that there are these two contributions and that both take place almost in the same range of temperatures, then the amount of charge that take part in any process determines the appearance of the homopolar peak. The homopolar reversal would occur if, under certain conditions, the amount of homocharge is larger than the amount of heterocharge. Therefore, the evolution of the spectra of the different cable samples with the annealing would depend on the way that these phenomena evolve. The evolution of any of these phenomena will also depend on the particular characteristics of the manufacturing process and on the cable composition.

According to these hypotheses the annealing of cables E and F do not make the homocharge overcome the heterocharge and, as a result, the current is not reversed. The reason could be the fact that the semiconducting layers of these cables are different and, so, diffuse different components into the insulation.

Then, in the case of the cables that show the current reversal (A, B, C, D), the evolution of the spectrum was explained by taking into account the following assumptions:

- At any temperature the TSDC current is governed basically by the overlap of two effects that compete with each other: one is heteropolar and the other is homopolar.

- During the annealing, both effects grow at different rates: the homopolar one rises faster until it becomes saturated.

- In the first stage, the heteropolar effect dominates over the homopolar one. The faster rise of the homopolar component makes the 105ºC peak decrease until it disappears, while the peak at 99ºC is being formed. This peak reaches its highest value when the homopolar process saturates.

- Once the homopolar process is saturated, heterocharge continues to increase until the resulting current recovers the heteropolar nature and the peak at 105ºC reappears in the spectrum.

Although the model presented in the Tamayo's thesis and summarized here was consistent with all the observations made up to the moment, the use of the pulsed electroacoustic in the research on the XLPE cables and its evolution with the annealing, has introduced new elements in the discussion. These new contributions are considered in chapter 9 of the present thesis.

Study on the 80ºC peak

Tamayo assumed that the TSDC peak at 80ºC is a structured peak resulting from the overlap of the relaxations at 57, 73 and 87ºC detected by means of the *Windowing Polarization* (*TSDC-WP*) and the *No Isothermally Windowing* (*TSDC-NIW*) techniques.

A linear dependence between the released charge and the applied voltage was observed. This implied the linearity of all the relaxations the peak is composed of.

This linear behavior is characteristic of the dipolar relaxations. However, Tamayo considered that the involved charge was free charge probably associated to impurities located in the amorphous region. These ionic species would move through microscopic distances from the starting position, giving rise to a Gerson-like polarization [55], which behaves heteropolarly and produces the same response with the field as a classical dipolar relaxation. Also, the presence of some polar components coming from the cross-linking by-products or other complex molecules could contribute to the 80ºC peak.

Study on the 99ºC peak

Since the general-order kinetics (see section 4.3.5.2) had been successful in fitting the free charge peaks of PET [37], which is also semi-crystalline, the same model was applied to the peaks associated to free charge in the XLPE (see Figure 3.2). In this model, for a constant heating rate v the discharge current along the warming ramp is given by

$$I = s_0 Q_0 \exp\left(-\frac{E_a}{kT}\right)\left(\frac{(b-1)s_0}{v}\int_{T_0}^{T}\exp\left(-\frac{E_a}{kT'}\right)dT' + 1\right)^{\frac{-b}{(b-1)}} \qquad (5.1)$$

where the fitting parameters are the frequency factor, s_0, the trapped charge, Q_0, the energy activation, E_a, and the kinetic order, b.

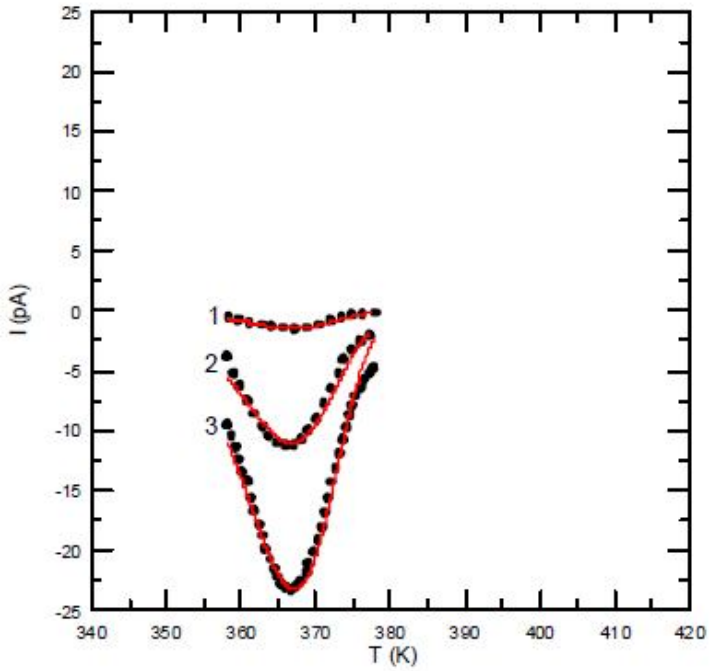

Figure 3.2. Homopolar peaks fitted to the general-order kinetics model. TSDC conditions: WP; T_p=40ºC; t_p=5min; V_p(1: 8kV; 2: 16kV; 3: 24kV) ●●●●●● (experimental curves) ——— (fitted values) [37].

The Figure 3.3 shows the trapped charge (Q_0) versus the poling voltage. The dependence is linear (with a correlation coefficient of 0.99). Although the linear behavior is expected in dipolar relaxations, it was argued that since the peak was homopolar this possibility must be discarded [44]. However, in the chapter 9 of this thesis a model in which the dipoles can respond homopolarly is proposed. In addition, it was claimed that previously reported *I-V* measurements showed that conduction in PE is limited by space charge associated with an exponential distribution of trap levels. Nevertheless, the existence of dipolar species in the XLPE insulation is also supported by the measurements.

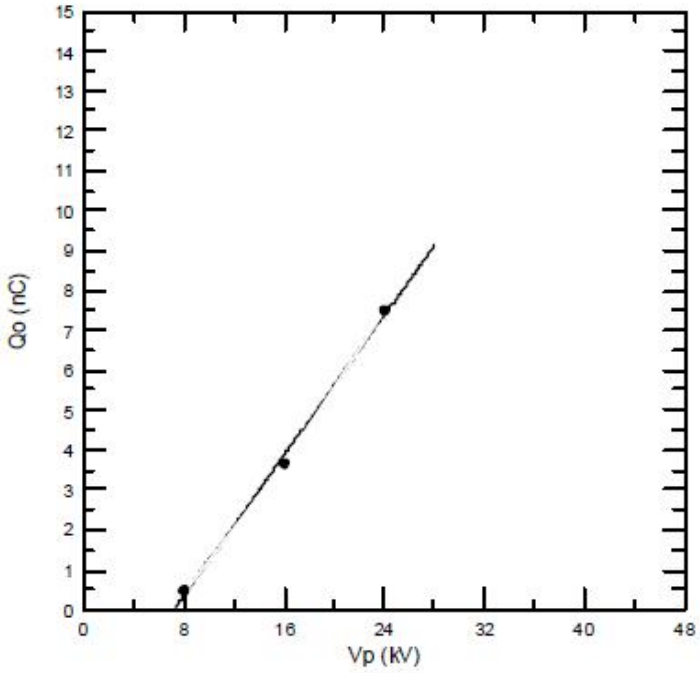

Figure 3.3. Trapped charge (Q_0) dependence on the poling voltage (V_p) from the values calculated by fitting the homopolar peak to the general-order kinetics model [37].

With respect to the kinetic order *b*, it presents small changes for different poling fields. Since this is the parameter affected by the highest uncertainty, it was assumed that in fact it was almost constant around 1.15. According the general-order kinetics model, the obtained value means that the most likely kinetic process is the recombination of charge carriers. However, for values tending to 1 (first-order kinetics) the discharge function is almost the same as for dipoles (see chapter 4).

Study on the 105ºC peak ("fusion" peak)

The 105ºC peak was also considered a free charge relaxation, so it was fitted to the general-order kinetics model. In this case, the kinetic order rises slightly with the polarization temperature (T_p). Its values fall between 1.2 and 1.5. The values are consistent with the model (the allowed range is $1<b<2$) and would imply that at low polarization temperatures the free charges relax by recombination, whereas by rising the T_p the retrapping probability increases. This could be due to the increase of the carrier mobility with the temperature, which agrees the fact that the conductivity rises with the temperature in the studied range.

3.2 Aims and objectives of the thesis

Although a lot of research on XLPE insulation properties has been developed, some aspects are still not fully understood. Tamayo [37] determined the TSDC spectra for many experimental conditions and monitored their behavior with annealing at temperatures close to the service conditions. The results of his research showed the influence of the crystalline fraction and the melting process on depolarization currents. In addition, some diffusion of chemical species from the semiconducting shield was observed at high temperatures. This diffusion was considered responsible for a transient current reversal that happens if cables are annealed. The homopolar current was associated with charge injected from the electrodes, during polarization, and trapped in defects generated by such diffusion. A critical temperature for conduction processes was found at 80ºC, where the resistivity behavior with annealing changes. Finally, the origin of observed TSDC peaks was discussed.

The purpose of this thesis is to study the research lines started by the work of Dr. I. Tamayo, and to use additional complementary techniques to check the assumed hypotheses. The main goals of the work are summarized below:

- To carry out conductivity measurements on entire cable samples to understand the true conduction mechanisms that take place in the insulation, since most of existing studies have been performed on thin film samples without the influence of SC screens and, usually, without the own additives of commercial XLPE insulation.

- Analyzing the behavior of conductivity with annealing at the melting range of temperatures and, especially, at the service temperature.

- Determining the possible influence of the additives, cross-linking by-products, semiconducting screens, aging, and other factors, on the observed behavior.

- Studying in depth the influence of crystalline fraction and the effect of crystallization and recrystallization processes on depolarization currents.

- Using complementary techniques to study the nature of the TSDC peaks observed in XLPE cables spectra.

- Using PEA technique to monitor the space charge behavior with annealing and comparing it with TSDC results. This could allow to find any relation between the transient current reversal and changes in the stored space charge.

References

[1] Papazyan, R. and Eriksson, R. *IEEE Transactions on Instrumentation And Measurement*. **52** (2003), 415.

[2] Dissado L. A. and Fothergill J. C. "Electrical Degradation and Breakdown in Polymers". Peter Peregrinus Ltd. on behalf of the Institution of Electrical Engineers, London, UK (1992).

[3] Frisch, K. C. and Patsis, A. in "Electrical properties of polymers" Edited by Seanor, D. A. Academic Press, New York, USA (1982), pp. 1–26..

[4] Lampert, M. A. and Mark, P. "Current Injection in Solids". Academic Press, New York, USA (1970).

[5] Pelissou, S.; St-Onge, H. and Wertheimer, M. R. *IEEE Trans. Electr. Insul.* **23** (1988), 325.

[6] Chen, G.; Banford, H. M.; Fouracre, R. A. and Tedford D. J. *Proceedings of the 3rd International Conference on Conduction and Breakdown in Solid Dielectrics.* Trondheim, Norway (1989), 277.

[7] Mizutani, T.; Jordan, I. B. *Annual Report of the 1974 Conference on Electrical Insulation and Dielectric Phenomena*. Downington, USA (1974), 640.

[8] Lewis, T. J.; IEEE Trans. Dielectr. Electr. Insul. **9** (2002), 717.

[9] Nath, R.; Kaura, T. and Perlman, M. M. *IEEE Trans. Electr. Insul*. **25** (1990), 419.

[10] Boudou, L.; Guastavino, J.; Zouzou, N.; Martinez-Vega, J.; *Proceedings of the IEEE 7th International Conference on Solid Dielectrics.* Eindhoven, the Netherlands (2001), 245.

[11] Boudou, L.; Guastavino, J.; Zouzou, N. and Martinez-Vega, J. *Polymer International*. **50** (2001), 1046.

[12] Boudou, L. and Guastavino, J. *J. Phys. D: Appl. Phys.* **35** (2002), 1555.

[13] Liu, T.; Fothergill, J.; Dodd, S.; Dissado, L.; Nilsson, U. H.; Fu, M. and Perrot, F. *2010 IEEE International Conference on Solid Dielectrics.* Potsdam, Germany (2010), 16.

[14] Albertini, M.; Peruzzotti. F.; Ghinello, I.; Montanari, G. C.; Bambi, S. and Motori, A. *Proc. 3rd Int. Conf. Electric Charge in Solid Insulators.* Tours, France (1998), 620.

[15] Fanjeau, O.; Truong, V. H. and Malec, D. *Proc. of the 1999 Int. Conf. Insul. Power Cables, 5th JICABLE*. Paris-Versailles, France (1999), C2.5, 678.

[16] Al-Saour; Chang, F.; Hampton, R. N. and Hobdell. S. B. *Proc. of the 1999 Int. Conf. Insul. Power Cables, 5th JICABLE*. Paris-Versailles, France (1999), C2.7, 685.

[17] Zhang, Y.; Lewiner, J.; Alquié, C. and Hampton, N. *IEEE Trans. Electr. Insul.* **3**, (1996) 778.

[18] Zebouchi, N. and The Giam, H. *Proc. of the 1999 Int. Conf. Insul. Power Cables, 5th JICABLE*. Paris-Versailles, France (1999), C2.8, 691.

[19] Fothergill, J. C.; Montanari, G. C.; Stevens, G. C.; Laurent, C.; Teyssedre, G.; Dissado, L. A.; Nilsson, U. H. and Platbrood, G. *IEEE Trans. Dielectr. Electr. Insul.* **10** (2003), 514.

[20] Dissado, L. A. *Proc. 3rd Int. Conf. Electric Charge in Solid Insulators.* Tours, France (1998), 141.

[21] Tamayo, I. Òrrit, J. and Diego J. A. *Proc. of the 2007 Int. Conf. Insul. Power Cables, 7th JICABLE*. Paris-Versailles, France (2007), C716.

[22] Li, Y. and Takada, T. *IEEE Electrical Insulation Magazine.* **10** (1994), 16.

[23] Kressmann, R.; Sessler G. M. and Günter, P. *IEEE Trans. Dielectr. Electr. Insul.* **3** (1996), 607.

[24] Armed, N. H. and Srinivas, N. N. *IEEE Trans. Dielectr. Electr. Insul*. **4** (1997), 644.

[25] Takada, T. *Trans. IEE Japan*. 117.A, **6** (1997), 545.

[26] Fukunaga, K. *IEEE Electrical Insulation Magazine.* 15 (1999), 6.

[27] Hozumi, N.; Suzuki, H.; Okamoto, T.; Watanabe, K. and Watanabe, A. *IEEE Trans. Dielectr. Electr. Insul.* **1** (1994), 1068.

[28] Dissado, L.A. *2010 IEEE International Conference on Solid Dielectrics.* Potsdam, Germany (2010), 641.

[29] Menegotto, J.; Demont, P.; Bernes, A. and Lacabanne, C. *J. Pol. Sci. Part B: Pol. Phys.* **37** (1999), 3494.

[30] McCrum, N. G.; Read, B. E. and Williams, G. "Anelastic and Dielectric Effects in Polymeric Solids". Dover Publications, Inc., New York, USA (1991), pp. 353-377.

[31] Berticat, P.; Bui Ai; The Giam, H.; Chatain, D. and Lacabanne, C. *Makromol. Chem.* **177** (1976), 1583.

[32] McCrum (1991) [30], pp. 141-145.

[33] Dreyfus, G.; Lacabane, C. and Rahal, A. *Journées d' études de la SEE. RGE*. **87** (1978), 870.

[34] Ronarc'h, D. and Haridoss, S. *J. Appl. Phys.* **52** (1981), 5916.

[35] Le Roy, S.; Baudoin, F.; Boudou, L.; Laurent C. and Teyssedre, G. *2010 IEEE International Conference on Solid Dielectrics.* Potsdam, Germany (2010), 703,

[36] Markiewicz, A. and Fleming, R, J. 1988 *J. Phys. D: Appl. Phys.* **21**, 349.

[37] Tamayo, I. "Estudio del comportamiento de la carga de espacio durante la fusión del XLPE en cables de media tensión por TSDC". Ph.D. Thesis. Universitat Politècnica de Catalunya, Terrassa, Spain (2002).

[38] Hashimoto, T.; Shiraki, M. and Sakai, T. *J. Polym Sci*. **13** (1975), 2401.

[39] Ieda, M.; Mizutani, T. and Suzuoki, Y. *IEEE Trans. Electr. Insul.* **25** (1990), 509.

[40] Das-Gupta, D. K. and Scarpa, P. C. N. *IEEE. Trans. Diel. Electr. Insul.* **3** (1996), 366.

[41] Matallana, J.; Bigarre, J.; Hourquebie, P.; Agnel, S.; Toureille, A.; Mirebeau, H.; Aladenize, J. B. and Coelho, R. *Proc. of 2nd Conference of the French Society of Electrostatics*. Montpellier (2000), 44.

[42] Borisova, E.; Kojkou, N. and Marchenco, S. *8th International Symposium on electrets (ISE 8)*. Paris, France (1994), 37.

[43] Dielectric Materials Physics Laboratory — DILAB (formerly: group of Electrical Properties of Insulating Materials), in Escola Tècnica Superior d'Enginyeries Industrial i Aeronàtutica de Terrassa (ETSEIAT), located in the Campus de Terrassa (Terrassa, Barcelona), from the Universitat Politècnica de Catalunya (UPC); http://dilab.upc.edu/.

[44] Tamayo, I.; Belana, J.; Cañadas, J. C.; Mudarra, M.; Diego, J. A. and Sellarès, J. *J. Polym. Sci. Part B Polym. Phys.* **41** (2003), 1412.

[45] Tamayo, I.; Belana, J.; Diego, J. A.; Cañadas, J. C.; Mudarra, M. and Sellarès, J. *J. Polym. Sci. Part B Polym. Phys.* **42** (2004), 4164.

[46] Belana, J.; Cañadas, J.; Diego, J. A.; Mudarra, M.; Díaz-Calleja, R.; Friederichs, S.; Jaïmes, C. and Sanchis, M.J. *Polym. Int.* **46** (1998), 11.

[47] Cartwright, G. A.; Davies, A. E.; Swingler, S. G. and Vaughan, A. S. *IEE Proc. Sci. Meas. Technol*. **143** (1996), 26.

[48] Hozumi, N. *9th International Symposium on electrets (ISE 9)*.Shangai, China (1996), 3.

[49] Hozumi, N.; Takeda, T.; Suzuki, H. and Okamoto,T. *IEEE Trans. Electr. Insul*. **5** (1998), 82.

[50] Kon, H.; Suzuoki, Y.; Mizutani, T.; Ieda, M. and Yoshifuji, N. *IEEE Trans. Electr. Insul*. **3** (1996), 380.

[51] Li, Y. and Takada, T. *J. Phys. D: Appl Phys*. **25** (1992), 704.

[52] Mizutani, T. *IEEE Trans. Diel. Electr. Insul.* **1** (1994), 923.

[53] Lee, S. H.; Park, J. K.; Lee, C. R. and Suh, K. S. *IEEE Trans. Diel. Electr. Insul.* **4** (1997), 425.

[54] Liu, R., Takada, T.and Takasu, N. *J. Phys. D: Appl. Phys.* **26** (1993), 986.

[55] Gerson, R. and Rohrbaugh, J. H. *J. Chem. Phys.* **23** (1955), 2381.

4. DESCRIPTION OF CABLE SAMPLES. EXPERIMENTAL TECHNIQUES AND SETUPS

4.1 Samples description

Medium voltage cables are used in electricity distribution to connect electrical substations with primary customers, or with transformers that serve secondary customers by means of low voltage cables. Cable samples were provided by General Cable with the goal to characterize different experimental or commercial designs. They are single conducting and, in the service regime, they operate within a voltage range from 12 kV to 20 kV and at a temperature around 90ºC. Three cable types are considered in this Ph.D. thesis, which share many composition features with the "cable D" studied in the Ph.D. thesis of Dr. I. Tamayo [1]. They are labeled with the letters S, L and R. In all the cases, the as-received samples consist, from inside to outside, of: (a) a 14.5mm of diameter aluminum core made up of nineteen twisted hexagonal wires, (b) an inner 0.50mm thick semiconducting layer, (c) a 15.5mm inner diameter and 24.6mm outer diameter insulating XLPE layer, (d) an outer 0.50mm thick semiconducting layer, (e) a metallic screen formed by cooper wires, and (f) a polyvinyl chloride (PVC) outer jacket (see the Figure 4.1). The XLPE of the insulating layer was cross-linked mixing low density PE with a cross-linking agent and heating it up to a temperature higher than 200ºC to produce a vulcanization reaction. Some partial degassing process was carried out directly during cable manufacture. The details of the cable composition can be seen in Table 4.1.

In addition to these three cable types, the cable D is also studied in chapter 9, due to its large homopolar response during a transient current reversal that results from annealing at high temperatures [1]. The cable D manufacturing characteristics are the following; Polyethylene base: CP104 from Repsol. Outer semiconducting layer: LE-0516 from Borealis. Cross-linking agent: di-tert-butyl peroxide. Cross-linking by-products: tert-butanol, acetone, methane, 2-methylpropane-2 and water. Antioxidant: 4,4 tiobis (3-methyl-6-tert-butylphenol). Manufacturing process: vulcanization with water vapour. Final temperature: 310ºC. Cooling time: 6 minutes. Cable D has a XLPE insulation of 7.5mm and 13.6mm of internal and external radii, and its SC layers are 1mm thick.

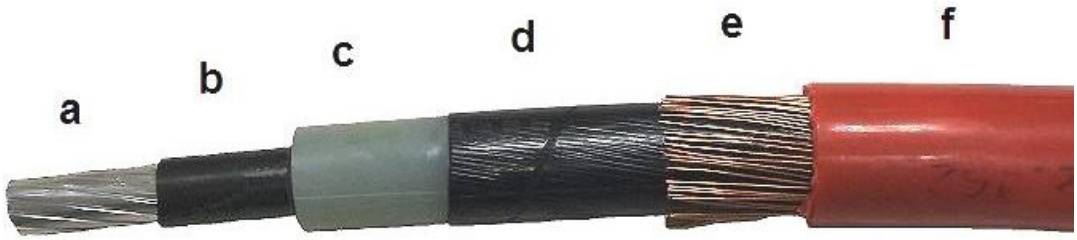

Figure 4.1. Medium voltage XLPE power cables configuration.

Cable type	S	L	R
PE base	1	1	2
Outer S.C.[e]	1	2	3
Inner S.C.[e]	1	1	2
Cross-Linking Agent	Di-tert-butyl peroxide	Di-tert-butyl peroxide	Di-tert-butyl peroxide
Cross-Linking By-Products	Tert-butanol; acetone; methane	Tert-butanol; acetone; methane	Tert-butanol; acetone; methane
Antioxidant[f]	Solid (1)	Liquid (2)	Solid (3)
Manufacturing Process	Cross-linking with N_2	Cross-linking with N_2	Cross-linking with N_2
Cooling Time	20 min approx.	20 min approx.	20 min approx.

Table 4.1. Manufacturing characteristics of the power cables studied in the present thesis.

Polyethylene base

1. Low density polyethylene.
2. Low density polyethylene that incorporated the antioxidant (3) when it was supplied to the power cable manufacturer.

Outer semiconducting layer

1. EVA (ethylene vinyl acetate) + ACN (acrylonitrile) + carbon black.
2. EVA + ACN + carbon black.
3. EVA + ACN + carbon black.

Inner semiconducting layer

1. EVA + PE + carbon black.
2. EEA (ethylene ethyl acrylate) + carbon black.

[e] The exact composition of semiconducting layers is confidential.
[f] The composition of antioxidants is confidential.

4.2 Thermally Stimulated Depolarization Currents (TSDC) technique

4.2.1 Introduction

This technique consists in combining electrical poling and thermal treatment to activate in a metastable way one or more relaxational mechanisms of a dielectric sample [2]. Then, the sample is heated at a constant rate to force the relaxation of these mechanisms. Such relaxation gives rise to a displacement current that is recorded together with the temperature of the sample. This thermogram is the so–called TSDC spectrum and reflects the relaxations undergone by the sample. The origin of this technique has to be found in the discovery of the *electrets* in 1919 by Eguchi [3]. An electret is a material that remains electrically polarized along a period very long compared to the time needed to form it. Eguchi used an electro-thermal treatment to obtain electrets but there are other methods to do so. In short, the TSDC technique involves the creation of a thermo-electret and the subsequent depolarization by thermal excitation.

TSDC and electret features have been widely described in the literature [4–7]. The aim of this section is to present some general aspects about the technique, and the dipolar and space charge relaxation theory.

4.2.2 Conventional TSDC

To form a thermo-electret (Figure 4.2) it is convenient to increase the temperature with the purpose of enhancing the free carrier mobility and speeding up the bound charge motion. When the *polarization temperature* (T_p) is reached, a poling field (F_p) is applied along two stages. Firstly, an isothermal polarization in which the conduction mechanisms that depend on the temperature are activated. Then, a non-isothermal polarization to “freeze” such activated mechanisms.

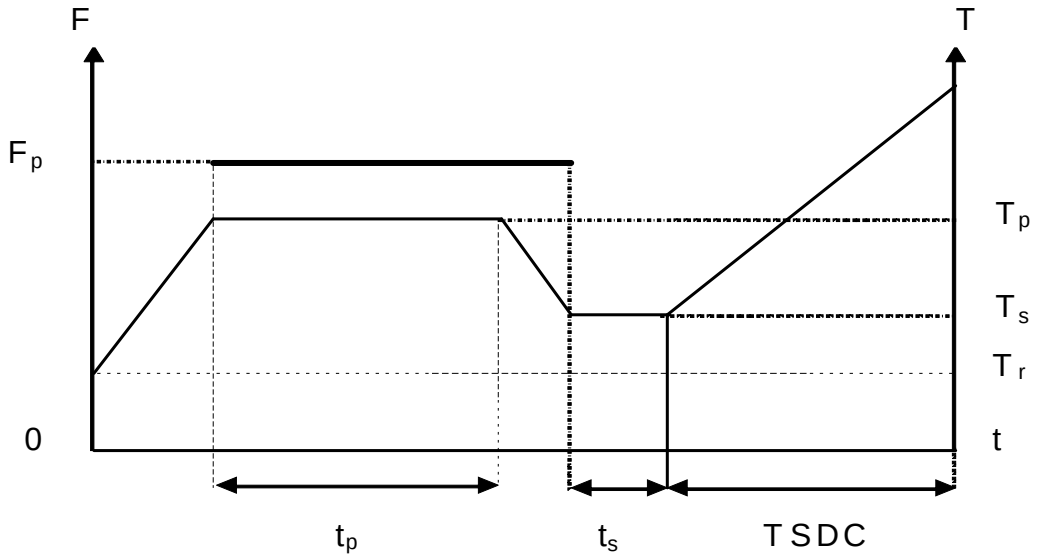

Figure 4.2. Diagram of the conventional thermo-electret formation stages.

The time along which the field is applied during the isothermal stage is called *isothermal polarization time* (t_p). When this time is over, the system is cooled down to the *storage temperature* T_s without removing the poling field. Sometimes T_s is the room temperature (T_r). At T_s the activated mechanisms during the polarization time tend to recover the equilibrium during the *storage time* (t_s). However, T_s is low enough so that depolarization of the sample takes place at a very low rate compared with the time-scale of the experiment. By this way an electret is formed. The sample is then heated at a constant rate (v_h) and the thermally activated depolarization current is recorded as a function of temperature to obtain a TSDC spectrum of the sample.

4.2.3 Mechanisms that can be activated during the formation of a thermo-electret

There can be several mechanisms that give rise to the polarization of the material when a thermo-electret is formed. In general, the sort of the stored charge in the electret depends on the material, the method employed to form it and the polarization conditions (poling field, temperature, polarization time, etc). The microscopic processes [8] that give rise to the polarization of the material are summarized below:

1. Polarization of *permanent dipoles* located in the material.
2. *Induced dipoles* polarization due to microscopic movements of ions in the molecules or in the unit cells in solids
3. *Charge injection* that leads to an excess charge distribution in the material.
4. *Maxwell-Wagner-Sillars* effect that give rise to an interfacial polarization in heterogeneous materials.
5. *Space charge* polarization by the movement of charge carriers and their subsequent trapping in localized states.

In polar materials, the interaction between the *dipolar momentum* and the applied electric field leads to the dipoles (1 in Figure 4.3) orientation and a resulting net dipolar momentum in the direction of the field.

If there is an air gap between the sample and the electrode that can be ionized and that can generate a *corona* discharge, the charge injection on the sample surface (*surface charge*) from electrodes can be considered (3 in Figure 4.3).

The space charges (5 in Figure 4.3), electrons and ions, are activated by the applied field and head towards the electrodes. The charge carrier motion along macroscopic distances is conditioned by the possible recombination with opposite charges, by trapping centers, by imperfections in the material and by its own mobility, which is a function of temperature. For these reasons, free charges remain localized in the material bulk, resulting in the formation of space charge regions.

Moreover, the existence of temperature gradients, which are significant in thick samples, can cause the charge carrier diffusion and, consequently, the configuration of an alternative spatial distribution that allows the formation of charge clouds that can be described as macroscopic dipoles.

Another bulk effect should be considered if the material is not homogeneous i.e. there are regions with different permittivities and conductivities (for instance, a semi-crystalline polymer in which there are amorphous and crystalline regions). Then the

different regions behave like small capacitors with a characteristic time that depends on the relation between the different conductivities, permittivities and region dimensions. Such phenomenon is known as Maxwell-Wagner-Sillars effect (4 in Figure 4.3). Both conductivity and permittivity are magnitudes that typically depend on the temperature; therefore the relaxation associated to this mechanism is thermally activated. In this model the free charges are placed in the interface between regions of different conductivity.

Finally, Gerson [9] proposed a polarization mechanism (6 in Figure 4.3) due to the displacement of space charges of opposite sign that can be separated at microscopic distances, responding to the polarization in the same way that the dipolar orientation.

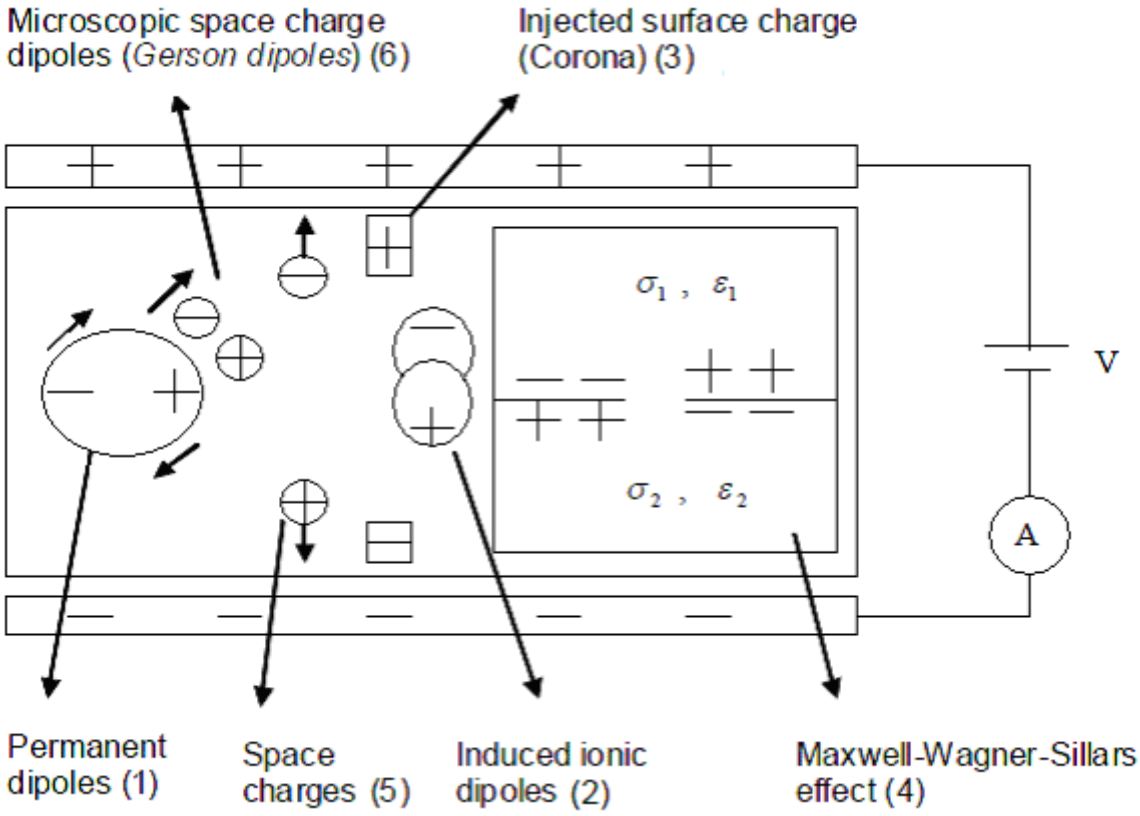

Figure 4.3. Diagram of the mechanisms that can be activated during the formation of a thermo-electret.

4.2.4 Windowing Polarization (WP)

The so-called *Windowing Polarization* (*WP*) [10] is a variation of the conventional TSDC that is used for the *Relaxation Map Analysis* (*RMA*) introduced by Lacabanne [11]. Firstly, the sample is heated up to T_p. Then, the poling field F_p is applied for a polarization time t_p. At the end of the isothermal polarization, the sample is cooled down to $T_{p\text{-}off}$ at which the field is removed. In some versions, the sample is maintained at this temperature during a time t_s, so an isothermal depolarization takes place. Once t_s is over, the sample is cooled down to the depolarization starting temperature T_d, at which it remains for a time t_d before the stimulated depolarization starts. By means of this procedure (Figure 4.4), the charge resulting from the polarization process is linked to a small range of temperatures determined by the width of the polarization window $\Delta T_w = T_p - T_{p\text{-}off}$, that usually is smaller than 10ºC [12].

If the polarization parameters are suitably chosen the obtained depolarization peak is almost "simple", that is, not much distributed, and can be described by an only *relaxation time* as a good approach. Then, by giving different values to the T_p along the range in which the studied relaxation takes place, several depolarization peaks are obtained. Such peaks constitute the elementary relaxation modes and are considered as Debye-like relaxations. If plotting them together, it results in a spectrum that is the so-called *relaxation map* of the material.

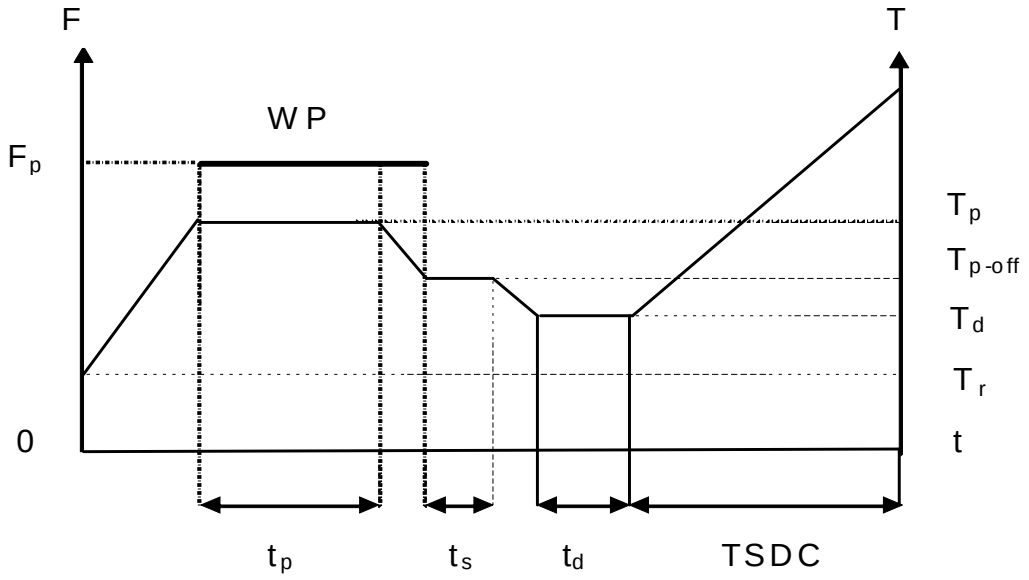

Figure 4.4. Diagram of the thermo-electret formation stages by Windowing Polarization (WP) according to Lacabanne [11].

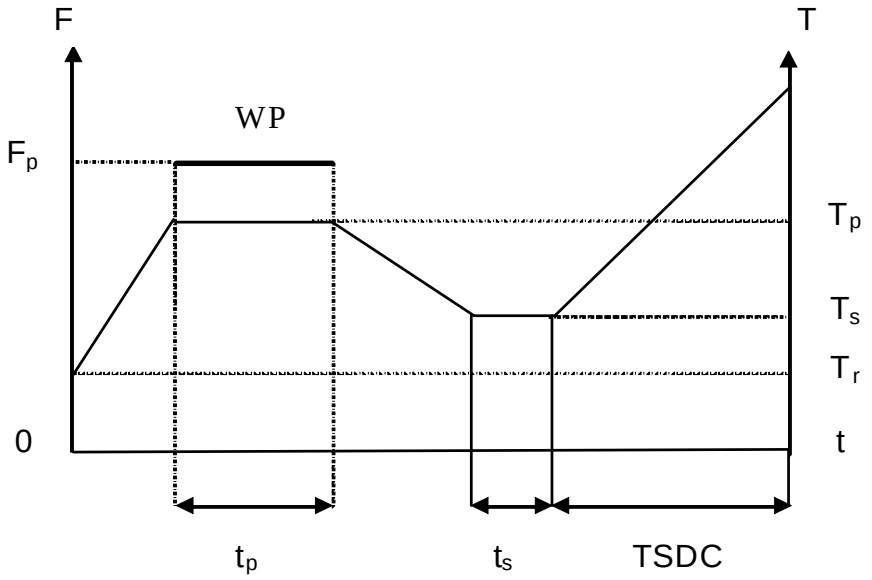

Figure 4.5. Diagram of the thermo-electret formation stages by null width window WP.

Also, the *null width window WP* technique (Figure 4.5) has to be considered. Is the WP version normally used by the DILAB group members and consists in polarizing only

isothermally ($\Delta T_w=0$). It is believed that by doing so the resolution of the technique in determining the elementary relaxation modes is improved [13,14].

4.2.5 No Isothermally Windowing (NIW) polarization

Another TSDC version is the *No Isothermally Windowing* (*NIW*) technique and consists in applying the poling field only in the no isothermal stage (Figure 4.6). Thus, polarization mechanisms are activated in a range of temperatures by applying the poling field at the starting polarization temperature T_{sp} and removing it at the ending polarization temperature T_{ep}, when the system is being cooled.

By using the NIW method, the isothermal annealing time and its effects on the sample and measurements can be minimized since, if $t_p=0$, it is not necessary to maintain the sample at a constant temperature. On the other hand, by modifying the no isothermal window width ($\Delta T_w=T_{sp}-T_{ep}$) it is possible to select the range of mechanisms and relaxations that will be activated.

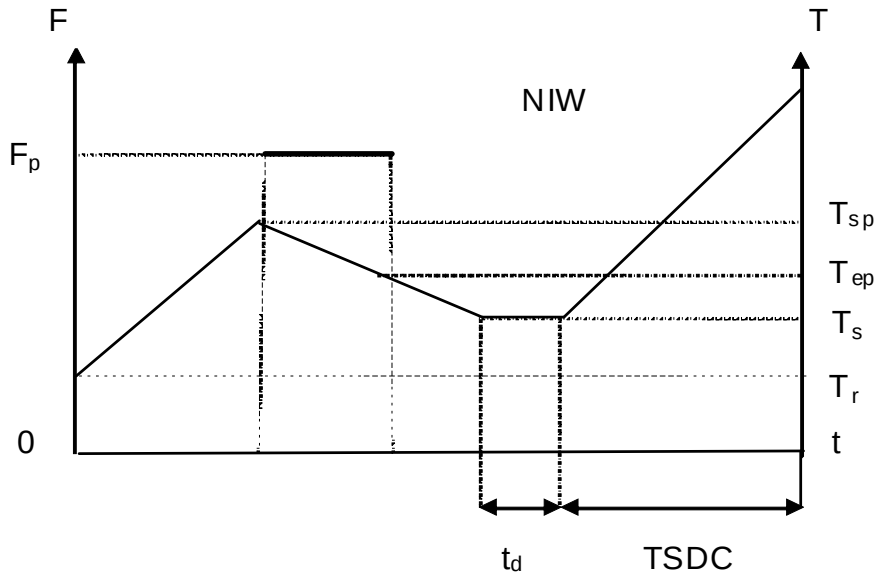

Figure 4.6. Diagram of the thermo-electret formation stages by no isothermally windowing (NIW).

4.2.6 Sign choice for the thermally stimulated currents polarity: heteropolar / homopolar

Depending on the sign of the discharge currents they are called *heteropolar*, when the polarity is the opposite to that of the charging currents, or *homopolar*, when the polarity is the same (not to be confused with the heteropolar/homopolar categories for the space charge measured by PEA; in that case, the polarity is determined for the charge, not the current, in function of the charging polarity of the closer electrode). In the present work, the sign associated with the heteropolar currents is the positive, whereas the negative sign implies homopolar behavior (Figure 4.7). This is the sign choice usual in the DILAB works.

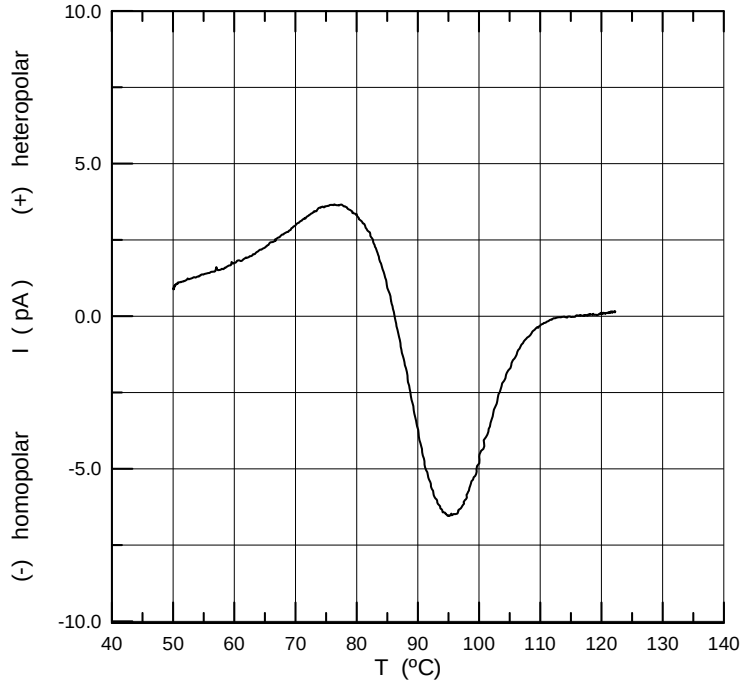

Figure 4.7. TSDC thermogram of an XLPE sample. Sign choice: (+) heteropolar, (−) homopolar.

4.2.7 Peak analysis of the TSDC spectrum

The TSDC spectra obtained by these processes show several peaks with different characteristics (temperature of the maximum, amplitude, width, etc) as can be seen in Figure 4.8. The analysis of these peaks and their evolution with thermal, electrical or chemical treatments can provide information about the molecular structure of the studied materials, the effect of the temperature on such structure, and the consequences of the treatments on the materials. In amorphous polymers, the glass transition temperature is normally associated to the so-called α peak. In this case, the relaxation is originated by cooperative segmental motions of the main chain. Below the T_g, there are other peaks, like β and γ relaxations, usually attributed to side groups motions. All these peaks also can be detected by the DEA technique. If the analyzed material is not polar, then neither TSDC nor DEA can be employed to detect them and it is necessary to use other techniques, like mechanical spectroscopy (DMA). If the material is polar, then the TSDC α, β and γ peaks are the response of the relaxation of polar groups when the mentioned main chain or side group motions take place. On the other hand, another TSDC peak is detected at higher temperatures ($T>T_g$) typically. This is the so-called ρ relaxation and it has not a polar origin but is related to the free charge located in polymer [15]. These are the four classic TSDC peaks of amorphous polymers. However, the number of peaks detected by TSDC, their designation, and their physical origin may change in function of the analyzed polymer. For instance, in crystalline polymers the peak labelled α is often related to the crystalline regions. In polyethylene, γ is associated with the glass transition, which takes place below 0ºC, and the β relaxation is related to side-branching [16]. And there are two alpha relaxations: α and α'. The first has been related to the molecular reorientation within the crystals [16,17]. In case of α', it is usually considered a crystal boundary phenomenon [16]. Anyway, since polyethylene is a non polar material, polar relaxations can not be detected by dielectric spectroscopy in

normal conditions. For this reason, although the presence of impurities or some degree of oxidation can provide the polyethylene with somewhat of polarity, usually the polymer is treated to make it polar. In the case of the XLPE used in power cable insulation, it is assumed that there are some impurities (cross-linking by-products, antioxidants) that can provide a polar response. Besides, there may be some degree of oxidation, which can be increased by aging treatments, enhancing this polar behavior.

Dipolar charge analysis

The behavior of dipoles leads to the relaxations analysis [19,20] and provides general information about the changes that affect the molecular chains, like *physical annealing* phenomena [21,22,14] and structural changes phenomena [23,24,25].

Free charge analysis

The free charge behavior provides information about the conductive processes in the material: doping phenomena [26,27,28], dielectric strength [29,30,31], crystallization phenomena [23,27], role of interphases [32,33,34] and diffusion [35,36]. Besides, the free charge peak study can be used to determine the charge trapping ability of the material. This parameter is important to correlate the space charge with the dielectric strength of insulating materials.

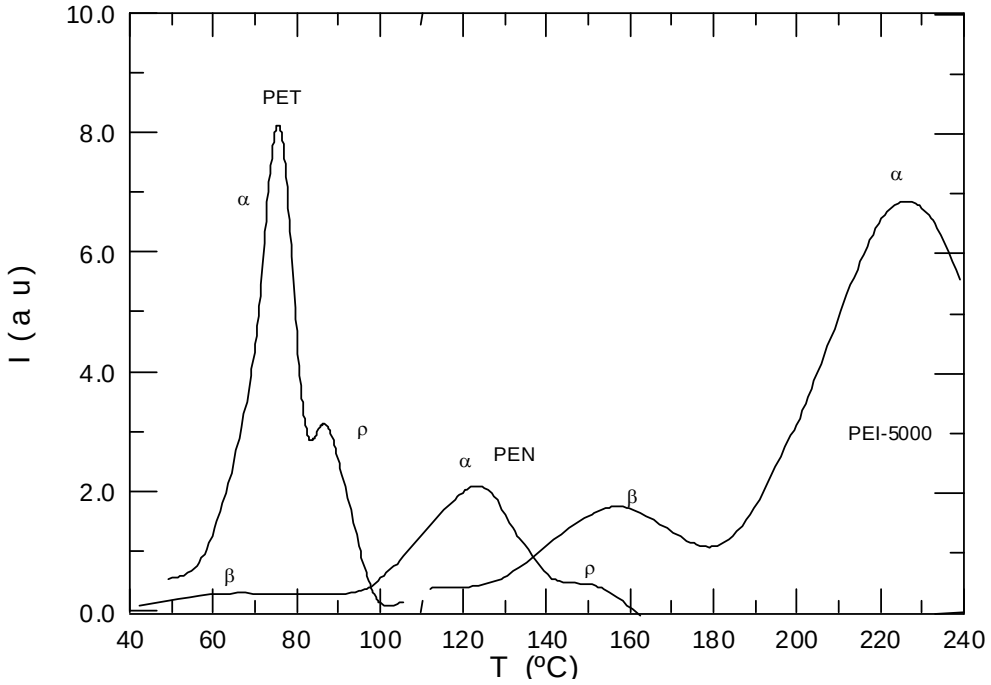

Figure 4.8. TSDC spectra of some polymers [18].

4.2.8 Dipolar and free charge relaxations

In polymers, the molecular chains bound to dipoles have different masses and lengths, so they relax at different times. The superposition of these slightly different relaxation times gives rise to a *distributed relaxation*. As a consequence, the TSDC peaks obtained for polymers usually are wide in comparison with other materials.

During the heating, the polar groups with low activation energy, Ea, are disoriented first, while those that need more energy to recover the equilibrium respond at higher temperatures. Thus, the obtained thermogram will show different peaks related to the different polar groups. Besides, the dipoles efficiency during the discharge is very high and they contribute totally to the depolarization currents.

On the other hand, the free charges moved away from their equilibrium position are localized in trapping centers and have the tendency to recover their original state. Their motion is caused by forces generated by their own local fields (*drift conduction*), or by diffusion forces that tend to eliminate the concentration gradients (*diffusion conduction*). During the heating process, free charges can acquire enough energy to be released from the local traps. Then, these charges can be trapped again (*retrapping*) or they can recombine with charges with opposite sign (*recombination*). This recombination can occur when a charge meets another released charge, a charge thermally generated form a neutral molecule dissociation, or the image charge in the electrode. If a recombination between free charges and their images in the electrodes occurs, then the free charge contribution to the discharge currents is not complete. The reason is that there is a decrease of the induced charge in the electrodes that gives rise to the recorded current.

Therefore, the efficiency of the free charge contribution to the recorded discharge current strongly depends on the electrodes blocking features. In case of sort-circuiting the material with both electrodes in perfect contact with the sample faces, the mean internal field is zero and the excess charges will not give rise to a detectable ohmic conduction current. However, if an electrode is separated (Figure 4.9), the system is blocked by the *air gap* and the mean internal field is now different from zero. This gives raise to a current due to the ohmic conduction and the diffusion.

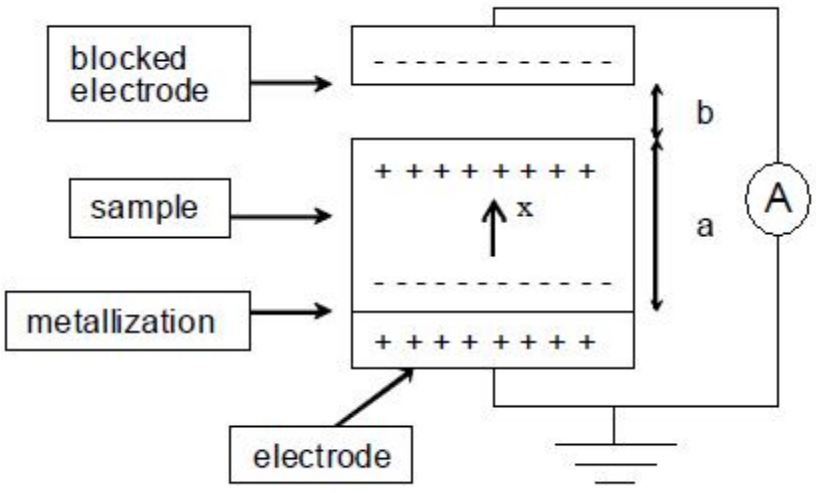

Figure 4.9. Electret depolarization with an air gap between one electrode and the sample.

In addition, the existence of an air gap between the sample and one electrode can originate the formation of a surface charge distribution during the polarization process via corona injection. When the sample is heated, this trapped charge is released by ohmic conduction through the not blocked electrode and, thus, it contributes to de discharge with the same sign of the charging current (homocharge).

As it can be seen, the different TSDC contributions have different efficiencies. The dipolar reorientation in polar polymers has an efficiency of 100%. On the other hand, the currents due to excess charge present an efficiency from 25 to 50% in *homoelectrets* and from 50 to 100% in *heteroelectrets*. Finally, the heterogeneity of semi-crystalline polymer may originate the Maxwell-Wagner-Sillars effect [37] with an efficiency that can take all values between 0 and 100%.

4.2.9 General expression of current density. The Bucci-Fieschi-Guidi (BGF) method

Once an electret has been formed, if the two metallic electrodes are short-circuited through an electrometer, it is possible to record the current evolution isothermally. This current is caused by the dipolar disorientation and the neutralization of the charge distributed in the bulk and in the surface. An equation that incorporates all the involved mechanisms would not be easy to solve. For this reason, the current density is usually expressed independently for any contribution. During TSDC the current density can be decomposed in two parts

$$J(x,t) = J_C(x,t) + J_D(x,t) \tag{4.1}$$

where J_C is the conduction current density and J_D is the displacement current. J_C is composed of the drift current $J_{dr}(x,t)$ and the diffusion current $J_{di}(x,t)$

$$J_{dr}(x,t) = (\rho(x,t) + \rho_e(T))\mu(T)F = \rho(x,t)^+ \mu(T)^+ F + \rho(x,t)^- \mu(T)^- F + \sigma(T)F \tag{4.2}$$

$$J_{di}(x,t) = -\delta \frac{\partial \rho}{\partial x} = \bar{\delta} \frac{\partial \rho^-}{\partial x} - \dot{\delta} \frac{\partial \rho^+}{\partial x} \tag{4.3}$$

where F is the electric field, $\rho(x,t)$ is the excess charge density, which is the responsible for the drift and diffusion currents, $\rho_e(T)$ is the charge density of the material in thermal equilibrium and gives raise to the ohmic conductivity of the material: $\sigma(T)=\rho_e(T)\mu(T)$, $\mu(T)$ is the carrier drift mobility and δ is the diffusion coefficient. The super index + or – refer to the positive and negative charge carriers.

The displacement current can be expressed from the time derivative of the electric displacement field

$$J_D(x,t) = \frac{\partial D}{\partial t} = \frac{\partial(\varepsilon_0 F + P)}{\partial t}. \tag{4.4}$$

The polarization density $P(x,t)$ can be decomposed in two components: a slow polarization, $P_s(x,t)$, and an almost instantaneous one, $P_i=(\varepsilon_\infty-\varepsilon_0)F$. If these components are introduced into equation (4.4), then

$$J_D(x,t) = \frac{\partial(\varepsilon_\infty F + P_s)}{\partial t}. \tag{4.5}$$

By taking into account the previous equations (4.1–5) and replacing J_C and J_D by their expressions in (4.1), the current density detected by the external ammeter is obtained

$$J(x,t) = \rho(x,t)\mu(T)F + \sigma(T)F - \delta\frac{\partial\rho}{\partial x} + \frac{\partial(\varepsilon_\infty F + P_s)}{\partial t}. \tag{4.6}$$

This equation provides a general description of the discharge of an electret. By integrating the previous equation along the sample thickness *a*, and taking into account that the total recorded discharge current is independent of *x*, the expression obtained is

$$J(t) = \frac{1}{a}\int_0^a \left(\rho(x,t)\mu(T)F + \sigma(T)F - \delta\frac{\partial\rho}{\partial x} + \frac{\partial(\varepsilon_\infty F + P_s)}{\partial t} \right) dx\ . \tag{4.7}$$

This expression is suitable for analyzing the typical depolarization processes, by considering that the polarization time is large enough to can suppose that the maximum reached polarization is the equilibrium polarization, *P(∞)*, of the sample at the studied temperature.

4.2.10 Charging and discharging with both electrodes in contact with the sample

To polarize dielectric materials without injecting surface charge, both electrodes have to be placed in direct contact with the sample (the distance *b* is zero in Figure 4.9). To obtain an almost perfect contact the both faces of the sample can be coated with metallic electrodes (Al, Au, Ag) in the vacuum. Alternatively, they can be painted with metallic paint. By this way, the presence of air between the electrodes and the sample is minimized. Once the electret has been formed, the sample is short-circuited to can study the depolarization phenomena. In a short circuit situation the electric field circulation is cancelled $\int_0^a F dx = 0$, as well as the diffusion component, $\int_0^a \delta\frac{\partial\rho}{\partial x}dx = 0$, which does not contribute much to the current density in this case due to the excess charges tendency to become neutralized with their image charges in the electrodes and that $\rho(a,t) \approx \rho(0,t)$. Thereby, the recorded current expression is now

$$J(t) = \frac{1}{a}\int_0^a \left(\rho(x,t)\mu(T)F + \frac{\partial P_s}{\partial t} \right) dx\ . \tag{4.8}$$

4.2.11 Polar discharge (uniform distribution)

By using large polarization times the material can reach the equilibrium polarization. The isothermal depolarization of an electret formed by this way will be analyzed in this subsection. However, to focus on the dipolar processes, the excess charge is considered zero. The relaxation of dipoles gives raise to depolarization currents due to the neutralization of their image charges among them. The image charges recombine in the external circuit in which the current is measured. Therefore, equation 4.8 can be written as

$$J(t) = -\frac{\partial P_s}{\partial t} \tag{4.9}$$

where a minus sign is added due to the fact that, during the depolarization, the current density and the polarization vectors have an opposite direction.

In the *Bucci-Fieschi-Guidi* (*BDR*) theory [38] the Debye model is assumed in both the polarization and the depolarization of an electret. For this reason, $P_s(t)$ can be described in terms of the Debye function for simple relaxations

$$P_s(t) = P(\infty)\exp\left(-\frac{t}{\tau}\right) \tag{4.10}$$

where τ is the relaxation time. Then, by differentiating $P_s(t)$ with respect to time and replacing in (4.9), the following expressions are obtained

$$J(t) = \frac{P(\infty)}{\tau}\exp\left(-\frac{t}{\tau}\right) \quad \Rightarrow \quad -\frac{dP_s(t)}{dt} = \frac{P_s(t)}{\tau}. \tag{4.11}$$

This equation could be used to describe the *isothermal depolarization* (*IDC*) of an electret in a simple first-order relaxation model. However, in TSDC measurements the sample is thermally stimulated. Therefore, there is not only a change in time but also in temperature. In this case, the relaxation time can not be considered as a constant, as it is a function of temperature. In a model with a simple relaxation time the *Arrhenius law* is usually employed:

$$\tau(T) = \tau_0 \exp\left(\frac{E_a}{kT}\right) \tag{4.12}$$

where k is the *Boltzmann constant* and τ_0 the natural relaxation time. But during the heating ramp T also depends on the time. So by considering the time relaxation dependency $\tau(T(t))$ in the equation (4.10) then

$$P_s(t) = P(\infty)\exp\left(-\int_0^t \frac{dt}{\tau}\right) \tag{4.13}$$

which may be introduced in the expression (4.11) to obtain

$$J(t) = \frac{P(\infty)}{\tau}\exp\left(-\int_0^t \frac{dt}{\tau}\right). \tag{4.14}$$

Besides, τ can be written as a function of temperature

$$J(t) = \frac{P(\infty)}{\tau_0}\exp\left(-\frac{E_a}{kT}\right)\exp\left(-\int_0^t \frac{dt}{\tau_0}\exp\left(-\frac{E_a}{kT}\right)\right). \qquad (4.15)$$

Normally, TSDC experiments are carried out with a constant heating rate. Then the temperature dependency on the time is linear

$$T = T_0 + vt \qquad (4.16)$$

where T_0 is the initial temperature of the depolarization ramp and v is the constant heating rate (usually the constant rate does not change in the whole process: v is also the same in the heating or cooling ramps during the electret formation). If replacing T with this expression the equation (4.15) is

$$J(t) = \frac{P(\infty)}{\tau_0}\exp\left(-\frac{E_a}{kT}\right)\exp\left(-\frac{1}{v\tau_0}\int_{T_0}^{T}\exp\left(-\frac{E_a}{kT}\right)dT\right). \qquad (4.17)$$

According to this expression, the dependency of $J(t)$ on T is determined by the product of two exponential functions which exponent is a function of $1/T$. The first factor of the expression dominates the beginning of the discharging peak, whereas the second one is more decisive around the temperature of maximum depolarization current, T_m. The fact that at different temperatures $J(t)$ is dominated by different functions implies an asymmetrical curve for the depolarization currents. For this reason, Chen [6] introduced an asymmetry factor

$$a = \frac{T_2 - T_m}{T_2 - T_1} \qquad (4.18)$$

where T_1 and T_2 are the temperatures that delimit the current peak. If a is lower than 0.5 then the depolarization peak is asymmetrical. A relation between the temperature of the maximum current, the activation energy and the pre-exponential factor can be established by equaling the temperature derivative of the current density to zero

$$\left.\frac{dJ}{dT}\right|_{T=Tm} = 0\ . \qquad (4.19)$$

The temperature that verifies equation (4.19) is that of the maximum density current $J(T)$. By solving this equation the T_m is obtained in function of E_a

$$T_m^{\,2} = \frac{E_a}{k}v\tau_0\exp\left(\frac{E_a}{kT_m}\right). \qquad (4.20)$$

This expression shows that the temperature of the maximum does not depend on the poling field, the polarization time or the polarization temperature. The natural parameters that can influence T_m are the activation energy E_a and the natural relaxation time. However, the heating rate v is a controlled experimental parameter that can

modify the peak position. An increase on *v* shifts the peak to higher temperatures and changes the experimental resolution.

4.2.12 Current generated by a space charge distribution

The space charge (bulk free charge) distribution due to the excess charge gives raise to a non-neutral situation in the dielectric bulk. This space charge polarization state is a lot more complex that the dipolar polarization. One of the most important difficulties present in the TSDC space charge analysis is the fact that the efficiency of space charge contribution to the recorded currents can range between 0 and 100%. During the charging process the poling field can generate new charges and move the existing ones, originating the space charge distribution. The charges motion can be interrupted by trapping phenomena. For instance, electrons can be trapped in the molecular net defects. During the discharge process, the thermal excitation causes that electrons initially trapped jump to the conduction band, where they are transported to the electrodes. Some of these charges recombine on the way. The poor efficiency is due to the fact that part of excess charges are neutralized with the image charges in the electrodes, preventing them to contribute to the current recorded in the external circuit. In addition, the space charges can be neutralized by carriers thermally generated, which are responsible for the ohmic conduction in the material, and that do not contribute at all to the detected current, when the electrodes are short-circuited, as the mean field is zero.

If an excess charge ($\rho \neq 0$) is supposed in a non polar material ($P=0$) the equation (4.8) is

$$J(t) = \frac{1}{a}\int_0^a \left(\mu^+(x,t)\rho^+(x,t) + \mu^-(x,t)\rho^-(x,t)\right)F(x,t)dx \qquad (4.21)$$

and by considering the Poisson's equation

$$\varepsilon_\infty \frac{\partial F}{\partial x} = \rho^+(x,t) - \rho^-(x,t) \qquad (4.22)$$

and the assumption of a situation in which the mobilities of the positive and the negative charges are the same, an equation in which the discharge currents depend quadratically on the electrical field limit values is obtained

$$J(t) = \frac{1}{2a}\mu\varepsilon_\infty\left[F^2(a,t) - F^2(0,t)\right]. \qquad (4.23)$$

The numeric solutions of the expression (4.21) may be calculated if the charge density spatial distributions are known. For instance, a distribution proposed by Van Turnhout [39] can be used

$$\rho^+(x,t) = \rho_0^+ \cos\left(\frac{\pi x}{2a}\right); \quad \rho^-(x,t) = \rho_0^- \operatorname{sen}\left(\frac{\pi x}{2a}\right) \quad 0 \le x \le a\,. \qquad (4.24)$$

By considering again the Poisson's equation (4.22) it is possible to found the electric field in function of time and position

$$F(x,t) = F(0,t) + \frac{2a}{\pi\varepsilon_\infty}\left[\rho_0^+ sen\left(\frac{\pi x}{2a}\right) + \rho_0^-\left(\cos\left(\frac{\pi x}{2a}\right) - 1\right)\right]. \quad (4.25)$$

If replacing $x=a$, the field in a, $F(a,t)$, is obtained. Then, it is possible to replace it in the expression (4.23) to obtain the density current

$$J(t) = \mu\left[\frac{2a}{\pi^2\varepsilon_\infty}\left(\rho_0^+ - \rho_0^-\right)^2 + \frac{2}{\pi}\left(\rho_0^+ - \rho_0^-\right)F(0,t)\right]. \quad (4.26)$$

Therefore, the discharge current depends on the space charge placed at the limits of the sample. Then, if there is a symmetric charge distribution the result is that $J=0$. Otherwise, since the difference of limit charges is not zero there is a drift current. But, then, the contribution of the diffusion current also has to be considered.

4.3 TSDC models for space charge relaxation in polymers

4.3.1 Introduction

In the literature, several theoretical models of the space charge relaxation phenomena in polymeric materials can be found. In this section, some of the models for TSDC discharges are briefly commented.

4.3.2 TSDC originated by ionic space charge

Some TSDC peaks are attributed to the motions of ionic charges, interstitial ions or ion vacancies, and they present the following features [40]:

1. The temperature of the maximum of the TSDC peak (T_m) is not well defined. Its value increases with the polarization temperature (T_p).
2. The peak area is not a linear function of the applied poling field, especially for low applied fields.
3. The shape of the peak does not allow to determine the activation energies.

However, some authors claim that the area of these peaks is approximately proportional to the field for low poling fields, and that the temperature of the maximum depends on the impurity concentration of the sample [41,42].

The dispersion of the results points out that the ionic space charge relaxation is more complex than the dipolar one. However, some models have been developed. An expression for the current has been proposed in Kunze et al. [41]:

$$I(T) = \frac{\sigma_0}{\varepsilon} Q_0 \exp\left(-\frac{E}{kT}\right)\exp\left[-\frac{\sigma_0}{\varepsilon\beta}\int_{T_0}^{T}\exp\left(-\frac{E}{k\theta}\right)d\theta\right] \quad (4.27)$$

where σ_0 is the preexponential factor of the thermally activated conductivity, β is the heating rate, $E=E_m+E_d/2$ is the total activation energy, E_m is the activation energy of the ion motion process, E_d is the molecular dissociation energy needed to provide ion species, T_0 is the initial temperature of the discharge and Q_0 is the charge present in the electrodes at this temperature.

4.3.3 Interfacial phenomena

When there are heterogeneities in a dielectric material the Maxwell-Wagner-Sillars (MWS) interfacial polarization phenomena may appear. The MWS theory is applied when there are regions of the material with different conductivities and permittivities. The simplest MWS model is a capacitor with two layers. This leads to an expression [7,43] of the current density in function of the permittivities and the conductivities of both materials

$$J = \frac{\left[\varepsilon_1\sigma_2(T)-\varepsilon_2\sigma_1(T)\right]\left[\varepsilon_2\sigma_1(T_p)-\varepsilon_1\sigma_2(T_p)\right]d_1d_2}{\left(\varepsilon_1 d_2+\varepsilon_2 d_1\right)^2\left[d_1\sigma_2(T_p)+d_2\sigma_1(T_p)\right]}V_p\exp\left[-\int_0^T\frac{dT'}{\beta\tau^*(T')}\right] \quad (4.29)$$

where *1* and *2* subindexes refer to the capacitor layers, ε is the permittivity, σ is the conductivity, d is the layer thickness, T_p is the polarization temperature, V_p is the poling voltage, β is the constant heating rate, and $\tau^*(T)$ is the relaxation time, which is

$$\tau^*(T)=\frac{\varepsilon_1 d_2+\varepsilon_2 d_1}{d_1\sigma_2(T)+d_2\sigma_1(T)}. \quad (4.29)$$

4.3.4 Creswell-Perlman model

The model of Creswell and Perlman for corona-charged sheets assumes a uniform distribution of charge –free and bound– in the material [44]. It is based on the following equations:

$$dJ=\frac{\rho_f dx v(x)}{d} \quad (4.30) \qquad J(x)=\rho_f\mu F(x) \quad (4.31) \qquad \frac{dF(x)}{dx}=\frac{\rho}{\varepsilon} \quad (4.32)$$

where in the equation (4.30) dJ is the contribution to the density current measured in the external circuit of a free charge sheet with a thickness dx, $\rho_f dx$ is the free charge per unit area in this charge sheet, $v(x)$ is the velocity of this free charge sheet and d is the sample thickness. The equation (4.31) is the Ohm's law, where μ is the carrier mobility and $F(x)$ is the electric field. The expression (4.32) is the Gauss's law, where ρ is the total –free and bound– charge density. For a constant heating rate β, this system has well defined solutions in two cases:

1) Slow retrapping:

$$J=\frac{\mu e^2\delta^2 {n_0}^2}{2\varepsilon d}\frac{\tau}{\tau_0}\exp\left[-\frac{E_a}{kT}-\frac{2}{\beta\tau_0}\int_{T_0}^{T}\exp\left(-\frac{E_a}{kT'}\right)dT'\right] \quad (4.33)$$

2) Fast retrapping:

$$J = \frac{\mu e^2 \delta^2 {n_0}^2}{2\varepsilon d} \frac{N_c}{N_t} \exp\left[-\frac{E_a}{kT} - \frac{2}{\beta \tau_0 N_t} \int_{T_0}^{T} N_c \exp\left(-\frac{E_a}{kT'} \right) dT' \right]. \qquad (4.34)$$

In this expressions δ is the penetration length of the charge sheet, e is the electron charge, τ is the free electrons mean lifetime, N_c is the effective concentration of conduction states, N_t is the trap concentration, and n_0 is the initial concentration of trapped electrons. The mean lifetime of an electron in a trap decays with temperature according to $\tau_0 \exp(E_a/kT)$, where E_a is the trap depth.

4.3.5 Kinetic models for TSDC

4.3.5.1 Introduction

The theory used to explain the thermoluminescence due to space charge relaxation processes is also suitable to explain the TSDC discharges with the same origin [45]. The theoretical description of such phenomena is based on the formalism of the chemical kinetics [46].

Figures 4.10, 4.11 and 4.12 show the processes on which the kinetic models are based. They consider discrete trapping levels and recombination centers.

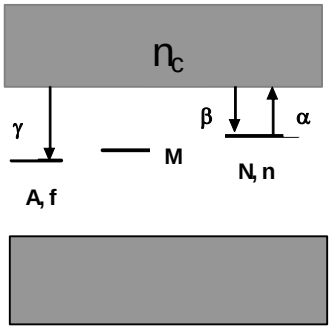

Figure 4.10. Electronic traps.

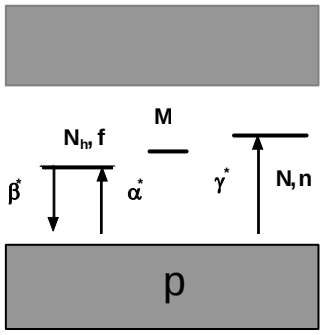

Figure 4.11. Hole traps.

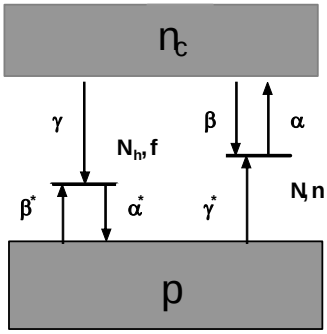

Figure 4.12. Electronic and hole traps.

There are three processes considered in the kinetic models:

1. **Single type of electronic traps model**: A single type of electronic traps with concentration N at a certain depth is considered. These traps are thermally connected with the conduction band by α and β transitions. Other types of traps are disconnected from the conduction band. The recombination centers have a concentration A and a recombination coefficient γ. The concentration of free electrons, filled traps and unfilled recombination centers are n_c, n and f, respectively.

2. **Single type of hole traps model**: It is analogous to the single type of electronic traps model but applied to holes and the valence band instead of electrons and the conduction band. In this case p is the holes concentration in the valence band, N_h is the hole trap concentration and α^*, β^* and γ^* are the transition rates and recombination coefficient.

3. **Model for a solid that contains electronic traps (which can behave as a hole recombination centers) and hole traps (that can behave as electron recombination centers).** This is a mixed model that includes the situations described in 1 and 2 models.

4.3.5.2 TSDC caused by a single type of electronic traps

This model considers the processes depicted in Figure 4.10. The trap concentration is N and the trap depth is E_a. In addition, there is another trap level with a concentration M, which is deeper and "thermally disconnected" in the working range of temperatures, that is, the traps of this level do not capture electrons nor release the trapped ones. There are also recombination centers. Those that are unfilled have a concentration f. According to the electrical neutrality condition:

$$f = n_c + n + M \tag{4.35}$$

where n_c is the free electrons concentration and n the filled traps concentration at E_a. The expression that determines the evolution of the electron density in the conduction band is:

$$\frac{dn_c}{dt} = \alpha n - \beta n_c(N - n) - \gamma n_c(n_c + n + M). \tag{4.36}$$

The first term on the right-hand side of this equation is related to the release of electrons, which is proportional to the number of trapped electrons at E_a level. The second one refers to the trapping of electrons, which is proportional to the product of the free electron concentration in the conduction band and the unfilled trap concentration. The third term on the right-hand side is related to recombination process, and it is proportional to product of free electrons concentration and the unfilled recombination centers, according to equation (4.35). If considering that M traps are thermally disconnected then

$$\frac{df}{dt} = \frac{dn_c}{dt} + \frac{dn}{dt} = -\gamma n_c(n_c + n + M) \tag{4.37}$$

In this model the only process that implies a reduction in the recombination centers concentration is the recombination of free electrons. Thus the current can be expressed as

$$I \propto \frac{df}{dt} = -\gamma n_c f\ . \tag{4.38}$$

When this model is applied to the thermoluminescence, a coefficient $\eta_{exp}<1$ that expresses the efficiency of the process usually is introduced, since there can be non-radiative relaxation processes, absorption losses, internal reflections on the sample surface, etc. Neither the TSDC have an efficiency of 100%. Therefore, the total released charge is not completely recorded by the outer ammeter, so it is not possible to measure absolute values of the studied magnitudes.

It is not possible to solve the system of equations (4.36), (4.37) and (4.38) analytically. For this reason, they are solved numerically for specific values of the governing parameters [47,48]. The parameter α, which determines the release rate of trapped electrons, is proportional to the function $exp(-E_a/kT)$. Due to the fast decay rate of this function, the usual numerical methods can not be applied in this case. Therefore, the Runge-Kutta-Gill method is used along with an appropriate choice of the calculation step size. However, the main problem is the fact that these methods can not determine the parameter values from an experimental discharge peak. To can evaluate the main parameters of these processes, some approximations, which are simpler and also allow classifying the peaks, were developed for certain conditions.

Two assumptions were made initially by Adirovich to explain the phosphorescence [49] and, later, they were introduced in TSDC [50,51]:

i) $\boldsymbol{n_c} << \boldsymbol{n}$: At every moment the concentration of electrons in the conduction band (or holes in the analogous case of single type of hole traps) is much lower than that of the trapped electrons (or trapped holes). In fact, at the equilibrium, the expected proportion between them is $n_0/n \approx exp(-E_a/kT)$ in the worst case. And the range temperatures at which these peaks usually take place verifies that $E/kT>10$. So the approximation is suitable.

ii) $\left| \dot{\boldsymbol{n}}_c << \dot{\boldsymbol{n}} \right|$: Here the upper dot symbolizes the time derivative. This condition implies that there is not a significant charge accumulation in the conduction band. Thereby, the equation (4.37) can be approximated as $\dot{f} \approx \dot{n}$.

Halperin and Braner [50] used these conditions to obtain the equation

$$I \propto \frac{df}{dt} = -\frac{\alpha\gamma n f}{\gamma f + \beta(N-n)} \tag{4.39}$$

which includes two unknown functions f and n and, so, it can not be solved without additional conditions. Nevertheless, it can be used as the starting point to obtain the limit cases, that is, the first- and second-order kinetics, by means of additional conditions. Then, the rest of the situations may be considered as intermediate order kinetics.

First-order kinetics

If the release followed by a quick recombination of free charge carriers is the main relaxation process, then retrapping can be neglected and the *first-order kinetics* model suggested by Randall and Wilkins [52] is obtained. When recombination is dominant, such condition can be expressed as

$$\gamma f >> \beta(N-n) \tag{4.40}$$

so the expression (4.39) can be replaced by

$$I \propto \frac{df}{dt} = -\alpha n \,. \tag{4.41}$$

By considering the condition ii) previously exposed, $\dot{f} \approx \dot{n}$, the obtained equation is

$$I \propto \frac{dn}{dt} = -\alpha n \,. \tag{4.42}$$

The α dependency on the temperature is $\alpha = s_0 exp(-E_a/kT)$, where E_a is the trapping depth and s_0 is a frequency factor. For a constant heating rate v the current is

$$I(T) = e n_0 s_o \exp\left(-\frac{E_a}{kT}\right)\exp\left[-\frac{s_0}{v}\int_{T_0}^{T}\exp\left(-\frac{E_a}{kT}\right)dT\right] \tag{4.43}$$

where n_0 is the trapped charges concentration at the initial temperature T_0.

Second-order kinetics

The second limit case is a solid in which the thermally activated carriers are trapped and released several times on average before they finally recombine. This can be expressed as

$$\beta(N-n) >> \gamma f \,. \tag{4.44}$$

In addition, it is possible to suppose that trapping is far from being saturated, $n << N$, and that $f \approx n$. As a result, by introducing that $\alpha = s_0 exp(-E_a/kT)$, and the condition (4.44) in (4.39), a second-order equation is obtained

$$I \propto \frac{df}{dt} \approx \frac{dn}{dt} = -s_0' n^2 \exp\left(-\frac{E_a}{kT}\right) \tag{4.45}$$

where $s_0' = s_0 \dfrac{\gamma}{\beta N}$. For a constant heating rate v, the solution of (4.45) is the Garlick and Gibson's equation [53]

$$I = e n_0^2 s_0' \exp\left(-\frac{E_a}{kT}\right)\left[1 + \frac{n_0 s_0'}{v}\int_{T_0}^{T}\exp\left(-\frac{E_a}{kT}\right)dT\right]^{-2} . \tag{4.46}$$

Mixed first- and second-order equation

In the *second-order kinetics* case, the condition $f \approx n$ seems to be the least plausible since in real samples a lot of defects and impurities can be found. Therefore, deep traps M have to be considered in equation (4.35), and only n_c is negligible.
It is also possible to suppose that the retrapping and recombination probabilities are similar: $\beta \approx \gamma$. All these considerations result in the following equation [54]

$$I \propto \frac{df}{dt} = -s' n(n+M)\,. \tag{4.47}$$

In this equation s' is a parameter proportional to α that depends on the temperature as $s' = s_0' \exp(-E_a/kT)$, where s_0' is a temperature independent pre-exponential factor.

Then, the previous equation can be expressed as

$$I \propto \frac{df}{dt} = -s_0'\, n^2 \exp\left(-\frac{E_a}{kT}\right) - s_0'\, Mn \exp\left(-\frac{E_a}{kT}\right) \tag{4.48}$$

whose solution [54] for a constant heating rate v is

$$I(T) = \frac{es' M^2 \kappa \exp\left[\dfrac{Ms'}{v}\displaystyle\int_{T_0}^{T} \exp\left(-\frac{E_a}{kT}\right)dT\right] \exp\left(\dfrac{E_a}{kT}\right)}{\left(\exp\left[\dfrac{Ms'}{v}\displaystyle\int_{T_0}^{T} \exp\left(-\frac{E_a}{kT}\right)dT\right] - \kappa\right)^2} \tag{4.49}$$

where $\kappa = \dfrac{n_0}{n_0 + M}$, and n_0 is the concentration of trapped charge carriers at the initial temperature T_0.

General-order kinetics

The previous kinetic models do not describe appropriately all the possible kinetic processes. Therefore, some authors introduced an empirical equation for intermediate processes, giving rise to the *general kinetic order* model [55,56]. The proposed equation is

$$I \propto \frac{dn}{dt} = -s_0' n^b \exp\left(-\frac{E_a}{kT}\right) \tag{4.50}$$

in which the frequency factor dependency on temperature has been already introduced, being s_0' a temperature independent pre-exponential factor whose International System units are $C^{1-b}s^{-1}$. The empiric parameter b determines the kinetic order and it can not necessarily take integer values. In the limit $b=1$ this expression becomes the Randall and Wilkins' equation (first-order kinetics) whereas in the upper limit, $b=2$, it tends to the Garlick and Gibson's equation (second-order kinetics). Although b values different from this two limits do not correspond with physical processes, the activation energies

obtained from this equation are in good agreement with true values [57]. The intermediate values can be understood as a balance between the ruling processes. However, in the literature there are data below the unit and over 3 (the effective range is $0.5 \leq b \leq 3.0$ [58]). This model successfully describes the space charge relaxation processes in PMMA [57,59,60], PEI [60,61] and PET [62]. Thus, according to the general kinetic model, the equation of the current for thermally stimulated discharges at a constant heating rate v, and for $b \neq 1$, is

$$I = es_0 n_0 \exp\left(-\frac{E_a}{kT}\right)\left(\frac{(b-1)s_0}{v}\int_{T_0}^{T}\exp\left(-\frac{E_a}{kT'}\right)dT' + 1\right)^{\frac{-b}{(b-1)}}. \quad (4.51)$$

4.3.6 The mobility model

4.3.6.1 Introduction

In this model [28] the charge carrier motions are due to the *hopping between localized states* which are separated by a potential barrier. The hopping probability increases with temperature in a way that the mobility μ obeys the Arrhenius law:

$$\mu = \mu_0 \exp\left(-\frac{E_a}{kT}\right) \quad (4.52)$$

where E_a is the potential barrier height. The fundamental equations are Poisson's equation (4.53), charge conservation equation (4.54) and Ohm's law (4.55):

$$div(\varepsilon\vec{F}) = \rho\,, \quad (4.53)$$

$$div\vec{J} + \frac{\partial\rho_c}{\partial t} = 0\,, \quad (4.54)$$

$$\vec{J} = \mu\rho_c\vec{F} \quad (4.55)$$

where ε is the material permittivity, $\boldsymbol{F(x,t)}$ the local electric field, $\rho(x,t)$ is the total excess charge density, $\boldsymbol{J(x,t)}$ is the local current density and $\rho_c(x,t)$ is the mobile charge density.

By assuming that all the charges that make up the space charge take part in the conduction, then

$$\rho = \rho_c\,. \quad (4.56)$$

On the other hand, if the presence of fixed charges with a density N is considered, then

$$\rho = \rho_c + N\,. \quad (4.57)$$

A model based on a constant mobile charge density and a mobility strongly dependent on the temperature is generally referred to as *mobility model*. According to Dreyfus et al. [28], the mobility model is the best for polymers and, especially, for the polyethylene.

4.3.6.2 Mobile charge distribution in the presence of a fixed charge distribution

The initial situation is shown in Figure 4.13. There is a mobile charge density ρ_c in the presence of a uniform fixed charge density N with the opposite sign. The total space charge is $\rho=\rho_c+N$. If the electrodes are not blocking, the mobile charge distribution expands across the sample but without loosing its uniformity.

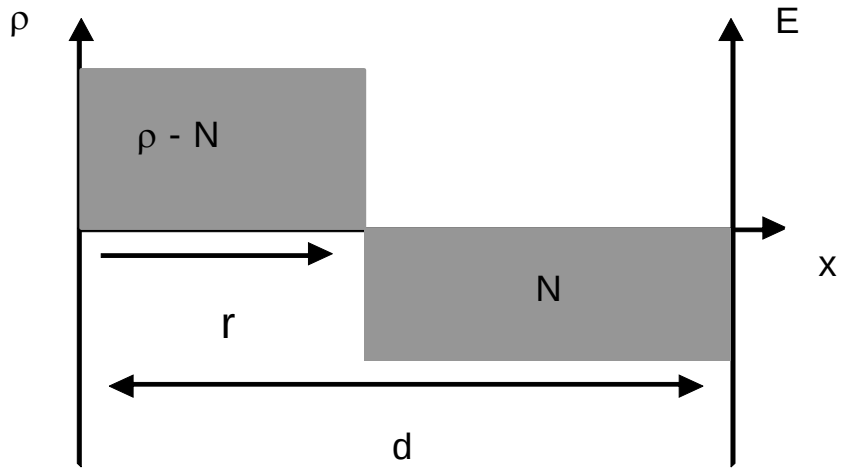

Figure 4.13. Mobile charge distribution in the presence of a uniform fixed charge distribution with the opposite sign.

Equations (4.53), (4.54) and (4.55) allow to determine the system evolution. By considering that the permittivity ε remains constant and that the space charge density ρ do not change with the distance r, the following differential equation is obtained:

$$\frac{d\rho}{dt}+\mu\rho\frac{\rho-N}{\varepsilon}=0\,. \tag{4.58}$$

Dreyfus et al. [28] obtained the following solution for the charge density

$$\rho(T)=\frac{N}{1+\left(\dfrac{N}{\rho(0)}-1\right)\exp\left[-\dfrac{1}{\tau_0 v}\displaystyle\int_{T_D}^{T}\exp\left(\frac{E_a}{kT}\right)dT\right]} \tag{4.59}$$

and determined the current density recorded in the outer circuit:

$$J(t)=\frac{\tau_0}{Nd}\exp\left(-\frac{E_a}{kT}\right)\frac{pR}{2}\left(pR-1\right)\left(R-1\right) \tag{4.60}$$

where $p=\dfrac{\rho}{N}$, $R=\dfrac{r}{d}$ and r is the distribution width at a given time.

The distribution width evolution is given by

$$\frac{dr}{dt} = \mu E(r) \tag{4.61}$$

which leads to

$$2\frac{dR}{du} = pR^2 - 2R + 1 \tag{4.62}$$

where $u = \frac{1}{b\tau_0}\int_{T_0}^{T} \exp\left(-\frac{E_a}{kT}\right)dT$. This differential equation has to be solved numerically.

It is noteworthy that under certain conditions it is possible to observe a polarity change in the depolarization current. Thus, when in the equation (4.60) it holds that *pR=1*, the mobile charge and the fixed charge densities are the same and the inversion takes place. It is possible to distinguish between three cases (Figure 4.14) corresponding to different current evolutions:

i) If the mobile charge density far exceeds the fixed charge density (case 1), then the front of the distribution reaches the second electrode before the condition *pR=1* is accomplished, and there is no current inversion.

ii) If the mobile charge density slightly exceeds the fixed charge density (case 2), then the condition *pR=1* can be accomplished before the front reaches the second electrode, and there is a current polarity inversion.

iii) If the mobile charge density is lower than the fixed charge density (case 3), then the current polarity is opposite to the case 1, and since *pR=1* is not accomplished, then there is no current polarity inversion.

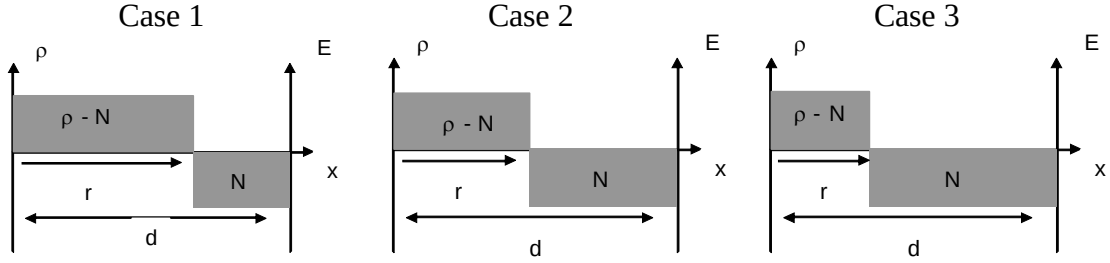

Figure 4.14. Different possible mobile charge distributions in the presence of a fixed charge distribution with the opposite sign.

For any given geometry, the differential equation system is

$$\frac{\partial\rho(\vec{r},t)}{dt} = -\mu(T)\left[\frac{\rho^2(\vec{r},t)}{\varepsilon} + \vec{F}(\vec{r},t)\bullet gr\vec{a}d\,\rho(\vec{r},t)\right] \tag{4.63}$$

$$div\left[\varepsilon\vec{F}(\vec{r},t)\right] = \rho(\vec{r},t)\,. \tag{4.64}$$

In plane geometry these equations can be written as [28]

$$\frac{\partial \rho(x,t)}{\partial t} = -\mu(T)\left[\frac{\rho^2(x,t)}{\varepsilon} + F(x,t)\cdot\frac{\partial \rho(x,t)}{\partial x}\right] \tag{4.65}$$

$$\varepsilon\frac{\partial F(x,t)}{\partial x} = \rho(x,t) \tag{4.66}$$

and they can also be expressed in cylindrical geometry

$$\frac{\partial \rho(r,t)}{\partial t} = -\mu(T)\left[\frac{\rho^2(r,t)}{\varepsilon} + F(r,t).\frac{\partial \rho(r,t)}{\partial r}\right] \tag{4.67}$$

$$\frac{\varepsilon}{r}\frac{\partial F(r,t)}{\partial r} = \rho(r,t)\,. \tag{4.68}$$

4.4 TSDC experimental setup

The experimental setups for TSDC measurements consisted of a forced-air oven controlled by a PID temperature programmer. Inside the chamber, two identical cable samples were placed close together in a parallel position. One was used to host the temperature probe inside the insulating layer, whereas TSDC measurements were performed on the other one. To polarize the sample, the cable core was positively biased with a high voltage source, whereas the outer semiconductor electrode was grounded. Once the polarization stage was finished, the external semiconducting layer was connected to an electrometer and the cable core was grounded. In some setups, a thermostatic bath is used to achieve a better control on the cooling rate. The brand and model of the used devices are specified in the experimental section of each chapter containing TSDC measurements, since different setups were used to perform the measurements. In Figure 4.15 an example of TSDC experimental setup is shown.

TSDC setups follow the diagram represented in Figure 4.16. They are operated as follows. Switch 1 is connected to terminal A during the poling stage and to terminal B whenever the poling field is off. Switch 2 is operated in the same way as switch 1, to protect the electrometer during the poling stage.

Figure 4.15. A TSDC experimental setup: (1) DeLonghi forced air oven; (2) Heizinger LNC 30000–2 high voltage source (0–30kV); (3) Eurotherm 808 PID temperature programmer; (4) Keithley 6514 electrometer; (5) computer with an analog-to-digital port; (6) Huber CC-245 refrigeration bath.

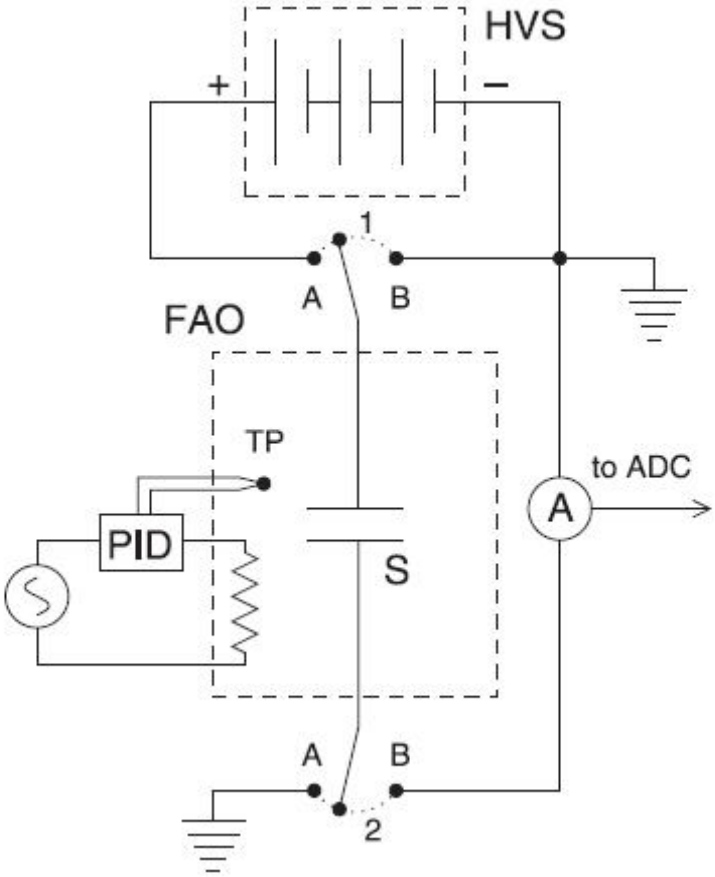

Figure 4.16. Diagram of the experimental setup: (HVS) high voltage source; (FAO) forced air oven; (S) sample; (PID) temperature programmer; (TP) temperature probe; (A) electrometer (connected to analog-to-digital port of computer).

The samples for TSDC measurements were cut form as-received cables. In some cases, a 2cm long section of insulating and semiconducting layers was removed from one end to make the electrical contact easy. The semiconducting layers were used as electrodes. To avoid short circuits, the external layer was partially removed from the ends of the samples, leaving a wide semiconducting strip centered in the sample. The cable core was used to make contact with the inner semiconducting layer. The contact with the outer semiconducting layer was made with an adjustable metallic clamp. The dimensions of the samples and their exact structure were not always the same, but they changed according to the particularities of the experiment and the applied field. Therefore the particular specifications of the samples used in each chapter can be found in the corresponding experimental section. A sample used in TSDC measurements and a diagram showing the generic structure of the sample and the connection with the electrodes, are shown in Figures 4.17 and 4.18.

Figure 4.17. Picture of a cable sample prepared for a TSDC measurement.

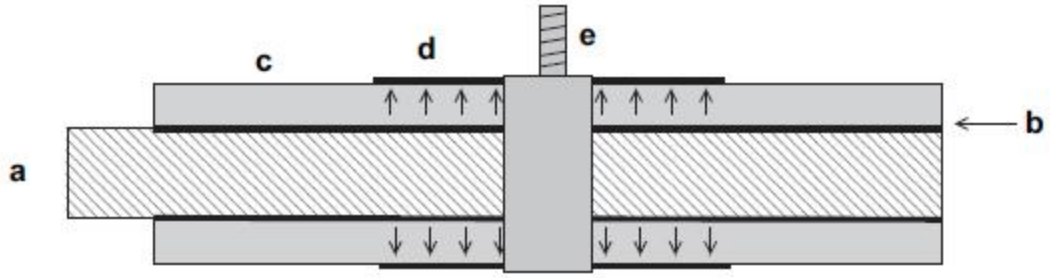

Figure 4.18. Diagram of the sample and of the connection with the electrodes: (a) cable core; (b) inner semiconducting layer; (c) XLPE insulating layer; (d) outer semiconducting layer; (e) adjustable clamp. The arrows represent the direction of the electric field at the zone where it is more intense.

4.5 Dynamic Electrical Analysis (DEA)

4.5.1 Introduction

The study of the dielectric materials behavior by means of time-varying electric fields allows to obtain information about the material polarization mechanisms. The Dynamic Electrical Analysis (DEA) can be used to measure the dielectric permittivity and the dielectric loss angle in function of the frequency and temperature. Thereby, the physical parameters of any relaxation can be obtained.

To characterize a dielectric material, several time functions for the applied electric field can be used. For instance, the step function is a sudden change in the electric field that leads to the so-called *Time-Domain Response*. Another important case consists in applying a sinusoidal field with a determined frequency. Thus, the *Frequency-Domain Response* is obtained.

4.5.2 Dielectric response for a time-varying electric field

For a given time-varying electric field *F=F(t)*, the relation between the electric displacement field *D* and the electric field *F* has to be considered to can analyze the dielectric response. If a linear dependency is assumed (*linear dielectrics*) it is possible to write

$$\vec{D}(t) = \varepsilon(t)\vec{F}(t) \tag{4.69}$$

where $\varepsilon(t)$ is the time-dependent permittivity of the material. In order to simplify the analysis of the dielectric response, we can start by considering the application of an electric field F_0 at the moment $t=0$. Thereby, the electric displacement $D(t)$ verifies that

$$\vec{D}(t) = \left[\varepsilon_\infty + (\varepsilon_S - \varepsilon_\infty)\psi(t)\right]\vec{F}_0 . \tag{4.70}$$

The first right-hand term $\varepsilon_\infty F_0$ is associated to the instantaneous material response due to an induced polarization, either electronic or ionic, where ε_∞ is the instantaneous permittivity. The second term, $(\varepsilon_s - \varepsilon_\infty)\psi(t)F_0$, where ε_s is the static permittivity and the factor $\psi(t)$ is the time-function that describes the delayed response, is related to a slow polarization due to dipolar mechanisms. The time-function limits are defined as

$$\psi(t) = \begin{cases} 0 & \text{si} \quad t = 0 \\ 1 & \text{si} \quad t = \infty \end{cases} \tag{4.71}$$

If at the initial time an additional field E_1 is applied, then the electric displacement will turn into

$$\vec{D}(t) = \left[\varepsilon_\infty + (\varepsilon_S - \varepsilon_\infty)\psi(t)\right]\left(\vec{F}_0 + \vec{F}_1\right). \tag{4.72}$$

Besides, by assuming the *Boltzmann superposition principle*, according to which the response of any dielectric material to successive excitations is the addition of the partial effects of each discrete variation, the equation is

$$\vec{D}(t) = \left[\varepsilon_\infty + (\varepsilon_S - \varepsilon_\infty)\psi(t)\right]\vec{F}_0 + \left[\varepsilon_\infty + (\varepsilon_S - \varepsilon_\infty)\psi(t)\right]\vec{F}_1 \tag{4.73}$$

But, if this second field is applied at a moment t_1, different from the initial, then the total displacement at a time $t>t_1$ is

$$\vec{D}(t) = \left[\varepsilon_\infty + (\varepsilon_S - \varepsilon_\infty)\psi(t)\right]\vec{F}_0 + \left[\varepsilon_\infty + (\varepsilon_S - \varepsilon_\infty)\psi(t - t_1)\right]\vec{F}_1 . \tag{4.74}$$

This can be repeated successively *i* times:

$$\vec{D}(t) = \sum_{t_i=-\infty}^{t_i=t} \left[\varepsilon_\infty + (\varepsilon_S - \varepsilon_\infty)\psi(t - t_i)\right]\vec{F}_i . \tag{4.75}$$

And for a continuous field variation, the displacement field of the dielectric at time *t* is

$$\vec{D}(t) = \varepsilon_\infty \vec{F}(t) + \int_{-\infty}^{t} (\varepsilon_S - \varepsilon_\infty) \psi(t-s) \frac{d\vec{F}}{ds} ds \,. \tag{4.76}$$

By integrating by parts it results in

$$\vec{D}(t) = \varepsilon_\infty \vec{F}(t) + (\varepsilon_S - \varepsilon_\infty) \int_{-\infty}^{t} \dot{\psi}(t-s) \vec{F}(s) ds \tag{4.77}$$

where

$$\phi = \dot{\psi} \,. \tag{4.78}$$

The time-function's derivative ϕ is the so-called *dielectric response function.* If the response function is known it is possible to obtain *D* for any electric field *F*.

As a particular case, a sinusoidal field may be considered. Then, for a frequency ω the function can be defined as $F(t) = F_0 e^{i\omega t}$. By replacing the field in the expression (4.77) and doing $u=t-s$, the equation becomes

$$\vec{D}(t) = \left[\varepsilon_\infty + (\varepsilon_S - \varepsilon_\infty) \int_0^\infty \phi(u) e^{-i\omega u} du \right] \vec{F}(t) \,. \tag{4.79}$$

Comparing the expression (4.79) with the (4.70) allows to observe that the linear proportionality between *E* and *D* is conserved:

$$\vec{D}(\omega, t) = \varepsilon^*(\omega) \vec{F}(\omega, t) \,. \tag{4.80}$$

Thereby, for time-varying fields the permittivity becomes a complex number that depends on the field frequency. The *complex dielectric constant or complex permittivity* ε^* can thus be decomposed into real ε' and imaginary ε'' parts,

$$\varepsilon^* = \varepsilon' - i\varepsilon'' \,. \tag{4.81}$$

The quotient $\varepsilon''/\varepsilon'$ gives the tangent of the phase angle between the vectors *D* and *F*, $tg(\delta)$, which is called *loss tangent*. ε' is related to the *reactive* response and the stored energy within the dielectric. ε'' is associated with the *resistive* response and the dissipation (or loss) of energy.

The complex permittivity can be obtained by introducing the expression (4.81) into the equation (4.80) and equaling to (4.79):

$$\varepsilon^*(\omega) = \varepsilon_\infty + (\varepsilon_S - \varepsilon_\infty) \int_0^\infty \phi(u) e^{-i\omega u} du \,. \tag{4.82}$$

Also the imaginary and real parts can be deduced:

$$\varepsilon'(\omega) = \varepsilon_\infty + (\varepsilon_s - \varepsilon_\infty)\int_0^\infty \phi(u)\cos(\omega u)du\,, \tag{4.83}$$

$$\varepsilon''(\omega) = (\varepsilon_s - \varepsilon_\infty)\int_0^\infty \phi(u)sen(\omega u)du\,. \tag{4.84}$$

The equations (4.83) and (4.84) show that the quotients $(\varepsilon'-\varepsilon_\infty)/\Delta\varepsilon$ and $\varepsilon''/\Delta\varepsilon$ are the *Fourier transforms* of the response function. Therefore, by performing the inverse Fourier transform of such quantities, the response function can be obtained if either the real or imaginary component of the permittivity is known. On the other hand, the quotient $\varepsilon''/\varepsilon'$ allows to evaluate the dielectric losses of the material. If the field is sinusoidal then the dissipated energy per unit volume and time is

$$W = \frac{\omega\varepsilon''\vec{F}_0^{\,2}}{2}\,. \tag{4.85}$$

As can be seen in Figure 4.19 $\varepsilon''=(D_0/F_0)sin(\delta)$, so the previous equation results in

$$W = \frac{\omega\vec{D}_0\vec{F}_0}{2}\sin\delta\,. \tag{4.86}$$

For small angles it holds that $sin(\delta)\approx tg(\delta)$, so the dissipated energy per unit volume and time is directly proportional to the loss tangent.

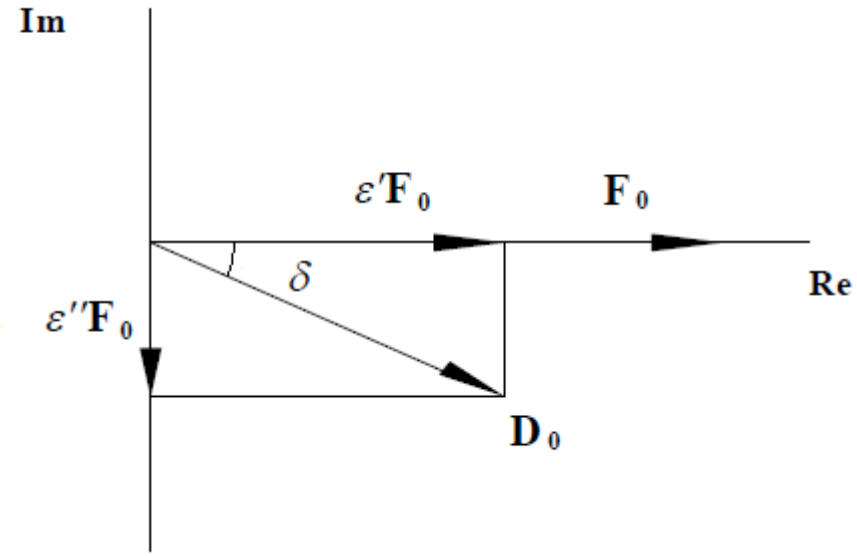

Figure 4.19. Complex diagram for vectors D_0 and F_0.

4.5.3 Debye model. Empirical corrections: Cole-Cole, Fuoss-Kirkwood, Cole Davison and Havriliak-Negami

4.5.3.1 Debye model

The Debye model has been also commented in the section 4.2.11 of this chapter, since it is also applied in the dipolar relaxation models used in TSDC analysis, and in chapter 2. It is the fundamental element in the classical interpretation of the dielectric relaxation processes. The *Debye dielectric response function* is $\phi(u) = \frac{e^{-\frac{u}{\tau}}}{\tau}$. By introducing it in equation (4.82) and integrating, the complex permittivity that results from this model can be expressed as

$$\varepsilon^*(\omega) = \varepsilon_\infty + \frac{\varepsilon_s - \varepsilon_\infty}{1 + i\omega\tau}. \tag{4.87}$$

Then, the real and imaginary parts are

$$\varepsilon'(\omega) = \varepsilon_\infty + \frac{\varepsilon_s - \varepsilon_\infty}{1 + \omega^2\tau^2}, \tag{4.88}$$

$$\varepsilon''(\omega) = \frac{\varepsilon_s - \varepsilon_\infty}{1 + \omega^2\tau^2}\omega\tau\ . \tag{4.89}$$

These equations can be used to determine graphically if a material fits the Debye model. By plotting ε'' versus ε' a semicircle with the center in $½(\varepsilon_s + \varepsilon_\infty)$ is obtained (Figure 4.20). This is the so-called *Cole-Cole plot*.

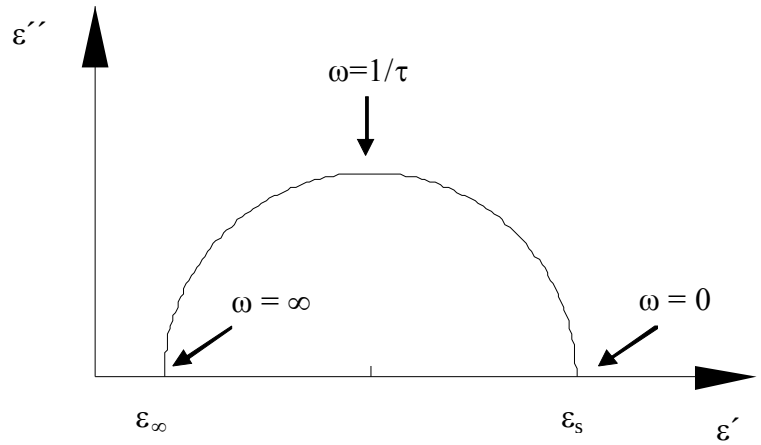

Figure 4.20. Cole-Cole plot.

The Debye model is based on *simple relaxation* processes, so the relaxation times are not distributed. For this reason, in order to obtain better agreement between theory and

experimental measurements, several empirical corrections of the Debye model have been proposed.

4.5.3.2 Empiric corrections to Debye model: Cole-Cole, Fuoss-Kirkwood, Cole-Davison and Havriliak-Negami

Cole-Cole

The equation introduced by K.S. Cole and R.H. Cole [63] is

$$\varepsilon^*(\omega) = \varepsilon_\infty + \frac{\varepsilon_s - \varepsilon_\infty}{1 + (i\omega\tau)^{1-\alpha}}; \quad 0 < \alpha < 1. \tag{4.90}$$

It can be seen that by doing α=0 the former expression results in the Debye equation (4.87). In this model, the function that links the imaginary part with the real one is again a semicircle, and it is given by

$$\left(\varepsilon' - \frac{\varepsilon_s + \varepsilon_\infty}{2}\right)^2 + \left(\varepsilon'' + \frac{\varepsilon_s - \varepsilon_\infty}{2}\,\mathrm{tg}\left(\frac{\pi\alpha}{2}\right)\right)^2 = \left(\frac{\varepsilon_s - \varepsilon_\infty}{2}\right)^2 \sec^2\left(\frac{\pi\alpha}{2}\right). \tag{4.91}$$

The differences between the two models are the radius and position of the semicircle center. The straight line joining the center to the point $(\varepsilon_\infty,0)$ has an angle of $\pi\alpha/2$ with respect to the abscissa axis. From the experimental data it is possible to measure this angle and then to determine the parameter α. On the other hand, the quotient between the distances of any point of the semicircumference to the points $(\varepsilon_\infty,0)$ and $(\varepsilon_s,0)$ provides the value of $(\omega\tau)^{1-\alpha}$. Thereby, if α has already been determined then the relaxation time τ can be calculated.

Fuoss-Kirkwood

The Fuoss-Kirkwood model [64] is based in the following equation:

$$\varepsilon''(\omega) = \varepsilon''_m \sec h\left(m \ln\left(\frac{f}{f_0}\right)\right) \tag{4.92}$$

where f_0 is the frequency at which ε'' takes the maximum value ε''_m, and m is a *shape parameter* that can take values from *0* to *1*. Besides, m is related to the width of the relaxation: the higher is the parameter value, the wider is the distribution.

Cole-Davison

The Cole-Davison equation [65] for the complex dielectric constant is

$$\varepsilon^*(\omega) = \varepsilon_\infty + \frac{\varepsilon_s - \varepsilon_\infty}{(1 + i\omega\tau)^\beta}; \quad 0 < \beta < 1. \tag{4.93}$$

This model is suitable for asymmetric semicircles in the Cole-Cole plot. This asymmetry is the main difference from the previous empirical models. Even so, it is easy to see that the Debye model (symmetric) is a particular case of the Cole-Davison model (asymmetric).

Havriliak-Negami

The expression proposed by Havriliak and Negami [66] is a combination of the Cole-Cole and Cole-Davidson formulae:

$$\varepsilon^*(\omega) = \varepsilon_\infty + \frac{\varepsilon_s - \varepsilon_\infty}{\left(1 + (i\omega\tau)^{1-\alpha}\right)^\beta}; \quad 0 < \alpha < 1; \quad 0 < \beta < 1. \tag{4.94}$$

The real and imaginary components of the permittivity can be deduced from this empirical equation. Thereby, by plotting ε'' versus ε', the slopes that the experimental curve takes in the x-axis points $(\varepsilon_\infty, 0)$ and $(\varepsilon_s, 0)$ allow to determine the α and β parameters.

The effect of the conductivity

If at a given temperature the material has a certain DC conductivity caused by the mobility of free charges, then a term proportional to the conductivity has to be introduced in the permittivity expression. If a Debye simple relaxation model is assumed, the complex permittivity becomes

$$\varepsilon^*(\omega) = \varepsilon_\infty + \frac{\varepsilon_s - \varepsilon_\infty}{\left(1 + (i\omega\tau)^{1-\alpha}\right)^\beta} - i\frac{\sigma}{\omega}. \tag{4.96}$$

From this equation it can be seen that the contribution of the conductivity becomes significant in the low frequency regime. This can also be observed in Figure 4.21.

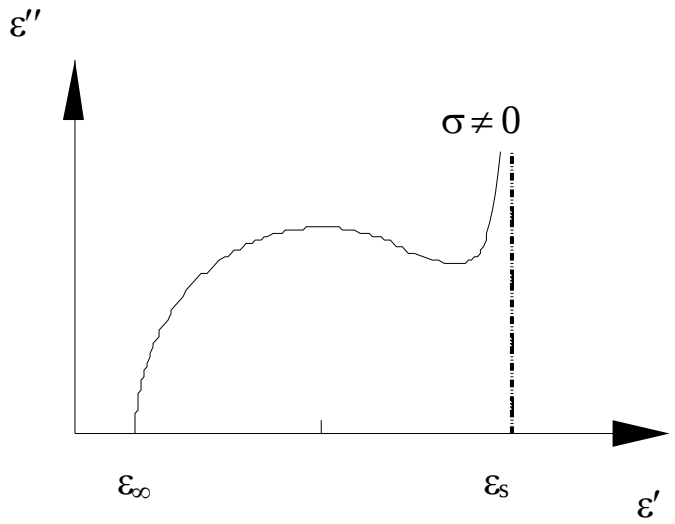

Figure 4.21. Conductivity effect on the Cole-Cole plot.

General expression for distributed relaxations

Experimentally, the dipolar behavior differs from the Cole-Cole semicircle either at low frequencies (conductivity contribution) or at high frequencies. This implies that there may be a distribution of relaxation times throughout the dipolar relaxation. This relaxation time distribution can be considered discrete or continuous.

For a group of dipoles with different relaxation times, the total dipolar orientation is a superposition of simple orientations. These dipolar orientations can be considered as Debye-like. Therefore, the total dielectric constant can be obtained from the addition of simple contributions. If a continuous distribution is considered, then the addition becomes an integral, and the permittivity is

$$\varepsilon^*(\omega) = \varepsilon_\infty + (\varepsilon_s - \varepsilon_\infty)\int \frac{g(\tau)d\tau}{(1+i\omega\tau)} \tag{4.97}$$

where $g(\tau)$ is the distribution function, which, in general, has been obtained experimentally in the case of polymers [67,68]. In addition, by using appropriate distribution functions it is possible to obtain the Cole-Cole, the Cole-Davidson or the Havriliak-Negami equations. Therefore, these empirical equations can be explained by considering systems of simple relaxation processes with relaxation times distributed according to different functions.

Currently, in addition to the previously described models, there is a wide range of empirical models and particular distribution functions that are useful for the specific analysis of certain relaxations (for instance, see those proposed by Jonscher [69], Dissado-Hill [70] and Friedrich [71]).

4.5.4 Activation energy calculation

The activation energy (E_a) is one of the most representative parameters of the relaxation analysis and, basically, it provides information about the energy barrier that space charges or dipolar groups have to overcome to can change their position or orientation, respectively, and, by this way, to can contribute to the different relaxations.

Although there are several ways to calculate the E_a, a calculation that allows evaluating the E_a in a practical way is described here. By assuming that the relaxation model is based in the relaxation time exponential function given by the Arrhenius equation:

$$\tau = \tau_0 \exp\left(\frac{E_a}{kT}\right) \tag{4.98}$$

and by replacing τ in the equation (4.89) it gives

$$\varepsilon''(\omega,T) = \frac{\frac{1}{2}(\varepsilon_s - \varepsilon_\infty)}{\cosh(E_a/kT + \ln\omega\tau_0)}. \tag{4.99}$$

The ε'' dependency on the temperature shows that for a fixed frequency the function returns a maximum value at a particular temperature $T_m(\omega)$. This maximum value is obtained when the argument of hyperbolic cosine in equation (4.99) is zero:

$$T_m(\omega) = -\left(\frac{E_a}{k \ln \omega\tau_0} \right) \tag{4.100}$$

and the corresponding relaxation time satisfies

$$\omega\tau\left(T = T_m\right) = 1. \tag{4.101}$$

By combining these two expressions with the equation (4.99) it gives

$$\varepsilon''(\omega, T) = \frac{\frac{1}{2}\left(\varepsilon_s - \varepsilon_\infty\right)}{\cosh\left[E_a\left(1/T - 1/T_m(\omega)\right)/k\right]}. \tag{4.102}$$

Once the imaginary permittivity dependency on the temperature is established, the parameters $\Delta\varepsilon$ and T_m can now be evaluated by means of the analysis of experimental curves. Then, E_a can be obtained by fitting the experimental data with the theoretical curves [71].

4.5.5 Complex conductivity

If a sinusoidal time-varying field is applied on a dielectric in which free carrier conduction can be neglected, it is possible to define a *complex conductivity*, σ^*, from the expression

$$\vec{J} = \frac{\partial \vec{D}(\omega, t)}{\partial t} = \varepsilon^*(\omega)\frac{\partial \vec{F}(\omega, t)}{\partial t} = i\omega\varepsilon^*(\omega)\vec{F}(\omega, t) = \sigma^*(\omega)\vec{F}(\omega, t) \tag{4.103}$$

where complex conductivity can be written as

$$\sigma^*(\omega) = \sigma'(\omega) + i\sigma''(\omega) \tag{4.104}$$

where

$$\sigma'(\omega) = \omega\varepsilon''(\omega); \qquad \sigma''(\omega) = \omega\varepsilon'(\omega). \tag{4.105}$$

If there is some free carrier electrical conduction in the material, then real conductivity has to be redefined as

$$\sigma'(\omega) = \omega\varepsilon''(\omega) + \sigma_0 \tag{4.106}$$

where σ_0 is the conductivity of free charge carriers. It can be seen that in this case the loss factor is

$$\varepsilon''(\omega) + \frac{\sigma_0}{\omega}. \tag{4.107}$$

Therefore, the conduction of free carriers has a dominant role on dielectric losses in the range of low frequencies.

In some materials it has been observed a *sublinear dispersive conductivity* of the form [73]

$$\sigma(\omega) = \sigma_0 + A\omega^n \tag{4.108}$$

where A is a parameter that depends on temperature, and n is a fractional exponent that ranges between 0 and 1 and has been interpreted by means of many body interactions among charge carriers. This relation is known as the *universal dynamic response* and is associated with materials with a high degree of disorder like polyethylene.

4.6 DEA experimental setup

A dielectric spectrometer BDS40 with a Novotherm temperature control system manufactured by Novocontrol (Figure 4.22) was used. The samples were 150μm thick XLPE films of 2cm diameter, which were cut from a MV cable using a lathe with a tool designed for this purpose, so that a 2cm width ribbon could be obtained (Figure 4.23).

Figure 4.22. BDS40 spectrometer with a Novotherm temperature control system.

Figure 4.23. XLPE ribbon obtained from a MV cable using a lathe

4.7 Isothermal Depolarization Currents (IDC)

IDC consist in recording the depolarization current of a sample after a poling field (F_p) was applied during a polarization time (t_p). Unlike in TSDC method, here the discharge takes happen isothermally (Figure 4.24). This makes possible to analyze the transient currents and the involved mechanisms (see the section 2.6). The experimental setup and sample preparation are the same as for TSDC technique (Figures 4.16, 4.17 and 4.18). However the operation is different. In this case, switch 2 is always connected to B so the charging of the sample can be also monitored.

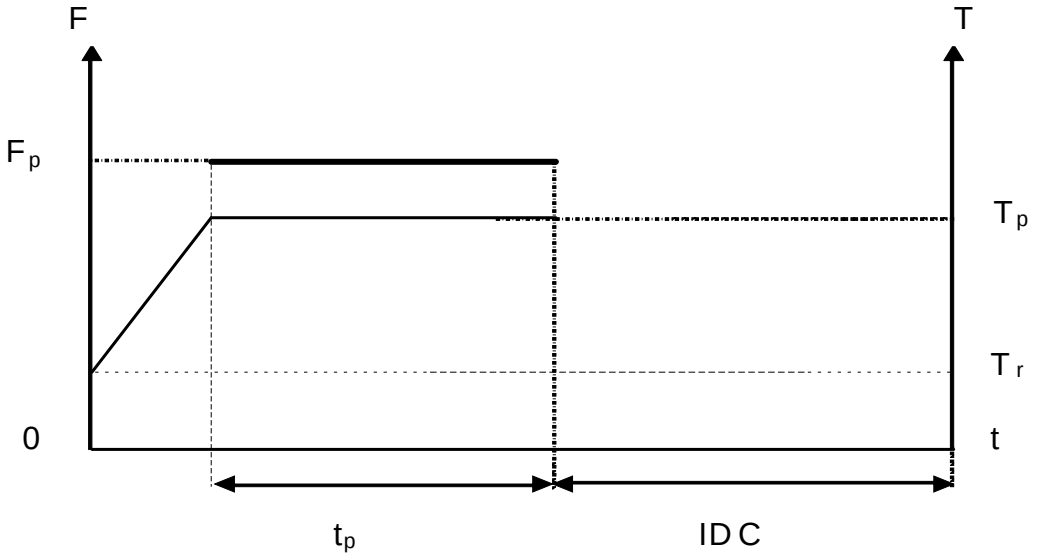

Figure 4.24. Diagram of the IDC method stages.

4.8 Absorption/Resorption Currents (ARC)

ARC measurements presented and analyzed in this Ph.D. thesis were performed by Dr. F. Frutos and Dr. M. Acedo of Departamento de Física Aplicada I, ETSII, Universidad de Sevilla.

Conductivity (σ) was determined by means of equation [74–76]

$$\sigma = \frac{\varepsilon_0}{C_0 U}(I_a(t) + I_r(t)) \tag{4.109}$$

where C_0 is the geometrical capacitance of the sample, $I_a(t)$ and $I_r(t)$ are the absorption and resorption currents (ARC), which have an opposite sign, U is the voltage applied to each cable sample and ε_0 is the vacuum permittivity. From measurements performed with a Hewlett-Packard HP-4192a LF impedance analyzer we got a value C_0=4.4pF. Equation (4.109) provides a convenient way to obtain σ because measurements require less time to be performed than with the usual current-voltage characteristics method since there is no need to reach a stationary current.

A sketch of the experimental setup can be seen in Figure 4.25. Previously to any measurement, the surface of the sample was cleaned with ethanol in order to avoid the effect of remains that may come from the mechanization process. The sample to be measured was placed inside a Carbolyte PF60 oven (Faraday cage). The oven was furnished with suitable connections for electrical measurements, using low noise coaxial connectors and cables, suitable for high voltage. Cable and connector junctions were silver soldered. A K-type thermocouple (Keithley 6517TP) placed inside the insulation of another identical sample, which was located close to the sample under test, was used to measure the sample temperature. The DC voltage source of a Keithley 6517 A electrometer was used to polarize the samples. To measure the absorption current, a voltage of +1kV (corresponding to a mean field of 0.22 MV/m) was applied to the inner electrode of the samples and the outer electrode was grounded through the aforementioned electrometer. After a period of time t_c, the inner electrode was switched to ground and the resorption current was recorded. In every case, we ensured that the background noise was lower than ±20fA (absolute value) before current measurement began. The charging period t_c (absorption current) was about the double of the discharging period (resorption current), 2000 and 1000s respectively, so that equation (4.109) can be used for conductivity calculations as a good approximation [76]. The entire setup of measuring instrument and screened oven was also placed inside another Faraday cage in order to prevent measurement fluctuations due to external perturbations.

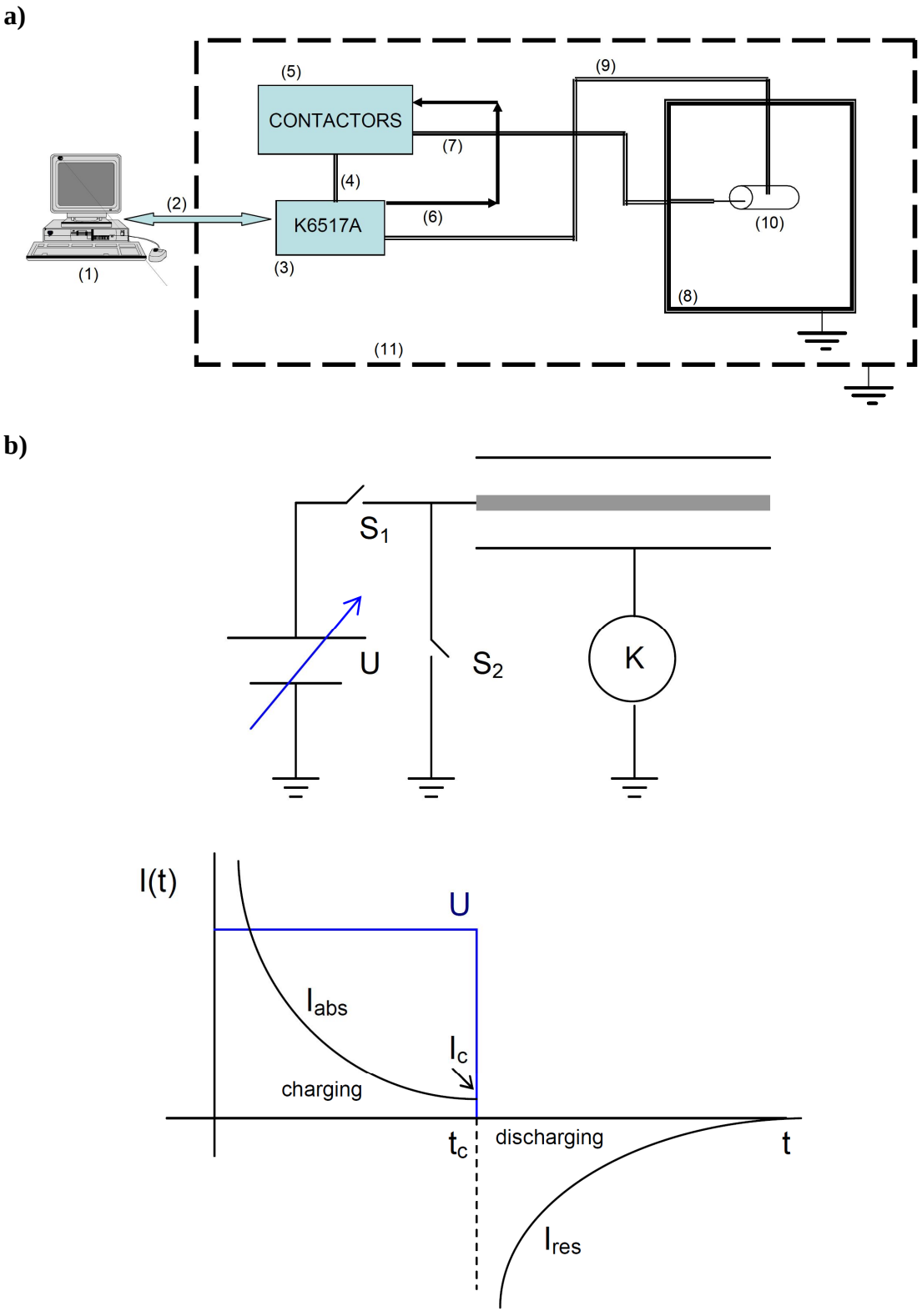

Figure 4.25. (a) Experimental setup for absorption/resorption current measurement (block diagram): (1) personal computer (Pentium IV processor); (2) GPIB cables; (3) Keithley 6517A electrometer; (4) DC source output of Keithley 6517A; (5) box of contactors; (6) control of contactors by digital output of Keithley 6517A; (7) high voltage output from contactors; (8) carbolite PF60 oven; (9) coaxial measuring cable; (10) sample; (11) Faraday cage (2m×1m×1m). (b) Simplified sketch of experimental setup for absorption/resorption current measurement and example of measurement: charging period, $0<t<t_c$ (S1 ON, S2 OFF) and discharging period, $t>t_c$ (S1 OFF, S2 ON); I_{abs}, absorption current; I_{res}, resorption current; I_c, conduction current; t_c, charging time; K, electrometer; U, charging voltage.

4.9 Pulsed Electroacoustic (PEA)

The PEA technique consists in applying an electrical pulse to the insulation that exerts forces on charges. The perturbation on charges produces an acoustic wave which is detected by a piezoelectric transducer located on the outer surface of the cable insulation.

Figure 4.26. Techimp PEA Cable measurement system.

The PEA measurements were performed by means of a commercial Techimp PEA Cable measurement system (see Figures 4.26, 4.27 and 4.28). The pulse amplitude was 4500V and the pulse length was 40ns. The frequency of the high voltage generator is 147Hz. The signal was processed by a Tektronix TDS 5032 digital phosphor oscilloscope. The average of 10000 waveforms (Wfms) was performed by the oscilloscope software (Tekscope 1.2.1). The deconvolution program is a Labview based software provided by Techimp.

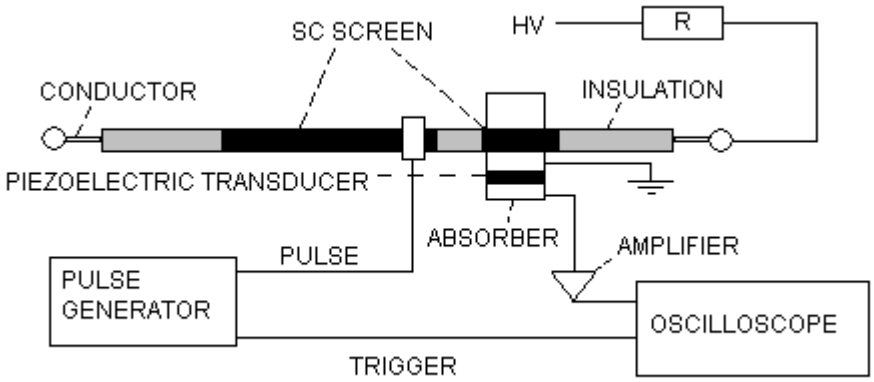

Figure 4.27. Sketch of the PEA system. Note the geometry of the sample required in this case.

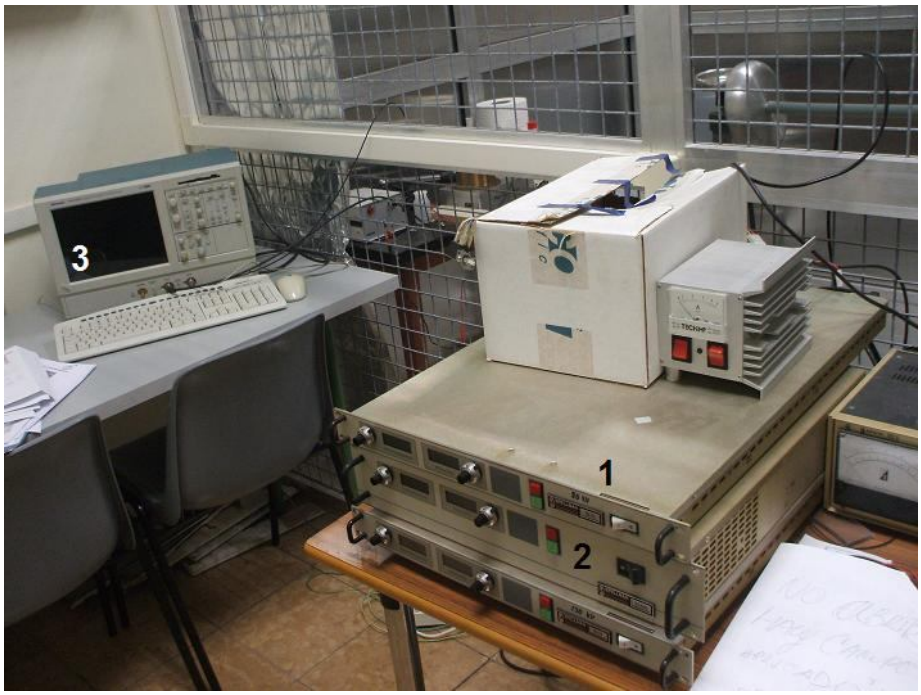

Figure 4.28. (1) Spellman SL80PN10/10001 0–80kV DC source to pole the samples; (2) Spellman SL6PN600/10007 0–5kV DC source for the pulse generator; (3) Tektronix TDS 5032 digital phosphor oscilloscope.

Figure 4.29. Oven used to anneal and to polarize long samples at high temperatures prior to PEA space charge measurements.

For PEA measurements 1.5m long samples cut from as-received cables were used. To improve the signal, a 5cm wide semiconductive screen stripe close to the measurement area was removed from the cable. In one side of this region without SC screen, it has been left 12cm of SC screen (measurement area). In the other side, it has been left 40cm of SC screen in which the pulse is applied. The proportion between the two SC screen

sections is related to the fact that the larger one is used like a decoupling capacitor. SC screen has been removed from the rest of the cable.

A long air forced oven was built (Figure 4.29) to anneal the 1.5m long cable samples. This oven was also used to pole the samples at high temperatures to form electrets, prior to measuring their stored space charge by PEA.

4.10 Differential Scanning Calorimetry (DSC)

A DSC-20 calorimeter controlled by a Mettler TC11 processor was used. Measurements were performed in samples cut from the cable and sealed in aluminum pans.

References

[1] Tamayo, I. "Estudio del comportamiento de la carga de espacio durante la fusión del XLPE en cables de media tensión por TSDC". Ph.D. Thesis. Universitat Politècnica de Catalunya, Terrassa, Spain (2002).

[2] Zielinski, M. and Kryszewski, M. *Phys. Stat. Sol. A*. **42** (1977), 305.

[3] Eguchi, M. *Phil. Mag*. **49** (1925), 178.

[4] Sessler, G. M. "Electrets". Laplacian, Morgan Hill, CA, USA, 3rd edition (1999), vol. 1.

[5] Hilczer, B. and Malecki, J. "Studies in electrical and Electronical Engineering 14: Electrets". Elsevier-PWN-Polish Scientific Warszawa, Poland (1986), pp. 285–311.

[6] Chen, R. and Kirsh, Y. "Analysis of Thermally Stimulated Processes". Pergamon, Oxford, UK, 1st edition (1981).

[7] Van Turnhout, J. "*Thermally Stimulated Discharge of Polymer Electrets"*. Elsevier Sci. Pub. Co. Amsterdam, Netherlands (1975).

[8] Sessler, G. M. in "Electrets". Edited by Sessler, G. M. Springer-Verlag Berlin Heidelberg, Germany (1980), pp. 13–80.

[9] Gerson, R. and Rohrbaugh, J. H. *J. Chem. Phys.* **23** (1955), 2381.

[10] Belana, J.; Colomer, P.; Montserrat, S. and Pujal, M. *Anal. Phys.* B, **78** (1982), 8.

[11] Lacabanne, C.; Goyaud, P. and Boyer, R. F. *J. Polym. Sci. B*: *Polym. Phys.* **18** (1980), 277.

[12] Mudarra, M. "Estudio de la Carga de Espacio en Polímeros Amorfos por Espectroscopia Dieléctrica". Ph.D. Thesis. Universitat Politècnica de Cataluña (2000), p. 89.

[13] Mudarra, M.; Joumba, A.; Belana, J. and Tourielle, A. *Polymer*. **40** (1999), 6977.

[14] Díaz-Calleja, R.; Friedericks, S.; Jaïmes, C.; Sanchis, M. J.; Belana, J.; Cañadas, J. C.; Diego, J. A. and Mudarra, M. *Polymer International*. **46** (1998), 20.

[15] Van Turnhout, J. "Thermally Stimulated Discharge of Polymer Electrets". Ph.D.Thesis. Leiden, The Netherlands (1972), p. 202.

[16] McCrum, N. G.; Read, B. E. and Williams, G. "Anelastic and Dielectric Effects in Polymeric Solids". Dover Publications, Inc., New York, USA (1991).

[17] Lewis, T. J.; *IEEE Trans. Dielectr. Electr. Insul*. **9** (2002), 717.

[18] Cañadas, J. C. "Estudio del Efecto de la Cristalización Fría y del Envejecimiento Físico en las Relajaciones de los Polímeros Mediante la Técnica de Corrientes Estimuladas Térmicamente". Ph.D. Thesis. Universitat Politècnica de Catalunya (1999).

[19] Colomer, P.; Montserrat S. and Belana, J. *J. Mat. Sci.* **33** (1998), 1921

[20] Mudarra, M.; Joumba, A.; Belana, J. and Toureille, A. *Polymer*, **40**, (1999) 6977.

[21] Díaz-Calleja, R.; Ribes-Greus, A. and Gómez-Ribelles, J. L. *Polym. Comm*. **30** (1989), 271.

[22] Fleming, R.J. *Proc. 6th Int. Symp. Electrets, IEEE Elect. Insul. Soc.* (1988), 118.

[23] Belana, J. and Pujal, M. *Polymer*. **29**, (1988) 1738.

[24] Diaz-Calleja, R.; Saiz, E.; Riande, E.; Gargallo, L. and Radic, D. *Journal of Non-Crystalline Solids*. **172–74** (1994) 985.

[25] Liu, S.F. and Lee, Y. D. *Macromol. Chem. Phys*, **198** (1997), 505.

[26] Goldied, D. M.; Macartney, R. A.; Gibson, G. and Gairns, R. S. *Philosophical Magazine B*. **75** (1997), 553.

[27] Cartwright, G. A.; Davies, A. E.; Swingler, S. G. and Vaughan, A. S. *IEEE, P-Sci. Meas. Tech*, **143** (1996), 26.

[28] Dreyfus, G.; Lacabanne, C. and Rahal, A. *Journées d' études de la SEE*. *RGE*. **87** (1978), 870.

[29] Zebouchi, N.; Hoang, T. G. and Ai, B. *J. Appl. Phys*. **81** (1997), 2363.

[30] Dissado, L. A. *Proc. 3rd Int. Conf. Electric Charge in Solid Insulators*. Tours, France (1998), 141.

[31] Zhang, Y.; Lewiner, J.; Alquié, C. and Hampton, N. *IEEE Trans. Electr. Insul.* **3** (1996), 778.

[32] Ditchi, T.; Alquié, C. and Lewiner, J. *IEEE. Trans. Electr. Insul*, **24** (1989), 403.

[33] Bostrôm, J. O., Campus, A., Nilson, U. H., Cartensen, P., Gustafsson, A., Farkas, A. A., Johannesson, K. *JICABLE 99-C2-12* (1999), 713.

[34] Sigmond, R. S. and Hegerberg, R. *Proc. 3rd Int. Conf. Electric Charge in Solid Insulators*. Tours, France (1998), 294.

[35] Bezille, J.; Janah, H.; Chan, J. and Hartley, M. D. *Proc. CEIDP*. Victoria, Canada (1992), 567.

[36] Tamayo, I.; Mudarra, M.; Diego, J. A.; Cañadas, J. C.; Sellarès, J.and Belana, J. *Proc. CSC´4, 4th Int. Conf. on Electric Charges in Non-Conductive Materials.* Tours, France (2001), 425.

[37] Van Turnhout, J. in "Electrets". Edited by Sessler, G. M. Springer-Verlag Berlin Heidelberg, Germany (1980), pp. 81–216.

[38] Bucci, C.; Fieschi, R. and Guidi, G. *Phys. Rev*, **148** (1966), 816.

[39] Van Turnhout, J. "Thermally Stimulated Discharge of Polymer Electrets". Ph.D. Thesis. Leiden (1972), pp. 97–137.

[40] Mudarra (2000) [10], p. 66.

[41] Kunze, I. and Müller, P. *Phys. Status Solidi*. **A13** (1972), 197.

[42] Podgorsak, E. B. and Moran, P. R. *Phys. Rev. B*. **8** (1973), 3405.

[43] Vanderschueren, J. and Gasiot, J. in "Thermally Stimulated Relaxation in Solids". Edited by Braünlich, P. Springer-Verlag Berlin Heidelberg, Germany (1979), pp. 135–223.

[44] Creswell, R. E. and Perlman, M. M. *J. Appl. Phys*. **41** (1970), 2365.

[45] Chen and Kirsh (1981) [5], p. 5.

[46] Braünlich, P.; Kelly, P. and Fillard, J.P. in "Thermally Stimulated Relaxation in Solids". Edited by Braünlich, P. Springer-Verlag Berlin Heidelberg, Germany (1979), pp. 35–92.

[47] Chen, R. *Chem. Phys. Lett*. **6** (1969), 1254.

[48] Kelly, P.; Laubitz, M.J. and Braünlich, P. *Phys Rev. B***. 4** (1971), 1960.

[49] Chen and Kirsh (1981) [5], p. 27.

[50] Halperin, A. and Braner, A. A. *Phys Rev*. **117** (1960), 408.

[51] Dussel, G. A. and Bubbe, R. H. *Phys Rev*. **155**, (1967) 764.

[52] Randall, J. T. and Wilkins, M. H. F. *Proc. Roy. Soc*. (London). **A184** (1945), 366.

[53] Garlick, G. F. J. and Gibson, A. F. *Proc. Phys. Soc*. **A60** (1948), 574.

[54] Chen and Kirsh (1981) [5], p.33.

[55] May, C. E. and Partidge, J. A. *J. Chem. Phys*. **40** (1964), 1401.

[56] Chen, R. *J. Electrochem. Soc*. **116** (1969), 1254.

[57] Mudarra, M.; Belana, J.; Cañadas, J.C. and Diego, J.A. *J. Polym. Sci. B: Polym. Phys*. **36** (1998), 1971.

[58] Chen and Kirsh (1981) [5], p. 34.

[59] Mudarra, M.; Belana, J.; Cañadas, J. C. and Diego, J. A. *Polymer*. **40** (1999), 2659.

[60] Mudarra (2000) [10], p. 157.

[61] Belana, J.; Cañadas, J.C.; Diego, J. A.; Mudarra, M.; Díaz-Calleja, R.; Fiedericks, S.; Jaïmes, C. and Sanchis, M. J. *Polym. Int*. **46** (1998), 11.

[62] Cañadas, J. C.; Tamayo, I.,Sellarès, J.; Diego, J. A., Mudarra, M.; Belana, J.; Díaz-Calleja, R. and García, A. *APTADM 2001, International Conference on Advances in Processing, Testing and Application of Dielectric Materials.* Poland (2001), 70.

[63] Cole, K. S. and Cole, R. H. *J. Chem. Phys.* **9** (1941), 341.

[64] Fuoss, R. and Kirwood, J. G. *J. Am. Chem*. Soc. **63** (1941), 385.

[65] Davidson, D. W. and Cole, R. H. *J. Chem. Phys.* **19** (1951), 1484.

[66] Havriliak, S. and Negami, S. *J. Polym. Sci*. C. **14** (1966), 99.

[67] Cañadas, J. C.; Diego, J. A.; Mudarra, M.; Belana, J.; Díaz Calleja, R.; Sanchis, M. J. and Jaïmes, C. *Polymer*. **40** (1999), 1181.

[68] Böttcher, C. J. F. and Bordewijk P. "Theory of Electric Polarization. Vol 2: Dielectrics in Time-dependent Fields". Elsevier , Amsterdam, The Netherlands (1980), pp. 45–137.

[69] Jonscher, A. K. Golloid Pol. Sci. **253** (1975), 231.

[70] Dissado, L. A. and Hill, R. M. *Nature*. **279** (1979), 685.

[71] Friedrich, C. Rheol. Acta. **30** (1991), 151.

[72] Cañadas (1999) [15], p. 74.

[73] León, C.; Lucía, M.L. and Santamaría J. *Physics Review B*. **55** (1997), 882.

[74] Hvidsten, S.; Faremo, H.; Benjaminsen, J. T. and Ildstad, E. *CIGRE paper 21–201*. CIGRE, Paris, France (2000), 1.

[75] Frutos, F.; Acedo, M.; Jadraque, A.; Mudarra, M.; Sellarès, J. and Belana, J. *Proceedings of 8th IEEE International Conference on Solid Dielectrics.* Toulouse, France, **1** (2004), 119.

[76] Acedo, M. "Relación entre la degradación del polietileno por arborescencias de agua y las propiedades eléctricas del material. Aplicación al diagnóstico del aislamiento

de los cables de distribución de energía". Ph.D. Thesis, Universidad de Sevilla, Sevilla, Spain (2004).

5. DSC AND TSDC CHARACTERIZATION OF CABLE SAMPLES USED IN THE PRESENT STUDY

A preliminary DSC and TSDC characterization of the samples provided by the manufacturer is presented. DSC measurements have been used to determine the crystallinity of the material, and allow to monitor structural changes that take place when the material is annealed at temperatures within the melting range. On the other hand, the TSDC spectra of the studied materials have been obtained for different annealings.

5.1 Experimental

The three kinds of cable (S, L, R) studied in this chapter are described in section 4.1.

The details on calorimetric measurements (DSC) are discussed in section 4.10.

To obtain samples with appropriate dimensions for the TSDC measurements, the cable was cut into 20cm long sections and, then, a 2cm long section of insulating and semiconducting layers was removed from one end. The external layer was partially removed from the ends of the samples, leaving an 8cm wide semiconducting strip centered in the sample. More details about the structure of the sample and the connection with the electrodes can be found in section 4.4.

The experimental setup for TSDC measurements consisted of a DeLonghi forced-air oven controlled by a Eurotherm 818S PID temperature programmer, a Heizinger LNC 20000–3 high voltage source, and a Keithley 6514 electrometer. The general description of TSDC experimental setups and their operation can be found in section 4.4.

5.2 Results and discusión

Differential Scanning Calorimetry

Figure 5.1 presents the DSC scans performed on as-received samples of the different studied cable insulations. The crystallinity (χ_c) calculated from the enthalpy of fusion is 0.270, 0.273 and 0.246 for the cables S, L and R, respectively. The fusion temperatures are 108.0ºC, 108.6ºC and 106.5ºC. Crystallinity changes only slightly with annealing for the temperatures and annealing times studied in this section [1].

In Figure 5.6, DSC diagrams of samples annealed for several annealing times at 90ºC can be observed. To can compare these curves with the TSDC results, all the samples were annealed an additional hour prior the DSC measurement. This is because since in the TSDC measurements performed in this chapter the cables had been poled for one hour at 90ºC, the samples used in DSC mesaurements should undergo the same heating process to present the same thermal history. This means that the samples with t_a=0 had, in fact, one hour of annealing.

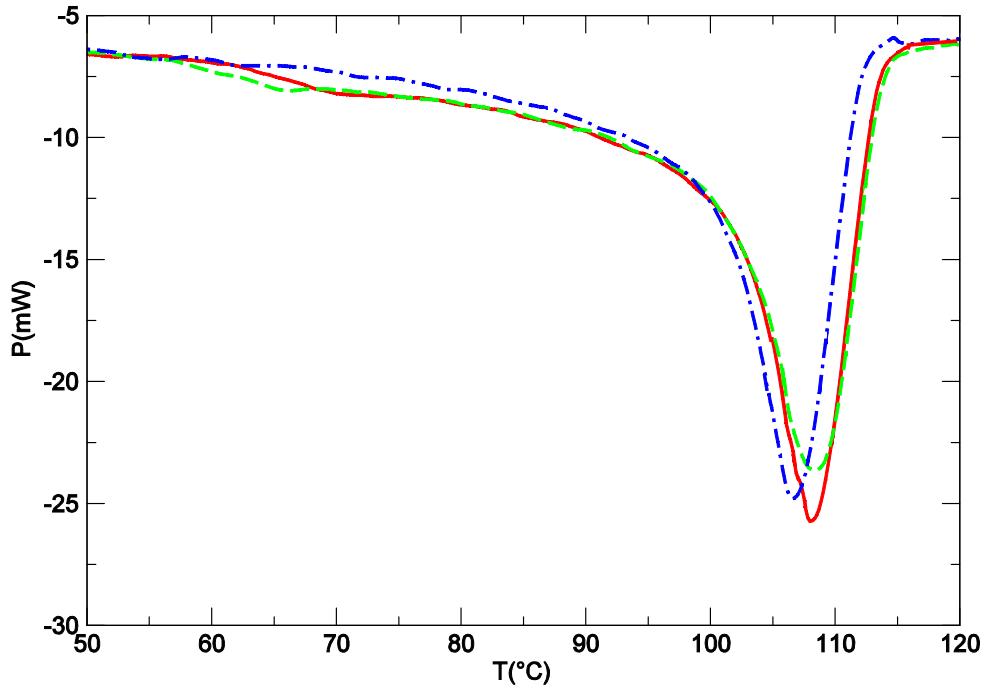

Figure 5.1. DSC curves for XLPE samples of S (—), L (— —) and R (— • —) as-received cables. Samples mass=20g; v_h=2ºC/min.

a)

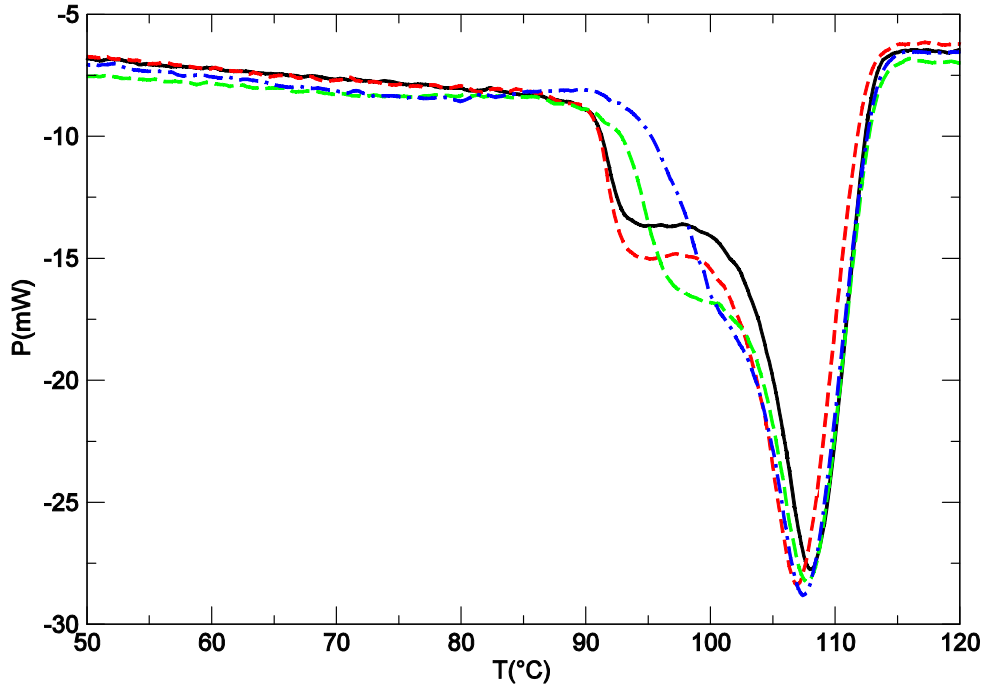

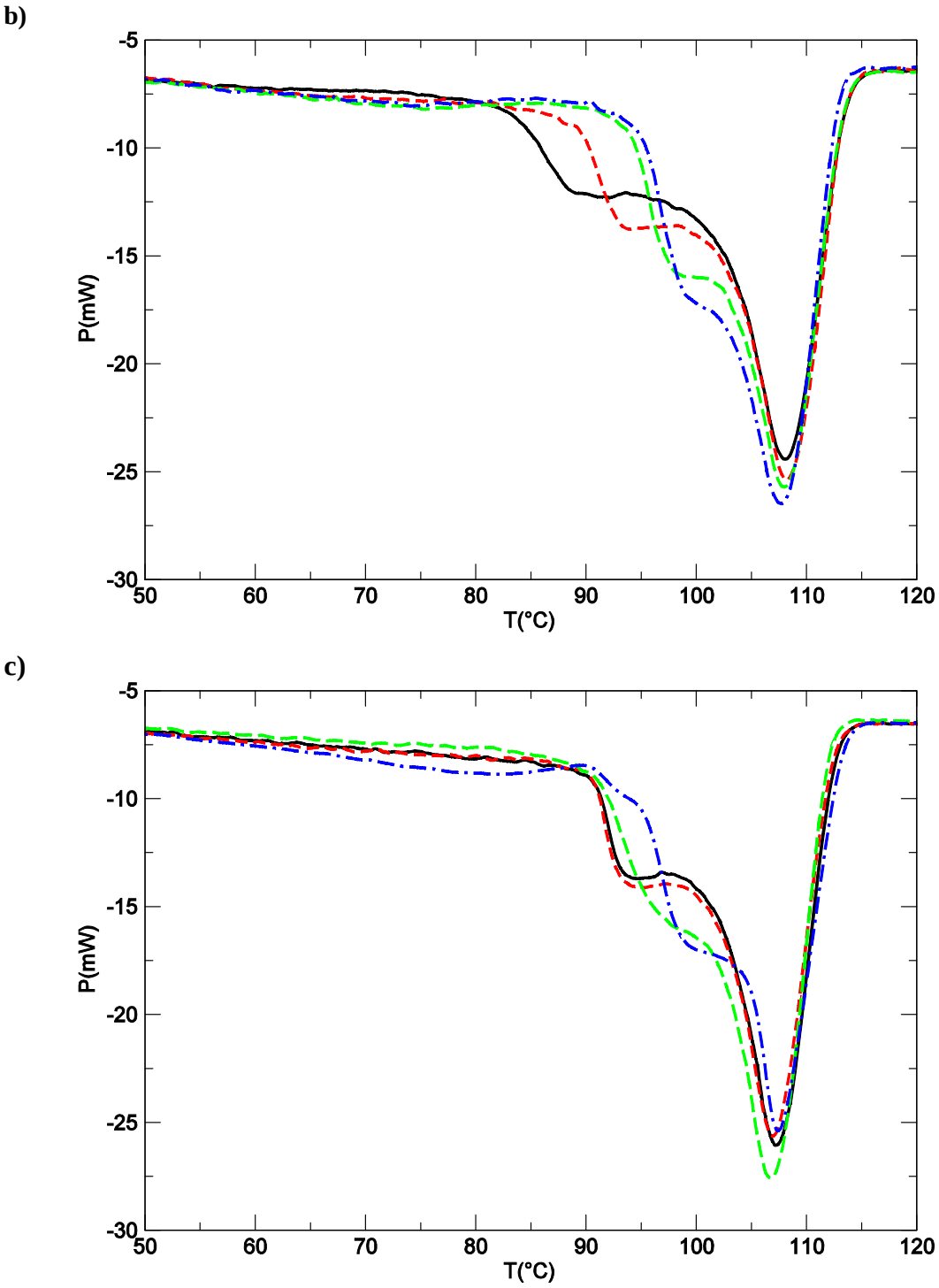

Figure 5.6. DSC diagrams for samples of cables S (a), L (b) and R (c), annealed at T_a=90ºC for different annealing times. Samples mass=20g; v_h=2ºC/min; t_a: 0 (—), 14h (– – –), 3d (— —) and 9d (— • —). Prior to make the DSC measurement, all the samples were heated from the room temperature to 90ºC for 1 hour, and cooled again. By this way, the thermal process of the samples used in TSDC (poled for one hour at 90ºC) is reproduced in the DSC samples.

Unlike as-received XLPE samples, DSC curves of cables annealed at 90ºC show a peak just below the main fusion peak. This new peak is associated with the recrystallization process that takes place in the melting range of temperatures (see chapter 7). When the material is annealed at 90ºC, the recrystallization of some fraction of the material

molten at this temperature leads to the formation of more stable crystals, which will melt afterwards at higher temperatures. This gives rise to a decrease of the crystalline fraction that melts below 90ºC and the consequent increase of the fraction melting at higher temperatures. Such increase results in a peak above the annealing temperature and below the main DSC fusion peak. As the annealing time increases more and more, this relative maximum shifts to higher temperatures. This implies that the crystals are more and more stables and, at some point, some chains are not longer accepted in crystalline structures. However, some of these chains crystallize during the cooling and, when the DSC heating ramp is performed, they melt at temperatures below the T_a. Thus, a small melting process can be detected below 90ºC in the samples with large annealings.

In the Figure 5.7, a DSC thermogram of the sample annealed at T_a=90ºC for 9 days is compared with a measurement made after the same sample was cooled down from the 150ºC. In the second case the sample had not experienced a recrystallization and the thermogram was the typical of an as-received sample. If the sample is annealed for one hour at 90ºC, then the recrystallization process is resumed.

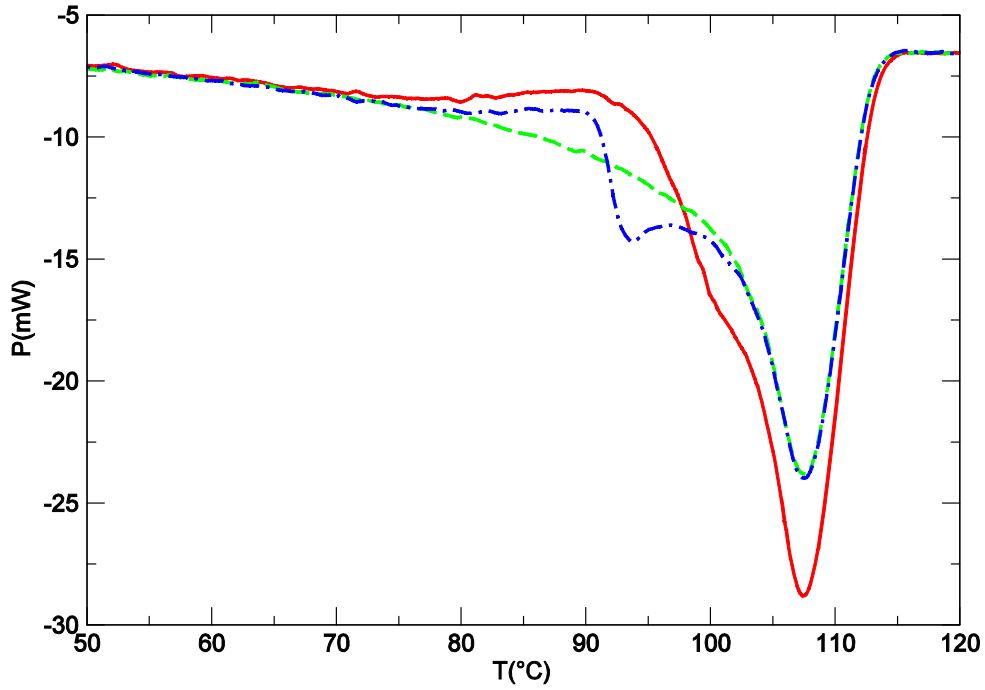

Figure 5.7. DSC curve for a cable S sample annealed at T_a=90ºC for 9 days (—). Once the previous sample was cooled, a DSC measurement was performed again on it (— —). Finally, the sample was heated up to 90ºC where it was annealed for 1 hour; then was cooled and a new DSC measurement was carried out (— • —). Samples mass=20g; v_h=2ºC/min.

Thermally Stimulated Depolarization Currents

With the aim to determine the differences among cables in service conditions, the TSDC behavior of the insulations for annealing and poling conditions close to the operational temperature was monitored. In order to minimize the influence of the semiconductors on TSDC response, conventional TSDC (see section 4.2.2) were performed on as-received samples from which both semiconducting layers had been completely removed. 8cm long electrodes were painted by using conducting aluminum paint.

In Figure 5.2, TSDC discharge curves for as-received cable samples without SC layers are shown. Cables S and L showed a heteropolar peak between 105ºC and 110ºC, which matches the fusion temperature of XLPE insulation. It can be identified with the heteropolar "fusion" peak found at about 105ºC in the cables studied by Tamayo (see chapter 3, [2]). In the case of cable R, a dominant peak appeared around 95ºC, while the fusion peak was clearly smaller than in the other two cases. In all the discharges, a small hump between 80 and 90ºC can be detected. A peak at 95ºC also appeared in an as-received S cable for different poling conditions (Figure 5.8) and in cable D [2].

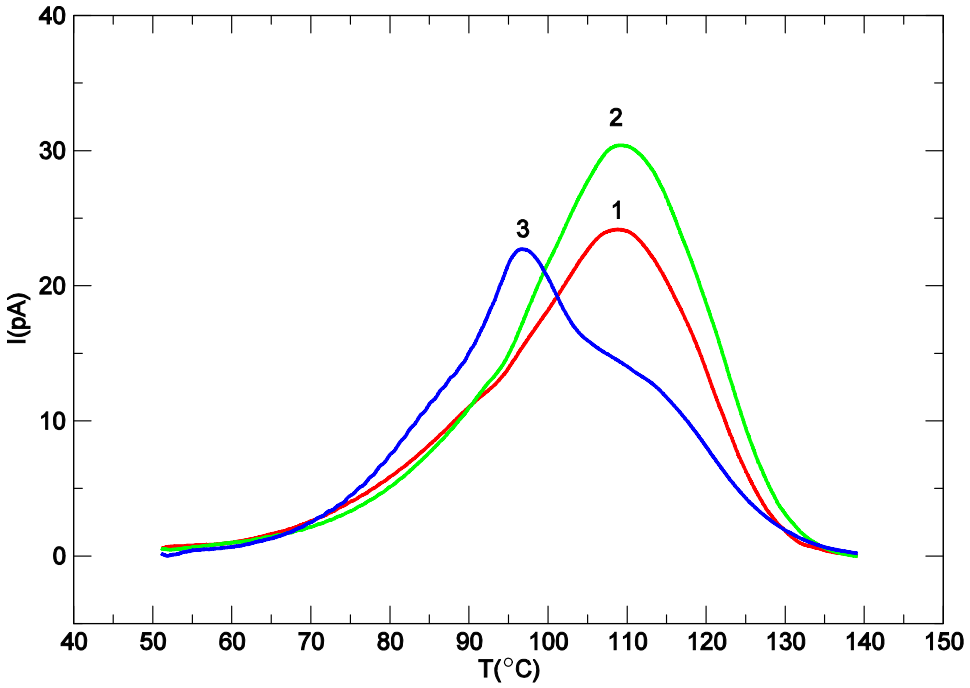

Figure 5.2. TSDC discharge curves for as-received cable samples without SC layers. TSDC (conventional) conditions: V_p=4kV; T_p=90ºC; t_p=1h; t_s=5min; T_s=50ºC; T_f=140ºC; v_h=v_c=2ºC/min; sample (1: S; 2: L; 3: R).

Apart from the inner semiconductor, the only difference between cable R, on the one hand, and cables S and L, on the other hand, is the polyethylene base (see the Table 4.1). In the case of cable R, the polyethylene acquired by the manufacturer already incorporated the antioxidant. Antioxidants can modify significantly the crystalline structure of the material and can act as traps for charge carriers during polarization [3]. Different antioxidants, and even different methods to incorporate them to insulation, can lead to different trap distributions and crystalline structures which can result in different TSDC responses. This could explain the differences in TSDC curve of cable R with respect to those of cables S and L.

In Figures 5.3, 5.4 and 5.5, the behavior of the spectra of cables S, L and R, respectively, with the annealing at 90ºC, can be observed. In all the cases, the TSDC response decreases with annealing. In the case of cable S, a complex relaxation with two dominant maximums around 90ºC and 100ºC is observed in annealed samples. Also, a hump between 80 and 90ºC and another between 100 and 110ºC can be observed on the discharge curve.

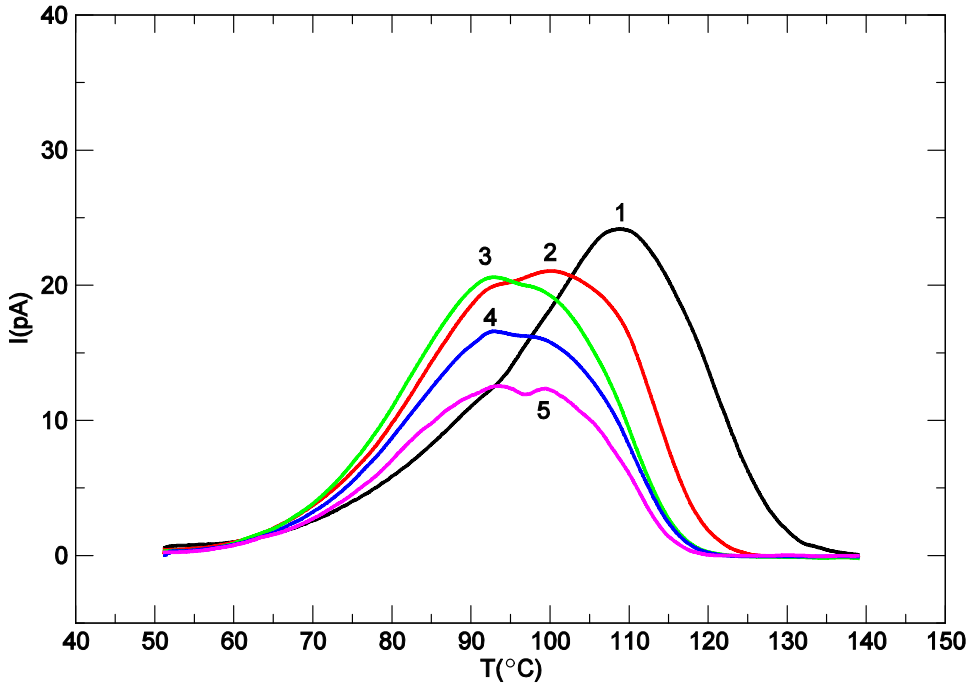

Figure 5.3. TSDC discharge curves for samples of cable S without SC layers, annealed at T_a=90ºC for different annealing times. TSDC (conventional) conditions: V_p=4kV; T_p=90ºC; t_p=1h; t_s=5min; T_s=50ºC; T_f=140ºC; v_h=v_c=2ºC/min; t_a(1: 0; 2: 14h; 3: 3d; 4: 9d; 5: 16d).

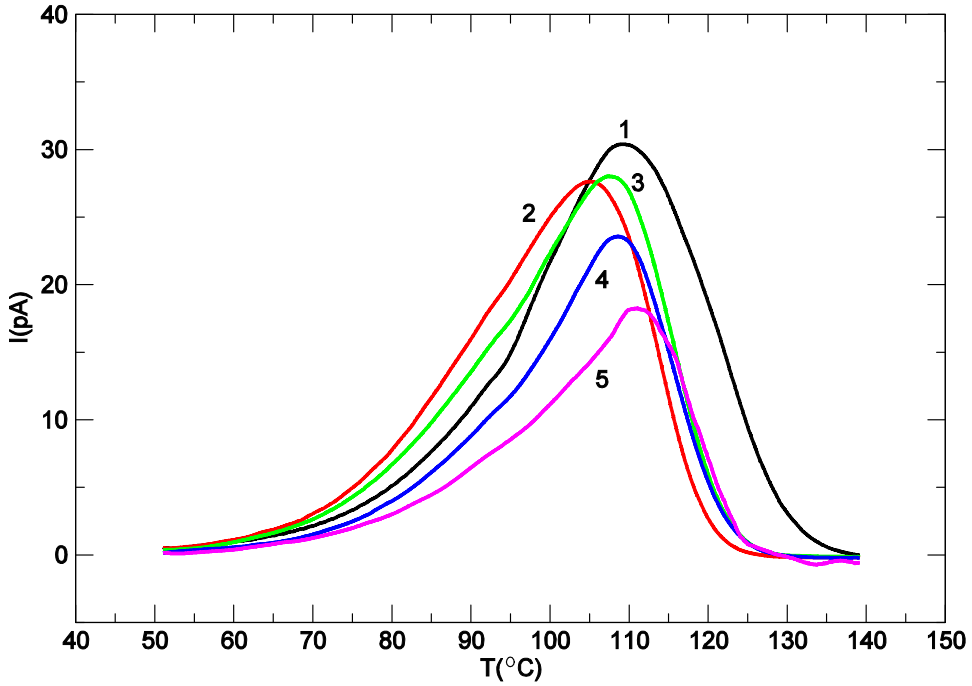

Figure 5.4. TSDC discharge curves for samples of cable L without SC layers, annealed at T_a=90ºC for different annealing times. TSDC (conventional) conditions: V_p=4kV; T_p=90ºC; t_p=1h; t_s=5min; T_s=50ºC; T_f=140ºC; v_h=v_c=2ºC/min; t_a(1: 0; 2: 14h; 3: 3d; 4: 9d; 5: 16d).

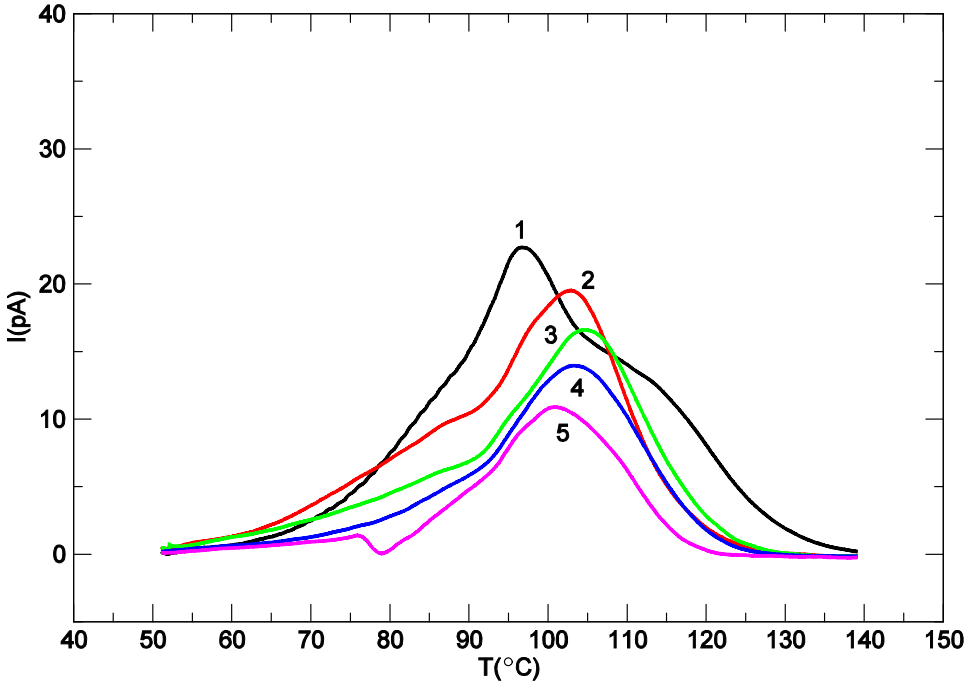

Figure 5.5. TSDC discharge curves for samples of cable R without SC layers, annealed at T_a=90ºC for different annealing times. TSDC (conventional) conditions: V_p=4kV; T_p=90ºC; t_p=1h; t_s=5min; T_s=50ºC; T_f=140ºC; v_h=v_c=2ºC/min; t_a(1: 0; 2: 14h; 3: 3d; 4: 9d; 5: 16d).

Tamayo observed a three stage process in TSDC spectra when XLPE cables are annealed (see chapter 3, [2]). First the TSDC response is fully heteropolar. By annealing the cable samples, the heteropolar contribution starts to decrease. In some cases, a homopolar peak appears below certain conditions and, eventually, the response becomes fully homopolar. With further annealing, the heteropolar sign is recovered. This process takes place at temperatures above a certain value located between 80ºC and 90ºC, and it occurs faster as the temperature increases. The decrease of the total heteropolar discharge when samples S, L and R are annealed is consistent with this three stage process.

On the other hand, this behavior also could be related to recrystallization. In chapter 7, the role of recrystallization when samples are poled isothermally is discussed. According to the proposed model, the crystalline fraction formed by recrystallization during the polarization stage remains polarized until it melts along the TSDC heating ramp, giving rise to the peak at about 105ºC. Since the recrystallization rate decreases with time, the fraction recrystallized during the polarization stage is lower as annealing time previous to TSDC increases. This would lead to a smaller heteropolar discharge as samples are annealed at 90ºC.

The differences between the TSDC spectra of cables S, L and R should be explained by the use of different antioxidants in the manufacture of the cables. On the other hand, although the thermal annealing and measurements were performed in samples without semiconducting layers, the diffusion of impurities from semiconductors during the manufacturing process should also be taken into account [2]. Nevertheless, the outer SC layers composition is very similar in the three cases and the inner SC is identical in the

cables S and L. Therefore, the SC diffusion seems not to be determining in the TSDC differences for samples annealed at 90ºC.

From experimental results it can be seen that TSDC technique has enough resolution to detect differences among cables with different manufacturing processes and/or compositions. Hereafter, the work will be centered in cable S (also, the cable D used by Tamayo will be employed in chapter 9). The reason is that cable S has more industrial interest than cable R, and it accumulated less space charge and behaved electrically better than cable L.

Once the response of the insulation had been obtained for annealing and poling conditions close to the service temperature, the goal was to characterize the complete samples –with their own SC layers acting as electrodes, according to the section 4.4– and their evolution with annealing. In order to avoid the recrystallization due to isothermal poling or annealing at temperatures within the melting range, the technique TSDC/NIW was used. A temperature of 140ºC was reached in the TSDC process to accelerate the evolution with thermal aging [2]. In Figures 5.8 and 5.9, consecutive discharges of an S sample with V_p=12kV, T_p=140ºC and V_p=18kV, T_p=120ºC are shown. In the former case, the first discharge obtained shows the heteropolar peak at 95ºC and a homopolar one at 128ºC. In the second discharge the homopolar peak shifts to 115ºC, the 95ºC peak disappears and a slight homopolar peak appears between 90ºC and 100ºC. As it was seen in the Dr. I. Tamayo's Ph.D. thesis, reaching high temperatures activates the homopolar mechanisms giving rise to a peak that appeared at 99ºC in cable D. With further annealing –each TSDC ramp implies a non-isothermal annealing– the response becomes fully heteropolar and the obtained spectrum is composed by two heteropolar peaks separated by a minimum between 90 and 100ºC.

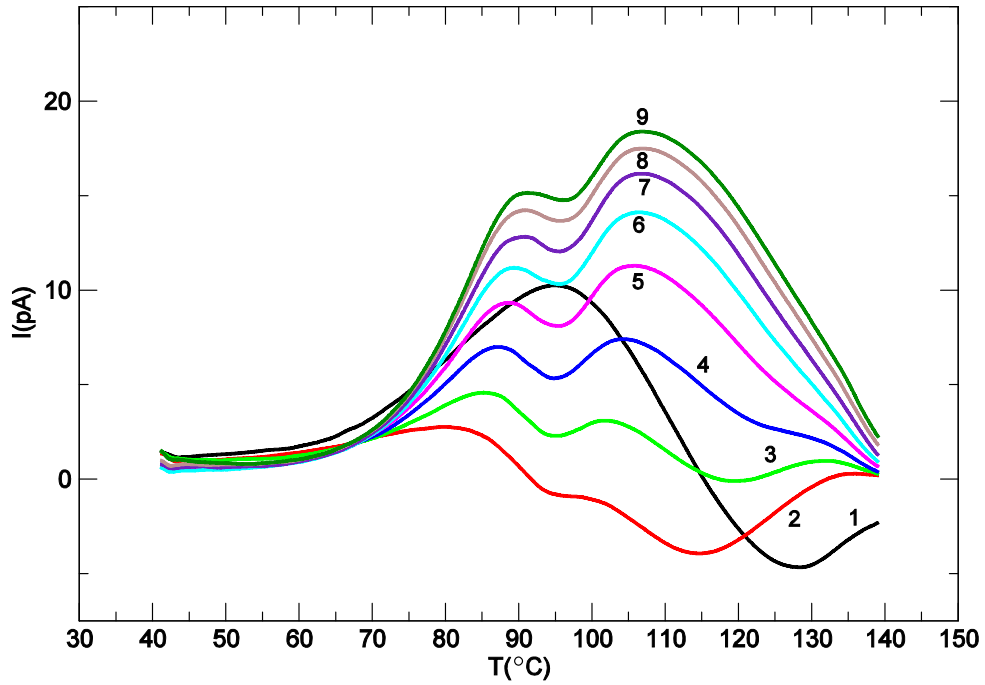

Figure 5.8. Consecutive discharges of an S sample. TSDC conditions: NIW (140ºC→40ºC) V_p=12kV; t_s=5min; T_s=40ºC; T_f=140ºC; v_h=v_c=2ºC/min.

With respect to the TSDC/NIW discharges obtained for a higher field (Figure 5.9), the first curve presents two homopolar peaks at 93 and 110ºC. In the subsequent discharges all the spectra are fully heteropolar.

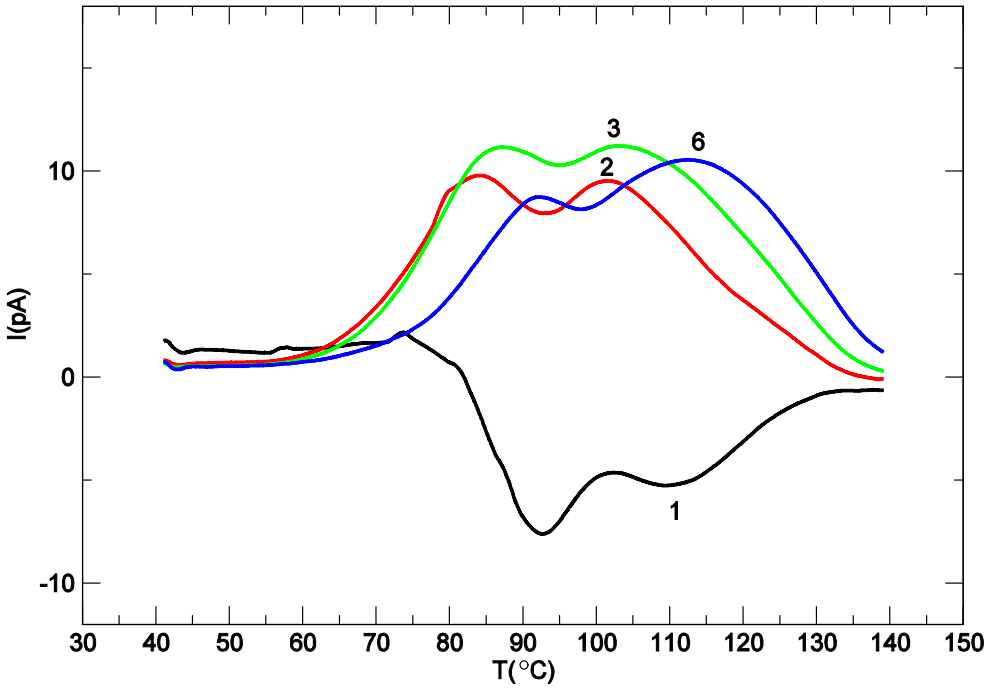

Figure 5.9. Consecutive discharges of an S sample. TSDC conditions: NIW (120ºC→40ºC) V_p=18kV; t_s=5min; T_S=40ºC; T_f=140ºC; v_h=v_c=2ºC/min.

5.3 Conclusions

Cable samples of three different types provided by the manufacturer, S, L and R, have been studied. Crystallinity values calculated from calorimetric measurements are 0.270, 0.273 and 0.246 for cables S, L and R, respectively. The fusion temperatures are 108.0ºC, 108.6ºC and 106.5ºC.

DSC measurements reveal a recrystallization process when the material is annealed at 90ºC. The recrystallization of some fraction of the material molten at this temperature leads to the formation of more stable crystals, which will melt afterwards at higher temperatures.

Although sample compositions are very similar, some differences in TSDC spectrum can be detected due to the high sensitivity of the technique. Two heteropolar peaks at 95ºC and around 105ºC along with a homopolar peak between 90 and 100ºC that were already reported in previous works, are observed in the new samples for different stages of annealing.

When cable samples are annealed, the TSDC response undergoes a three stage process (heteropolar→homopolar→heteropolar) that has been described in previous works. Apart from the well known transient peak between 90 and 100ºC, another homopolar peak appears initially at higher temperatures in cable S TSDC spectra.

References

[1] Boukezzi, L.; Boubakeur, A.; Laurent, C. and Lallouani, M. *Iranian Polymer Journal*. **17** (2008), 611.

[2] Tamayo, I. "Estudio del comportamiento de la carga de espacio durante la fusión del XLPE en cables de media tensión por TSDC". Ph.D. Thesis. Universitat Politècnica de Catalunya, Terrassa, Spain (2002).

[3] Boudou, L.; Guastavino, J.; Zouzou, N.; Martinez-Vega, J.; *Proceedings of the IEEE 7th International Conference on Solid Dielectrics*. Eindhoven, the Netherlands (2001), 245.

6. CONDUCTIVITY OF XLPE INSULATION IN POWER CABLES. EFFECT OF ANNEALING

The aim of this chapter is to present and discuss experimental results concerning conductivity in cable XLPE insulation, in order to contribute to a better understanding of conductive processes that take place in it. The study was carried out directly in cable samples to better reflect the behavior of the whole system at service. Therefore the measured conductivity is an "effective conductivity" of the cable XLPE insulation. In order to analyze the effect of the service conditions on the system, cable samples were annealed at several temperatures and for several annealing times. The influence of the semiconducting screens was also considered. Conductivity measurements were performed by using two different methods: absorption/resorption currents technique (time domain), and dynamic electrical analysis (frequency domain). Complementary techniques were also used to obtain additional information about the processes that take place into the bulk material.

6.1 Introduction

Due to the non-polar character of PE, conduction processes should be associated with the presence of free charge carriers. Nevertheless, polar contribution may arise from the existence of carbonyl groups C=O that are produced by oxidation of PE, and from polar impurities.

It is well-known that PE conductive properties are conditioned by its morphology [1–8] and that insulation degradation can be related to volume space charges [9]. Particularly, conduction and space charge formation in low density polyethylene were studied including the temperature range of interest for cable diagnostics [10]. In the last few years, there has also been a growing interest in the study of insulation properties under the application of DC voltage, the corresponding formation of space charge distributions and its relation with the remaining lifetime of the cable [11–13].

Although it is generally considered that carriers responsible for PE conduction are basically electrons [13,14], ions coming from additives and cross-linking by-products should be considered also. Current versus voltage (*I-V*) characteristics studied in LDPE by Stetter [15] at 42ºC, 82ºC and 110ºC, indicate that for low electric fields (*F*) an ohmic behavior is observed; for higher electric fields, conduction can be interpreted on the basis of a quadratic law on *F*, which depends on temperature and reveals the existence of traps. Finally, for higher electric fields, a third region can be found where current follows Child's law with full traps, and conduction can be interpreted from general criteria of the theory of space charge limited currents (SCLC) [16]. More recently, several authors have also observed that current-voltage characteristics in PE can be explained by SCLC model [17,18]. Pélissou et al. [17] studied the isochronal current-voltage characteristics in LDPE for a wide temperature range below and above its melting point. They concluded that at low average electrical fields the behavior is ohmic, but between 5 and 50 MV/m it becomes highly nonlinear, following $J \propto V^n$ with $n>2$. This result suggests that an exponential distribution of traps may be present [18]. In another study of *I-V* characteristics, Mizutani shows that current is limited by the electrode, following a Richardson-Schottky law for high electric fields ($F>4\text{x}10^7$ V/m) [19].

Nath, Kaura and Perlman [20] apply the band theory to LDPE by developing a mathematical model based on hopping of carriers which are injected into amorphous regions. They consider a SCLC and a process of charge-trapping at amorphous-crystalline interfaces. In addition, they suppose that the density of trapping centers is high enough so that the interaction between them results in an effective lowering of the traps depth (Poole-Frenkel effect). In this model, the "distance between traps" parameter is introduced and it has a constant value. Even more recently, in the same research line, it is concluded that electronic transport is bound to thermally activated hopping, which is assisted by electric field with very low activation energy [21]. From charge distribution studies and, specifically, by applying the electroacoustic pulse technique (PEA), the presence of periodical charge packets between electrodes could be detected for high electric fields [22].

Referring to the nature and depth of traps, it has been proposed that impurities and/or chain defects could be responsible for their existence in the material. Ieda has performed a detailed study on PE inquiring into both aspects [23]. Thus, the presence of cross-linking by-products and impurities diffused from the SC shields into the XLPE cable can promote charge trapping and hopping processes. Infrared spectroscopy (IR) has been widely used in identifying these components as well as the oxidation phenomena in XLPE [24–28]. Most of the by-products of thermo-oxidative processes are carbonyl groups that show absorbency peaks at $1741cm^{-1}$ (aldehyde absorption) [29–32], $1635cm^{-1}$ (vinylene absorption), $966cm^{-1}$ (transvinylene absorption) [26,29,30] as well as hydroxyl groups (-OH) with absorbency peaks at $3300cm^{-1}$ and $3500cm^{-1}$ [30]. Cross-linking by-products such as acetophenone and cumyl alcohol can also be monitored by IR, with absorbency peaks at $953cm^{-1}$, $766cm^{-1}$, $700cm^{-1}$, $860cm^{-1}$ and $1170cm^{-1}$ for cumyl alcohol [33], and $1695cm^{-1}$, $1263cm^{-1}$, $1360cm^{-1}$, $761cm^{-1}$ and $690cm^{-1}$ for acetophenone [33,34]. Bamji et. al. [35] also attributes to acetophenone some contribution to the $1305cm^{-1}$ absorption peak, usually associated with the amorphous fraction of XLPE [36]. Acrylate species and other components are shown to diffuse from the SC shields into the XLPE with thermal aging [28,37]. These components can be identified as well by IR measurements as they show absorbency peaks at $1736cm^{-1}$ [36].

In this chapter, the conductive processes that take place in XLPE insulation are studied at temperatures close to service conditions temperature for a typical power cable. In section 6.3, two cases are considered: (i) when insulation keeps its original semiconducting (SC) screens and, (ii) when the original screens are replaced by metallic electrodes. In this way, by using complementary time/frequency domain measurement techniques, the incidence of components diffusion from SC screens towards the insulation bulk is evaluated. Several annealing temperatures are also used to analyze the conductivity dependence on temperature. Once the temperature and semiconducting screens influence have been evaluated, in section 6.4 the study is focused on the conductivity evolution of complete cable samples (with SC), for very long annealing times at the working temperature of power cables (≈90ºC). In addition to the conductivity measurements, infrared spectroscopy (IR) is used to detect chemical changes into the material associated with the annealing processes.

6.2 Experimental

ARC measurements presented and analyzed in this Ph.D. thesis were performed by Dr. F. Frutos and Dr. M. Acedo of Departamento de Física Aplicada I, ETSII, Universidad de Sevilla.

Power cable with a 4.5mm thick XLPE insulation (see the characteristics of the S cable type in Table 3.1 for the XLPE composition) was supplied by General Cable S.A. Annealing processes were carried out on 7cm long sections cut from as-received cables. A new sample was used in each measurement in order to avoid the effects of previous measurements.

6.2.1 Absorption/Resorption Currents (ARC)

Samples were cable sections of 7cm length. ARC technique was applied to two different types of samples: *XLPE cylinders* without SC shields and complete cable samples. In the case of XLPE cylinders, inner and outer SC screens were removed by using a lathe and they were replaced by adapted copper electrodes for an optimal fitting to the inner and outer surfaces of the XLPE insulation. This procedure allowed us to carry out measurements of the electrical properties of the XLPE insulation, avoiding the effects of the SC screens. In the case of cable samples, only the outer SC screen was partially removed, so that a centered ring of 2cm width was left. This ring and the inner screen were used as electrodes. It is well known that reliable measuring of high impedance insulation requires very careful guarding and shielding of the measured object. This is of particular importance when measuring small samples [38] or short cables [39]. One metallic ring on each side of the outer electrode, 2mm aside of the latter, were used as guard electrode in order to avoid the effect of surface conductivity and the dispersion of the field lines. The experimental setup and the method for determining the conductivity are described in section 4.8. By comparing the results obtained from both kinds of sample, it is possible to study the effect of SC screens during the treatments.

In section 6.3, each sample was subjected to annealing at a temperature T_a ($50°C<T_a<100°C$) for a time t_a. Several annealing times were used for each temperature. The longest annealing times used at each temperature were determined by the kinetics of the changes observed in the conductivity properties and their order of magnitude was typically 10^2–10^3 hours. Measurements were performed at the annealing temperature.

In section 6.4 the longest annealing time was 90 days in all the cases. Moreover, the annealing temperature, T_a, it was always 90ºC, although conductivity measurements were taken at several temperatures for any considered annealing time, in order to apply the conduction thermal behavior model obtained in section 6.3.

6.2.2 Dynamic Electrical Analysis (DEA)

Frequency domain characterization was performed via dynamic electrical analysis in conditions of isothermal annealing. The experimental setup specifications and sample description are detailed in section 4.6. Frequency swepts between 0.01Hz and 1MHz for different annealing periods of time ranging from 0 to 72h were performed. Real and imaginary parts of the conductivity were recorded as a function of the frequency for

each annealing time and annealing temperature value in order to carry out the discussion of the results.

6.2.3 Fourier Transform Infrared and weight loss measurements

Fourier Transform Infrared (FTIR) measurements were performed with a Nicolet 510M spectrometer on 6x6mm XLPE sheets, with the invaluable assistance of Teresa Lacorte (Department of Materials Science and Metallurgy, Technical University of Catalonia). Samples 300μm thick were cut directly from the cable by mechanical methods at different depths from the external surface.

Weight loss measurements were performed in a 7cm cable section by means of an analytical balance Mettler Toledo AG245.

6.3 Electrical conduction dependence on annealing temperature. Semiconducting screens effect on the conductivity. DEA measurements

6.3.1 Results

6.3.1.1 Time domain measurements (absorption/resorption currents)

Experimental results have been grouped by temperature of annealing and measurement, i.e., whether these were carried out at temperatures T_a below or above a critical temperature, T_c, whose value is approximately 80ºC. The experimental data has been arranged this way in order to emphasize the noticeable change in the evolution of conductivity versus annealing time, observed at T_c [43].

Annealing below T_c

For cable samples as well as for XLPE cylinders (samples without SC screens), the general behavior of conductivity versus annealing time consisted in a continuous decrease. This decreasing trend was associated with different levels of conductivity fluctuations until reaching an apparent quasi-stationary state after a period of several days. These fluctuations are more noticeable in the case of XLPE cylinder with copper electrodes, especially at low temperatures (Figure 6.1), and continued at least for our total period of annealing time, t_a>1 month, in the case of T_a=50ºC. They could be attributed to problems at the electrical contacts. Even considering the slight variations in the nature and geometry of our samples, it is nearly impossible to achieve a perfect fitting between copper electrodes and XLPE. This fact probably leads to charge injection (corona effects, partial discharges, etc.) that occasionally may cause sharp fluctuations in the instantaneous values of our measurements.

In Figure 6.2, also for T_a=50ºC, conductivity measurements for a cable sample (cable sample with SC screens) are shown. Due to the clear homogeneity in the decreasing conductivity trend, the measurement period was restricted to less than 4 days. Only during the very first hours of measurement conductivity fluctuations could be detected.

The variations of conductivity in both types of samples (cable samples and XLPE cylinders) for annealing temperatures of 60 and 70ºC are depicted in Figures 6.3 and 6.4. Their behavior is not very different from the conductivity evolution described for

50°C. In conclusion, for $T_a<T_c$=80ºC, we determine that the measured conductivity when using SC screens (cable samples) is clearly lower than conductivity obtained when using copper electrodes (XLPE cylinders). It can be noted that the higher the annealing temperature, the lower the relative variation of the conductivity of the material during the annealing process.

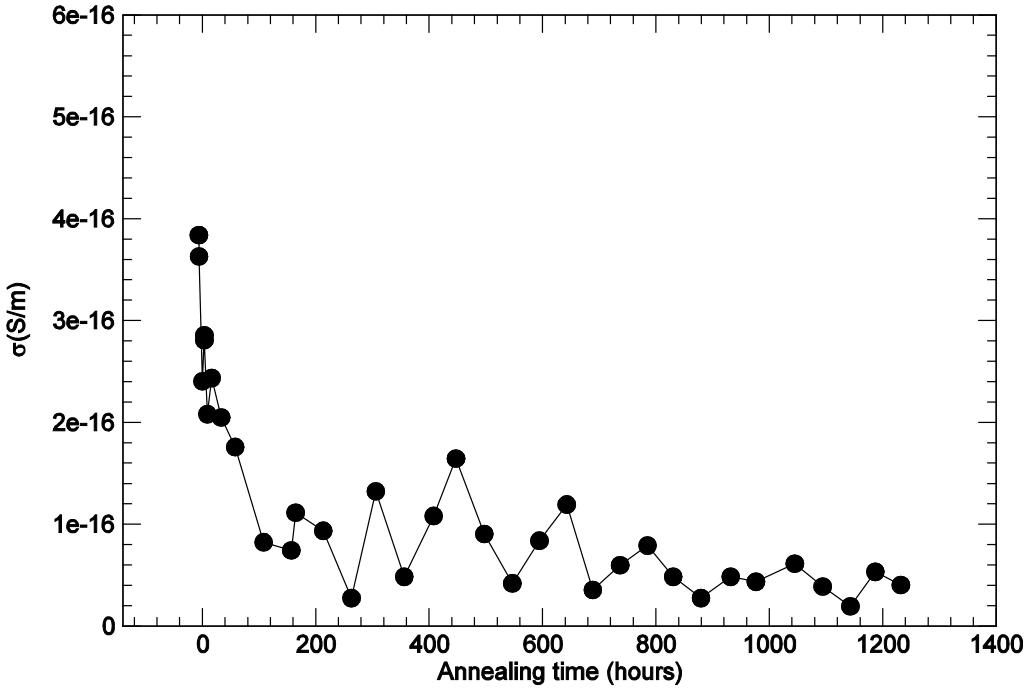

Figure 6.1. Conductivity versus annealing time for a XLPE cylinder (cable sample without semiconducting screens) at 50°C in isothermal conditions.

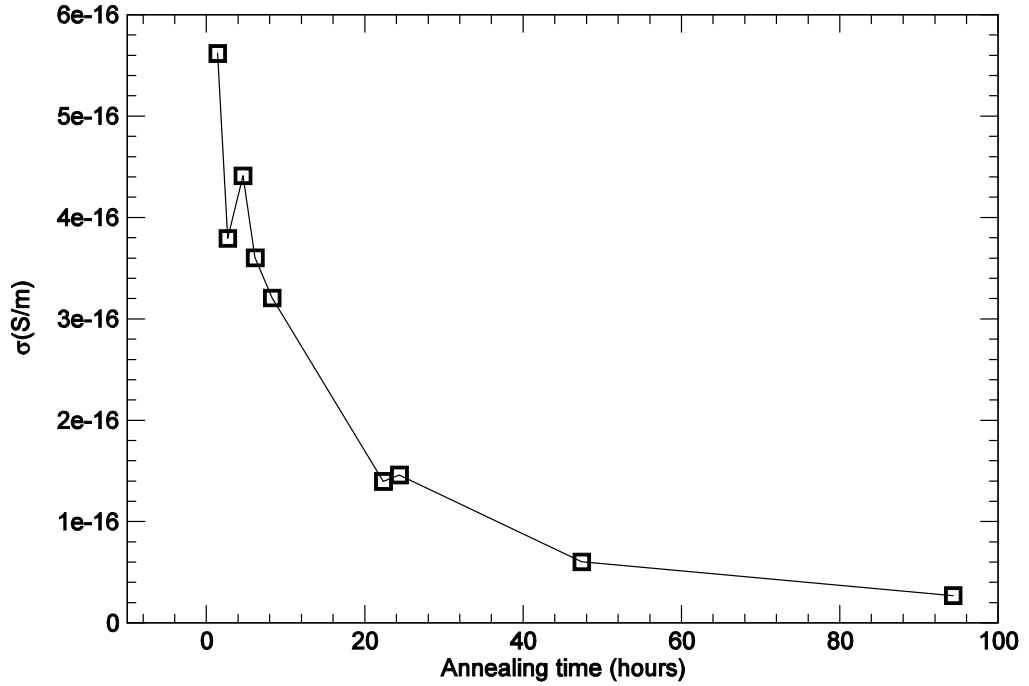

Figure 6.2. Conductivity versus annealing time for a cable sample ("complete" cable sample with semiconducting screens) at 50°C in isothermal conditions.

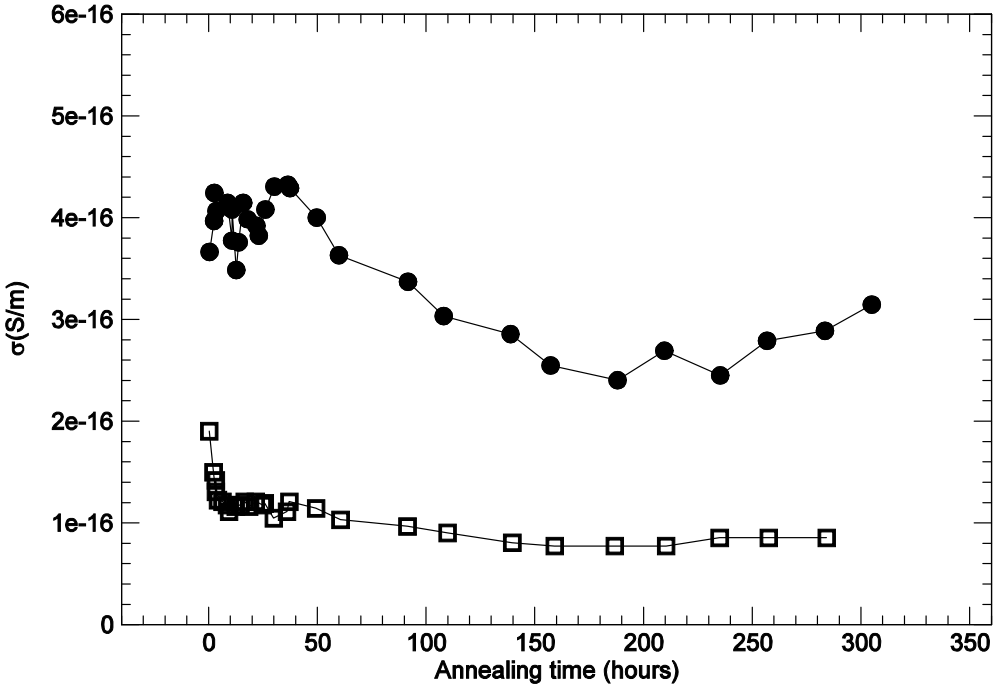

Figure 6.3. Conductivity versus annealing time for a cable sample (□) and a XLPE cylinder (●) at 60°C in isothermal conditions.

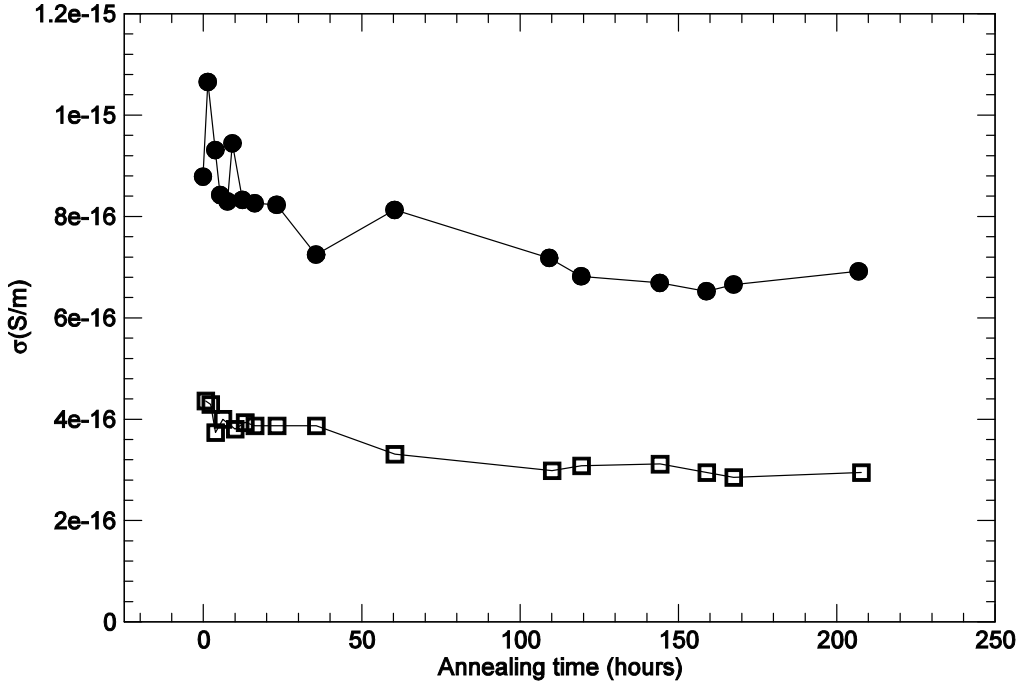

Figure 6.4. Conductivity versus annealing time for a cable sample (□) and a XLPE cylinder (●) at 70°C in isothermal conditions.

Annealing above T_c

In Figures 6.5, 6.6 and 6.7 we depict the variations in conductivity (σ) as a function of the annealing time for temperatures ranging from 80 to 100°C. Initially, for both sample

types, $\sigma=f(t)$ decreases quickly until a minimum value is measured, and thereafter, σ begins to increase. From then on, conductivity behaves very differently for the cable sample with SC electrodes and for the XLPE cylinder with copper electrodes.

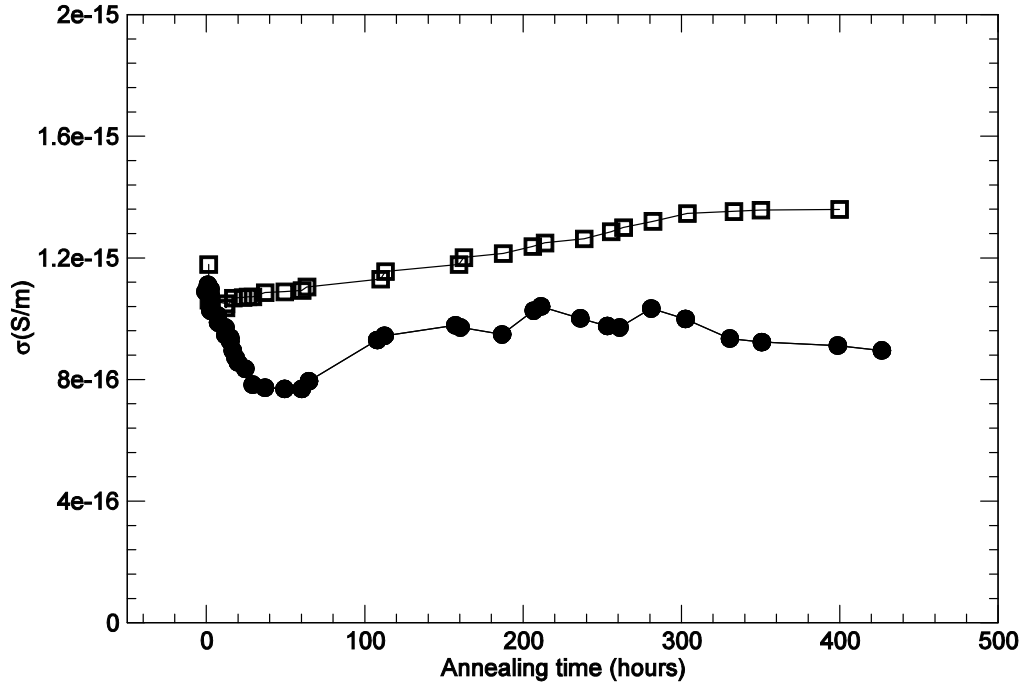

Figure 6.5. Conductivity versus annealing time for a cable sample (□) and a XLPE cylinder (●) at 80°C in isothermal conditions.

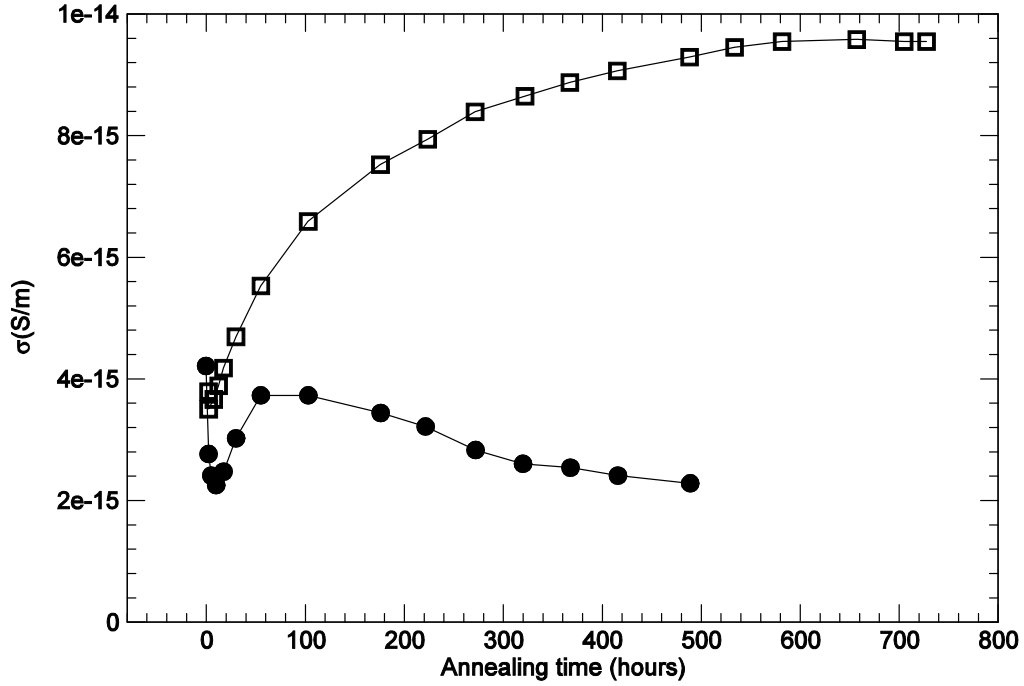

Figure 6.6. Conductivity versus annealing time for a cable sample (□) and a XLPE cylinder (●) at 90°C in isothermal conditions.

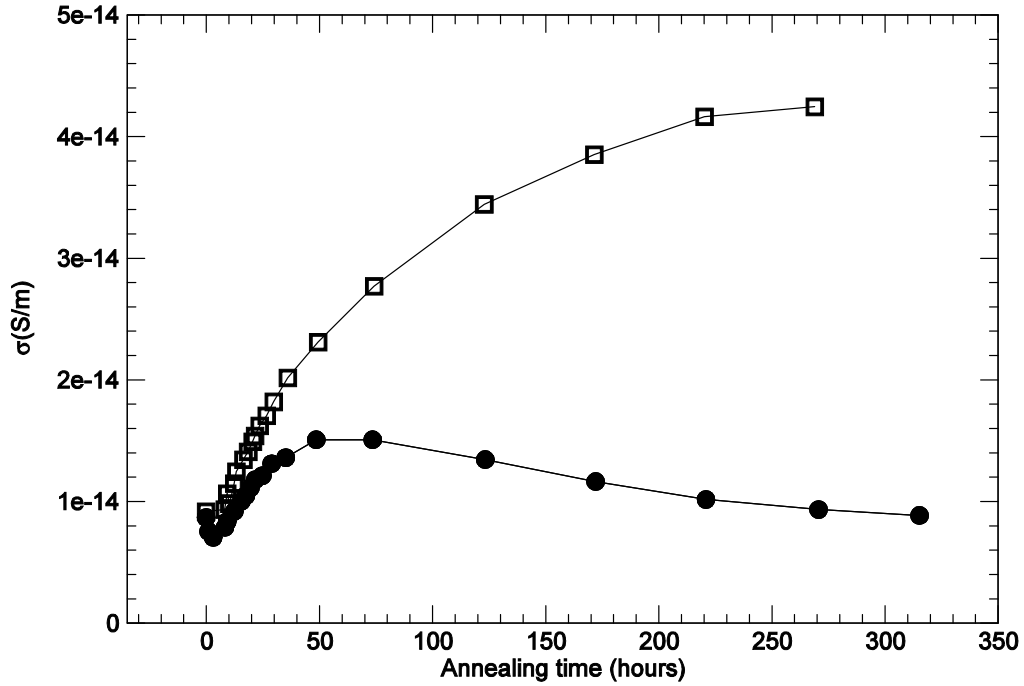

Figure 6.7. Conductivity versus annealing time for a cable sample (□) and a XLPE cylinder (●) at 100°C in isothermal conditions.

In the case of copper electrodes (XLPE cylinders), conductivity increases up to a maximum value, and its values decrease monotonically afterwards, which is accompanied by different levels of fluctuations until a quasi-stationary value is reached. The higher the annealing temperature, the shorter the time required to reach this maximum value of conductivity. As an example, at 80°C, it can be observed that this time is several days and fluctuations are very significant, whereas at 100°C, this time is only of a few days and oscillations are almost imperceptible.

In the case of SC electrodes (cable samples), a monotonic increase in conductivity reaches a quasi-stationary maximum final value. The higher is the annealing temperature, the higher is the relative increment of conductivity in comparison with its initial value. This percentage increment is approximately 450% for T_a=100°C (Figure 6.7).

6.3.1.2 Frequency domain measurements (DEA)

Two separate behaviors could be clearly distinguished in the frequency and annealing temperature ranges we used during the conductivity measurements. Some representative results are shown in Figures 6.8, 6.9 and 6.10.

In the case of frequencies higher than 1 Hz, we observed a decrease in the real part of complex conductivity (σ') with annealing time for all annealing temperatures ranging from 80 to 105°C.

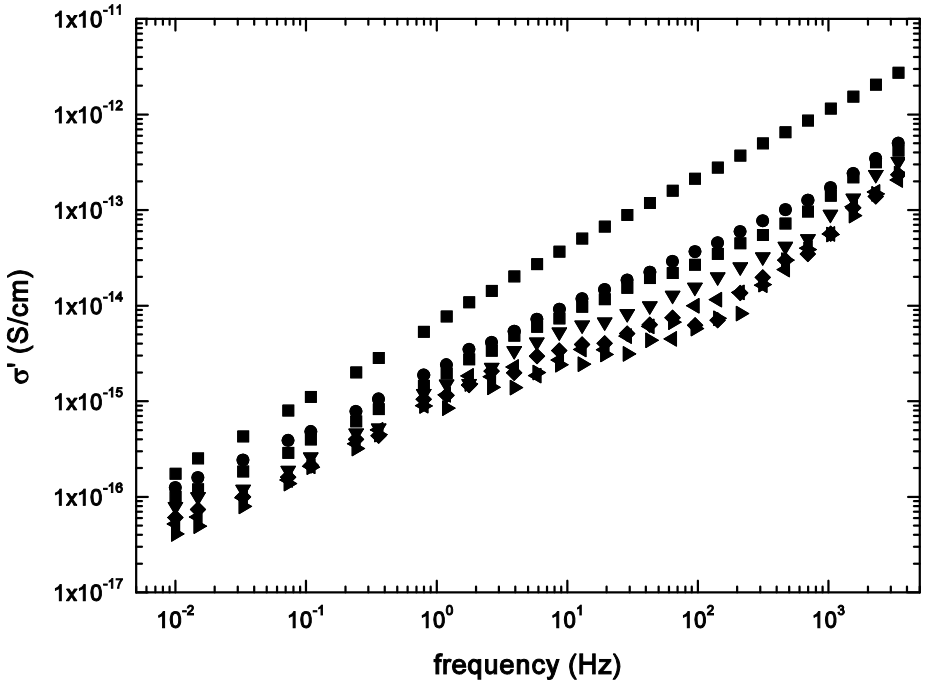

Figure 6.8. Variations of the real part of complex conductivity (σ') versus frequency by using isochronal curves obtained by DEA technique, for an annealing temperature of T_a=80ºC: (■) t_a=0h; (●) t_a=1h; (▲) t_a=3h; (▼) t_a=12h; (♦) t_a=24h; (◄) t_a=36h; (►) t_a=72h.

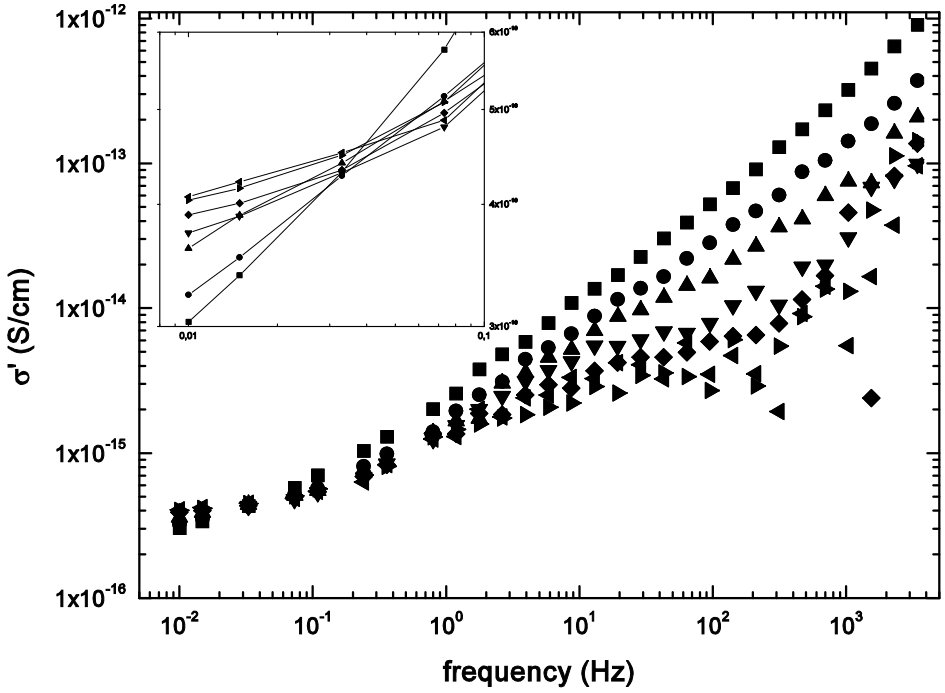

Figure 6.9. Variations of the real part of complex conductivity (σ') versus frequency by using isochronal curves obtained by DEA technique, for an annealing temperature of T_a=95°C: (■) t_a=0h; (●) t_a=1h; (▲) t_a=3h; (▼) t_a=12h; (♦) t_a=24h; (◄) t_a=36h; (►) t_a=72h.

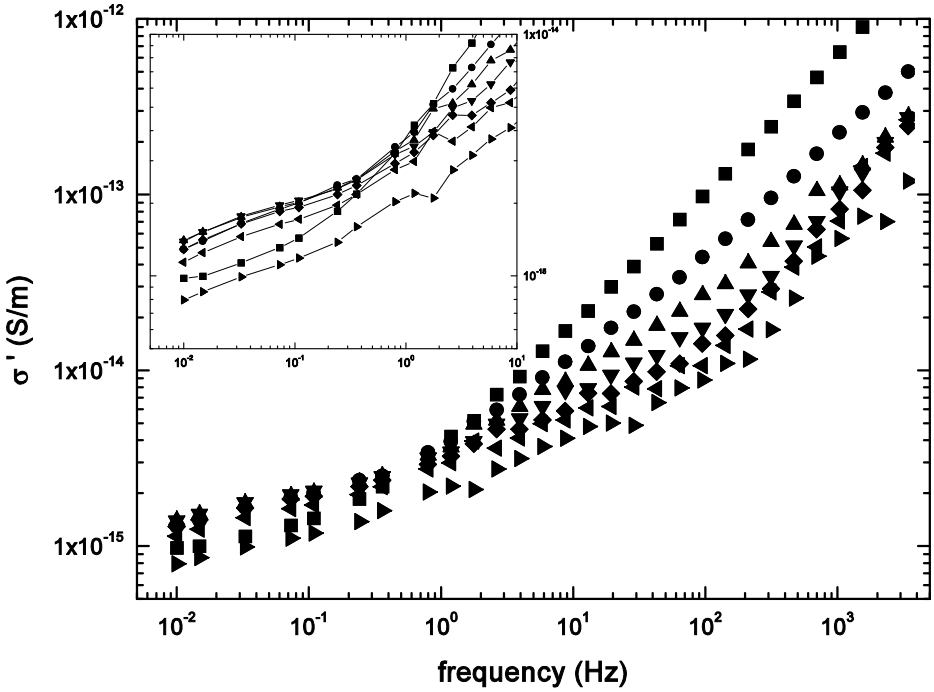

Figure 6.10. Variations of the real part of complex conductivity (σ') versus frequency by using isochronal curves obtained by DEA technique, for an annealing temperature of T_a=100 °C: (■) t_a=0h; (●) t_a=1h; (▲) t_a=3h; (▼) t_a=12h; (♦) t_a=24h; (◄) t_a=36h; (►) t_a=72h.

In the case of frequencies lower than 1Hz, two different behaviors were observed. First, for temperatures below 95°C, σ' decreases monotonically with annealing time, and this evolution becomes faster as temperature grows. Furthermore, the range of variation of the conductivity values is also smaller. Secondly, for temperatures above 95°C, σ' initially increases (for example, at T_a=100ºC, it increases for approximately 12h), but thereafter decreases to previous values. Rising and decreasing periods become shorter as temperature grows.

6.3.2 Discussion

Firstly, in order to properly interpret the results, it is very important to take into account that DEA measurements are performed only in XLPE samples, but not directly in sections of cable. These flat samples were cut from a ribbon that had been previously obtained from the insulation of a MV cable, as described in section 4.6. Therefore, these XLPE DEA samples do not have SC screens as electrodes on their surfaces. For this reason, their results should only be compared with those corresponding to XLPE cylinders (cable samples without SC screens) measured by using the ARC technique.

Secondly, we can confirm that effectively, ARC and DEA results on XLPE samples are in good agreement, according to the conductivity trends with increasing annealing times, both for low and high temperatures. In the case of low temperatures, conductivity always decreases with annealing time and particularly, referring to DEA measurements, this reduction is observed for the real part of complex conductivity along the entire frequency range that was examined (Figure 6.8). For higher annealing temperatures, we have also found that experimental results obtained by using both techniques are comparable. At low frequencies (Figures 6.9 and 6.10), the real part of conductivity

initially increases with annealing time but afterwards, it decreases again. Particularly, for T_a=100ºC, an absorption peak at 0.03 Hz could be present (Figure 6.10). Nevertheless, for higher frequencies, there is a continuous reduction of the real part of complex conductivity, which produces a crossover frequency for isochronal curves (curves obtained for different annealing times). This crossover frequency increases with T_a.

A global explanation of the different behaviors for conductivity that have been described in previous sections can be established on the basis of the existence of two prevailing types of conduction mechanisms in the material. Both mechanisms are associated with electronic carriers. On the one hand, there is a band conduction mechanism, slightly dependent on temperature (in our range of temperatures), but which is efficient over the entire studied domain of frequencies and annealing times. On the other hand, there is a hopping conduction mechanism [44] between localized states, in the mobility gap, which is both temperature and electric field dependent. This hopping process is only efficient above a critical temperature value, due to the increment of defect or impurity concentration associated with diffused components from the SC screens [37]. Dissociation of typical species present in MV cable insulation, such as cross-linking by-products, may also play a role in this process.

Hopping conduction is greatly enhanced by the diffusion of different components from SC screens to XLPE insulation, which implies that there are two determining conditions for hopping conduction to be a prevailing mechanism: (a) the existence of SC screens and (b) temperatures above T_c (i.e. service temperatures of power distribution MV cables) to increase the diffusion of the aforementioned components [28,45].

Temperatures below T_c

The assumptions made above can explain the differences in the behavior of conductivity between XLPE cylinders and cable samples detected by ARC measurements. Below T_c, electronic band conduction is the prevailing mechanism, as diffusion at these temperatures can be neglected during annealing procedures [23]. To explain the differences of conductivity observed between the two kinds of samples, we assume that both SC electrodes (cable sample) and copper electrodes (XLPE cylinders) have a blocking character and they limit electric current. This effect is even more noticeable in the case of SC electrodes (Figures 6.3 and 6.4). For both types of electrodes, their blocking behavior could be associated with the presence of components diffused from SC screens during the manufacturing process. These components act as trapping centers, and trapped charge limits the flow of electric current. In the case of copper electrodes (XLPE cylinders), mechanical procedures developed to eliminate outer and inner SC screens also remove the most external layers of the insulating XLPE material – where trap concentrations are the highest– consequently leading to an important decrease in effective trapping and then resulting in higher values of conduction current and conductivity.

The reduction of conductivity versus annealing time –especially for very short annealing times–, can be explained on the basis of a recrystallization process that takes place for this range of temperatures (see the chapter 7): XLPE crystals suffer a reconfiguration, approaching to perfect crystals and, possibly, of larger dimensions that results in a decrease of conductivity.

These hypotheses also explain the behavior observed by DEA. We must remember that, by using this technique, we have only XLPE samples (without SC layers), and consequently DEA results should be compared only with ARC measurements performed on XLPE cylinders (with copper electrodes and without SC screens). As we have already shown (Figures 6.1, 6.3 and 6.4), these measurements clearly exhibited a reduction in conductivity with increasing annealing time that can also be associated with the decrease in the real part of the complex conductivity in DEA measurements (Figure 6.8).

Temperatures above T_c

Above the critical temperature and at the final stage (long annealing times), cable sample conductivity is noticeably higher than conductivity for XLPE cylinders (copper electrodes). Within this temperature range, hopping conduction processes between traps combine with those based on electronic band transport. The increase in the concentration of traps has two different sources. On the one hand, we must consider chemical species diffused from SC screens and, on the other hand, ions provided by cross-linking by-products decomposition.

Concerning samples furnished with copper electrodes, the first –and most important– source of traps is not available, which explains quite obviously their corresponding lower values of conductivity as it is observed in Figures 6.5, 6.6 and 6.7. Furthermore, curves depicted in these figures show that, initially, during the very first hours of annealing, the variation of conductivity versus annealing time is similar for both types of electrodes: it begins with a decrease. We should first take into consideration that significant diffusion of components from semiconductor through insulation volume requires a certain time and, secondly, that the higher the temperature, the more efficient the diffusion process becomes. In this way, the process that initially appears is electronic band conduction and consequently, as we remarked in last subsection ($T_a<T_c$), the conductivity diminishes with annealing time. After a certain annealing time, in the case of cable samples, trap generation –both from cross-linking by-products and diffused components from SC screens– becomes an effective process, and a noticeable increase of conductivity with annealing time takes place. This is because the increment of trapping centers inside the XLPE insulator enhances hopping conduction between them. Finally, this conductivity increase does not continue indefinitely, but it reaches a saturation level. Our experimental results are compatible with the literature [21] and with the theoretical model of Nath, Kaura and Perlman [20], although our results indicate that the parameter associated with the distance between localized states should be a time and temperature dependent one, because it is conditioned by the density of traps, which changes with the diffusion process during annealing procedures.

In the case of XLPE cylinders (copper electrodes), the generation of traps is restricted to the source from cross-linking by-products, whereas this is the process responsible for conductivity growing after its initial decrease. Once this source of traps is exhausted, and taking into account that many of these generated species are volatile, the contribution to the conductivity by hopping between traps progressively diminishes until a nearly constant value is attained. This final regime is based on electronic conduction over extended states and is marked by the material equilibrium structure at the corresponding temperature.

The preceding explanations can justify to a great extent two aspects clearly defined in the curves in Figures 6.5, 6.6 and 6.7. On the one hand, the higher the temperature, the faster the minimum value in conductivity is reached after the initial decrease. This is due to the fact that high temperatures enhance the rates of diffusion and decomposition of cross-linking by-products, making the process of hopping conduction between traps more efficient for shorter times. On the other hand (in the case of copper electrodes), the higher the temperature, the faster the conductivity regime of electronic band transport is achieved (due to the depletion of ions proceeding from cross-linking by-products).

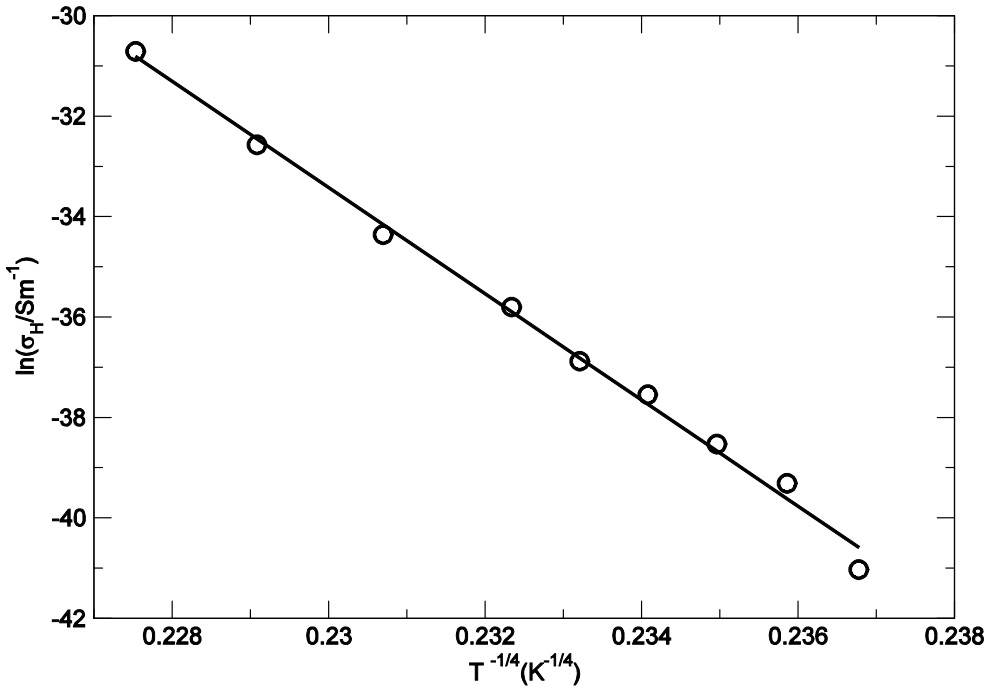

Figure 6.11. Mott's plot to characterize the conductivity by hopping processes between localized states.

This explanation is also valid for experimental values obtained by DEA. At low frequencies (below f=0.1 Hz for T_a=95ºC and below f=1 Hz for T_a=100ºC –Figures 6.9 and 6.10–) we can observe that initially, the real part of conductivity tends to increase, then it acquires a maximum value and afterwards it diminishes with annealing time. This behavior agrees with the relaxation associated with ions present inside XLPE. They are generated by dissociation of by-products so that, temporarily, the contribution of ions is enhanced while annealing time grows. However, as these elements are mainly volatile, they disappear gradually. As a consequence, their contribution to the real part of conductivity progressively decreases and finally, electronic transport processes prevail again, as one can reasonably interpret from Figure 6.9 (see curve corresponding to the larger annealing time, t_a=3 days). In this model, the crossover frequency of isochronal curves is due to the difference in the evolution of conductivity, at high and low frequencies, with annealing time. Furthermore, this crossover frequency is also dependent on T_a. The higher is the temperature, the higher is the crossover frequency. For this reason, a precise determination of T_c by measurements in the frequency domain is much more difficult than its determination in the time domain: as annealing temperature decreases, this crossover frequency decreases as well, and, regrettably, this

frequency eventually is lower that the frequencies that can be reached experimentally in our setup.

In Figure 6.11, we have represented as a *Mott plot* ($ln(\sigma)$ versus $T^{-1/4}$) the contribution to conductivity of the hopping mechanism between traps in the case of the "complete" cable samples with $\sigma_H=\sigma-\sigma_{EX}$, where σ is the total conductivity and σ_{EX} is the contribution to conductivity by extended states. The values for conductivities were obtained from the quasi-stationary regimes (saturation values), corresponding to long annealing times, for different annealing temperatures. A linear behavior of $ln(\sigma_H)$ versus $T^{-1/4}$ can be estimated, which implies that the transport mechanism is basically via thermally assisted hopping conduction [44]. The resulting value for conductivity by extended states is $\sigma_{EX}=1.65\text{x}10^{-17}$S/m. Hill [46] also found a similar relation between conductivity and annealing temperature, by considering a field assisted hopping conductivity at the limit of low electric fields, which is evidently one of the important experimental conditions in the present work.

6.4 Very long annealing times at service temperature. Infrared spectroscopy (IR). Results and discussion

6.4.1 Time domain measurements (absorption/resorption currents)

Stationary conductivity (σ) of cable samples measured by ARC at temperatures (T_m) between 50ºC and 97ºC are plotted in Figures 6.12 and 6.13 as a function of annealing time (t_a) at 90ºC. All curves show a maximum in conductivity that appears for t_a around 15 days at the lower measuring temperatures (50 and 60ºC, Figure 6.12). This maximum becomes more noticeable when T_m increases, and shifts towards higher annealing times, up to 30 days, when T_m=97ºC (Figure 6.13).

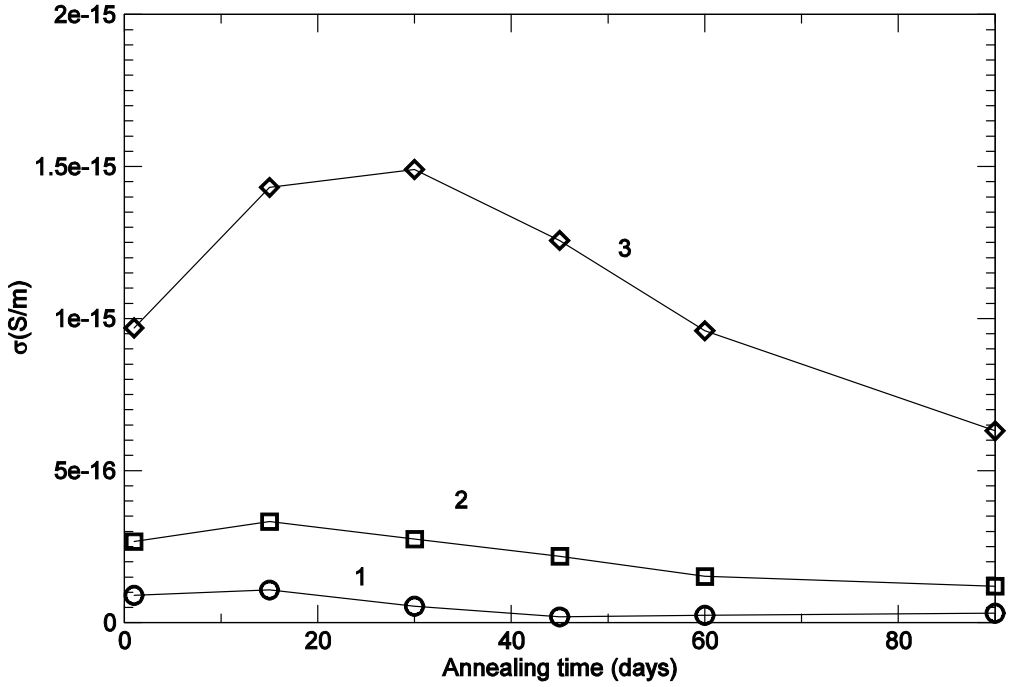

Figure 6.12. Conductivity in XLPE cable insulation versus annealing time at 90ºC: (1) T_m=50ºC; (2) T_m=60ºC and (3) T_m =72ºC.

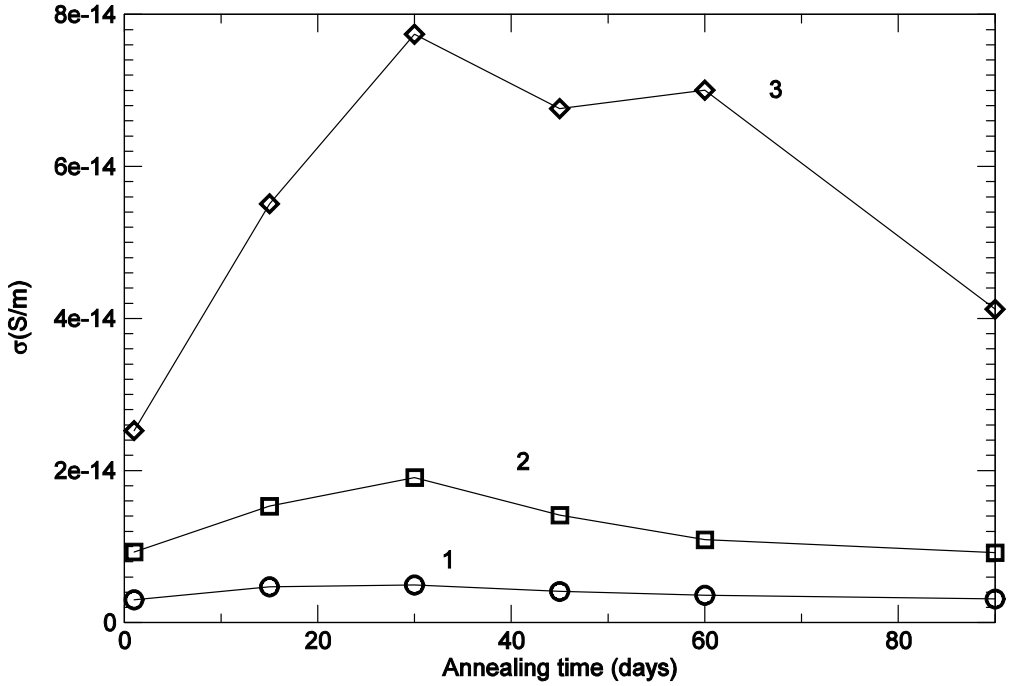

Figure 6.13. Conductivity in XLPE cable insulation versus annealing time at 90ºC: (1) T_m=78ºC; (2) T_m =90ºC and (3) T_m =97ºC.

According to the previous section, the increase in σ is probably due to the presence and dissemination through the insulation of chemical components diffused from the semiconducting shields. This fact generates internal charge and trapping centers that enhance σ. The conductivity behavior could also be affected by an oxidation process, but FTIR measurements discussed in section 6.4.2 discard this option at the studied temperatures.

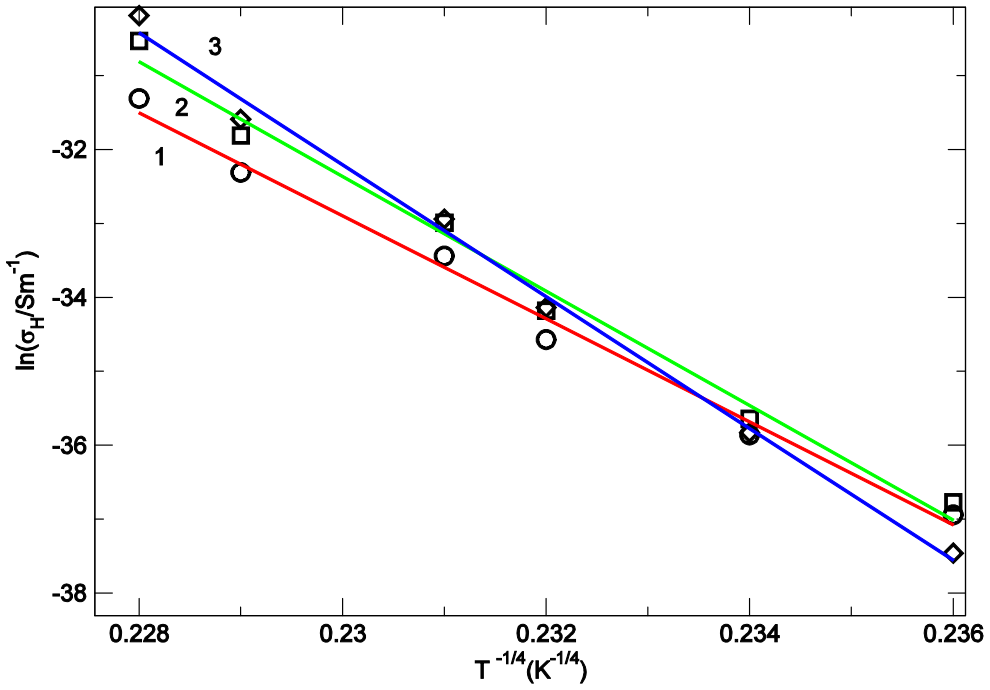

Figure 6.14. Mott's plot: (1,○) t_a=1 days, (2,□) t_a=15 days, (3,◊) t_a =30 days

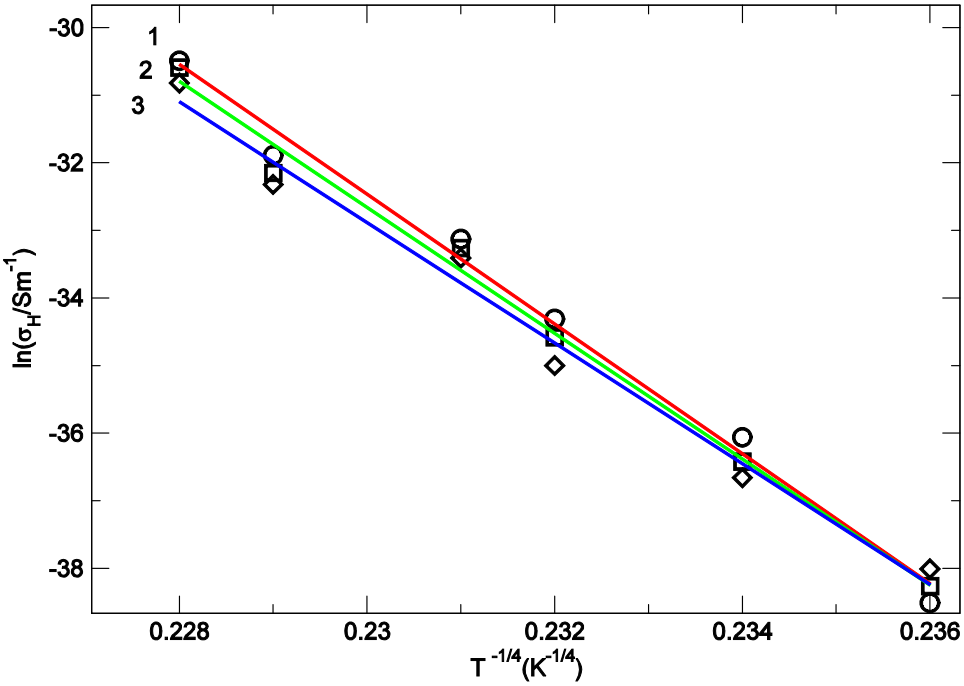

Figure 6.15. Mott's plot: (1,○) t_a=45 days, (2,□) t_a=60 days, (3,◊) t_a=90 days.

To analyze the contribution of hopping mechanisms to σ, we have represented in Figures 6.14 and 6.15 the experimental results as a Mott plot ($ln(\sigma_H)$ versus $T^{-1/4}$), where we have used the value of the contribution of extended states, σ_{EX}, obtained in section 6.3.2 to calculate σ_H ($\sigma_H=\sigma-\sigma_{EX}$, $\sigma_{EX}=1.65\times10^{-17}$S/m). A linear behavior of $ln(\sigma_H)$ versus $T^{-1/4}$ can be estimated from these figures, which implies that the transport mechanism via thermally assisted hopping considered in the previous section stands for any annealing time. In fact, this good agreement between data and the aforementioned law is more evident for long annealing times.

In the previous section, cross-linking by-products were considered responsible for the maximum observed in the case of XLPE cylinders without SC screens. However, they probably are not responsible for the maximum observed in the cable samples conductivity evolution for long annealing times, as the following experimental results suggest. Measurements of weight loss versus time during annealing can inform us about the presence and removal of cross-linking by-products in cable samples. Figure 6.16 shows these measurements in a 7cm long cable section annealed at 90ºC up to 110 days. It must be noted that weight measurements were performed in full cable sections to reproduce as close as possible annealing conditions of the ARC experiments. We can see that weight loss is very fast at the beginning (in the first hours) and sample mass becomes almost stable after 30–40 days of annealing. In addition, measurements of σ in annealed XLPE cable with and without SC shields carried out in the previous section also indicated that the presence of the SC shields is determining in the behavior of this magnitude. In those measurements, annealing up to 400 hours at 90ºC with the SC shields resulted in increments in σ up to five times the value obtained when annealed without the SC shield. These results suggest that the presence and diffusion of cross-linking by-products is not the main reason of the observed maximum in σ for very long annealing times. However, long term diffusion of acrylate species and other components from the SC shields into the XLPE [28,37] can explain this behavior.

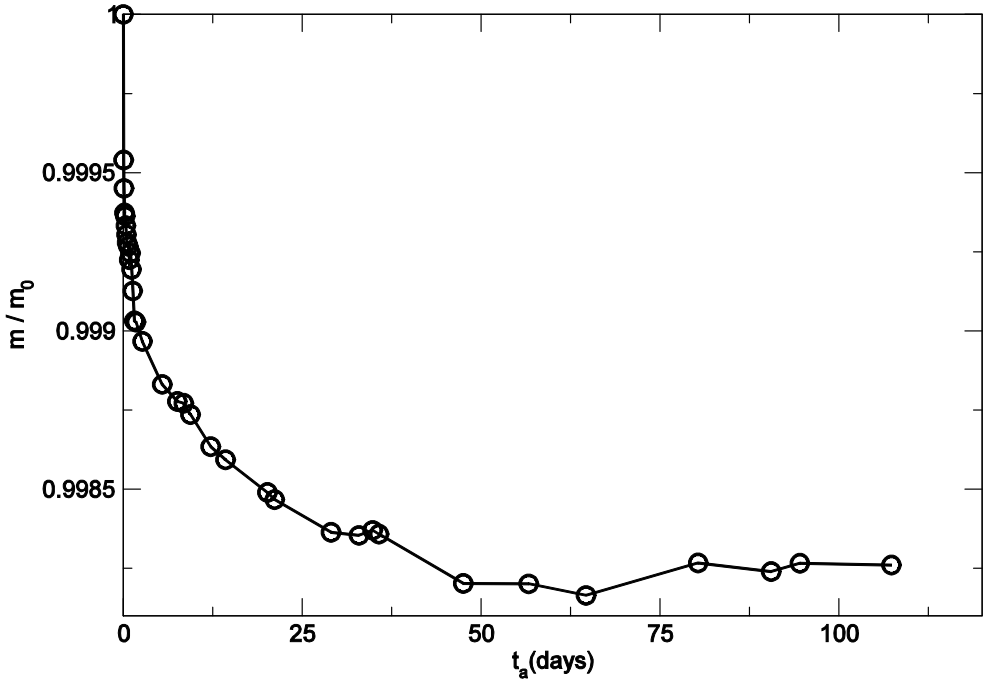

Figure 6.16. Mass loss in XLPE insulation versus annealing time at 90ºC.

Assuming that conductivity in XLPE is associated with a hopping mechanism, as the Mott plot suggests (Figures 6.14 and 6.15), we can adequately explain the observed change in σ after long annealing times as follows. In the hopping mechanism, the difference in energy and the distance between traps should modulate the whole process. If we take into account a possible diffusion of components from the SC layers into the XLPE bulk (as previous works suggest [37]) annealing should promote an increase in conductivity because of the increase in traps density. This phenomenon can explain the increase in σ observed for annealing times up to 30–40 days. The observed decrease in σ for long annealing times can be produced by the decrease of the diffusion rate. Once this diffusion from the SC shields is almost exhausted, further annealing results in the progressive decrease of the total diffused component concentration in the insulation and, consequently, of conductivity.

6.4.2 FTIR measurements

To corroborate the assumption made in the last paragraph in the previous section, Fourier Transform Infrared spectroscopy measurements (FTIR) were performed at different depths in the XLPE insulation of as-received cable and cable annealed up to 93 days at 90ºC. As discussed above (see section 6.1) this technique is well suited to follow XLPE degradation, to detect the presence of cross-linking by-products, as well as to identify acrylate species and other possible components diffused from the SC shields into the XLPE bulk. Measurements were performed in four layers cut from the insulation surface down to 1.2 mm depth (layer 1: XLPE surface in contact with the SC shield, layer 4: XLPE at 1.2 mm depth).

As an example of the obtained spectra, figures 6.17 and 6.18 show the measured curves in layer 2 for different annealing times. No clear presence of acetophenone or cumyl-alcohol peaks (953cm^{-1}, 766cm^{-1}, 700cm^{-1}, 860cm^{-1}, 1170cm^{-1}, 1695cm^{-1}, 1263cm^{-1}, 1360cm^{-1}, 761cm^{-1} and 690cm^{-1}) can be noticed, although we must take into account

some resolution limitations in these measurements. Traces of acrylate species and other components with peaks at 1736cm^{-1} can be noticed in the curves, but they can not be clearly seen, in part because of the proximity to the carbonyl group peak at 1741cm^{-1}, which is related to oxidation processes (see section 6.1 for details and references).

We will focus our analysis of FTIR results on two indexes evaluated to obtain quantitative information on the thermo-oxidative degradation; the carbonyl band at 1741cm^{-1} (aldehyde absorption) and the double band index at 1635cm^{-1} (unsaturated groups). Intensities of both peaks have been evaluated relative to the crystalline XLPE band at 1898cm^{-1}. Possible presence of cross-lining by-products has also been analyzed with the 1305cm^{-1} absorption peak, which Bamji et. al. [35] associates with some contribution of acetophenone groups.Table 6.1, 6.2, 6.3 and 6.4 show the relative intensities of these peaks in the four analyzed layers after different annealing times. As a general trend, for a given layer no evolution in any absorbency peak can be established. This result indicates that oxidation does not take place during annealing at 90 ºC. No trace of acetophenone contribution can be clearly noticed either. If the results for different layers are compared, a slight decrease in the carbonyl and double band indexes with the depth is observed. Figure 6.19 shows the relative absorbency of these two peaks (related to thermo oxidative processes) averaged in the seven measurements performed in each layer. The observed decreasing behavior indicates that oxidation is higher in the external surface of the cable and decreases towards the internal surface. These oxidation processes take place probably during the manufacturing process.

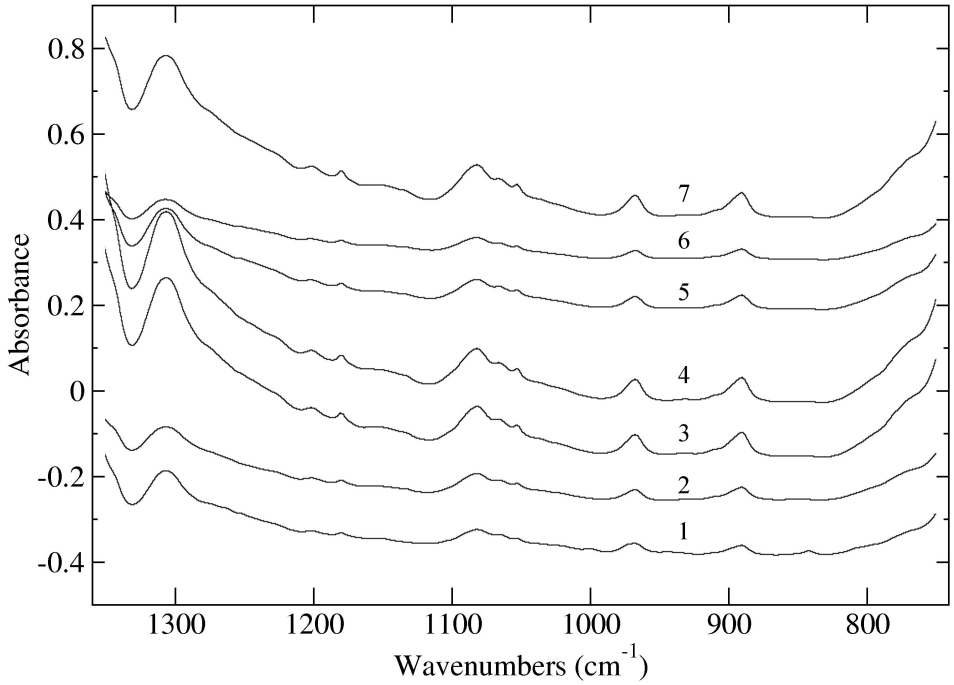

Figure 6.17. FTIR spectra of layer 2 (0.4mm depth) XLPE insulation for different annealing times: (1) as-received; (2) t_a=1 days; (3) t_a=15 days; (4) t_a=30 days; (5) t_a=45 days; (6) t_a=60 days and (7) t_a=90 days.

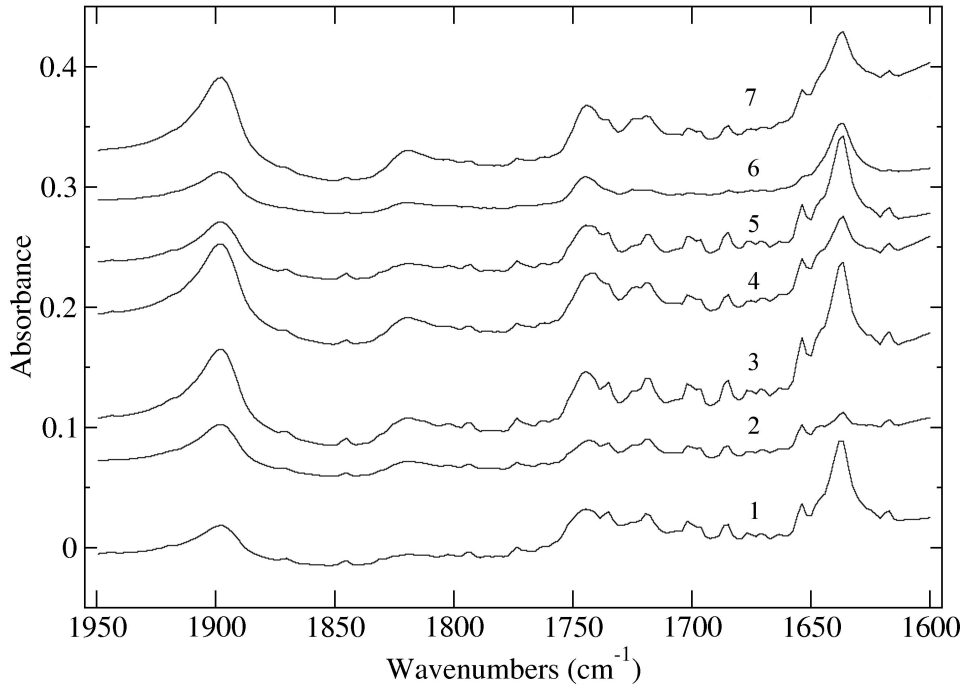

Figure 6.18. FTIR spectra of layer 2 (0.4mm depth) XLPE insulation for different annealing times: (1) as-received; (2) t_a=1 days; (3) t_a=15 days; (4) t_a=30 days; (5) t_a=45 days; (6) t_a=60 days and (7) t_a=90 days.

Sample	Acetophenone Index ($I_{1305/1898}$)	Carbonyl Index ($I_{1741/1898}$)	Double band Index ($I_{1635/1898}$)
As-received	3.16	1.51	5.67
1d at 90ºC	2.20	1.49	4.21
14d at 90ºC	1.22	1.28	2.83
30d at 90ºC	1.31	1.33	2.84
45d at 90ºC	2.11	0.64	1.83
60d at 90ºC	2.01	1.98	3.70
75d at 90ºC	1.50	1.41	3.05
92d at 90ºC	2.32	1.51	3.05

Table 6.1. FTIR indexes. Layer 1 (300μm depth).

Sample	Acetophenone Index ($I_{1305/1898}$)	Carbonyl Index ($I_{1741/1898}$)	Double band Index ($I_{1635/1898}$)
As-received	3.9	0.15	3.77
1d at 90ºC	3.37	0.73	2.53
14d at 90ºC	1.92	0.36	0.54
30d at 90ºC	2.94	0.47	1.25
45d at 90ºC	3.17	0.40	0.64
60d at 90ºC	2.67	0.65	1.91
75d at 90ºC	2.03	0.63	1.67
92d at 90ºC	2.23	0.43	0.75

Table 6.2. FTIR indexes. Layer 2 (600μm depth).

Sample	Acetophenone Index ($I_{1305/1898}$)	Carbonyl Index ($I_{1741/1898}$)	Double band Index ($I_{1635/1898}$)
As-received	3.93	0.05	2.13
1d at 90ºC	2.31	0.33	0.61
14d at 90ºC	2.52	0.43	0.93
30d at 90ºC	2.03	0.42	1.45
45d at 90ºC	1.70	1.55	3.50
60d at 90ºC	2.95	0.41	0.54
75d at 90ºC	1.73	0.48	0.80
92d at 90ºC	3.09	0.30	0.43

Table 6.3. FTIR indexes. Layer 3 (900μm depth).

Sample	Acetophenone Index ($I_{1305/1898}$)	Carbonyl Index ($I_{1741/1898}$)	Double band Index ($I_{1635/1898}$)
As-received	2.25	0.06	0.46
1d at 90ºC	2.04	0.14	0.43
14d at 90ºC	3.55	0.25	0.36
30d at 90ºC	2.48	0.31	0.67
45d at 90ºC	2.35	0.41	0.64
60d at 90ºC	3.24	0.37	0.62
75d at 90ºC	1.67	0.31	0.33
92d at 90ºC	2.40	0.45	0.72

Table 6.4. FTIR indexes. Layer 4 (1200μm depth).

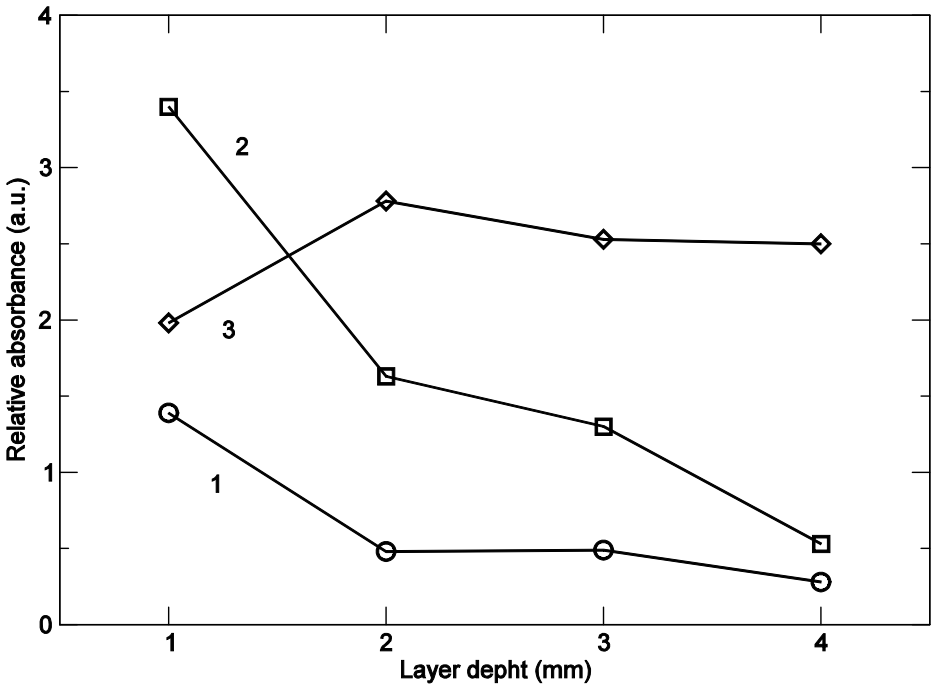

Figure 6.19. Absorbency of (1) carbonyl band (1741cm^{-1}), (2) double band index (1635cm^{-1}) and (3) 1305 cm^{-1} absorption peaks relative to XLPE band at 1898cm^{-1}, averaged in the seven measurements performed in each layer.

6.5 Conclusions

The conductive properties of MV power cables with XLPE insulation have been studied for a range of annealing temperatures that includes the service temperature of power distribution cables (≈90°C). Significant differences have been observed in the behavior of cable samples with SC screens and without them (XLPE cylinders). SC screens

condition very much the electrical behavior of the entire cable. It has been concluded that in order to understand the thermoelectrical aging of power cables, it is necessary to take into account the SC screens in both theoretical and experimental research. Furthermore, research devoted both to understand aging/breakdown processes and to improve insulation quality in MV and HV power cables should be carried out on "complete" cable sections, i.e., including extruded SC layers.

In order to determine the evolution of conductivity with annealing time, some measurements have been performed by using two different methods: absorption/resorption current technique (time domain), and dynamic electrical analysis (frequency domain). Good correlation between results of measurements carried out in both domains (time and frequency) has been obtained, as well as a plausible explanation for them, based on the coexistence of two conduction mechanisms. The first mechanism involves extended states, being slightly dependent on temperature (at least for our temperature interval of interest). The second mechanism operates by carrier hopping between traps at low fields and is thermally assisted. This latter mechanism is only efficient from a certain critical temperature T_c, between 70ºC and 80ºC, due to the increase of defect or impurity concentration associated with diffused components from the SC screens. These defects or impurities may act as trapping centers of charge injected from the electrodes and are responsible for the observed conductivity increase in cable samples with annealing. Dissociation of species present in cable insulation, such as cross-linking by-products, also plays a role in this process. In the case of XLPE cylinders, the second is the only available source of traps. Once this source is exhausted, and taking into account that many of these generated species are volatile, the contribution to the conductivity of the hopping mechanism progressively diminishes until a nearly constant value is attained. In the case of entire cable samples, the diffusion of chemical species from SC screens can maintain the increase in conductivity for longer annealing times.

Diffusion of components from SC screens into XLPE occurs during the manufacturing process, and continuously during annealing at temperatures above 80ºC. However, after 30 days at 90ºC it decreases, and conductivity tends to decrease as well. FTIR results are consistent with this model and refuse the influence of thermo-oxidative processes at this temperature.

References

[1] Lindenmeyer, P. H. and Holland, V. F. *J. Appl. Phys.* **35** (1964), 55.

[2] Phillips, P. J. *IEEE Trans. Electr. Insul*. **13** (1978), 69.

[3] Muccigrosso, J. and Phillips, P. J. *IEEE Trans. Electr. Insul.* **13** (1978), 172.

[4] Cartwright, G. A.; Davies, A. E.; Swingler, S. G. and Vaughan, A. S. *IEEE Proc. Sci. Meas. Tech.* **143** (1996), 26.

[5] Campus, A.; Lafin, B. and Sterzynski, T. *Proceedings of the 6th IEEE ICSD*. Vasteras, Sweden (1998), 357.

[6] Fothergill, J. C.; Montanari, G. C.; Stevens, G. C.; Laurent, C.; Teyssedre, G.; Dissado, L. A.; Nilsson, U. H. and Platbrood, G. *IEEE Trans. Dielectr. Electr. Insul.* **10** (2003), 514.

[7] Wang, X.; Yoshimura, N.; Tu, D.; Tanaka, Y. and Takada, T. *Proceedings of the 1998 International Symposium on Electrical Insulating Materials.* Toyohashi, Japan (1998), 109.

[8] Yahagi, K. *IEEE Trans. Electr. Insul*. **15** 1980, 241.

[9] Dissado L. A. and Fothergill J. C. "Electrical Degradation and Breakdown in Polymers". Peter Peregrinus Ltd. on behalf of the Institution of Electrical Engineers, London, UK (1992).

[10] Marat-Mendes, J. N.; Neagu, R. M. and Neagu, E. R. *J. Phys. D: Appl. Phys.* **37** (2004), 343.

[11] Cavallini, A.; Fabiani, D.; Mazzanti G. and Montanari G. C. *IEEE Trans. Dielectr. Electr. Insul*. **9** (2002), 514.

[12] Cavallini, A.; Fabiani D.; Mazzanti, G.; Montanari, G. C. and Simoni, L. *Conference Record of the 2000 IEEE International Symposium on Electrical Insulation.* Anaheim, USA (2000), 473.

[13] Nothingher, P.; Toureille, A.; Santana, J.; Martinotto, L. and Albertini, M. *IEEE Trans. Dielectr. Electr. Insul*. **8** (2002), 972.

[14] Zebouchi, N.; Hoang, T. G. and Bui, A. *J. Appl. Phys*. **81** (1997), 2363.

[15] Frisch, K. C. and Patsis, A. in “Electrical properties of polymers” Edited by Seanor, D. A. Academic Press, New York, USA (1982). pp. 1–26.

[16] Lampert, M. A. and Mark, P. “Current Injection in Solids”. Academic Press, New York, USA (1970).

[17] Pelissou, S.; St-Onge, H. and Wertheimer, M. R. *IEEE Trans. Electr. Insul.* **23**

(1988), 325.

[18] Chen, G.; Banford, H. M.; Fouracre, R. A. and Tedford D. J. *Proceedings of the 3rd International Conference on Conduction and Breakdown in Solid Dielectrics.* Trondheim, Norway (1989), 277.

[19] Mizutani, T.; Jordan, I. B. *Annual Report of the 1974 Conference on Electrical Insulation and Dielectric Phenomena*. Downington, USA (1974), 640.

[20] Nath, R.; Kaura, T. and Perlman, M. M. *IEEE Trans. Electr. Insul.* ***25*** (1990), 419.

[21] Bambery, K. R.; Fleming, R. J. and Holboll, J. T. *J. Phys. D. Appl. Phys.* **34** (2001), 3071.

[22] Hozumi, N.; Takeda, T.; Suzuki, H. and Okamoto, T. *IEEE Trans. Dielectr. Electr. Insul.* **5** (1998), 82.

[23] Ieda, M. *IEEE Trans. Electr. Insul.* **19** (1984), 162.

[24] Gulmine, J. V. and Akcelrud, L. *Polym. Test.* **25** (2006), 932.

[25] Kim, C.; Jin, Z.; Jiang, P.; Zhu Z. and Wang, G. *Polym. Test*, **25** (2006), 553.

[26] Vatansever, A. and Phillips, P. J. *IEEE Trans. Electr. Insul.* **24** (1989), 1121.

[27] Dalal, S. B. and Gorur, R. S. *IEEE Trans. Dielectr. Electr. Insul.* **12** (2005), 139.

[28] Hermann, H.; Thomas, J. and Stevens, G. *Proceedings of 8th IEEE International Conference on Solid Dielectrics.* Toulouse, France, **2** (2004), 623.

[29] George, G. A.; Celina, M.; Vassallo, A. M. and Cole-Clarke, P. A. *Polym. Degrad. Stab.* **48 (**1995), 199.

[30] Gamez-García, M.; Bartnikas, R. and Wertheimer, M. R. *IEEE Trans. Electr. Insul.,* **25** (1990), 688.

[31] F. Khabbaz, A. C.; Albertsson, A. C. and Karlsson, S. *Polym. Degrad. Stab.* **63** (1999), 127.

[32] Corrales, T.; Catalina, F.; Peinado, C.; Allen, N. S. and Fontan, E. *J. Photochem. Photobio. A Chem.* **147** (2002), 213.

[33] Amyot, N.; Lee, S. Y; Davis E. and Lee, I. H. *Proceedings IEEE Conference on Electrical Insulation and Dielectric. Phenomena.* Victoria, BC, Canada (2000), 743.

[34] Smedberg, A.; Boström, J. O.; Wald, D. and Peters, R. *Proc. of the 2007 Int. Conf. Insul. Power Cables, 7th JICABLE.* Paris-Versailles, France (2007), 280.

[35] Bamji, S. S.; Bulinski, A. T.; Suzuki, H.; Matsuki, M. and Iwata, Z. *J. Appl. Phys.* **74** (1993), 5149.

[36] David, E.; Parpal, J. L. and Crine, J. P. *Conference Record of the 1994 IEEE International Symposium on Electrical Insulation*. Pittsburgh, PA, USA (1994), 170.

[37] Tamayo, I.; Belana, J.; Diego, J.A.; Cañadas, J.C.; Mudarra, M. and Sellarès, J. *J. Polym. Sci. Part B Polym. Phys.* **42** (2004), 4164.

[38] Frutos, F.; Acedo, M.; Radu, I.; Jiménez, A.; Pérez-Gómez, J. A. Filippini, J. C.; and Jadraque, A. *Proceedings of the 7th International Conference on Conduction and Breakdown in Solid Dielectrics.* Eindhoven, Holland (2001), 167.

[39] Werelius, P.; Thärning, P.; Erikson, R.; Holmgren, B. and Gäfvert, U. *IEEE Trans. Diel. Electr. Insul.* **8** (2001), 27.

[40] Hvidsten, S.; Faremo, H.; Benjaminsen, J. T. and Ildstad, E. *CIGRE paper 21–201*. CIGRE, Paris, France (2000), 1.

[41] Frutos, F.; Acedo, M.; Jadraque, A.; Mudarra, M.; Sellarès, J. and Belana, J. *Proceedings of 8th IEEE International Conference on Solid Dielectrics.* Toulouse, France, **1** (2004), 119.

[42] Acedo, M. "Relación entre la degradación del polietileno por arborescencias de agua y las propiedades eléctricas del material. Aplicación al diagnóstico del aislamiento de los cables de distribución de energía". Ph.D. Thesis, Universidad de Sevilla, Sevilla, Spain (2004).

[43] Tamayo, I. "Estudio del comportamiento de la carga de espacio durante la fusión del XLPE en cables de media tensión por TSDC". Ph.D. Thesis. Universitat Politècnica de Catalunya, Terrassa, Spain (2002).

[44] Mott, N. F. and Davis, E. A., "Electronic processes in non-crystalline materials". Clarendon Press, Oxford, UK (1971).

[45] Tamayo, I.; Belana, J.; Cañadas, J. C.; Mudarra, M.; Diego, J. A. and Sellarès, J. *J. Polym. Sci. Part B Polym. Phys.* **41** (2003), 1412.

[46] Hill, R. M. *Philos. Mag.* **23** (1971), 1307.

7. TSDC ANALYSIS OF MV CABLE XLPE INSULATION (I): STUDY OF XLPE RECRYSTALLIZATION EFFECTS IN THE MELTING RANGE OF TEMPERATURES

7.1 Introduction

In previous works, using the TSDC technique, a wide heteropolar peak was observed in the spectra [1]. It is placed between 50 and 110ºC and it has its maximum at about 105ºC. Due to the coincidence between the maximum and the melting point and according to the data available, this peak was attributed to the release of space charge that was trapped in the crystalline fraction although it could also be associated with amorphous-crystalline interfaces (see chapter 3; [1]).

Usually, TSDC curves are related to a relaxation time distribution so the spectra are composed of broad peaks. This problem can be avoided using the so-called windowing polarization method (WP) [2]. Within this technique, the sample is polarized at a fixed temperature (T_p) and, when the sample is cooled, the polarizing field is switched off a few degrees below or even at the same polarization temperature. By this procedure, the TSDC thermogram that is obtained consists of an almost elementary contribution. Moreover, WP allows one to resolve complex relaxations into its elementary components because only polymer chains that regain mobility at temperatures near T_p will contribute to the TSDC discharge [3].

A complex relaxation can be analyzed using WP if a range of polarization temperatures is employed. In this way, the existence of an optimal polarization temperature (T_{po}) can be observed in polar or space charge relaxations [4–6]. Below the T_{po}, increasing the polarization temperature increases chain segment and charge carrier mobilities and the number and depth of available traps, so a higher polarization temperature will yield a more intense peak. Above the T_{po} the effect is the opposite. When even higher polarization temperatures are employed, chain segment mobility or charge carrier energy is too high and results in lower polarization and, therefore, in a less intense peak.

This behavior, however, should not be expected in the case of the XLPE spectra in the melting range of temperatures (50–110ºC according to DSC measurements). During melting there is a decreasing amount of crystalline fraction as temperature increases. If the 105ºC peak is related to the crystalline fraction, it should decrease as the polarization takes place at higher temperatures. Thus, the application of the TSDC/WP technique to XLPE during the melting process should give peaks with decreasing areas as T_p increases, without any T_{po}.

TSDC data coming from XLPE cables presented in this chapter reveal a somewhat more complicated behavior. An optimal polarization temperature T_{po} is observed when the samples are polarized throughout the melting range, which does not agree with the expected behavior. DSC curves reveal as well the existence of recrystallization processes when the sample is annealed within the melting temperature range.

In this chapter, the spectra of XLPE electrets using polarization temperatures between 50 and 110ºC are analyzed. The TSDC technique has been applied to cable samples that have been polarized by WP. Polarization was performed in some experiments heating up the sample to T_p from room temperature (*melting curves*) and in others cooling down

the sample from the melt (*solidification curves*). The analysis of these results in comparison with the expected behavior of the peak allows us to discuss the origin of the 105ºC relaxation.

In this way, the behavior of the TSDC spectra obtained during the melting and the solidification of the sample are interpreted successfully in terms of recrystallization. This leads to a better understanding of the mechanisms that give rise to this relaxation.

7.2 Experimental

The cable samples used in this chapter belong to the cable S type. The as-received cable S design and composition characteristics are described in the section 4.1.

DSC measurements (see section 4.10 for details) were performed in 10mg XLPE samples cut from the cable. The results are presented in Figure 7.1 for the as-received material (reference curve) and show that melting takes place between 50 and 110ºC. The fusion maximum lies at approximately 105ºC. DSC measurements in samples annealed within the melting temperature range show recrystallization processes and are discussed below.

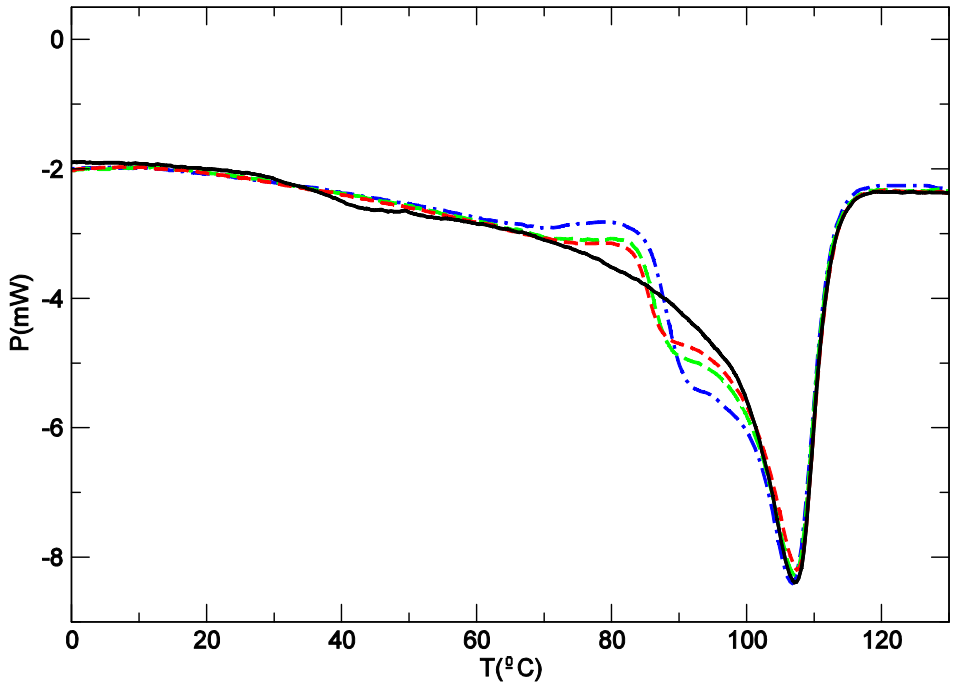

Figure 7.1. DSC curves after annealing at 80ºC for different annealing times: reference (—), 15 min (– – –), 60 min (— —) and 12h (— • —).

The experimental setup for TSDC consists of a Heraeus forced air oven controlled by a Eurotherm 902 PID temperature programmer, a Brandenburg 807R (3–30kV) potential source and a Keithley 6514 electrometer (see section 4.4 for a more detailed description of the TSDC setup and operation).

TSDC experiments were performed using the null width polarization windowing method, a particular case of the WP technique. All the TSDC experiments begin at an initial temperature (T_i), the sample is then heated (or cooled) to the polarization

temperature (T_p) at a rate (v_1). Once the sample is at T_p, the polarizing potential (V_p) is applied after a time t_d. V_p is applied for a poling time (t_p). Once t_p is over, the poling potential is switched off and the sample is cooled at the same rate v_1 until the storage temperature (T_s) is attained. The sample remains at T_s for a short storage time (t_s) and then it is heated at a rate v_2 and the TSDC discharge recorded. To ensure that there is not any influence from thermal history, the sample is discarded after the TSDC current has been recorded. In all the experiments V_p=10kV and v_2=2ºC/min. Unless otherwise stated T_i=35ºC, v_1=2ºC/min, t_d=2.5min, t_p=5min, T_s=50ºC and t_s=5min.

X-ray powder diffraction measurements were performed in a Bragg–Brentano $\theta/2\theta$ Siemens D-500 diffractometer (radius=215.5mm) with Cu Kα radiation, selected by means of a secondary graphite monochromator. The divergence slit was of 0.3º and the receiving slit of 0.05º. The starting and the final 2θ angles were 1.5º and 50º, respectively. The step size was 0.05º and the measuring time of 10s per step.

7.3 Results and discussion

7.3.1 Behavior of TSDC/WP spectra for different T_p during melting and solidification

In the first place, the influence of T_p on the spectra during melting will be studied. Several TSDC/WP experiments were performed using different T_p, which are always in the melting range of temperatures. At the beginning of the experiment, the sample is heated until T_p is attained. In this way, the material is partially molten when the electric field is applied. To avoid influence from thermal history, each measurement is performed on its own, as-received, sample. The results are presented in Figure 7.2. We will refer to these spectra as the *melting* TSDC spectra.

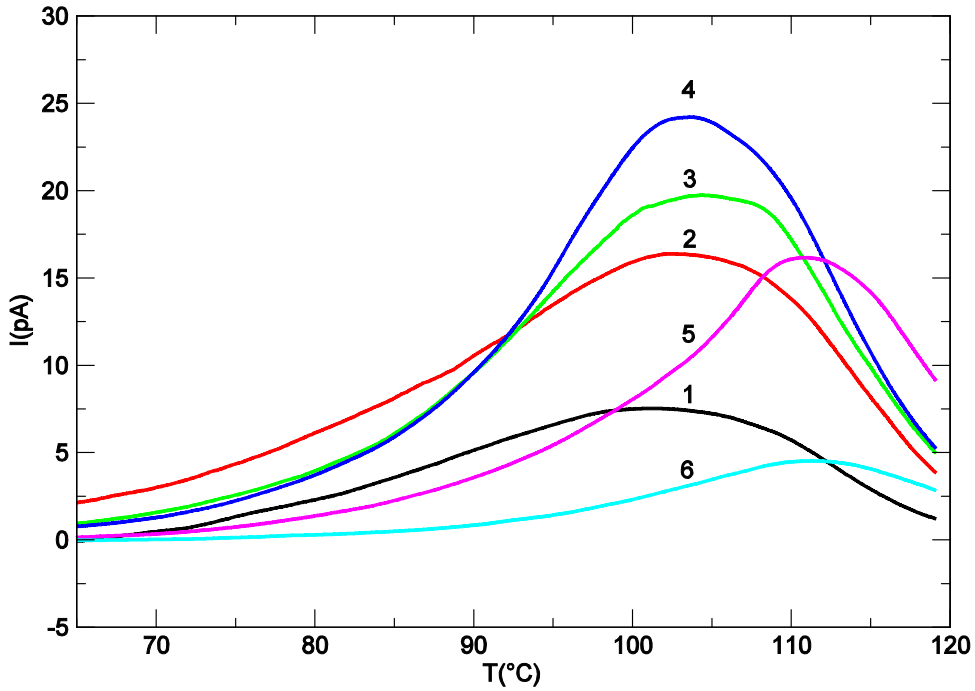

Figure 7.2. TSDC/WP spectra for T_p=55ºC (1), 60ºC (2), 80ºC (3), 90ºC (4), 100ºC (5) and 110ºC (6).

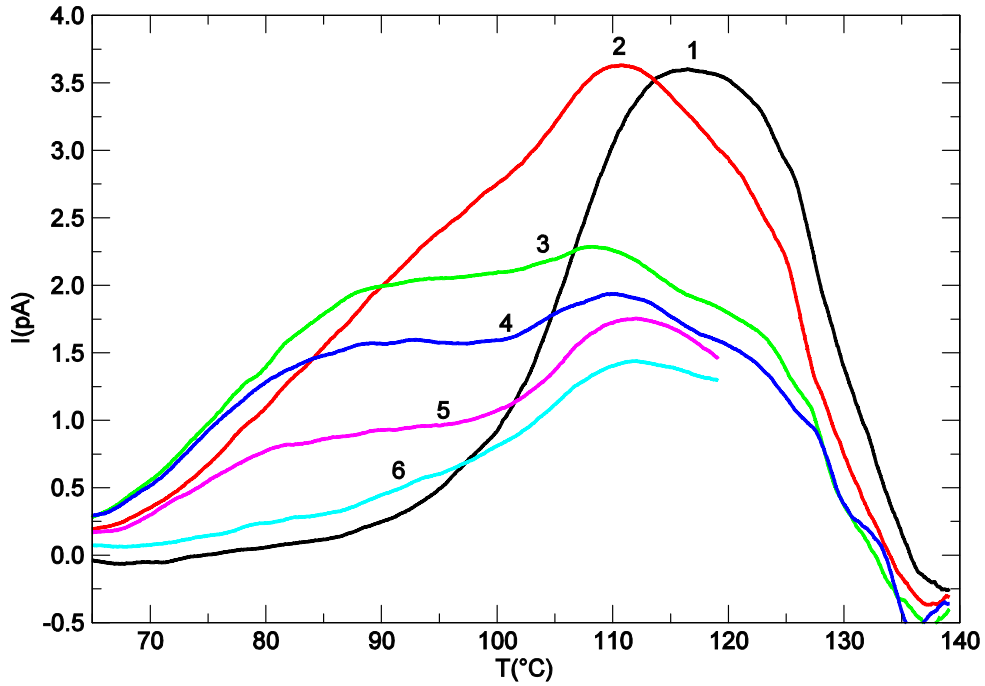

Figure 7.3. TSDC/WP spectra with T_i=140ºC for T_p=105ºC (1), 85ºC (2), 75ºC (3), 70ºC (4), 65ºC (5) and 55ºC (6).

On the other hand, in Figure 7.3 we also present results of TSDC discharges. These ones have been obtained using an initial temperature T_i=140ºC and then cooling the sample until T_p is attained. In this case, the field is applied after the partial solidification of the sample. As in the previous experience, each TSDC/WP experiment has been performed using a new as-received sample. We will refer to these spectra as the *solidification* TSDC spectra. A broad spectrum is obtained in this case, appearing as two overlapped peaks at 80 and 110ºC. The appearance of the peak at 80ºC can be explained by the combination of the heteropolar peak with a homopolar peak between 90 and 100ºC, which appears if samples are annealed at high temperatures (see chapters 5 and 9). In this case, since the samples reached 140ºC, the homopolar mechanism should be activated. The combination of these two phenomena with opposite polarities can result in two heteropolar peaks separated by a minimum (see chapter 9 for more details). Also, a peak at 80ºC has been reported in previous works [1,7], where it was attributed to a Gerson-like polarization.

In both cases, melting and solidification TSDC, the spectra show a T_{po} at approximately 95ºC. As mentioned in the introduction, this behavior is usual in polymer relaxations. Nevertheless it should not be the behavior of the 105ºC relaxation that can be observed in TSDC discharges of XLPE using T_p between 50 and 110ºC. If the sample is polarized at higher temperatures there is a progressively less crystalline fraction, due to melting that takes place in this temperature range. Therefore, the spectra corresponding to the 105ºC relaxation, that is associated with the crystalline fraction, is expected to have less area and to present no T_{po}.

To explain this behavior, that apparently is not consistent with our previous knowledge on the origin of this peak, we have performed some experiments that allow us to interpret it in terms of recrystallization that takes place during the annealing of the sample at the polarization temperature (recrystallization process presents a maximum efficiency at temperatures just below the fusion peak).

The most remarkable feature related to these results is the low intensity obtained in all the curves of Figure 7.3, which is almost ten times lower than the measurements in Figure 7.2. Again recrystallization considerations can explain this fact: calorimetric measurements showed that recrystallization processes are much more important when the material is heated to T_a from room temperature than when it is cooled down to T_a from the melt.

To analyze the effect of annealing at T_p in the recrystallization of the material, some calorimetric and X-ray diffractometry measurements were carried out and are described in the next section.

7.3.2 DSC and X-ray diffractometry measurements

DSC is well suited to the study of melting processes in materials, as all these processes involve heat transfer between the sample and the environment. By this technique it has been possible to detect recrystallization processes in XLPE [8].

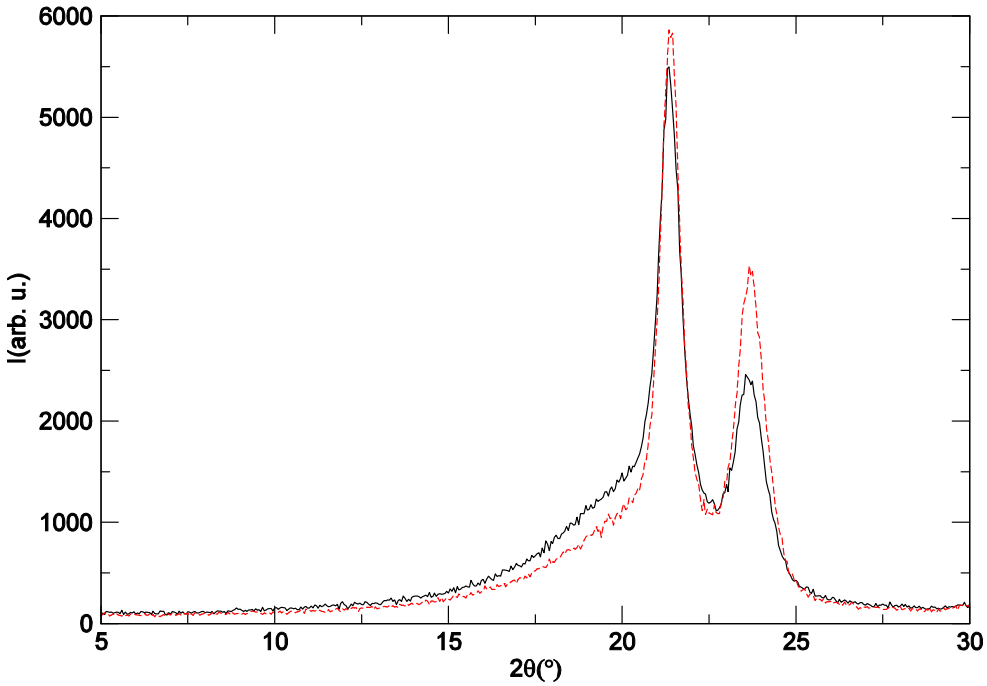

Figure 7.4. X-ray diffraction experiments for an as-received sample (—) and a sample annealed previously for 12h at 80ºC (- - -).

The reference curve in Figure 7.1 shows the thermogram obtained in the melting process of an as-received XLPE sample. We can observe a progressive increase in the transformation rate (directly related to the DSC signal) that has a maximum at 105ºC approximately. When the sample is annealed at T_a=80ºC, the recrystallization of some fraction of the material molten at this temperature, promotes the formation of more stable crystals, which will melt afterwards at higher temperatures. Curves corresponding to these annealed samples show the increase in the fraction of the material that melts above 80ºC (with the corresponding decrease in the fraction that melts below this temperature). We can see in these results as well that the recrystallization rate decreases as annealing time increases. The amount of recrystallization achieved during the first

hour of annealing is roughly the same as that achieved during the next 11h (see Figure 7.1).

In Figure 7.4 the results of X-ray diffractometry are presented. Measurements were performed on two samples. One sample was measured as-received. The other one was previously annealed for 12h at 80ºC. The diffraction peaks that correspond to the annealed sample are sharper than the ones that correspond to the as-received sample. The taller and narrower peaks indicate a more defect-free crystalline structure and/or an increase in the lamellar thickness when the sample has been annealed. This evolution agrees with the presence of recrystallization processes during the annealing at 80ºC and corroborates the obtained calorimetric results.

7.3.3 Influence of annealing previous to polarization

Results presented in section 7.3.1 suggest that the heteropolar response in the TSDC/WP spectrum is mainly influenced by recrystallization of the material during the polarization stage, at temperatures within the melting temperature range. The influence of recrystallization on the polarization can explain the existence of a T_{po} –since recrystallization process presents a maximum efficiency at certain temperatures– and the low intensity obtained in the solidification curves with respect the melting ones. To check this hypothesis, the TSDC spectrum of a sample annealed for 60 min at T_p, previous to polarization, was recorded. In this case, a lower heteropolar response is expected because the recrystallization rate decreases with time. Figure 7.5 shows the results obtained in this case, compared with the spectra of a sample with no previous annealing. The heteropolar peak of the sample with longer annealing is lower than the other one, in good agreement with this hypothesis.

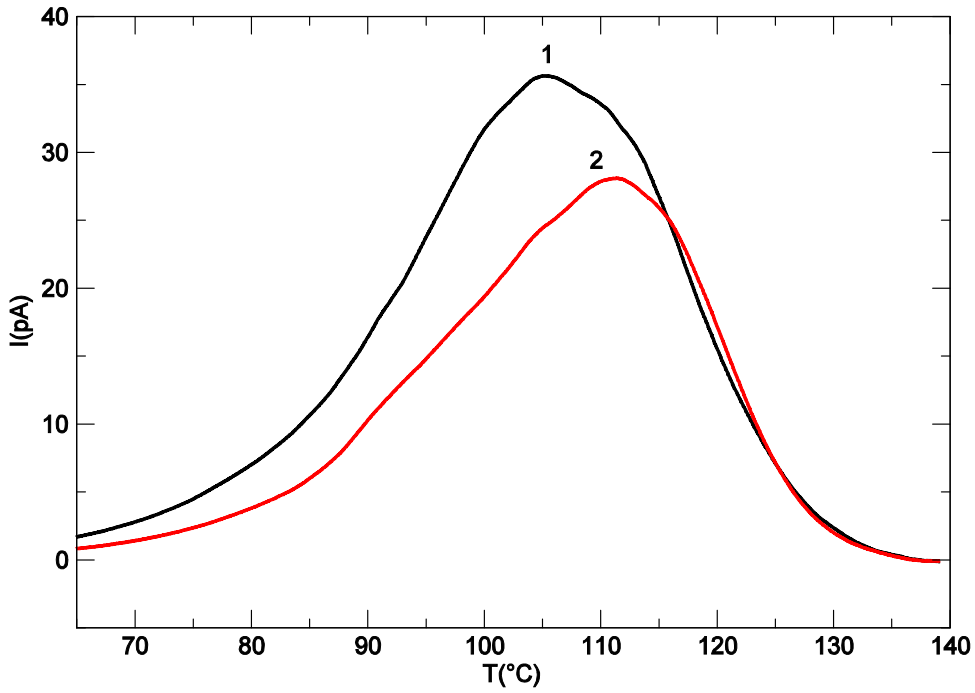

Figure 7.5. TSDC/WP spectra obtained with T_p=80ºC and t_p=60min for t_d=2.5 min (1) and t_d=60min (2).

7.3.4 Effect of the cooling rate

Further evidence supporting the role of crystal formation during polarization in the heteropolar response is presented in Figure 7.6. In this experiment the samples were cooled down from the melt to T_p at different cooling rates (v_1). As v_1 decreases, the crystalline structure of the material is closer to the expected one in isothermal crystallization. On the other hand, for high cooling rates, the crystals will not have as much time to form and during the polarization time there will be a more active recrystallization process. Thus, recrystallization processes during polarization at T_p should be less important if lower v_1 are used. The results presented in Figure 7.6 show the expected decrease in the heteropolar response, in good agreement with model prediction. In this case, a homopolar current at low temperatures in those curves corresponding to the lower cooling rates can be observed as well. This peak was also reported in previous results [1,7,9] and according to chapter 9 is associated with a transient relaxation, which is related to thermal annealing. In section 7.3.1, the presence of this homopolar contribution was also assumed to explain the split of the heteropolar peak into two peaks at 80 and 110ºC. The appearance and increase of a net homopolar current when the cooling rate is reduced can be explained by both, the greater thermal annealing when the rate is low, and the decrease of the 105–110ºC peak.

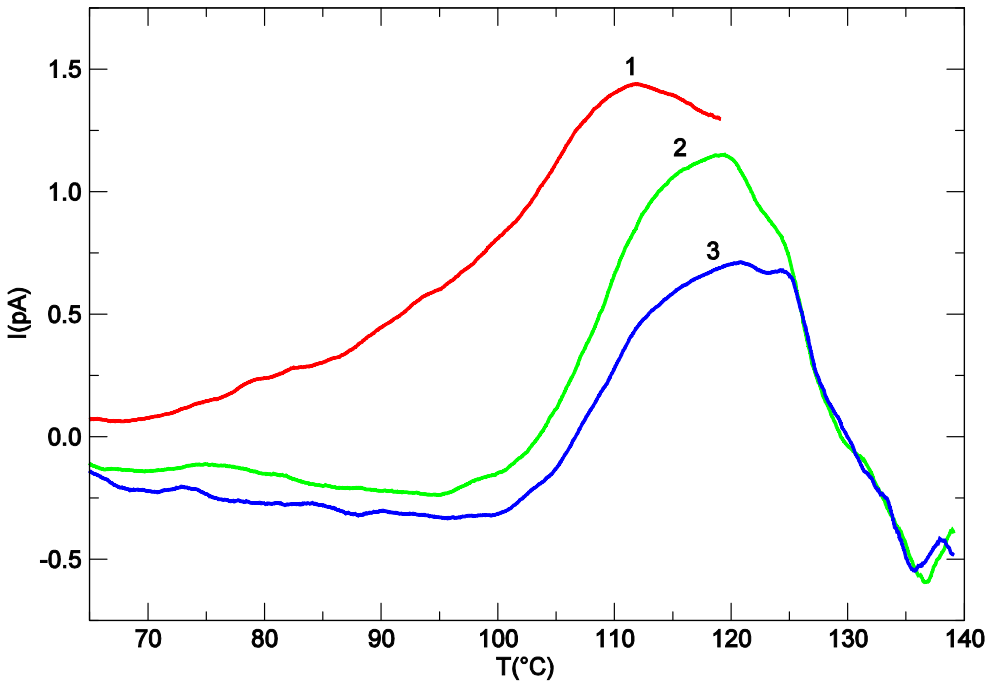

Figure 7.6. TSDC/WP spectra showing the influence of cooling rate with T_i = 140ºC and T_p=55ºC for v_1=2ºC/min (1), 1ºC/min (2) and 0.5ºC/min (3).

7.3.5 Discussion

The results presented in sections 7.3.1, 7.3.2, 7.3.3 and 7.3.4 show that recrystallization plays a fundamental role in the origin of the heteropolar TSDC/WP response of XLPE. However, a point that is not straightforward to interpret is the origin of this current.

This peak could be directly related to charges trapped in the interfaces between the amorphous and the crystalline phase. It could also be due to space charge placed throughout the crystalline fraction and not only in the fraction grown during

recrystallization. Nevertheless, if we assume only these possibilities several contradictions arise. Certainly, the results presented in Figures 7.2 and 7.3 show the presence of an optimal polarization temperature (T_{po}) around 90–95ºC in both the cases. At this temperature an important fraction of the material is molten. As a consequence, less amorphous-crystal interface surface and crystalline fraction are present than at lower temperatures. This fact does not agree with the observed decrease in the depolarization current for T_p below T_{po}. Also, the intensities of the discharge currents are about 10 times smaller when the field is applied during solidification than when it is applied during melting. This fact seems to contradict that the charge of the peak could come just from the amorphous-crystal interface, although the emergence of the transient homopolar contribution associated with a larger annealing also could explain such behavior.

On the one hand, it is known that there can be large amounts of space charge trapped at the surface of crystalline regions [10] and its contribution to the heteropolar 105ºC fusion peak is highly probable (see chapter 9). On the other hand, experimental results discussed in this chapter seem to support that the charge of the 105ºC peak should be explained by also taking into account the new crystalline fraction generated during recrystallization. Thus, we have to consider two contributions to the fusion peak of TSDC/WP discharges. One is the current originated by the recombination of free charges trapped in amorphous-crystalline interfaces when crystals are melting. The other one is related to the melting of the polarized crystalline fraction originated during recrystallization. The first contribution presumably has a decreasing trend with the increase of T_p in WP experiments. The second one rises with temperature as recrystallization becomes more and more effective, and it is dominant for the TSDC/WP method. The combination of the two effects may give rise to the observed behavior.

At this point, the origin of the polarization due to the recrystallization processes should be discussed. In these processes, small fractions of the melted material, at a certain temperature, recrystallize in a more defect-free and stable crystal. The recrystallization is promoted by the annealing of the sample, within the melting temperature range, during polarization at T_p. It is much more important when the material is heated to T_p from room temperature than when it is cooled down from the melt, which could explain that intensities in Figure 7.3 are lower than those shown in Figure 7.2. This new crystalline fraction grows in a polarized state due to the applied electric field and develops a depolarization current when it melts during the TSDC measurement.

The analysis of the effect of the annealing previous to polarization also supports that recrystallization plays a fundamental role in the TSDC response (Figure 7.5). We can see in this figure that if we perform a previous annealing on the sample (at the polarization temperature) for one hour before polarization, the peak intensity decreases. This fact is clearly in agreement with the assumption that recrystallization is the cause of the observed effect. During the annealing previous to polarization, recrystallization has taken place actively but the crystals were grown from non-polarized material since the polarizing field was not applied. After the first hour, the recrystallization rate has decreased notably and the total amount of polarized crystalline phase formed is smaller. The resulting polarization turns out to be not so high.

Although PE is not a polar polymer the cross-linking of the material for cable manufacturing could explain the polar behavior that follows from the previous model.

The XLPE material studied is cross-linked during the extrusion process by the addition of di-t-butyl peroxide. Although the cable is subjected to temperatures around 200ºC to promote cross-linking, according to the manufacturing process, it can be assumed that around 20% of the cross-linking reaction is not completed.

In the cross-linking process a peroxide ion is attached to the polymer chain and is used to bind to another chain. Once the bond has been made the ion is released. Nevertheless some ions may remain attached to polymer chains if they could not complete the process. These ions would be located at the polymer chains providing them with some dipolar moment. If recrystallization takes place under an applied field, crystals grow from polarized layers that will give rise to a crystal polarized in its whole volume. A stable polarization should be obtained by this process, as the material will only depolarize when the polarized new crystalline fraction melts.

Another possible explanation of the origin of polarization in the crystalline fraction grown during recrystallization can arise from the free charge present in the material. Space charge in the inter-lamellar regions will move when a polarizing electric field is applied. The result is, probably, microscopic displacement of space charges limited mainly by the presence of crystalline interfaces. Also, during polarization there is a free charge injection from electrodes. Some of the injected charges are trapped in the amorphous-crystalline interfaces (see chapter 9; [10]). If recrystallization takes place during the poling stage, some of these displaced or injected charges could end up inside the newly grown crystalline fraction, due to the rearrangement of crystalline interfaces.

7.4 Conclusions

In this chapter we have analyzed the behavior of TSDC/WP spectra of as-received XLPE cable samples for several polarization temperatures in the melting temperature range, by either heating the material from room temperature to T_p (melting curves) or cooling down from the melt (solidification curves).

TSDC/WP results show a heteropolar peak between 50 and 110ºC, with a maximum at 105ºC. These measurements reveal that there is an optimal polarization temperature (T_{po}) around 90–95ºC. This behavior indicates that the observed peak is not directly related to the total crystalline fraction as in this case one would expect a monotonic decrease in the TSDC response with increasing polarization temperatures.

On the other hand, DSC and X-ray diffractometry results show that recrystallization processes exist when the sample is annealed in the melting range of temperatures. During these processes, the recrystallization of some fraction of the material, partially molten at this temperature, promotes the formation of more stable and defect-free crystals. The results indicate that the recrystallization rate decreases with annealing time and that it is more important if the sample is heated from room temperature to T_p than if it is cooled down from the melt.

The observed TSDC response is explained in terms of the formation of a new crystalline phase by recrystallization during the polarization stage. This new crystalline fraction grows in a polarized state due to the applied electric field and develops a depolarization current when it melts during the TSDC measurement.

Two experiments have been performed to confirm this hypothesis. In one of them, a sample has been annealed at 80ºC previously to polarization. The obtained heteropolar peak is lower than the case with no previous annealing. In the other one, several cooling rates have been employed. It has been found that the higher is the rate, the larger is the heteropolar response. Both results agree with the aforementioned hypothesis.

However, free charge located in amorphous-crystalline interfaces also has to be taken into account in agreement with observations. The assumption made consists in considering both the interfacial charge and the crystalline fraction polarized due to recrystallization as responsible of the 105ºC peak, although the second contribution is dominant in the case of the TSDC/WP method.

References

[1] Tamayo, I.; Belana, J.; Cañadas, J. C.; Mudarra, M.; Diego, J. A. and Sellarès, J. *J. Polym. Sci. Part B: Polym. Phys.* **41** (2003), 1412.

[2] Zielinski, M. and Kryszewski, M. *Phys. Status Solidi*. **42** (1977), 305.

[3] Chen, R. and Kirsh, Y. "Analysis of Thermally Stimulated Processes". Pergamon, Oxford, UK, 1st edition (1981).

[4] Belana, J. Colomer, P. Pujal, M. and Montserrat, S. *An. Fís. B.* **81 (**1985), 136.

[5] Belana, J.; Mudarra, M.; Calaf, J.; Cañadas, J. C. and Menéndez, E. *IEEE Trans. Electr. Insul*. **28** (1993), 287.

[6] Belana, J.; Mudarra, M.; Colomer, P. and Latour, M. *J. Mater. Sci.* **30** (1995), 5241.

[7] Tamayo, I.; Belana, J.; Diego, J. A.; Cañadas, J. C. Mudarra, M. and Sellarès, J. *J. Polym. Sci.Part B: Polym. Phys.* **42** (2004), 4164.

[8] Peterlin, A. and Roeckl, E. *J. Appl. Phys.* **34 (**1963), 102.

[9] Tamayo, I. "Estudio del comportamiento de la carga de espacio durante la fusión del XLPE en cables de media tensión por TSDC". Ph.D. Thesis. Universitat Politècnica de Catalunya, Terrassa, Spain (2002).

[10] Ye-Wen, Z.; Ji-Xiao, L.; Fei-Hu, Z.; Zong-Ren, P.; Chang-Shun, W. and Zhong-Fu, X. *Chinese Phys. Lett*. **19** (2002), 1191.

8. COMBINED TSDC AND IDC ANALYSIS OF MV CABLE XLPE INSULATION: IDENTIFICATION OF DIPOLAR RELAXATIONS IN DIELECTRIC SPECTRA

8.1 Introduction

TSDC are particularly useful to study overlapping relaxations since its high resolution allows to distinguish between relaxations with close relaxation times. This is what happens in the case of XLPE, where a large number of relaxations can be identified in the TSDC spectrum [1]. Unfortunately, some problems arise during the study of XLPE cables by TSDC that makes it difficult to analyze the resulting spectra.

In first place, TSDC spectra of XLPE insulation are strongly dependent on thermal history [1]. Its effects can be minimized by performing each experiment on its own as-received sample.

Another problem is that cables are unusually thick compared with more commonly used samples. Since there is a practical limit on the applied voltage that experimental setups can supply, usually only relatively low electric fields can be used to pole them. The space charge or dipolar character of a relaxation can be determined studying how the polarization of the sample is related to the poling field [2] but in the low electric field limit space charge and dipolar relaxations behave in a similar way. As a consequence, this kind of analysis is not able to give conclusive results in this case.

A way to overcome this difficulty is to employ a complementary technique to obtain information that can lead to the identification of one or several peaks. In this chapter we consider isothermal depolarization currents (IDC) as a complementary technique. There are several reasons that make this approach compelling. In first place, both techniques measure essentially the same physical effect, displacement current, so correlation between data obtained using both techniques is straightforward [3].

Moreover, in theory we can distinguish between three types of current in IDC data, which are presented in a log-log plot in Figure 8.1. In Section 8.3.1 we will discuss the physical causes of each of these currents, give the expressions that they follow and discuss its range of validity. This theoretical distinction of different IDC can provide information about TSDC spectra, if a relation between isothermal and thermally stimulated relaxations is established.

Of course, in practice it could be difficult to distinguish between these three types of current since a meaningful log-log plot may require much more decades of data than the available ones.

Combining TSDC and IDC we expect to confirm previous assumptions about relaxations found in the TSDC spectrum of MV XLPE cables (see chapters 5), and to demonstrate how the correlation of TSDC with IDC data can improve our understanding of relaxation mechanisms in situations where the usual analysis of TSDC data can be difficult, or even impossible, to carry out.

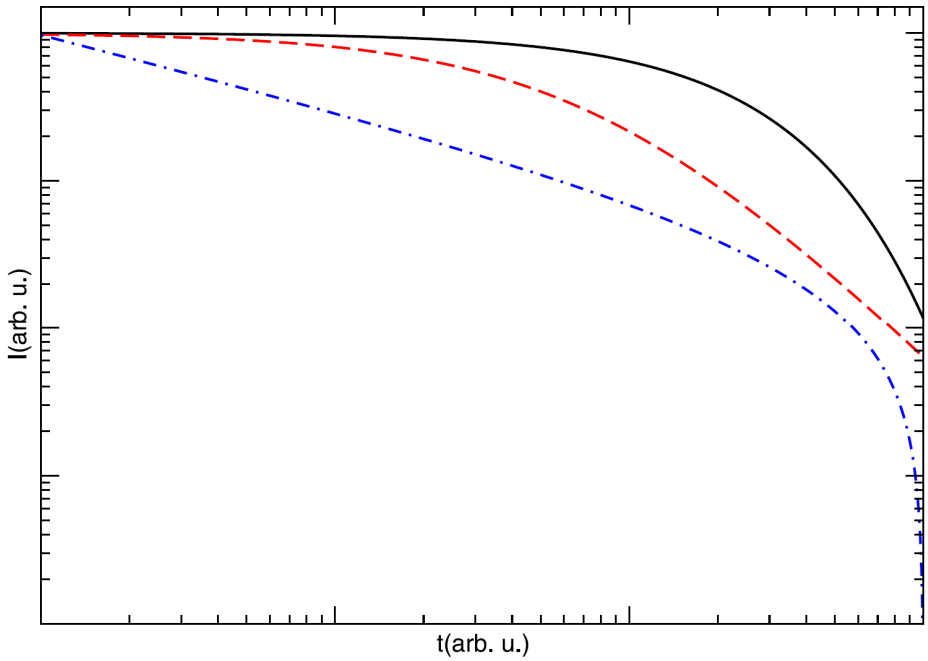

Figure 8.1. Log-log plot of three types of currents: (—) exponential; (— —) inverse square; (— • —) power.

8.2 Experimental

The samples used in this chapter belong to the cable S type. Cable was provided by General Cable from a single cable reel manufactured industrially. In this way, it was assured that the composition and the manufacturing process was the same for all the samples. The as-received cable S design and composition characteristics are described in section 4.1.

To make the sample, the cable was cut into 20cm long sections and, then, a 2cm long section of insulating and semiconducting layers was removed from one end. The external layer was partially removed from the ends of the samples, leaving an 8cm wide semiconducting strip centered in the sample. More details about the structure of the sample and the connection with the electrodes can be found in section 4.4. The average mass of cable samples was 135g. The capacity of cable samples at 5 kHz and 25ºC, measured with an HP 4192A LF impedance analyzer, was 27pF.

The general description of IDC and TSDC experimental setups and their operation can be found in chapter 4. The IDC setup consists of a Köttermann 2715 forced air oven controlled by a Eurotherm 818P PID temperature programmer, a Brandenburg 807R (3–30kV) potential source and a Keithley 6514 electrometer. The employed TSDC setup differs only in that it uses a Heraeus forced air oven and a Keithley 616 electrometer. In fact, both setups can be used either for IDC or TSDC

IDC measurements were performed at several temperatures (T_p) between 90 and 110ºC in 2ºC steps. The poling time (t_p) was 1800s and the discharge current was recorded for 2400s.

The effects of thermal expansion at the different temperatures need not be taken into account because it has been checked that the difference between the external diameter

of the XLPE insulation at 90ºC (24.8mm) and 110ºC (25.0mm) is about 1%. Once cooled, the external diameter does not return to its original value but to 24.6mm, in both cases. It has also been checked that due to annealing the change in mass is less than 1g and the change in capacity (5 kHz, 25ºC) is less than 1pF, in both cases.

TSDC/NIW spectra were obtained by cooling down from 140ºC (T_p) with a 12kV applied voltage until 40ºC (ΔT=100ºC), and, after 5 min (t_s), heating up to 140ºC again. Samples were poled without an isothermal poling stage so t_a=t_p=0. The heating or cooling rate of all the ramps was 2ºC/min.

The measurement conditions remained fairly constant throughout the experiments, with a room temperature around 25ºC.

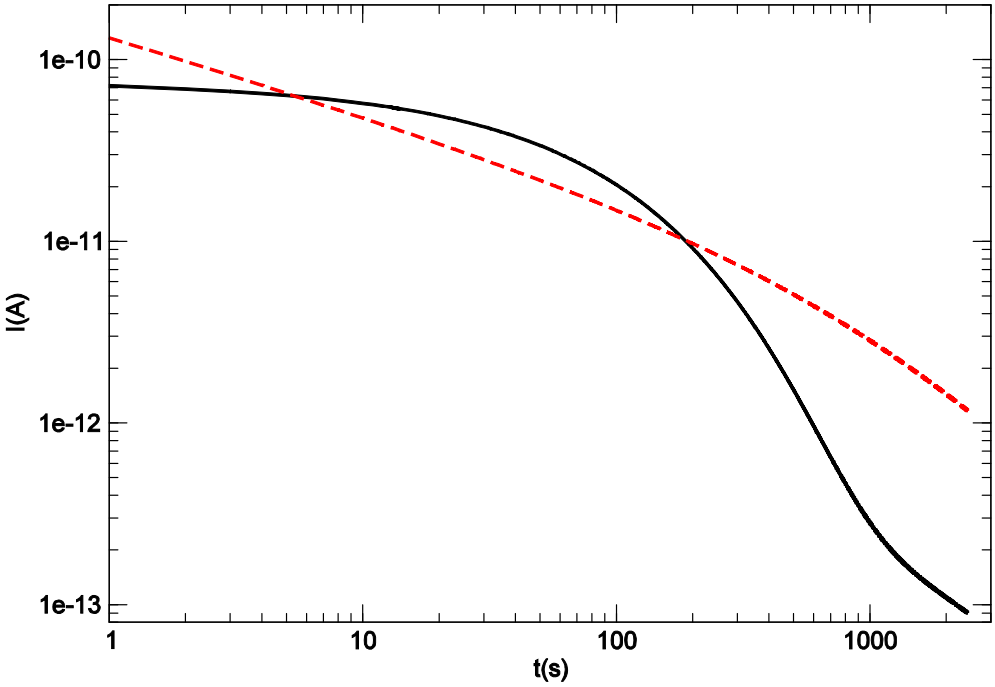

Figure 8.2. IDC curve for T_p=104ºC, t_p=1800s and V_p=10kV in a log-log diagram: (—) experimental; (— —) power law fit.

Figure 8.2 presents an example of IDC experimental data. The best power law [4] fit is also plotted. The fit was very unsatisfactory and therefore it was necessary to consider other possibilities. Adding an exponential term to the power term was revealed as the best way to overcome this problem, as seen in Figure 8.3. The details will be given in the next section. However, to ensure that the effect that was measured had its origin on the dielectric properties of the cable insulation several previous experiments were performed.

An experiment was performed with a guard ring to ensure that the effect was not due to a superficial current. The exponential current was not affected.

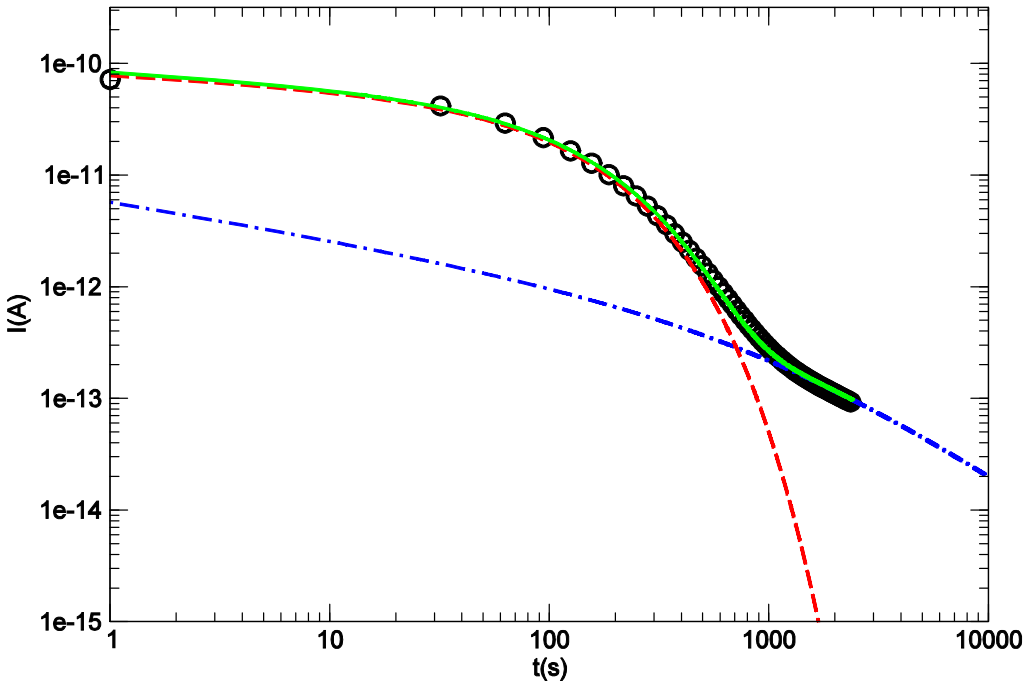

Figure 8.3. IDC curve for T_p=104ºC, t_p=1800s and V_p=10kV in a log-log diagram; (—) theoretical fit; (— —) KWW component; (— • —) power law component.

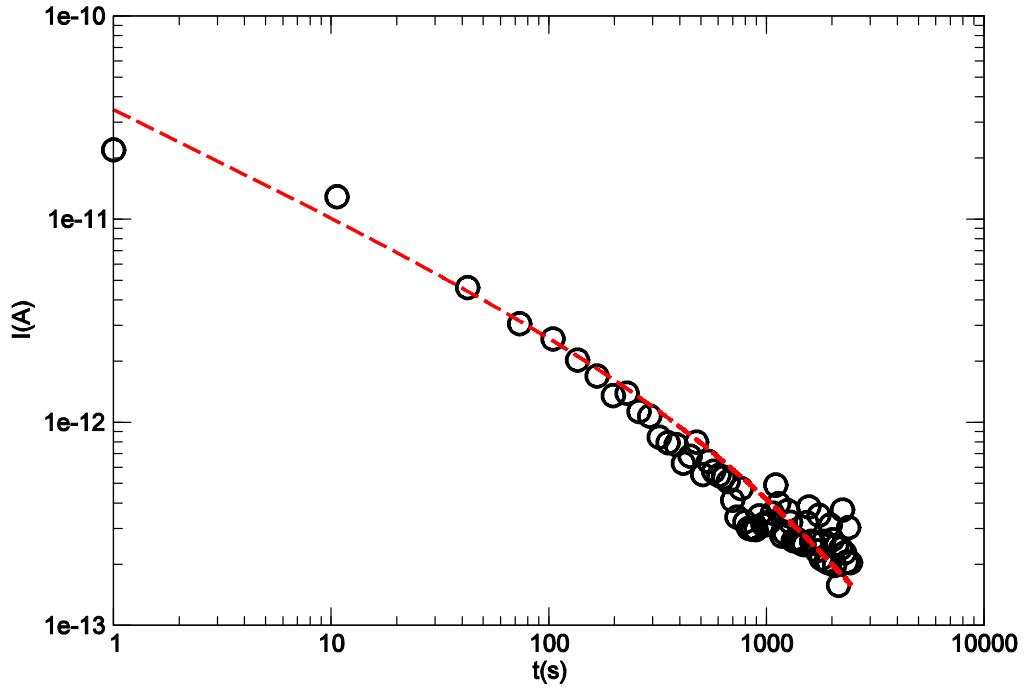

Figure 8.4. IDC curve for a 2×2cm XLPE sample 160μm thick with T_p=92ºC, t_p=1800s and V_p=1kV in a log-log diagram; (— —) power law fit.

Next, IDC measurements were performed on 2×2cm samples with thickness 160μm, at 92ºC and poling with a 1kV electric potential. Samples were obtained using a lathe with a special cut tool to convert the XLPE insulating layer into a roll and circular aluminum electrodes of 1cm of diameter were vacuum deposited at the center of both sides of the samples. The data obtained did not show exponential behavior (Figure 8.4). Then, the question we had to answer was which one of these three elements was the cause of the exponential current: size, cylindrical shape or electrodes (semiconductors).

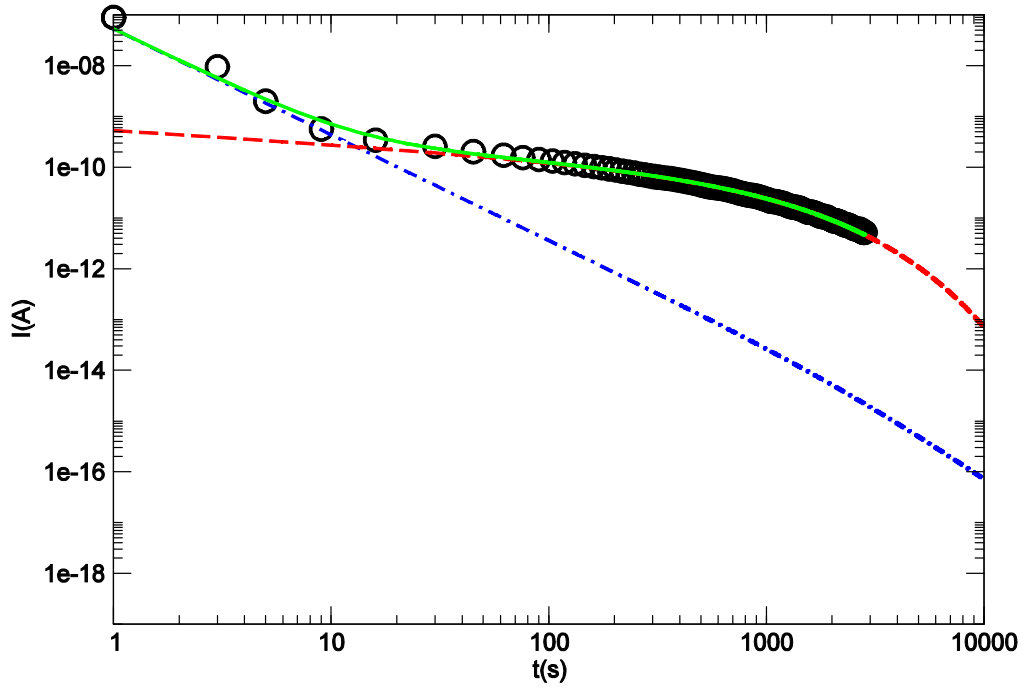

Figure 8.5. IDC curve for a cable sample without external semiconducting layer with T_p=92ºC, t_p=1800s and V_p=10kV in a log-log diagram; (—) theoretical fit; (— —) KWW component; (— • —) power law component.

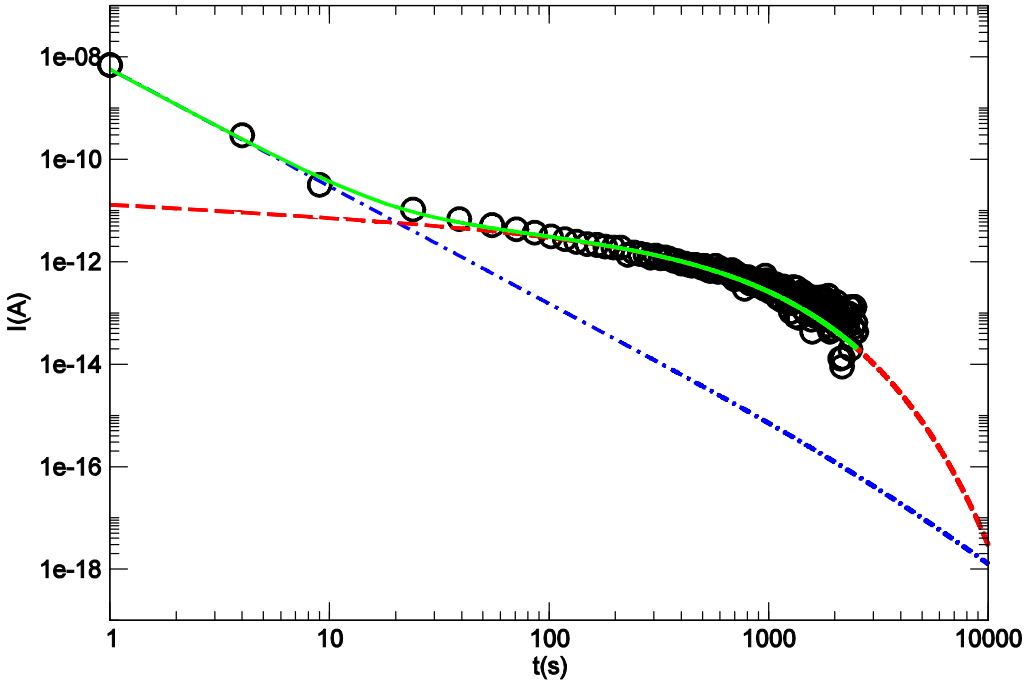

Figure 8.6. IDC curve for a cable sample without inner semiconducting layer with T_p=92ºC, t_p=1800s and V_p=10kV in a log-log diagram; (—) theoretical fit; (— —) KWW component; (— • —) power law component.

To address this question, we performed IDC measurements at 92ºC with a 10kV electric potential, in first place with a cable from which we had removed the external semiconducting layer (Figure 8.5). Then, we did the same with another sample without the inner one, removing the core by traction and the semiconducting layer with a drill (Figure 8.6). Finally, we removed both semiconducting layers from a cable sample and we repeated the same experiment (Figure 8.7). The curves that were recorded show the

exponential relaxation in all three cases. It is also present in the curve obtained for a cable sample without semiconductors when a field with the opposite polarity was applied (Figure 8.8).

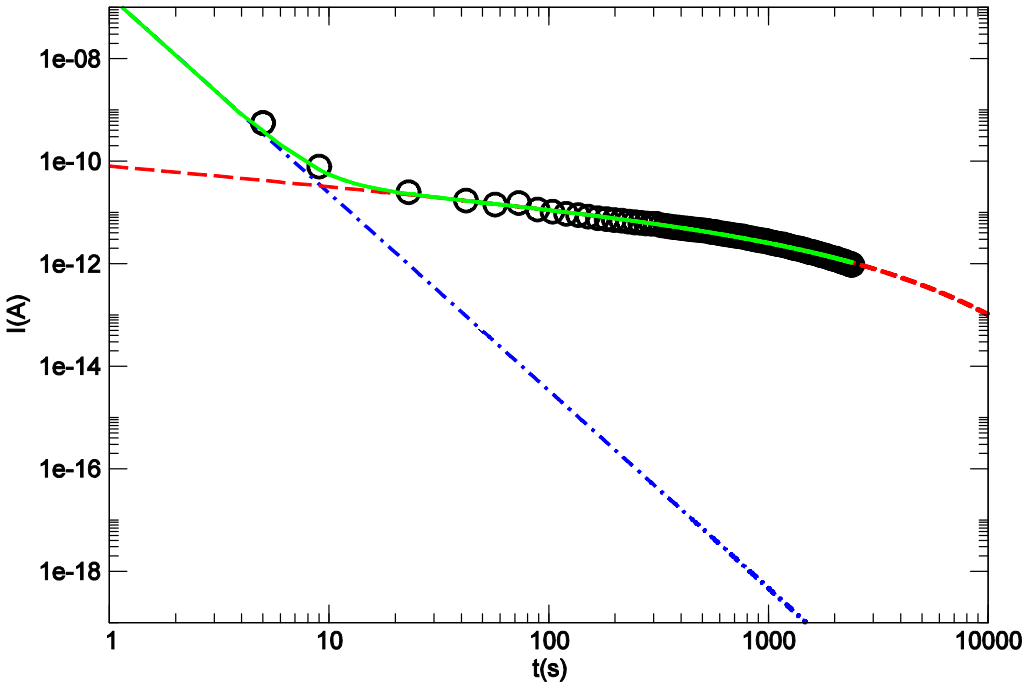

Figure 8.7. IDC curve for a cable sample with no semiconducting layers with T_p=92ºC, t_p=1800s and V_p=10kV in a log-log diagram; (—) theoretical fit; (— —) KWW component; (— • —) power law component.

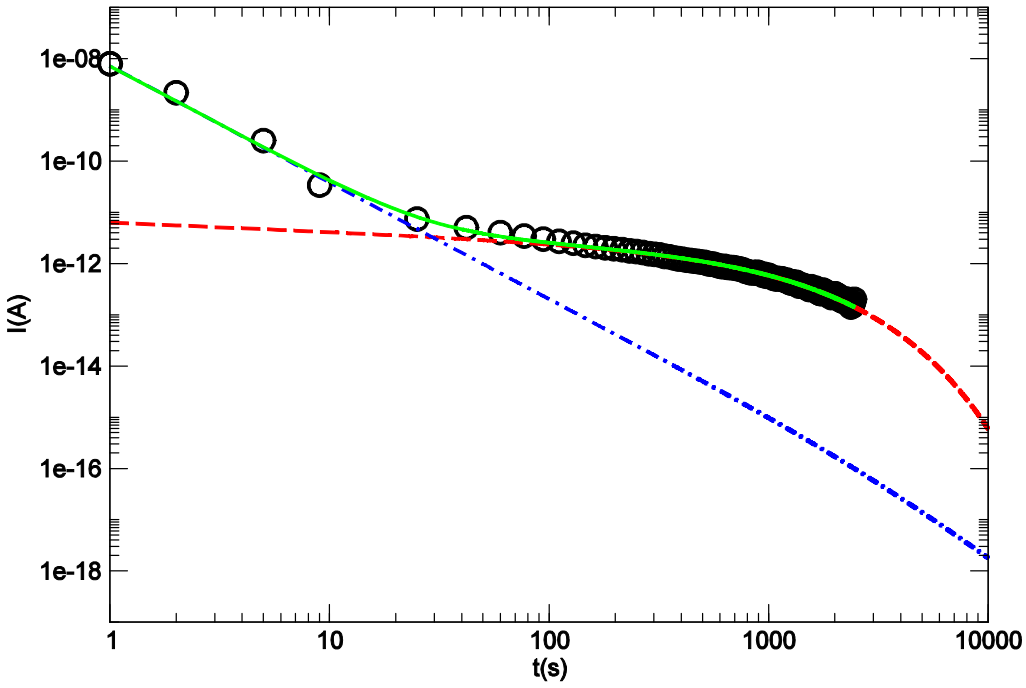

Figure 8.8. IDC curve for a cable sample with no semiconducting layers with T_p=92ºC, t_p=1800s and an opposite polarity with a voltage of V_p=10kV in a log-log diagram; (—) theoretical fit; (— —) KWW component; (— • —) power law component.

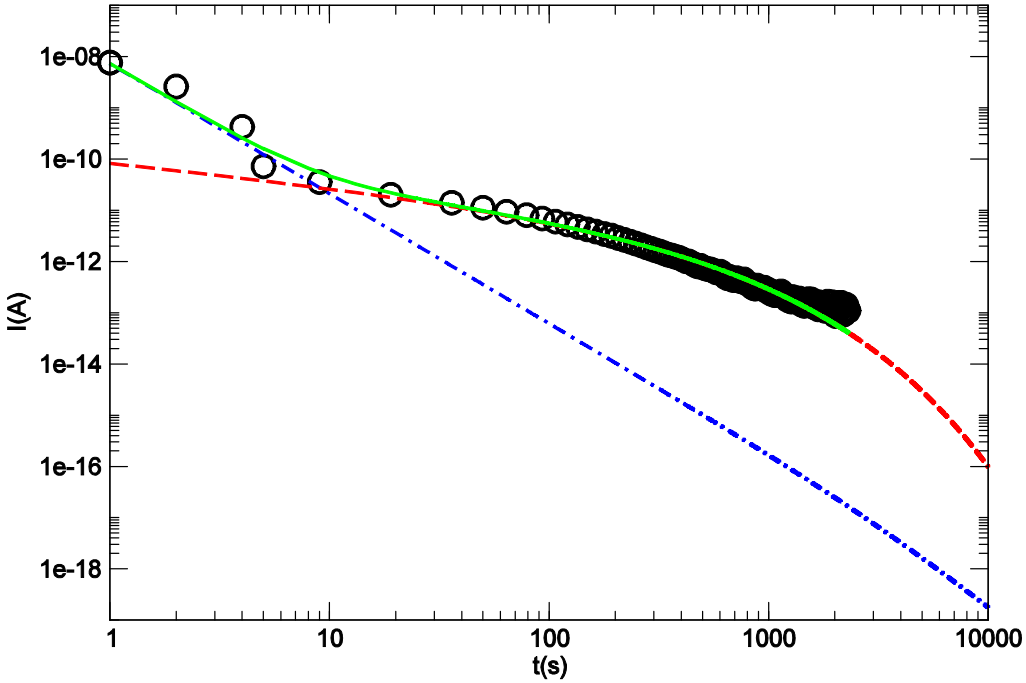

Figure 8.9. IDC curve for a cuboid-shaped sample of 4.5×4.5×50mm with T_p=104ºC, t_p=1800s and F_p=2.2kV/mm in a log-log diagram; (—) theoretical fit; (— —) KWW component; (— • —) power law component.

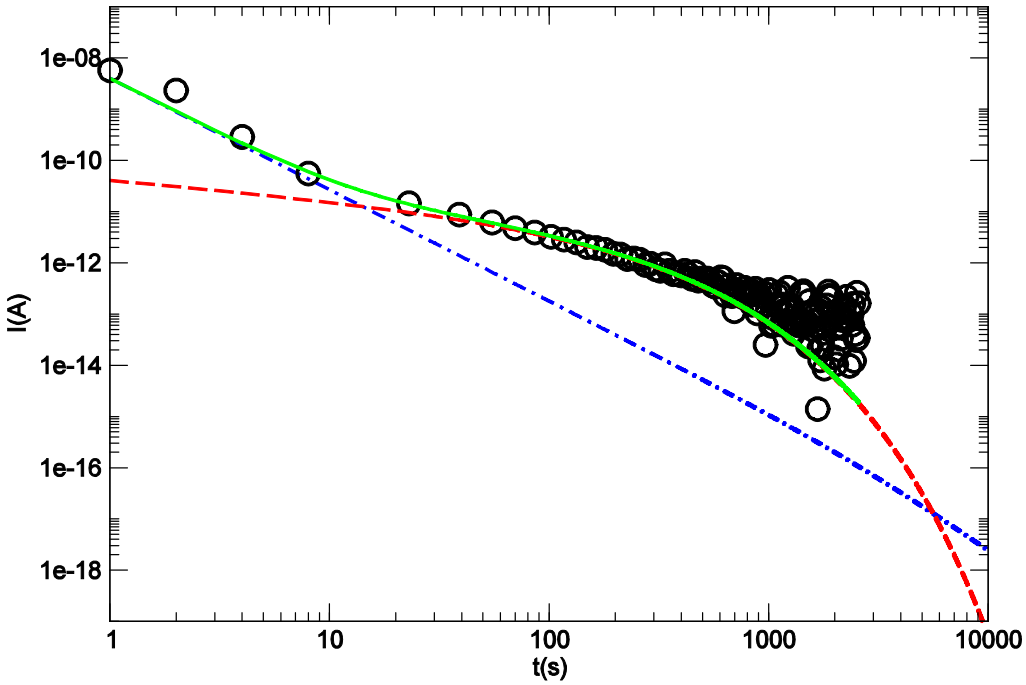

Figure 8.10. IDC curve for a 2×2cm XLPE sample 2mm thick with T_p=92ºC, t_p=1800s and F_p=2.2kV/mm in a log-log diagram; (—) theoretical fit; (— —) KWW component; (— • —) power law component.

Once we discarded the influence of any semiconductor layer we had to consider the effect of cylindrical shape. To this end, we cut from the XLPE insulation a cuboid-shaped sample of 4.5×4.5×50mm and vacuum deposited two electrodes on opposite faces of 4.5×50mm. By performing measurements in the same conditions than in the previous tests, we found the existence of the exponential relaxation again (Figure 8.9). Consequently, the size turned out to be the determining factor for the appearance of

such phenomenon. This was finally corroborated by performing a measurement with a 2×2cm sample with thickness 2mm. Unlike the response of 16mm thick samples, in this case the exponential relaxation was detected (Figure 8.10), although not very pronounced. In these experiences a field of 2.2kV/mm was applied by modulating the voltage proportionally to the thickness.

8.3 Results and discussion

8.3.1 General equations

As a first approximation, we can assume that polarization is a first-order process, described by

$$\frac{dP}{dt} = \frac{P_{eq} - P}{\tau}. \tag{8.1}$$

In the case of depolarization P_{eq}=0 and equation (8.1) becomes

$$\frac{dP}{dt} = -\frac{P}{\tau}. \tag{8.2}$$

The solution of this equation can be written as

$$P(t) = P_0 \phi[z(t)], \tag{8.3}$$

in terms of the reduced time

$$z(t) \equiv \int_0^t \frac{dt}{\tau} \tag{8.4}$$

and the dielectric decay function

$$\phi(t) \equiv \exp(-x). \tag{8.5}$$

The displacement current density is defined as

$$J = -\frac{dP}{dt}. \tag{8.6}$$

It can also be written in terms of the reduced time and the dielectric decay function, as

$$J = -P_0 \phi'(z) \frac{dz}{dt} = -P_0 \frac{\phi'(z)}{\tau}, \tag{8.7}$$

where in the last equality we have substituted the derivative of *z(t)* by its expression. From equation (8.5) we have that

$$\phi'(t) = -\exp(-x) \tag{8.8}$$

and therefore

$$J = P_0 \frac{\exp(-z)}{\tau}, \tag{8.9}$$

which is the first-order displacement current density.

The previous equations describe an exponential relaxation. They can be modified to describe the so-called stretched exponential behavior represented by the Kohlrausch-Williams-Watts (KWW) model. Within this model, equation (8.9) is generalized replacing the dielectric decay function given by equation (8.5) by a more general expression

$$\phi_\beta(t) \equiv \exp\left(-x^\beta\right) \tag{8.10}$$

where β>0. Although in its origin KWW was introduced as an empirical improvement to existing models, nowadays it is usually interpreted as a way to take into account a distribution of relaxation times [5]. In the case β=1 we fall back into the proper exponential relaxation described by equation (8.5). We will refer to any of these relaxations as exponential because the shape of the current curve is similar but we will use the KWW model in all the fits since it provides a more accurate description of the current.

The derivative of the dielectric decay function becomes

$$\phi'_\beta(t) = -\beta x^{\beta-1} \exp\left(-x^\beta\right) \tag{8.11}$$

and, as a consequence, the KWW displacement current density is

$$J = P_0 \beta z^{\beta-1} \frac{\exp\left(-z^\beta\right)}{\tau}. \tag{8.12}$$

We can now apply equation (8.12) to two interesting cases: isothermal depolarization currents (IDC) and thermally stimulated depolarization currents (TSDC). In the first case we can safely assume that τ does not change with time, since this is the behavior predicted by the Arrhenius or the WLF models. This leads to a great simplification of equation (8.4) for the IDC case

$$z(t) = \frac{t}{\tau}. \tag{8.13}$$

Substituting in equation (8.12) we obtain

$$J(t) = P_0 \beta \frac{t^{\beta-1}}{\tau^\beta} \exp\left[-\left(\frac{t}{\tau}\right)^\beta\right] \tag{8.14}$$

This is the stretched exponential current, or, simply, exponential current. In a log-log plot it has only a horizontal asymptote for short times.

In fact, we can expect that the IDC has also a free charge component that we denote as power current [4,6]

$$J(t) = Ct^{\alpha}\left[1-\left(\frac{t_p}{t}+1\right)^{\alpha}\right] \tag{8.15}$$

where α<0. In a log-log plot it appears with two asymptotes. For short times it approximates to an oblique asymptote whereas for long times it tends to a vertical asymptote.

Therefore we will fit the IDC to

$$J(t) = Ct^{\alpha}\left[1-\left(\frac{t_p}{t}+1\right)^{\alpha}\right] + Dt^{\beta-1}\exp\left[-\left(\frac{t}{\tau}\right)^{\beta}\right]. \tag{8.16}$$

Since intensity is proportional to density current, provided the area of the electrode, we can fit intensity curves using this expression.

The second case is somewhat more complicated because depolarization takes place during a heating ramp. Assuming a constant heating rate ν, temperature will be given by

$$T(t) = T_d + \nu t\,. \tag{8.17}$$

Since it is usual to plot *J* in terms of *T*, we express *z* as a function of temperature

$$z(T) \equiv \frac{1}{\nu}\int_{T_d}^{T}\frac{dT}{\tau(T)} \tag{8.18}$$

so we can compare the experimental plot to [7]

$$J(T) = P_0\exp\left\{-z^{\beta}(T) + \ln\left[\frac{\beta}{\tau(T)}z^{\beta-1}(T)\right]\right\}. \tag{8.19}$$

As in the previous case $I(T)\propto J(T)$ and the expression can be applied to intensity curves.

Among the possible causes of a power law discharge current are dipole depolarization, Maxwell-Wagner-Sillars relaxation, electrode polarization or recombination of trapped space charge [6].

Exponential current is often due to depolarization of molecular dipoles but it can also be due to recombination of trapped space charge, that is taken out of its traps by thermal excitation, when there is no probability of retrapping [8]. In fact, recombination without retrapping happens when the displacement of space charge during polarization has been

so small that trapped charges act like small dipoles, sometimes called *Gerson dipoles* [9].

Therefore we will attribute exponential current to dipolar relaxation, including under this denomination depolarization of molecular dipoles and recombination of Gerson dipoles.

When there is a strong probability of retrapping, the recombination of trapped space charge must be modeled as a higher-order process [10]. We can obtain the IDC current from the depolarization, given by

$$\frac{dP}{dt} = -\frac{P^n}{\tau} \tag{8.20}$$

where τ can no longer be interpreted as a relaxation time. The solution of this equation assuming that τ is constant (isothermal depolarization) is

$$P(t) = \left[P_0^{1-n} - (1-n)\frac{t}{\tau} \right]^{\frac{1}{1-n}} \tag{8.21}$$

and

$$J(t) = \left[J_0^{\frac{1-n}{n}} - (1-n)\frac{t}{\tau^{1/n}} \right]^{\frac{n}{1-n}} \tag{8.22}$$

A current arising from trapped space charge recombination with a high retrapping probability, would correspond to the case $n=2$

$$J(t) = \left[J_0^{-\frac{1}{2}} + \frac{t}{\tau^{1/2}} \right]^{-2} . \tag{8.23}$$

We will refer to such a current as inverse square current. Its log-log plot tends to a horizontal asymptote for short times and to an oblique asymptote for long times. In fact, this kind of current is often modeled better using an empirical value for *n* between 1 and 2, which would indicate an intermediate case between no retrapping and strong retrapping probability. Such empirical value would replace the 2 in the exponent for a higher integer. Nevertheless, the shape of the current would be the same so we will refer anyway to any current of this kind as inverse square current.

It should be emphasized that the inverse square and the exponential cases imply a narrow distribution of relaxation times. When there is a broad distribution of relaxation times, either space charge or dipoles can yield a power current.

8.3.2 As-received samples characterization

8.3.2.1 Data analysis

In Figure 8.11 five experimental curves are presented, together with the result of their fit. These curves represent well the behavior shown by the eleven isothermal experiments performed between 90ºC and 110ºC.

These temperature limits have been chosen because below 90ºC the exponential relaxation is hardly noticeable. On the other hand, above 110ºC homopolar currents appear making it very difficult to analyze the experiments. More or less, this temperature range coincides with the fusion peak studied by DSC that begins at 90ºC and has a maximum at 110ºC. Incidentally, this temperature range also includes the operating temperature of the cables.

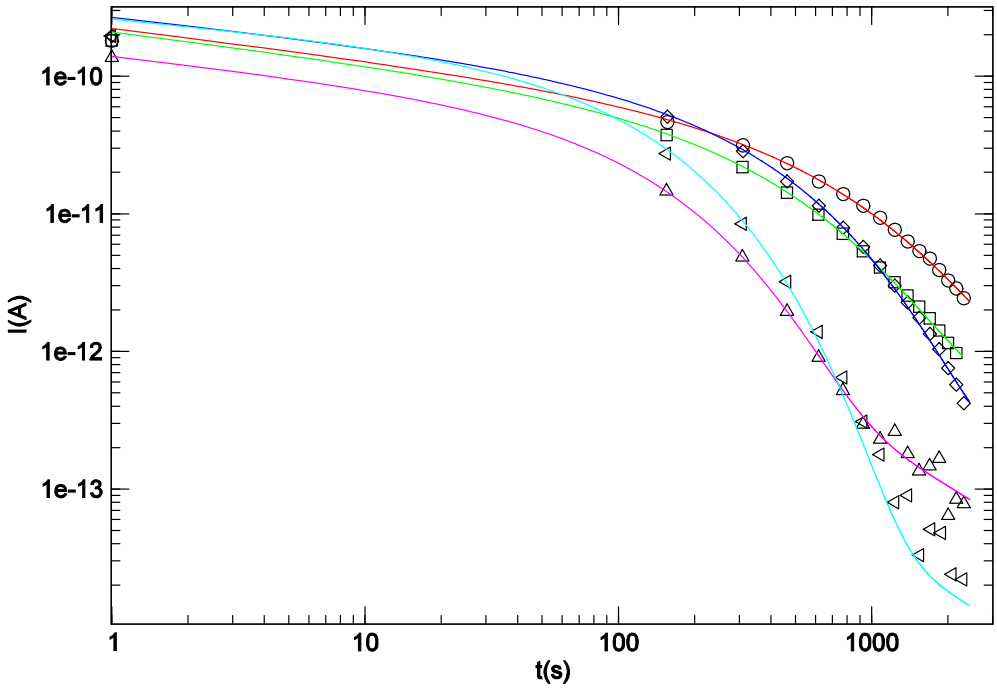

Figure 8.11. IDC curves and theoretical fits in a log-log diagram for t_p=1800s, V_p=10kV and T_p: ○ 92ºC; ◊ 96ºC; □ 100ºC; △ 104ºC; ◁ 108ºC.

It is very difficult to establish the exact nature of the power current. In fact, it could also be an inverse square current since it is not easy to register enough decades of data to distinguish between both types of current. A plausible explanation is that it is due to electrode polarization. It is very hard to find electrodes that are completely transparent to current. Therefore a certain amount of charge is probably retained at the electrodes. Its depolarization can give rise to the observed power current. Recombination of trapped space charge is also possible, especially if it is due to disappearance of traps due to the melting of the material.

Nevertheless, the task of determining the exact nature of the process that yields this current is a very difficult one [11]. Moreover, it does not matter for the aim of this chapter, because we are focused only on currents that can cause one of the observed TSDC peaks of an as-received sample, and this is not the case for the power current.

The exponential relaxation shows the typical behavior of a thermally activated process. For lower temperatures it shows up later. As a consequence, at low temperatures the power current determines the IDC response for short times while the exponential current is the responsible of the larger time response. Instead, at higher temperatures the opposite interplay between currents occurs, as it can be seen in Figure 8.11.

The numeric result of all the fits is presented in Table 8.1. The values of C tend to diminish with increasing temperatures while D remains more or less constant. The parameter α that characterizes the power current changes as a consequence of structural change, most probably the fusion of the material. Instead, the parameter β does not change significantly throughout all the experiments. This can be interpreted as a sign that the exponential current is not related to XLPE itself but to some other component incorporated at the manufacturing process. Anyway, we will assume that β does not depend on temperature and we will take it as a characteristic parameter of the relaxation.

T(ºC)	C(A)	α	β	D(A)	τ(s)
90	1.01×10^{-10}	−1.29	0.82	8.66×10^{-11}	7.59×10^{2}
92	4.12×10^{-11}	−0.09	0.77	2.02×10^{-10}	5.29×10^{2}
94	1.56×10^{-11}	−0.15	0.84	1.71×10^{-10}	3.37×10^{2}
96	2.35×10^{-11}	−0.12	0.77	1.95×10^{-10}	3.10×10^{2}
98	6.33×10^{-12}	−0.13	0.78	2.11×10^{-10}	3.07×10^{2}
100	1.43×10^{-11}	−0.30	0.79	2.78×10^{-10}	2.81×10^{2}
102	8.98×10^{-12}	−0.14	0.80	2.87×10^{-10}	1.84×10^{2}
104	6.41×10^{-12}	−0.30	0.88	7.90×10^{-11}	1.19×10^{2}
106	2.46×10^{-11}	−0.41	0.76	2.12×10^{-10}	1.12×10^{2}
108	3.20×10^{-12}	−0.48	0.83	2.90×10^{-10}	1.02×10^{2}
110	3.56×10^{-12}	−0.46	0.87	2.55×10^{-10}	7.01×10^{1}

Table 8.1. Fit results of the IDC curves for as-received samples.

We can assume that the behavior of the τ parameter in Table 8.1 follows Arrhenius law

$$\tau = \tau_0 \exp\left(\frac{E_a}{kT}\right) \tag{8.24}$$

as it can be seen in Figure 8.12. The linear regression plotted in this figure reads $ln(\tau) = -35.7+1.53\times10^4/T$, this is, $\tau_0=3.29\times10^{-16}$s and $E_a=1.32$eV.

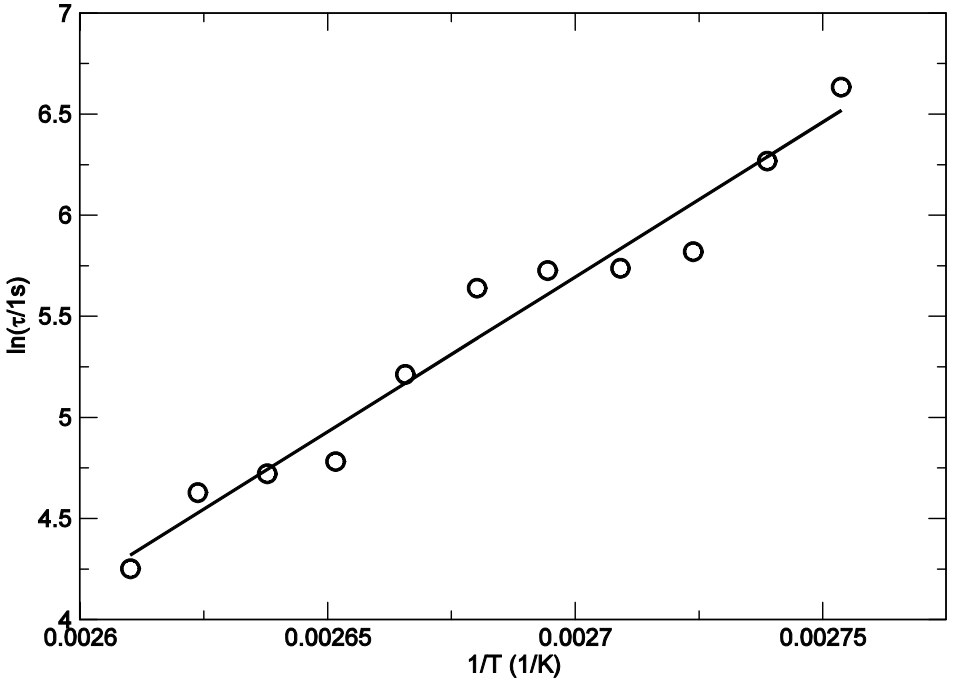

Figure 8.12. Arrhenius plot: (○) relaxation time versus T^{-1}, (—) linear regression.

8.3.2.2 Discussion

It has been observed that, aside from the usual power current, IDC experiments show an exponential current that can be fitted successfully to a KWW model. Through these fits, a relaxation time for the exponential current can be obtained for each IDC experiment. The KWW parameter itself seems to be constant, allowing a great simplification of the data analysis. As a consequence, the exponential current can be described in terms of three parameters: E_a, τ_0 and β.

Equation (8.19) can be employed to predict the shape of the TSDC current in terms of the obtained parameters. Of course, we will obtain just one of the many peaks present in the TSDC spectrum but if we compare the calculated current with the experimental spectrum we can identify the TSDC peak that corresponds to the exponential current found by IDC.

This comparison can be seen in Figure 8.13. We can see that the predicted KWW peak fits rather well to the main peak of the TSDC spectra of an as-received sample, placed at 368K (95ºC). A 3K shift towards lower temperatures has been applied to the predicted curve to obtain a better concordance. This difference can be due to a temperature gradient inside the oven or, simply, to uncertainty in the fit results. As usual in most relaxation models, the KWW model tends to underestimate the amount of current before

the maximum of the peak. Other than these two disparities, the agreement between both peaks is noticeable.

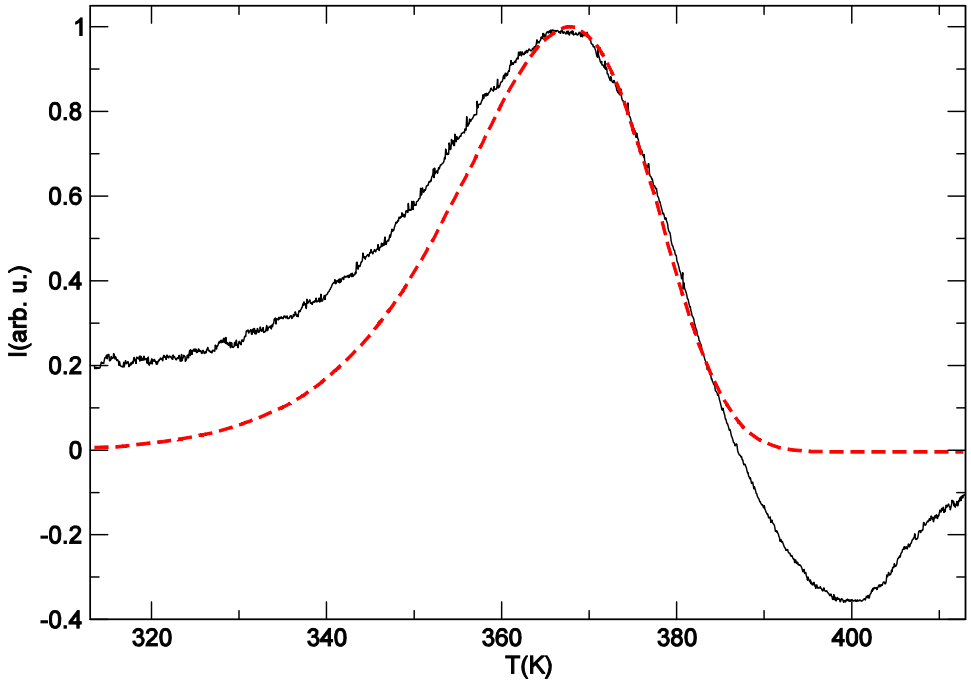

Figure 8.13. (—) TSDC curve for T_p=140ºC, T_s=40ºC, t_s=5 min and v=2ºC/min; (— —) simulated TSDC from equation (8.19) and for E_a=1.32eV, τ_0=3.29×10^{16}s and β=0.8.

Taking this into account, we state that the IDC exponential current and the 95ºC TSDC peak are due to the same physical cause. We will discuss in the following lines which could be that cause. The most probable origin of the exponential current is polarization of molecular dipoles in the cable bulk. We have seen that usually dipolar currents adopt an exponential form, whenever the distribution of relaxation times has a narrow shape.

The shape of the current is also compatible with recombination of Gerson dipoles, but, since the material is partially molten, it does not seem feasible that there exists a stable trap structure that could give a well-behaved exponential current with constant parameters in relation to temperature.

Although PE is a non-polar polymer, the cross-linking of the material for cable manufacturing could result in the existence of dipolar molecules. In the cross-linking process a peroxide ion is attached to the polymer chain and it is used to bind to another chain. Once the bond has been made the ion is released. Nevertheless some ions may remain attached to polymer chains if they could not complete the process. These ions would be located at the polymer chains providing them with some dipolar moment. Also, dipolar current can come from additives present in the bulk of the cable, either introduced during the manufacturing process (traces of reticulant, antioxidant...) or generated when high temperatures are reached (impurities diffused from SC shields, dissociation of by-products).

To check these hypotheses, several TSDC experiments have been performed on the same cable sample. The spectra are plotted in Figure 8.14. It can be seen that after the first experiment the peak at 95ºC disappears. Even though the subsequent spectra keep

changing, the peak does not show up again. The most likely cause of the peak is, therefore, some additive or by-product that does not stand a single heating ramp until 140ºC.

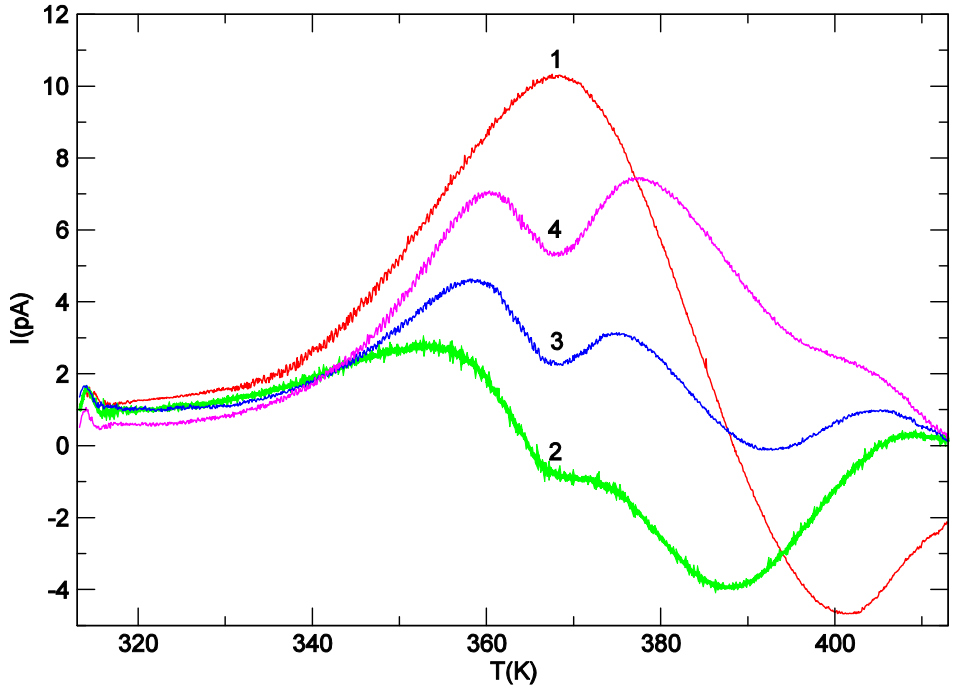

Figure 8.14. TSDC curves for T_p=140ºC, T_s=40ºC, t_s=5min and v=2ºC/min. The experience number with the sample is given next to the curve.

On the other hand, we discard from previous experiments described in section 8.2 that the current comes from the semiconductor layers. Moreover, since these layers are conductive to a certain degree it is not probable that a large electric field builds inside these layers during polarization.

Finally, the fact that the exponential relaxation is not noticed in thin film samples suggests that the intensity of the power current is proportional to the surface. Thus, in samples with a high surface-to-volume ratio the exponential current would be masked by the power current. As explained previously, it is not our goal to dilucidate the origin of the power current but we will point out that proportionality to the surface is to be expected if it comes from electrode polarization, just to mention one possible cause.

8.3.3 Annealed samples characterization

8.3.3.1 Data analysis

It has been shown that the TSDC spectra change with the annealing at high temperatures. In order to apply the IDC technique to identify and to analyze the TSDC peaks obtained for aged cables, several samples were annealed at 140ºC for 3 hours. The obtained IDC curves presented a significant initial discharge within the first 10s, not detected in as-received samples (Figure 8.15).

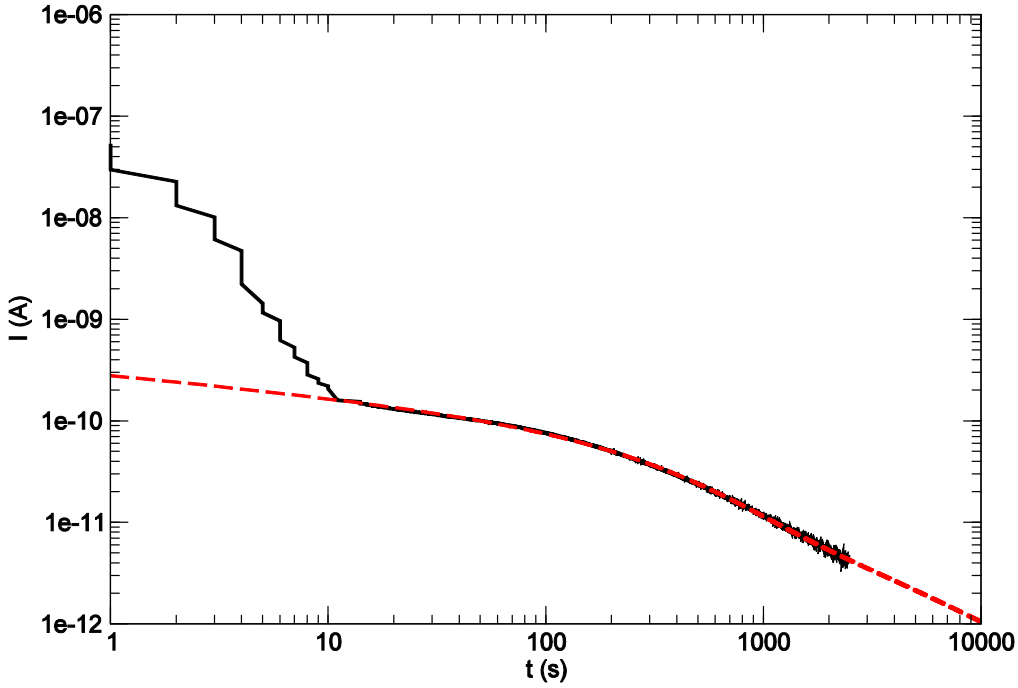

Figure 8.15. IDC curve for a sample annealed 3h at 140ºC with T_p=90ºC, t_p=1800s and V_p=10kV in a log-log diagram: (—) experimental; (— —) theoretical fit.

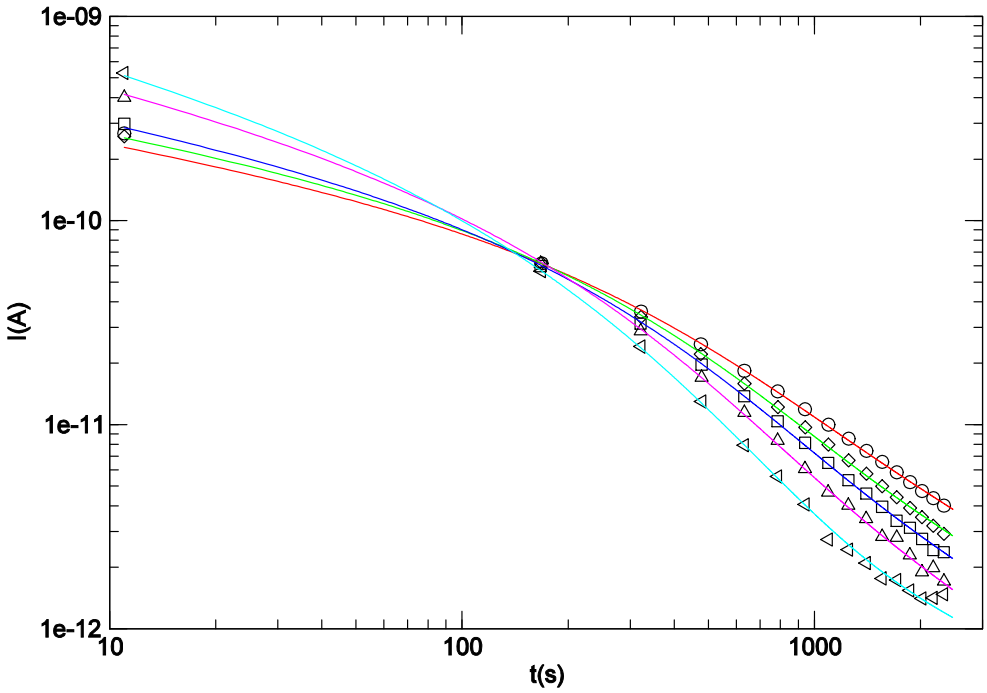

Figure 8.16. IDC curves and theoretical fits in a log-log diagram for samples annealed 3h at 140ºC, with t_p=1800s, V_p=10kV and T_p: ○ 92ºC; ◊ 96ºC; □ 100ºC; △ 104ºC; ◁ 108ºC.

This phenomenon could be easily explained by considering the increase of the space charge stored near the electrodes with annealing (see chapter 9; Figure 9.5). It was also checked by PEA that the space charge accumulated close to the electrodes decays very fast when the poling field is removed. The detected increase in the initial depolarization current present in the annealed samples is, therefore, consistent with the observed

increase of the stored space charge. This change in the discharge behavior involves another current component which makes the equation 8.16 not suitable for fitting the experimental data. A satisfactory procedure was to fit the experimental curve starting from ten seconds and thus avoiding the first slope (Figure 8.15). By using this method, the experimental IDC curves for annealed samples at temperatures placed between 90 and 110ºC, in 2ºC steps, were successfully fitted. In Figure 8.16 some of these fittings can be observed.

8.3.3.2 Discussion

The parameters obtained from the fittings are shown in the Table 8.2. It can be seen that β is not longer constant but decreases as the temperature increases. This means that the distribution of relaxation times in the exponential current now depends on the structural elements that change as the material melts.

T(ºC)	C(A)	α	β	D(A)	τ(s)
90	1.70×10^{-10}	−0.15	0.80	1.67×10^{-10}	2.89×10^{2}
92	2.34×10^{-10}	−0.28	0.74	2.87×10^{-10}	2.29×10^{2}
94	1.85×10^{-10}	−0.27	0.74	3.10×10^{-10}	2.20×10^{2}
96	1.91×10^{-10}	−0.30	0.73	3.94×10^{-10}	2.00×10^{2}
98	2.03×10^{-10}	−0.34	0.71	4.60×10^{-10}	1.81×10^{2}
100	2.68×10^{-10}	−0.39	0.75	5.25×10^{-10}	1.49×10^{2}
102	2.42×10^{-10}	−0.42	0.70	6.65×10^{-10}	1.39×10^{2}
104	2.28×10^{-10}	−0.45	0.65	9.91×10^{-10}	1.20×10^{2}
106	1.09×10^{-10}	−0.03	0.60	1.46×10^{-9}	1.09×10^{2}
108	1.83×10^{-10}	−0.01	0.59	1.77×10^{-9}	8.92×10^{1}
110	1.85×10^{-10}	−0.01	0.61	1.82×10^{-9}	7.42×10^{1}

Table 8.2. Fit results of the IDC curves for samples annealed 3h at 140ºC.

The obtained relaxation times fit the Arrhenius equation for thermally activated processes. Accordingly, the logarithm of the relaxation times was plotted in function of the reciprocal of the temperature and a linear behavior was found (Figure 8.17). The corresponding fitting provided the activation energy and the pre-exponential factor for the annealed cable case: $\tau_0=8.02\times10^{-9}$s, $E_a=0.76$eV.

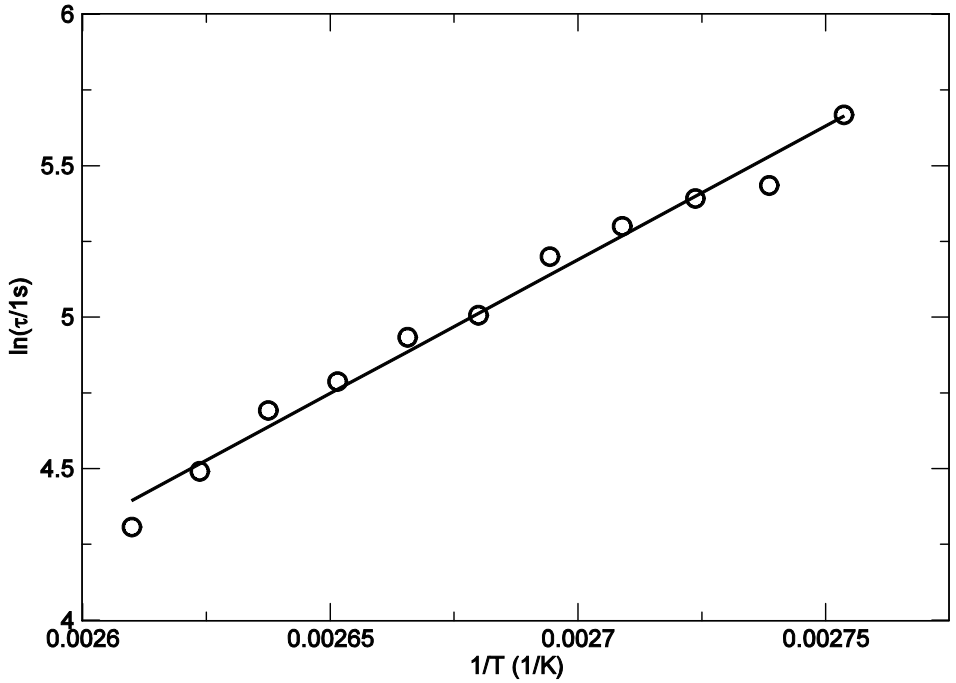

Figure 8.17. Arrhenius plot for samples annealed 3h at 140ºC: (○) relaxation time versus T^{-1}, (—) linear regression.

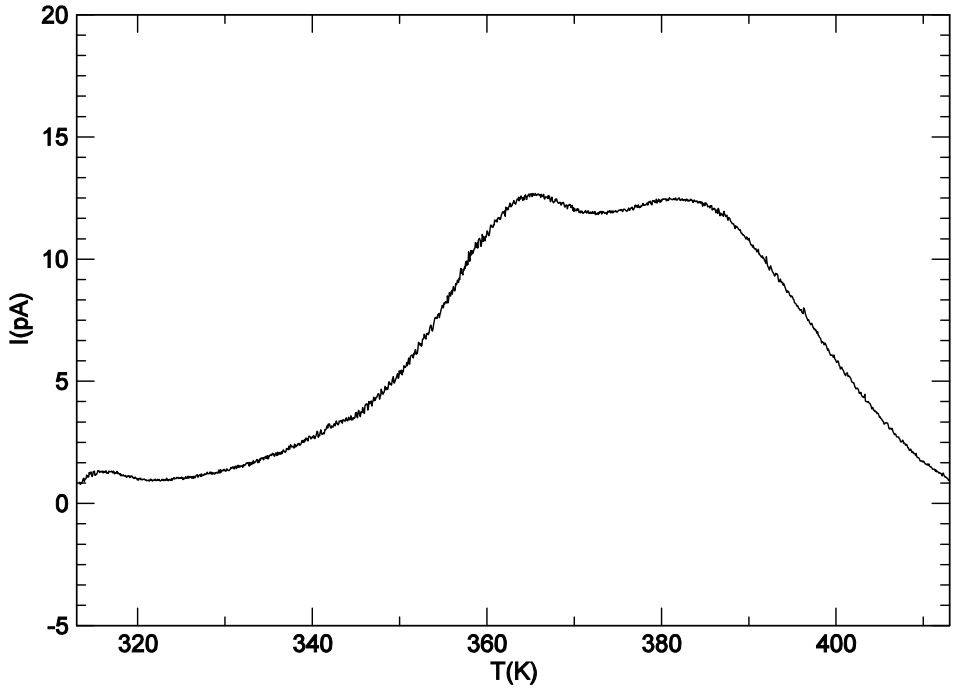

Figure 8.18. TSDC curve for a sample annealed 3h at 140ºC with T_p=140ºC, T_s=40ºC, t_s=5min and v=2ºC/min.

In the Figure 8.18, the TSDC discharge obtained for an annealed sample is shown. A complex spectrum is observed, so the TSDC curve cannot be reproduced by the equation 8.16 with a single β. This is consistent with the fact that at different temperatures different values of β are obtained by IDC (Table 8.2). These results show that the dominant exponential contribution to the isothermal depolarization current is not thermally stable in the annealed samples. This lack of stability makes impossible to

apply the method developed in this chapter, despite some information can be obtained from measurements and fittings. On the other hand, the uncertainity in the exact nature of dipolar relaxation is in this case enhanced due to the impossibility to correlate IDC and TSDC. Several dipolar-like phenomena can provide the exponential current: space charges slightly separated (Gerson dipoles), polar especies coming from the dissociation of manufacturing by-products, polar impurities diffused from SC shields, molecules with an attached ion generated by cross-linking processes at high annealing temperatures (around a 20% of the cross-linking reaction is not completed in the as received samples). Therefore, further research on TSDC spectrum and IDC discharges is needed to fix the mechanisms that give rise to the observed behavior.

8.4 Conclusions

IDC measurements have been performed on as-received cable samples at temperatures close to service conditions. To fit the recorded current successfully it has been necessary to assume the presence of two different contributions: a power law current and a stretched exponential contribution determined by the KWW equation.

A set of measurements on samples with different sizes, shapes and configurations has determined that the exponential current only appears in samples with a thickness greater than a critical value.

Relaxation times obtained from IDC curves, recorded at temperatures ranging from 90ºC to 110ºC, have been fitted to the Arrhenius equation. From the fitting, an activation energy value and a pre-exponential factor have been obtained.

The KWW stretching exponent has been revealed to be almost constant in the studied range of temperatures. This allows us to simulate a TSDC relaxation from the parameters of the isothermal exponential current. The obtained thermo-stimulated current shows a peak that matches the 95ºC peak found in the TSDC spectrum of studied samples. This points out the dipolar character of the 95ºC peak. Therefore, a new method to determine the dipolar character of a TSDC peak consisting in to use a complementary technique like IDC has been established. This can be useful especially when the applied field is low and the classical method is not conclusive.

IDC does not give further clues on the exact nature of the exponential current. In fact, the dipolar current could be produced either by molecular dipoles or dipoles created by microscopic displacement of charge carriers. Anyway, the stability of the current in a wide temperature range, including the fact that the KWW stretching exponent almost does not change with the melting of crystalline fraction, and the way the peak depends on thermal history, allows us to infer that its cause is not in the XLPE itself, but in some additive introduced during the manufacturing process.

Unlike the as-received samples, in samples annealed 3 hours at 140ºC the stretching exponent changes with the temperature. In addition, TSDC performed on annealed samples present a complex spectrum. Therefore, simulating the TSDC curves with a single stretching exponent obtained from IDC measurements is not possible in this case.

References

[1] Tamayo, I.; Belana, J.; Cañadas, J. C.; Mudarra, M.; Diego, J. A. and Sellarès, J. *J. Polym. Sci. Part B Polym. Phys.* **41** (2003), 1412.

[2] Belana, J.; Mudarra, M.; Calaf, J.; Cañadas, J. C.; and Menéndez, E. *IEEE Trans. Electr. Insul.* **28** (1993), 287.

[3] Ménégotto, J.; Demont, P. and Lacabanne, C. *Polymer*. **42** (2001), 4375.

[4] Das-Gupta, D. K. *IEEE Trans. Dielectr. Electr. Insul*. **4** (1997), 149.

[5] Álvarez, F.; Alegría, A.; Colmenero, J. *Phys. Rev. B.* **47** (1993), 125.

[6] Adamec, V. and Calderwood, J.H. *J. Phys. D: Appl. Phys.* **11** (1978), 781.

[7] Alegría, A.; Goitiandía, L. and Colmenero, J. *Polymer*. **37** (1996), 2915.

[8] Randall, J. T., Wilkins, M. H. F. *Proc. Roy. Soc*. (London). **A184** (1945), 366.

[9] Gerson, R. and Rohrbaugh, J. H. *J. Chem. Phys*. **23** (1955), 2381.

[10] Garlick, G. F. J. and Gibson, A. F. *Proc. Phys. Soc*. **A60** (1948), 574.

[11] Ferreira, G. F. L. and de Almeida, L. E.C. *Phys. Rev. B*. **56** (1997), 11579.

[12] Tamayo, I.; Belana, J.; Diego, J.A.; Cañadas, J.C.; Mudarra, M. and Sellarès, J. *J. Polym. Sci. Part B Polym. Phys.* **42** (2004), 4164.

[13] Tamayo, I. "Estudio del comportamiento de la carga de espacio durante la fusión del XLPE en cables de media tensión por TSDC". Ph.D. Thesis. Universitat Politècnica de Catalunya, Terrassa, Spain (2002).

9. TSDC ANALYSIS OF MV CABLE XLPE INSULATION (II): STUDY OF AN INITIAL TRANSIENT RELAXATION

9.1 Introduction

In previous works [1,2,3] a heteropolar TSDC spectrum was observed in as-received XLPE cable samples (see chapter 3). Moreover, the changes in the TSDC profiles resulting from heating the insulation to a predetermined temperature and holding it for a certain time (annealing) were studied. Thus, a peak at approximately 99ºC was observed, which initially decreased with annealing, and then it became homopolar at an intermediate step. For longer annealing times, this homopolar peak increased, it reached a maximum value, and it decreased again, eventually regaining the heteropolar sign. The full development of the transient process described above can be observed in Figure 9.1, which corresponds to a sample annealed at 120ºC. This process was explained assuming two overlapped contributions: a heteropolar one that was active at any step in the annealing process and a transient homopolar one, which was associated with the diffusion of components from the cable semiconducting shield into the insulation bulk. These components would act as trapping centers for charges injected from the electrodes. The transient current sign inversion was related to such injected carriers, but as diffusion of components was exhausted, the always present heteropolar mechanism eventually prevailed.

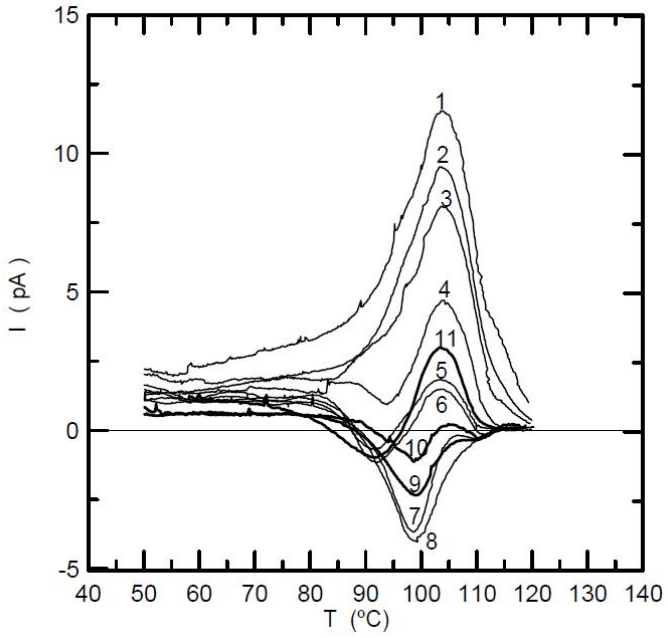

Figure 9.1. TSDC spectra for samples annealed at T_a=120ºC for various times of annealing time t_a=1: 0.5h; 2: 1h; 3: 1.5h; 4: 3.5h; 5: 5.5h; 6: 7.5h; 7: 12h; 8: 17h; 9: 30h; 10: 35h; 11: 47h. NIW processes: T_p=50ºC; V_p=16 kV; T_f=40ºC. Samples were cut from cable D, and they have the geometry indicated in the experimental section, with 7.5 and 13.6mm inner and outer radii, respectively [3].

In this chapter we carry out a sequential application of PEA and TSDC techniques to XLPE insulation of power cables subjected to annealing at high temperatures. The aim is to obtain a better understanding of the transient behavior in the TSDC spectrum described above by introducing results obtained by PEA. Measurements are performed on cable D samples, since most experimental data on this phenomenon have been

obtained from this kind of cable [3]. Cable S samples, which also undergo a transient homopolar peak (see chapter 5), are studied too. First, it is argued that the contaminants generated from chemical reactions that take place at high temperatures during cable manufacturing are the main cause of the transitory relaxation, and then there is an analysis of the behavior of the charges activated when electrets are formed, during the transient stage. A new hypothesis is presented, which associates the observed phenomena with the interaction between the free charge trapped in the crystals surface and the charge located in intercrystalline zones, where the contaminants are mainly located.

9.2 Experimental

The samples consisted of an aluminum core and a XLPE insulation of 7.5mm and 13.6mm (cable D) and 7.75mm and 12.3mm (cable S) of internal and external radii, respectively. All cables were manufactured using the same base polyethylene CP 104 (Repsol) and di-ter-butyl as cross-linking agent, but with two different antioxidants, so two kind of samples were used (D and S). Cables were vulcanized in N_2. The most important cross-linking by-products are ter-butanol, acetone, methane and 2-phenylpropanol-2. More details about cables D and S composition can be found in section 4.1.

The study has been carried out in the temperature range between 50 and 110ºC, along which melting of the crystals takes place, as it is indicated by DSC measurements. Cable samples were annealed at several temperatures T_a for various times of annealing t_a. In order to form the electrets, 20cm long samples has been cut from cables. Strips of 5cm were removed from each end of the outer semiconducting screen. In this way the effective external electrode is formed by a 10cm wide strip centered on the sample. This electrode was grounded during the polarization, while the inner semiconducting screen was positively biased.

The conventional method used to form electrets consists of the application of an electric field (F_p) to the sample during a time (t_p), at a temperature (T_p), which is higher than room temperature (T_r) usually. The sample is then cooled down to a temperature T_s, while the electric field remains applied, and then the TSDC discharge may be carried out. If the polarization was carried by the non isothermal window method (NIW), the electric field F_p is applied only during the cooling of the sample, in the temperature range from T_i down to T_s (see section 4.2.5). This polarization method, which was used in previous works [1,2,4], prevents morphological changes or isothermal crystallization in the samples. In all the cases, the cooling and heating rates were 2.5ºC/min.

TSDC measurements were carried out heating the polarized samples from the initial temperature of fusion (50ºC) up to 140ºC, which resulted in a record of the spectrum of the material. It was observed that all the charge activated during the polarization process had been released at 140ºC. The experimental setup for TSDC measurements consisted of a Heraeus forced-air oven controlled by a Eurotherm 818P PID temperature programmer, a Heizinger high voltage source, and a Keithley 6514 electrometer (see section 4.4 for a more detailed description of the TSDC setup and operation).

For the application of pulsed electroacoustic technique (PEA), samples were cut from cable and were polarized by NIW technique from 140ºC down to room temperature.

The determination of the charge distribution profile by PEA was always carried out at room temperature. Both techniques applied as complementary techniques become quite successful to understand charge trapping and transport processes [5]. The PEA experimental setup and sample preparation are described in section 4.9.

9.3 Results

In order to explain the origin of the transient behavior observed in Figure 9.1, a comparative study between TSDC and PEA measurements on samples equally annealed has been carried out. An as-received cable D sample has been subjected to progressive annealing steps at 140ºC. After each step, while the sample was cooled from 140 to 40ºC, it was polarized to form an electret by the NIW method applying a 12kV to the sample. Once the sample was polarized, the charge profile in the insulation was determined by PEA and the electret was depolarized by TSDC immediately afterwards. This information was obtained step by step during the annealing process at 140ºC. This was done in order to study the changes in the TSDC discharges and correlate these results with the charge profiles within the material, which were obtained by PEA.

Initially, the depolarization current obtained from an as-received sample is heteropolar over all the temperature range, but with annealing the heteropolar contribution decreases, and after 2 hours of annealing at 140ºC, the discharge becomes homopolar (Figure 9.2, curves 3 and 4). For longer annealing times, the peak decreases and the current regains a heteropolar sign again. This process has not been plotted in Figure 9.2 as it looks like the one in Figure 9.1.

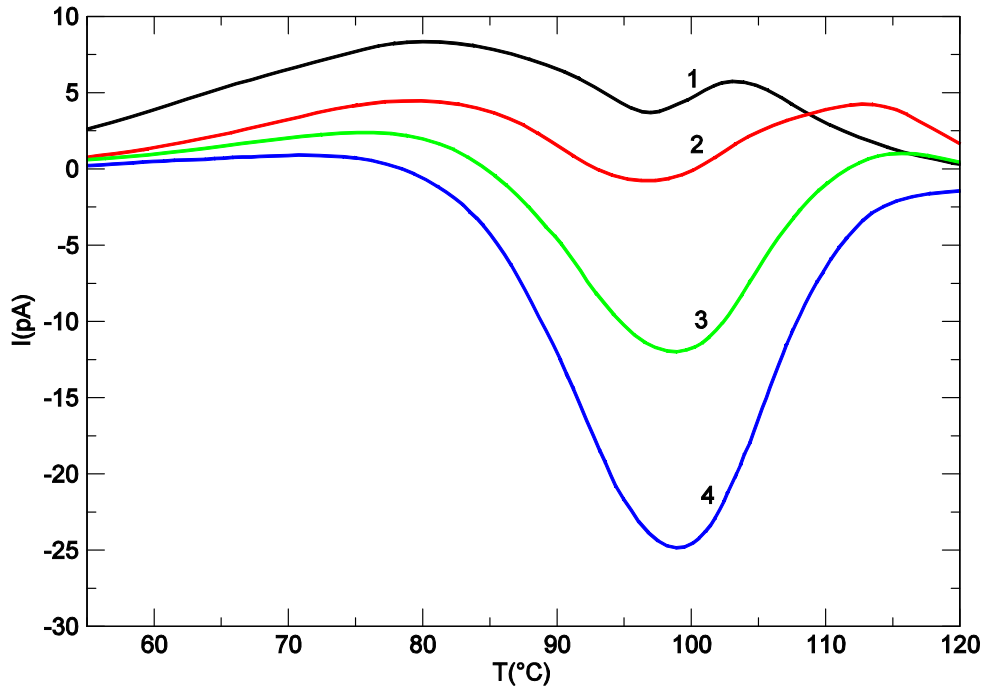

Figure 9.2. TSDC discharges for D cable samples for various annealing times t_a. NIW polarization processes. Annealing temperature T_a=140ºC; T_p=140ºC; V_p=12kV; T_f=40ºC; t_a= 1: 0h; 2: 1h; 3: 2h; 4: 3h.

Figure 9.3 shows the charge profile obtained by PEA before TSDC measurements. The profile in the case of a virgin sample consists of a positive peak close to the cathode (hereafter we will refer to it as π peak) and a small and negative peak close to the anode that is hardly noticeable. As we stated before, the current recorded by TSDC is

heteropolar at this step. Initially it increases with annealing, it splits in two peaks and, afterwards, it decreases progressively. Eventually, it vanishes for longer annealing time, but the TSDC discharge results in the largest homopolar peak (curve 4, Figure 9.2). Concerning PEA results, π is a free charge peak that might be associated with the peak observed in the corresponding TSDC discharge. As in initial annealing steps, TSDC curves are heteropolar and they have a relatively large discharge current, π peak should discharge to the anode in order to explain the discharge current observed (curve 2, Figure 9.2). But if we take into account TSDC curves corresponding to longer annealing times, which are homopolar over the whole temperature range, π peak should discharge to the cathode in this case (curve 3, Figure 9.2). These results are contradictory, as there is a positive peak close to the anode in all cases, and they indicate that there is no simple and straight correlation between this peak and TSDC discharges. If we also assume that π peak causes the corresponding TSDC spectrum, another contradiction arises as when π is minimum the corresponding TSDC peak is maximum (curve 4, Figure 9.2).

All these results suggest the existence of mechanisms that contribute to TSDC discharges in XLPE cable insulation that are not detectable in charge profiles obtained by PEA. Therefore, polar mechanisms, associated with either permanent or induced dipoles should be considered to explain TSDC discharges. Free charges displaced along very small distances and that could not be detected by PEA due to resolution limitation should be considered also [6,7].

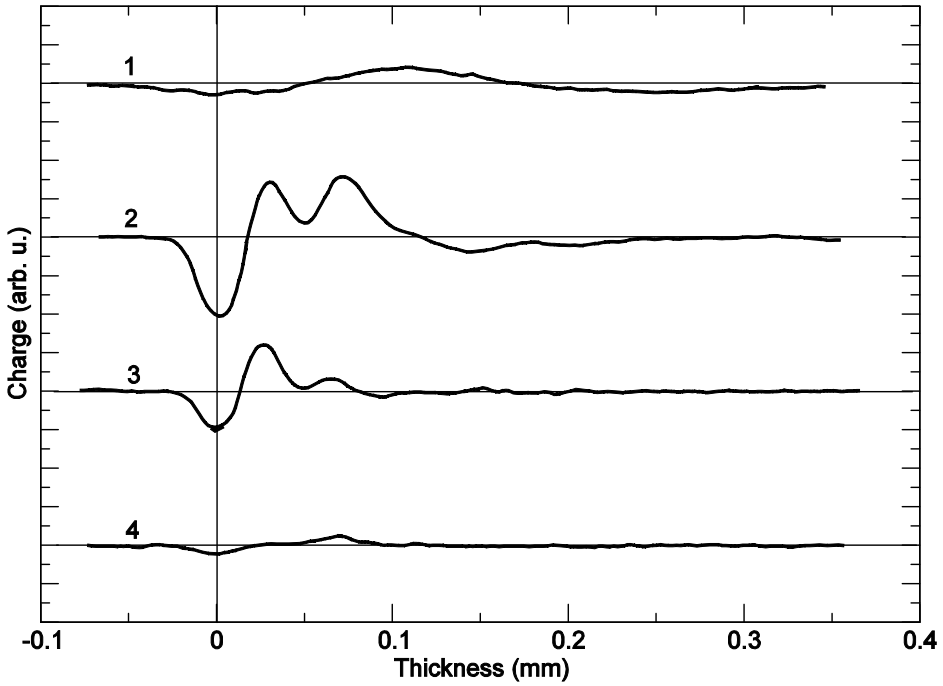

Figure 9.3. Charge profiles obtained by PEA from the samples of Figure 9.2. As PEA is a non destructive technique, charge profiles measurements were carried out before TSDC discharge. Cathode is located at 0.0. Only the region close to the cathode is plotted in order to increase the resolution. The anode is located at 6.0mm, out of the range plotted.

Similar comparative TSDC-PEA measurements were performed with group S cable samples annealed at 120ºC up to 7 days. In this case three applied voltages (V_p=60, 80 and 100kV) were used and polarization was performed by the NIW method between 120 and 50ºC. Evolution of TSDC curves in this case is similar to the evolution

observed in cable D samples presented in Figure 9.1. After 7 days of annealing, a similar discharge curve is obtained for the three applied voltages (Figure 9.4).

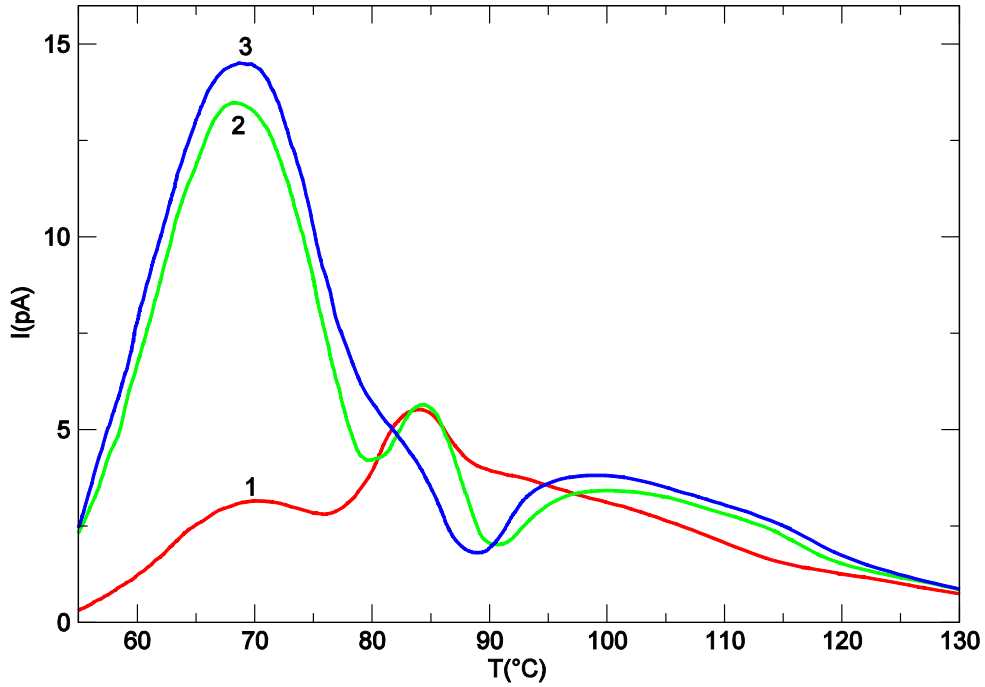

Figure 9.4. TSDC discharges obtained from cable S samples annealed at T_a=120ºC for t_a=168h. They were conventionally polarized at a polarization temperature T_p=90ºC for a polarization time t_p=1h. Then samples were cooled to a temperature T_f=45ºC with electric field applied. The voltages applied were V_p=60kV (1); 80kV (2) and 100kV (3).

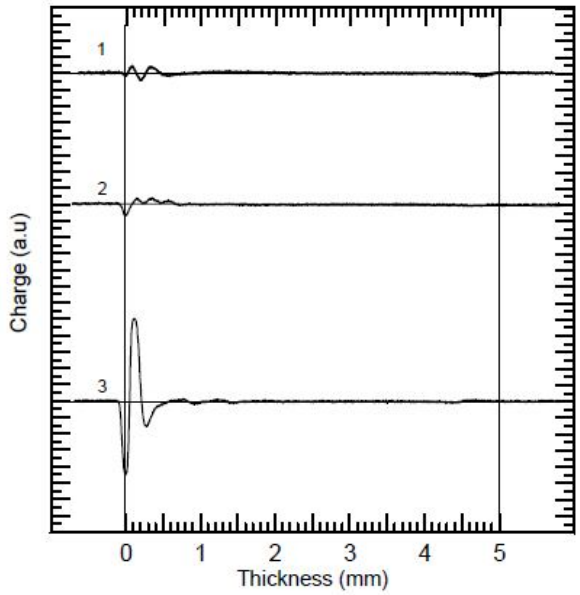

(a)

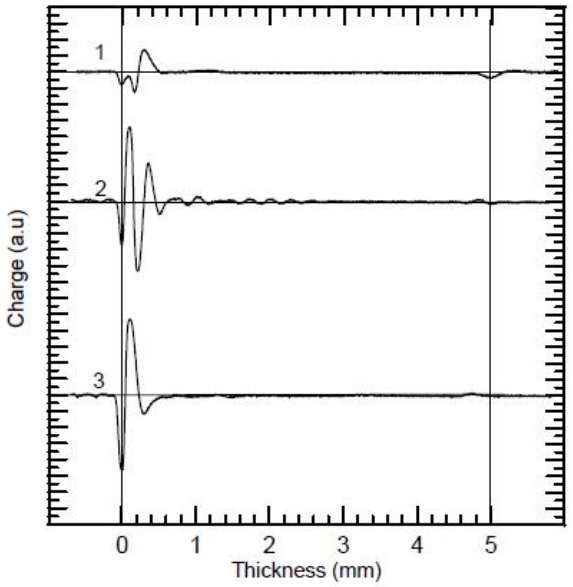

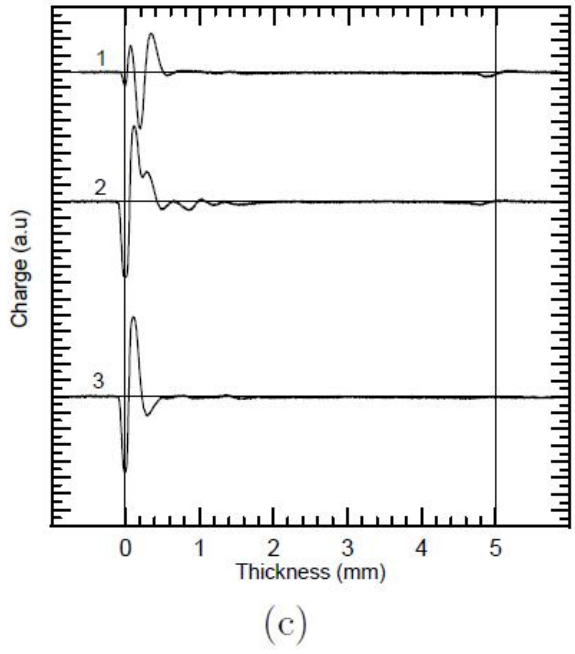

Figure 9.5. Charge profiles obtained by PEA from cable S samples for various applied voltages and annealing times. T_a=120ºC. Conventionally polarized electrets at a polarization temperature T_p=90ºC for a polarization time t_p=1h. Samples were cooled to a temperature T_f=45ºC with an applied electric field. The voltages applied were V_p=20kV (figure a); 60kV (figure b) and 100kV (figure c). Annealing time t_a= corresponds to 0h (1); 8h (2) and 168h (3) in all figures. Cathode is located at 0.0 in all cases.

The charge profiles of the aforementioned samples can be seen in Figure 9.5. It can be noticed that curves 2, which corresponds to t_a=8h, i.e. an annealing time within the transient duration, are different for all voltage applied, but curves 3, which were determined after 168 hours annealing, are very similar in all cases. This result indicates

that eventually the cable insulation reaches a stable situation with annealing time. Assuming that dipoles do not contribute to PEA profiles, these measurements point out that trapped charges are conditioned by the transient behavior and finally they reach a stable distribution after a long annealing time, resulting in similar profiles, so that the effect of the applied voltage is not noticeable by PEA measurements in the final stage.

Cable D and S were manufactured following the same process and using the same base polyethylene and cross-linking agent, but with different antioxidant. Therefore, the results obtained are in good agreement and they are consistent with the association of the transient process with additives used in the cable manufacturing or with by-products resulting from processing, which evolve when the cable is subjected to annealing. Some of these compounds are volatile and they may be removed progressively by degassing, but at a different rate. We have studied the total charge associated with the homopolar peak in the TSDC discharge after annealing the samples. In the case of TSDC peaks related to polar mechanisms, the total released charge in the discharge is a linear function of the applied voltage and no linear correlation is expected in the case of peaks related to space charge [8]. In Figure 9.6 total released charge (Q) has been plotted as a function of the applied voltage and a linear correlation is observed. This result indicates that this peak should be associated with a uniform mechanism, which may be originated by induced or permanent dipoles, which can explain that no direct correlation between PEA and TSDC was observed.

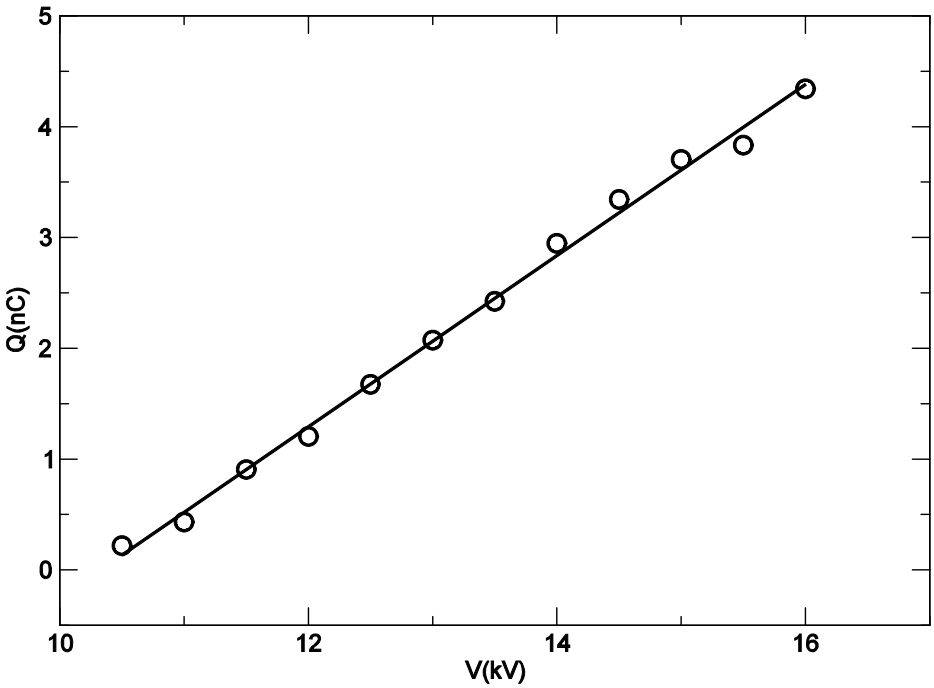

Figure 9.6. Total charge of the homopolar peak released during TSDC discharge vs. the voltage applied. Cable D samples were polarized by NIW processes. The polarization parameters were: T_p=120ºC; T_s=40ºC.

9.4 Discussion

An explanation to the presence of a transient step that results in the emergence of a homopolar peak by TSDC is required. This explanation must be associated with some mechanism unnoticeable by PEA, and it has also to take into account the fact that certain by-products resulting from the cross-linking process are removed during this transition. We shall consider that XLPE cable insulation must contain a large number of

small crystalline regions, since cable is cooled quickly at the end of the manufacturing process. As-received cable was subjected to a degassing process at the production plant (3h at 80ºC), however this process is not completed and we shall assume some initial concentration of cross-linking by-products in the cable. Another important fact we must as well consider is that cross-linking process is not completed during the manufacturing process. According to the factory, about 15-20% of cross-linking agent remains unreacted in the as-received cable. During annealing at high temperatures both processes will go on simultaneously, with the generation of new cross-linking by-products during the reaction and the degasification of new and existing by-products. We have checked this point by measuring the mass loss of a sample during the annealing (section 6.4.1). Conductivity also shows a short-term transient behavior above 80ºC in samples without semiconducting screens, which was explained in terms of cross-linking by-products decomposition and volatilization (see chapter 6).

We assume that the material is conformed by the mixture of two phases with different conductivity σ_a and σ_c, which correspond to the conductivity of the amorphous and crystalline phases respectively ($\sigma_a > \sigma_c$). Continuity equation and differences in the conductivities lead to the accumulation of charge $+q_s(t)$ in the region where the current reaches the crystal and $-q_s(t)$ in the exit region, as long as the crystal size allows this. Therefore, when the sample is polarized the crystal surfaces faced to the anode become charged positively.

Since the current densities $J_a > J_c$, then

$$J_c = J_a - \frac{dq_s(t)}{dt} \tag{9.1}$$

as it can be seen in Figure 9.7. Charge at the surfaces becomes “frozen” when the samples are cooled. It has been observed by electrostatic force microscopy that high space charge density can be trapped at the surface of spherulites [9]. While the poling field is applied, dipoles located in interlamellar zone are oriented. These dipoles are associated with volatile compounds thermally generated during annealing. Their orientation may be partially limited by the field F_s, which results from the charge density formed in the surface of the crystals and it is opposite to the applied poling field F_p, since F_p exceeds F_s.

Once the sample is cooled and the field F_p is removed, the dipoles of the amorphous intercrystalline zone are subjected to the field F_s created by the “frozen” charge (Figure 9.7). As F_p exceeds F_s, some of the dipoles located in the material (the most mobile ones) may become immediately reoriented on removing F_p, so they do not cause any current associated with polarization under F_s during the subsequent heating. In the case of the least mobile dipoles, they become reoriented progressively, during the TSDC discharge, with the increase in their mobility with temperature. In this case, they generate a current with one or more peaks during the TSDC scan. It is easy to infer that the current associated with this reorientation will be heteropolar (opposite to the charging current).

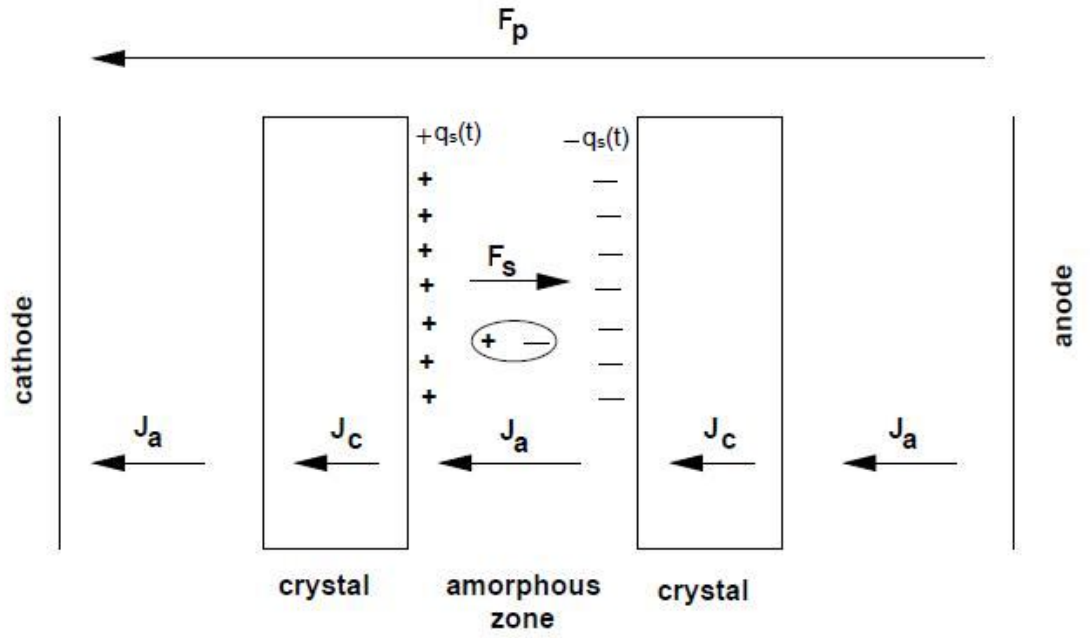

Figure 9.7. Accumulation of charge $q_s(t)$ in the amorphous-crystalline interphases due to the differences of the conductivity σ between amorphous (σ_a) and the crystalline (σ_c) regions. It has been assumed that $\sigma_a > \sigma_c$. The arrows indicate the polarizing field F_p, the field created by charge $q_s(t)$, and the current densities J in the amorphous phase and in the crystal directions during the polarization.

When the temperature is high enough to melt these small crystals, then charge trapped in the crystal surfaces is released. As $q_s(t)$ relaxes due to recombination, F_s decreases progressively and the dipoles loose the acquired orientation. This disorientation will generate the homopolar peak in the TSDC spectrum. We must notice that simultaneously, the recombination of $+q_s$ with $-q_s$ occurs, which will generate a heteropolar discharge peak in the TSDC spectrum. Nevertheless, as it can be seen in Figure 9.5 at certain stage of annealing, the peak associated with the homopolar mechanism is larger than the associated with the heteropolar one. As the latter is related to trapped charge neutralization, its contribution to the current measured its lower than dipoles contribution, as its efficiency is lower than for dipoles, especially when recombination takes place at short distances [8]. For this reason, we can observe homopolar peaks greater that the free charge ones when dipolar mechanism is very significant. In fact, trapped charge liberation and dipolar disorientation occur at the same time above 90ºC. Therefore the discharge current can be considered the sum of the heteropolar and the homopolar (dipolar disorientation) contributions.

According to the presented model, TSDC discharges of as-received samples can be heteropolar (cable D, Figure 9.1) or present a noticeable homopolar contribution, depending on the initial concentration of cross-linking by-products in the sample. With annealing, however, generation of new polar components takes place and the TSDC spectrum develops in all cases a homopolar contribution. If the concentration of contaminants is high enough (this occurs at the first stages of annealing) the dipolar current may exceed the heteropolar one widely, resulting in a completely homopolar peak. Due to the progressive disappearance of dipoles caused by degasification of contaminants, the heteropolar current becomes dominant again.

The superposition of the heteropolar current of the detrapped charge and the homopolar current of dipoles can be seen in Figure 9.8. It shows that the addition of both contributions can originate different peaks depending on the by-products present. These curves have been calculated conveniently in order to show this process at temperatures above 90ºC, which corresponds to the temperature range over which melting of the most developed lamellae happens. The resulting curve is in good agreement with a curve corresponding to an intermediate step of the transient, for example curve 3 in Figure 9.2.

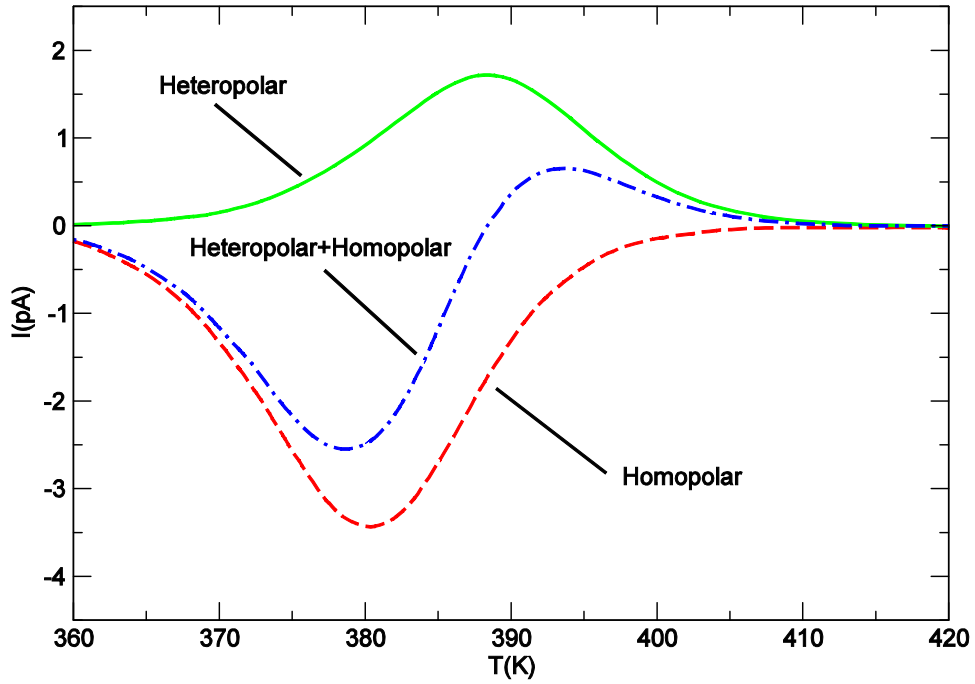

Figure 9.8. Simulated TSDC resulting from the addition of a heteropolar and a homopolar peaks which helps to understand the shape of the transient peak observed in TSDC discharge. Discharges have been calculated using general kinetic order model (see chapter 4) [1,10–12]. Parameters of homopolar peak: Q_0=−60.5mC; s_0=0.31×10^{34}s^{-1}; E_a=2.35eV; b=1.7. Parameters of heteropolar peak: Q_0=30.5mC; s_0=0.31×10^{34}s^{-1}; E_a=2.40eV; b=1.7 (Q_0 is the total released charge, s_0 the pre-exponential factor, E_a the activation energy and b the kinetic order).

Once the by-products have been eliminated by annealing at high temperatures, the resulting TSDC curve should be characteristic of the insulating material for given conditions of polarization. Thus, TSDC discharges obtained from repeated processes of NIW polarization applied to the same sample tend to converge to a steady curve, after some repetitions, due to the cumulative annealing (for instance, see Figure 5.8 in chapter 5).

9.5 Conclusions

PEA and TSDC provide complementary information on similar sample configuration. PEA measurements show that for long annealing times charge profiles converge to a common shaped profile, in which a positive peak is observed close to the cathode. In TSDC measurements a transient homopolar peak is noticed when cable insulation is subjected to annealing. It has been checked that the area of this homopolar peak is proportional to the applied voltage, so that it indicates that this peak is originated by a uniform (dipolar) mechanism.

No straightforward relation between TSDC discharges and space charge detected by PEA can be established. Therefore, TSDC curves should be explained by considering mechanisms that are not detectable in charge profiles obtained by PEA, like polar mechanisms associated with either permanent or induced dipoles, or charges with opposite polarities displaced along very small distances.

A model to explain the TSDC transient behavior based on a dipolar mechanism is proposed. This model can explain both, the transient character of the peak observed by TSDC (as it is associated with polar species that can be removed by annealing) and the homopolar sign of the depolarization current. During the polarization, dipoles in the amorphous regions are oriented in the applied field direction and charge is injected and trapped on the surfaces of the crystals. When the sample is depolarized to record the TSDC, dipoles, which are then subjected to the electric field originated by trapped charges, are activated again by this field. When the crystals melt, this trapped charge is released and it moves through the amorphous region and eventually recombines, originating a heteropolar current. Then dipoles regain equilibrium and they originate a homopolar current.

At certain stage of annealing, the peak associated with the homopolar mechanism is larger than the associated with the heteropolar one. As both processes occur at the same temperature range, the total current (the sum of both contributions) is homopolar because the response of the dipolar mechanism is dominant at this stage, since it is a more effective relaxation process. With annealing, dipoles associated with volatile species disappear and, eventually, the total current becomes heteropolar again, and the current originated by released charge recombination becomes dominant.

The presented model is consistent with some complex spectrums that can not be explained just by taking into account the observable space charge dynamics. Future research could confirm the potential of this model and study its range of validity. Thus, other complementary techniques and analytical tools, such as computer simulation, could be used to check the assumed hypothesis.

References

[1] Tamayo, I.; Belana, J.; Cañadas, J. C.; Mudarra, M.; Diego, J. A. and Sellarès, J. *J. Polym. Sci. Part B Polym. Phys.* **41** (2003), 1412.

[2] Tamayo, I.; Belana, J.; Diego, J.A.; Cañadas, J.C.; Mudarra, M. and Sellarès, J. *J. Polym. Sci. Part B Polym. Phys.* **42** (2004), 4164.

[3] Tamayo, I. "Estudio del comportamiento de la carga de espacio durante la fusión del XLPE en cables de media tensión por TSDC". Ph.D. Thesis. Universitat Politècnica de Catalunya, Terrassa, Spain (2002).

[4] Vanderschueren, J. and Gasiot, J. in "Thermally Stimulated Relaxation in Solids". Edited by Braünlich, P. Springer-Verlag Berlin Heidelberg, Germany (1979), pp. 135–223.

[5] Omori, S.; Matsushita, M.; Kato, F. and Ohki, Y. *Jpn. J. Appl. Phys.* **46** (2007), 3501.

[6] Fukushi, N. "Charge Transport and Electrostatics with Their Applications". Wada, Y.; Perlmann, M. M.; Kokado, H., Eds. Elsevier, New York, USA (1979), pp. 307–311.

[7] Gerson, R. and Rohrbaugh, J. H. *J. Chem. Phys.* **23** (1955), 2381.

[8] Van Turnhout, J. "*Thermally Stimulated Discharge of Polymer Electrets*". Elsevier Sci. Pub. Co. Amsterdam, Netherlands (1975).

[9] Ye-Wen, Z.; Ji-Xiao, L.; Fei-Hu, Z.; Zong-Ren, P.; Chang-Shun, W. and Zhong-Fu, X. *Chinese Phys. Lett.* **19** 2002, 1191.

[10] Chen, R. and Kirsh, Y. "Analysis of Thermally Stimulated Processes". Pergamon, Oxford, UK, 1st edition (1981).

[11] Mudarra, M. and Belana, J. *Polymer*. **38** (1997), 5815.

[12] Mudarra, M.; Belana, J.; Cañadas, J. C. and Diego, J. A. *J. Polym. Sci. B: Polym. Phys*. **36** (1998), 1971.

10. FINAL CONCLUSIONS

Conductivity of XLPE insulation in power cables. Effect of thermal annealing

1. Significant differences in the behavior of the conductive properties of XLPE cable samples with SC screens and without them (XLPE cylinders) have been observed at temperatures within the melting range (50–110ºC). SC screens condition very much the electrical behavior of the entire cable and, therefore, they have to be taken into account in both theoretical and experimental research.

2. Good correlation between results of measurements carried out in time and frequency domain has been obtained.

3. A plausible explanation for the results based on the coexistence of two conduction mechanisms is proposed. On the one hand, there is a charge transport by extended states slightly dependent on temperature in the studied range of temperatures. On the other hand, there is a conduction mechanism by thermally assisted hopping between localized states at low fields.

4. The contribution of the hopping mechanism has been successfully fitted to the Mott's law ($ln(\sigma) \propto T^{-1/4}$) for hopping between localized states.

5. The hopping conduction mechanism is efficient from a certain critical temperature T_c, between 70ºC and 80ºC, due to the increase of defect or impurity concentration. Such increase is associated with species diffused from SC screens. These defects or impurities may act as trapping centers of charge injected from the electrodes and are responsible for the observed conductivity increase in cable samples with annealing.

6. Dissociation of species present in cable insulation, such as cross-linking by-products, also can generate trapping centers and contribute to the conductivity increase. In the case of XLPE cylinders, this is the only available source of traps. Once this source is exhausted, and taking into account that many of these generated species are volatile, the contribution of the hopping mechanism to the conductivity progressively decreases until a nearly constant value is attained.

7. In the case of entire cable samples, diffusion of chemical species from SC screens can maintain the increase in conductivity for longer annealing times.

8. After 30 days at 90ºC, the diffusion rate decreases. Once this diffusion from the SC shields is almost exhausted, further annealing results in the progressive decrease of the total diffused component concentration in the insulation and consequently in conductivity.

9. FTIR results are consistent with this model and refuse the influence of thermo-oxidative processes at this temperature.

TSDC study of XLPE recrystallization effects in the melting range of temperatures

1. TSDC/WP results show a heteropolar peak between 50 and 110ºC, with a maximum at 105ºC. There is an optimal polarization temperature (T_{po}) around 90–95ºC. This behavior indicates that the observed peak is not directly related to the total crystalline fraction as in this case one would expect a monotonic decrease in the TSDC response with increasing polarization temperatures.

2. DSC and X-ray diffractometry results show that recrystallization processes exist when the sample is annealed in the melting range of temperatures. The recrystallization rate decreases with annealing time and it is more important if the sample is heated from room temperature to T_p, than if it is cooled down from the melt.

3. The behavior of the 105ºC heteropolar peak with the polarization temperature is explained by taking into account the recrystallization role when the insulation is isothermally polarized. During recrystallization, the new crystalline fraction grows in a polarized state due to the applied electric field, and develops the depolarization current when it melts during the TSDC measurement.

4. Two experiments have been performed to confirm this hypothesis. In one of them, the sample has been annealed previously to polarization. In the other one, several cooling rates have been used. Both experiments give results that agree with the aforementioned hypothesis.

5. Free charge located in amorphous-crystalline interfaces also can contribute to the 105ºC peak, although polarization due to the recrystallization effect is dominant when isothermal polarization (TSDC/WP null window polarization) is used.

Combined TSDC and IDC analysis of MV cable XLPE insulation: identification of dipolar relaxations in dielectric spectra

1. Isothermal depolarization currents of as-received cable samples at temperatures close to service conditions can be considered as the combination of two different contributions: a power law current and a stretched exponential contribution determined by the KWW equation.

2. The exponenatial contribution can not be noticed in thin film samples. The determining factor for its appearance is neither the shape nor the contact with SC layers, but the thickness.

3. The relaxation time of the stretched exponential current is thermally activated and fits the Arrhenius equation.

4. The KWW stretching exponent can be considered as a constant in the studied range of temperatures.

5. It is possible to simulate a TSDC relaxation from the parameters of the isothermal exponential current. The obtained peak matches the 95ºC peak

present in the TSDC spectrum of as-received samples. By this way, the dipolar character of the 95ºC peak is confirmed.

6. Unlike the as-received samples, in samples annealed 3 hours at 140ºC the stretching exponent changes with the temperature. Therefore, simulating the TSDC curves with a single stretching exponent obtained from IDC measurements is not longer possible.

7. Despite some uncertainty in the exact nature of the analyzed relaxations, correlation of IDC data with TSDC data shows promise in the study of systems where high electric fields can not be applied.

Study of an initial transient relaxation by TSDC and PEA

1. PEA and TSDC techniques have been combined to study the evolution of the XLPE cable samples with annealing and, in particular, the transient homopolar reversal first detected by Tamayo.

2. PEA measurements show that for long annealing times charge profiles converge to a common shaped profile, in which a positive peak is observed close to the cathode.

3. In TSDC measurements a transient homopolar peak is noticed when cable insulation is subjected to annealing at high temperatures. The area of this homopolar peak is proportional to the applied voltage, so that it would indicate that this peak is originated by a uniform mechanism.

4. No straightforward relation between TSDC discharges and space charge detected by PEA can be established. Therefore, TSDC curves should be explained by considering mechanisms that are not detectable in charge profiles obtained by PEA, like polar mechanisms –associated with either permanent or induced dipoles– or charges with opposite polarities displaced along very small distances.

5. A model based on a dipolar mechanism that can explain both, the transient character of the peak observed by TSDC and the homopolar sign of the depolarization current is proposed.

6. During polarization, dipoles in the amorphous regions are oriented in the applied field direction and charge is injected and trapped on crystals surfaces.

7. During the TSDC heating ramp, dipoles, which are then subjected to the electric field originated by charges trapped on crystals surfaces, are activated by this field newly. When the crystals melt, this trapped charge is released and it moves through the amorphous region and eventually recombines, originating a heteropolar current. Then dipoles regain equilibrium and they originate a homopolar current.

8. At certain stage of annealing, the peak associated with the homopolar mechanism is larger than the associated with the heteropolar one. As both

processes occur at the same temperature range, the total current (the sum of both contributions) is homopolar because the response of the dipolar mechanism is dominant at this stage, since it is a more effective relaxation process.

9. With further annealing, dipoles associated with volatile species disappear and, eventually, the current originated by released charge recombination becomes dominant, and, therefore, the total current regains the heteropolar condition.

10. Future research could check the assumed hypothesis and explore the applicability of the model.

APPENDIX: PEER-REVIEWED PUBLICATIONS ASSOCIATED WITH THIS THESIS

1. Diego, J. A.; Belana, J.; Òrrit, J.; Sellarès, J.; Mudarra, M. and Cañadas, J. C. "TSDC study of XLPE recrystallization effects in the fusion range of temperatures". *Journal of Physics D. Applied Physics*, **39** (2006), 1932–1938.

2. Frutos, F.; Acedo, M.; Mudarra, M.; Belana, J. Òrrit, J. Diego, J. A. Cañadas, J. C. and Sellarès J. "Effect of annealing on conductivity in XLPE mid-voltage cable insulation". *Journal of Electrostatics*, **65** (2007), 122–131.

3. Òrrit, J.; Cañadas, J. C.; Sellarès, J. and Belana, J. "Identification of dipolar relaxations in dielectric spectra of mid-voltage cross-linked polyethylene cables" *Journal of Electrostatics*, **69** (2011), 119–125.

4. Diego, J. A.; Belana, J.; Orrit, J.; Cañadas, J. C.; Mudarra, M.; Frutos, F. and Acedo, M. "Annealing effect on the conductivity of XLPE insulation in power cable". *IEEE Transactions on Dielectrics and Electrical Insulation*, **18** (2011), 1554–1561.

5. Belana, J.; Diego, J. A.; Orrit, J.; Tamayo, I. and Mudarra, M. "Study of an initial transient relaxation in cable XLPE insulation by TSDC and PEA". *IEEE Transactions on Dielectrics and Electrical Insulation*, **18** (2011), 2074–2082.